12-2018

Non-Contact Evaluation Methods for Infrastructure Condition Assessment

Sattar Dorafshan
Utah State University

NON-CONTACT EVALUATION METHODS FOR INFRASTRUCTURE

CONDITION ASSESSMENT

by

Sattar Dorafshan

A dissertation submitted in partial fulfillment
of the requirements for the degree

of

DOCTOR OF PHILOSOPHY

in

Civil and Environmental Engineering

Approved:

_____   _____
Marc Maguire   Paul Barr
Major Professor   Committee Member

_____   _____
Marvin W. Halling   Yan Sun
Committee Member   Committee Member

_____   _____
Calvin Coopmans   Laurens H. Smith, Ph.D.
Committee Member   Vice President for Research and
                                     Dean of the School of Graduate Studies

UTAH STATE UNIVERSITY
Logan, Utah

2018

ABSTRACT

NON-CONTACT EVALUATION METHODS FOR INFRASTRUCTURE

CONDITION ASSESSMENT

by

Sattar Dorafshan, Doctor of Philosophy

Utah State University, 2018

Major Professor: Dr. Marc Maguire
Department: Civil and Environmental Engineering

The United States infrastructure, e.g. roads and bridges, are in a critical condition.

Inspection, monitoring, and maintenance of these infrastructure in the traditional manner

can be expensive, dangerous, time-consuming, and tied to human judgment (the

inspector). Non-contact methods can help overcoming these challenges. In this

dissertation two aspects of non-contact methods are explored: inspections using

unmanned aerial systems (UASs), and conditions assessment using image processing and

machine learning techniques.

In chapter two, UASs applications for bridge inspections are investigated through

past studies and project. At its best, current technology limits UAS use to an assistive tool

for the inspector to perform a bridge inspection faster, safer, and without traffic closure.

However, as the study shows profiting from UASs is only possible when certain

conditions are met. In the third chapter, the minimum requirements in terms of, UAS,

camera, lighting conditions, and clearance, to find fatigue cracks in steel bridge are

investigated. The results showed that when these requirements are met, UASs can match human inspections. In order to determine the human effects on the UAS inspections of steel bridges, several UAS inspections were carried out which is the subject of the fourth chapter. In chapters five, a variety of common edge detectors in the spatial domain (Roberts, Prewitt, Sobel, and Laplacian of Gaussian) and in the frequency domain (Butterworth and Gaussian), are used to detect concrete cracks from visual images. Chapter six compares the performance of the same edge detectors and deep convolutional neural networks (DCNN), in fully trained, transfer learning, and classifier modes. Chapter seven investigates the feasibility of using a DCNN in inspection of concrete decks and buildings using UASs. Chapter eight presents a dataset with more 56,000 fully labeled images of three types of concrete structures. In chapter nine, applications of infrared thermography for in-line weld inspections are investigated. Finally, chapter ten is conclusions.

(404 pages)

PUBLIC ABSTRACT

NON-CONTACT EVALUATION METHODS FOR INFRASTRUCTURE

CONDITION ASSESSMENT

Sattar Dorafshan

The United States infrastructure, e.g. roads and bridges, are in a critical condition. Inspection, monitoring, and maintenance of these infrastructure in the traditional manner can be expensive, dangerous, time-consuming, and tied to human judgment (the inspector). Non-contact methods can help overcoming these challenges. In this dissertation two aspects of non-contact methods are explored: inspections using unmanned aerial systems (UASs), and conditions assessment using image processing and machine learning techniques. This presents a set of investigations to determine a guideline for remote autonomous bridge inspections.

ACKNOWLEDGMENTS

Completion of this research was not easy and if it was not for Dr. Marc Maguire's support, this dissertation would have ended up with the first two chapters only. I was very lucky to have Dr. Maguire as my advisor, mentor, boss, and friend. He has encouraged me to become a better academic and a more confident person, through his friendly mentorship, firm trust, and encouragement. After six years of grad school, I can easily say that my goal is to be like him when I am an adviser.

I would like to thank Dr. Marv Halling, and Dr. Paul Barr from department of civil and environmental engineering, not just for being on my committee; but for their strong roles in improving my Ph.D. program either as instructors or as supervisors in mutual research projects. I also want to show my gratitude to Dr. Cal Coopmans from department of electrical and computer engineering for his collaboration in this dissertation. Several parts of this research could not be completed without Dr. Coopmans's technical and intellectual support. A special thanks to Dr. Yan Sun from department of mathematics and statistics for agreeing to be on my committee.

I want to show my gratitude to the following individuals which their help definitely improved this study: Hunter Buxton, Hannah Young, Dan Robinson, all from Utah State University, Leslie Campbell from Purdue University, Dr. Robert Thomas from Clarkson University, and Nathaniel Colton.

Sattar Dorafshan

CONTENTS

LIST OF TABLES

Table   Page

LIST OF FIGURES

Figure   Page

Figure   Page

Figure   Page

Figure   Page

CHAPTER I

INTRODUCTION

The United States infrastructure, e.g. roads and bridges, are in critical conditions.

Inspection, monitoring, and maintenance of these infrastructure in the traditional manner

can be expensive, dangerous, time-consuming, and tied to human judgment (the

inspector). Non-contact methods can help overcoming these challenges. In this

dissertation two aspects of non-contact methods are explored: inspections using

unmanned aerial systems (UASs), which are investigated in chapters two, three, and four,

and structural conditions assessment using image processing and machine learning

techniques, which are investigated in chapters five, six, seven, eight, and nine.

In chapter two, UASs applications for bridge inspections are investigated through

past studies and project. This chapter shows that the current technology limits UAS use to

an assistive tool for the inspector to perform a bridge inspection faster, safer, and without

traffic closure. The major challenges for UASs are satisfying restrictive Federal Aviation

Administration regulations, control issues in a GPS denied environment, pilot expenses

and availability, time and cost allocated to tuning, maintenance, post-processing time,

and acceptance of the collected data by bridge owners.

Chapter three studies the feasibility of using UAS for fatigue crack detection in

bridges with fracture critical members (FCM) through real-time (field) and post-flight

(desk) visual inspection. The effects of surface illumination on the minimum crack-to-

camera (MCC) distance at which a fatigue crack can be detected was investigated in the

laboratory. Mock field inspections evaluated the achievable crack-to-platform (ACP)

distance in GPS-denied and windy environments, and determine if known cracks can be

identified at achievable standoff distances. Finally, two FCM inspections demonstrated the field performance of UAS in identifying fatigue cracks. Results highlight the importance of camera specifications and surface illumination in determining the required standoff distance of crack detection. Furthermore, the results demonstrate the difficulties in obtaining clear images with unstable UAS in GPS-denied or windy environments. Nevertheless, the best performing platform tested in this study exhibited performance comparable to the average of 30 human inspectors at a fatigue crack identification training structure. The limited results presented here proved the feasibility of using UAS for fatigue crack detection in FCM inspections of steel bridges, but highlighted the shortcomings of UAS for this type of hands-on inspection.

Chapter four investigates the use of Unmanned Aerial Systems (UASs) for the inspection of bridges with fracture critical members to find fatigue cracks. The research team had four inspectors inspecting a probability of detection (POD) training structure at the at the Steel Bridge Research, Inspection, Training, and Engineering (S-BRITE) center at Purdue University to locate the fatigue crack(s) on the POD frame specimens. The results of these inspections were compared to results of 30 hands-on inspections in terms of hit rate, hit to call ratio, inspection time, and length of the largest crack missed. In general, the desk inspections and the field inspections had comparable hit rates and hit to call ratios; however, the type and location of the inspected specimens significantly affected the results of the UAS-assisted inspections. The results indicate the superiority of hands-on inspections to UAS-assisted inspections in terms of hit rate, hit to call ratio, and inspection time; however, the UAS-assisted inspections matched or even exceeded the hands-on results in certain scenarios. In addition, the desk inspections resulted in

detecting smaller cracks (8% smaller than the field inspections and 11% smaller than the hands-on inspections). Regardless, the results can be considered satisfactory since none of the inspectors had previous UAS-assisted inspection training or experience.

Chapter five discusses image processing algorithms for detection of defects in concrete. Such algorithms are useful for improving the accuracy of crack detection during autonomous inspection of bridges and other structures. The authors propose a generic image processing algorithm for crack detection, which includes the major steps of filter design, edge detection, image enhancement, and segmentation. The edge detection was carried out by six filters in the spatial (Roberts, Prewitt, Sobel, and Laplacian of Gaussian) and frequency (Butterworth and Gaussian) domains. These algorithms are applied to fifty images each of defected and sound concrete and an inspector attempted to identify cracks in binary images. The performance of the six filters is compared in terms of accuracy, precision, minimum detectable crack width, computational time, and noise-to-signal ratio. In general, frequency domain techniques were slower than spatial domain methods due to computational intensity of the Fourier and inverse Fourier transformations used to move between the spatial and frequency domains. Frequency domain methods also produced noisier images than spatial domain methods. Crack detection in the spatial domain using the Laplacian of Gaussian filter proved to be the fastest, most accurate, and most precise method, and resulted in the finest minimum detectable crack width.

Chapter six compares the performance of the same edge detectors, but on the pixel level, and deep convolutional neural networks (DCNN) for image-based crack detection in concrete structures. A dataset of 19 high definition images (3420 sub-images,

319 with cracks and 3101 without) of concrete is analyzed using the six edge detection

schemes (Roberts, Prewitt, Sobel, Laplacian of Gaussian, Butterworth, and Gaussian) and

using the AlexNet DCNN architecture in fully trained, transfer learning, and classifier

modes. The relative performance of each crack detection method is compared here for the

first time on a single dataset. Edge detection methods accurately detected 53–79% of

cracked pixels, but they produced residual noise in the final binary images. The best of

these methods was useful in detecting cracks wider than 0.1 mm. DCNN methods were

used to label images, and accurately labeled them with 99% accuracy. In transfer learning

mode, the network accurately detected about 86% of cracked images. DCNN methods

also detected much finer cracks than edge detection methods. In fully trained and

classifier modes, the network detected cracks wider than 0.08 mm; in transfer learning

mode, the network was able to detect cracks wider than 0.04 mm. Computational times

for DCNN are shorter than the most efficient edge detection algorithms, not considering

the training process. These results show significant promise for future adoption of DCNN

methods for image-based damage detection in concrete. To reduce the residual noise, a

hybrid method was proposed by combining the DCNN and edge detectors which reduced

the noise by a factor of 24.

Chapter seven investigates the feasibility of using a Deep Learning Convolutional

Neural Network (DLCNN) in inspection of concrete decks and buildings using small

Unmanned Aerial Systems (sUAS). The training dataset consists of images of lab-made

bridge decks taken with a point-and-shoot high resolution camera. The network is trained

on this dataset in two modes: fully trained (94.7% validation accuracy) and transfer

learning (97.1% validation accuracy). The testing datasets consist of 1620 sub-images

from bridge decks with the same cracks, 2340 sub-images from bridge decks with similar

cracks, and 3600 sub-images from a building with different cracks, all taken by sUAS.

The sUAS used in the first dataset has a low-resolution camera whereas the sUAS used in

the second and third datasets has a camera comparable to the point-and-shoot camera. In

this study it has been shown that it is feasible to apply DLCNNs in autonomous civil

structural inspections with comparable results to human inspectors when using off-the-

shelf sUAS and training datasets collected with point-and-shoot handheld cameras.

Chapter introduces SDNET2018 which is an annotated image dataset for training,

validation, and benchmarking of artificial intelligence based crack detection algorithms

for concrete. SDNET2018 contains over 56,000 images of cracked and non-cracked

concrete bridge decks, walls, and pavements. The dataset includes cracks as narrow as

0.06 mm and as wide as 25 mm. The dataset also includes images with a variety of

obstructions, including shadows, surface roughness, scaling, edges, holes, and

background debris. SDNET2018 will be useful for the continued development of

concrete crack detection algorithms based on deep convolutional neural networks

(DCNNs), which are a subject of continued research in the field of structural health

monitoring. The authors present benchmark results for crack detection using

SDNET2018 and a crack detection algorithm based on the AlexNet DCNN architecture.

SDNET2018 is freely available at https://doi.org/10.15142/T3TD19.

The feasibility of using infrared thermography (IRT) for in-line weld inspection is

investigated in chapter nine. Welded specimens include steel angles and plates with

complete joint penetration welds. Defects in specimens were manufactured which

included cracks, inclusions, lack of fusion, porosity, and overpass. After initial UT

inspection, the regions with defects were identified. Using a heat gun, the condition of the in-line inspection is mimicked by increasing the temperature of the specimens to a certain point. A thermal camera is used to record the temperature decay of the specimens with time. An exponential fit function is fitted to each pixel of the recorded sequence through time. It is observed that the regions with possible defects (previously identified in UT inspection) lose the temperature faster; therefore, the area under the exponential fit function is smaller of defected regions compared to the sound regions. Eventually all specimens are cut at the locations with possible defects which showed reasonable agreement with the UT and IRT inspections. Despite the success of the proposed IRT method in identifying defects, the high number of false positives reported limits using IRT for weld inspection. This can likely be resolved with more investigation. The most likely solution to reduce the number of false positives is using a thermal camera with high operating temperature, at least 10,000 °C, and higher sensitivity, 0.1°C. Nevertheless, using IRT in its infancy and likely a viable technique and has vast potential to improve weld manufacturing and inspection.

Finally, chapter ten is dedicated to the conclusions.

Chapters two through nine of this dissertation are individual research items, either published or submitted for publication in journal and conferences. Therefore, there has been collaboration between the author of the dissertation and co-authors. In order to acknowledge the co-authors work, the role of each co-author in preparation of each chapter is shown in Table 1-1. In this table, the numbers in the parenthesis indicate the chapter number that each co-author contributed to.

Table1-1 Co-authorship

Role	Co-authors			
	Marc Maguire	Robert Thomas	Leslie Campbell	Calvin Coopmans
Conceptualization	Yes (2-9)	-	-	Yes (7)
Methodology			Yes (4)	Yes (7)
Validation	Yes (2-9)	-	Yes (3,4)	-
Analysis	-	-	Yes (4)	-
Resources	Yes (2-9)	-	-	Yes (7,8)
Data Curation	-	-	Yes (3, 4)	-
Writing-Review & Editing	Yes (2-9)	Yes (3, 5-8)	Yes (4)	Yes (7)
Visualization	-	-	Yes (4)	-
Supervision	Yes (2-9)	-	-	Yes (7)
Project Administration	Yes (2-9)	-	-	-
Funding Acquisition	Yes (2-9)	-	-	

CHAPTER II

BRIDGE INSPECTION: HUMAN PERFORMANCE, UNMANNED AERIAL

SYSTEMS AND AUTOMATION

Abstract

Unmanned Aerial Systems (UASs) have become of considerable private and commercial interest for a variety of jobs and entertainment in the past 10 years. This chapter is a literature review of the state of practice for the United States bridge inspection programs and outlines how automated and unmanned bridge inspections can be made suitable for present and future needs. At its best, current technology limits UAS use to an assistive tool for the inspector to perform a bridge inspection faster, safer, and without traffic closure. The major challenges for UASs are satisfying restrictive Federal Aviation Administration regulations, control issues in a GPS denied environment, pilot expenses and availability, time and cost allocated to tuning, maintenance, post-processing time, and acceptance of the collected data by bridge owners. Using UASs with self-navigation abilities and improving image-processing algorithms to provide results near real-time could revolutionize the bridge inspection industry by providing accurate, multi-use, autonomous three-dimensional models and damage identification.

Introduction to Bridge Inspection

According to the Federal Highway Administration's (FHWA) annual report, the number of deficient bridges in the United States was 142,915 in 2015, which is more than 23% of the of the total number of bridges in the United States [1]. The deficiency ratio, defined as the ratio of structurally and non-structurally deficient bridges, to total number

of bridges, has decreased significantly from 38% in 1992 to 23% in 2015. Fig.2-1 shows

the deficiency ratio of the United States' bridges based on the latest annual report from

FHWA from 1992 through 2015. This trend suggests gradual, but consistent

improvement of bridge inventory conditions over the past 21 years. However, the

American Society of Civil Engineers (ASCE) gives a grade of C$^+$ for the United States

infrastructure [2]. Improvements in inspection efficiency may allow bridge maintenance

engineers and managers to do more inspections at a lower cost. The FHWA stopped

tracking non-structurally deficient bridges effective with the 2016 archived data. The

number of structurally deficient bridges in 2016 was 54,365 which was 9% of the total

number of bridges.

Every bridge deteriorates as it ages and is managed by a Bridge Management

System (BMS) that often takes into account stochastic processes based on routine bridge

inspection information [3,4]. The evolution of bridge inspections in the United States is

tied to high profile collapses. Currently, inspections are performed periodically, usually

on a 24-month cycle, allowing the inspectors to monitor the defects and deterioration.

Bridge Inspection Program Evolution

The West Virginia bridge failure, also known as the Silver Bridge collapse,

occurred at 5 p.m. on December 15, 1967, when an eyebar-to-pin connection fractured,

causing a 445 m portion of the bridge to collapse and resulted in 46 casualties [5]. After

this incident, federal authorities decided to coordinate bridge management programs

throughout the United States by introducing the Federal Highway Act of 1968. The

National Bridge Inspection (NBI) program was initiated to enforce periodic inspections

of bridges in 1968 as a direct result of this act. This program was expanded to the

National Bridge Inspection Standards (NBIS) in 1971 to prescribe the proper inspection

process and frequency and to designate official bridge inspectors [6].
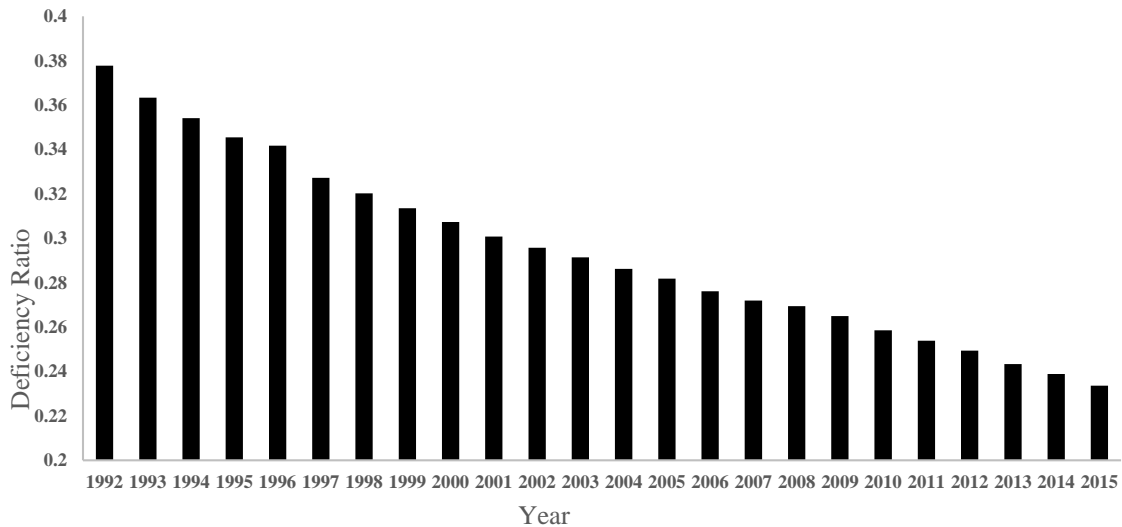
Fig.2-1 Gradual decrease in deficiency ratio of the bridges in United States since 1992 to the last published data in 2015

The Mianus River bridge collapse on I-95 in 1983, which was due to hanger

assemblies, and the Schoharie Creek bridge failure in 1987, which was due pier scour,

heightened concerns over bridge inspection procedures [7]. After these incidents, federal

authorities provided guidelines regarding inspection of fracture critical and underwater

members. The NBIS was constantly being revised but was the only reference for

inspectors in the United States until 1991 when congress mandated that the state

Departments of Transportation (state DOTs) come up with a comprehensive state-specific

BMS [8]. Part of this program included development of a rigorous software package

called "PONTIS" which is a decision-making tool bridge managers use for bridge evaluations and is constantly updated with reports, pictures, core logs, and other relevant bridge data [9,10]. At the same time, the National Cooperative Highway Research Program (NCHRP) developed a BMS software termed "BRIDGIT." The goal of BRIDGIT was to provide guidelines to manage decisions for either local or state bridge inspection agencies [11]. FHWA has been in charge of preparing and updating a national inspection procedure manual since 1990 called the Bridge Inspector's Reference Manual (BIRM) [12]. This manual has also been updated several times and includes different methods, technologies, and procedures for inspection. In addition, the National Bridge Inventory (NBI) has gathered more than 14 million inspection data since 1983, which is accessible to the public on the FHWA website [13]. Dekelbab et al. called this database the most comprehensive source of information on bridges in the United States [14]. Fig.2-2 summarizes the history of bridge inspection manuals and programs since 1968.

Visual and Physical Inspections

Visual inspections are the oldest and most frequent type of bridge inspection. Visual inspections can involve walking on the deck, using binoculars to see a point of interest, or using either scaffolding or an Under Bridge Inspection Truck (UBIT) for regions that are difficult to access. BIRM defines two types of methods for hard-to-reach areas: access equipment and access vehicles. The equipment includes ladders, rigging, scaffolding, boats, climbers, floats, boatswain chairs, free climbing, etc. The most common access vehicles used in bridge inspection practice are man-lifts, scissor lifts, bucket trucks, and UBIT [12].
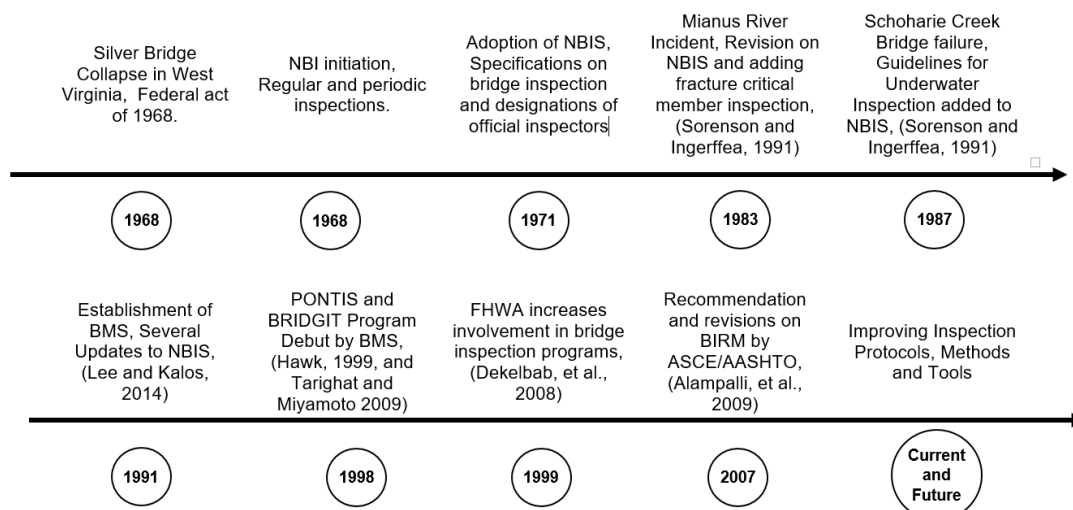
Fig.2-2 A time-line review on bridge inspection regulations in the United States since 1968 to the last published data in 2018

UBITs provide a proper view of hard to reach areas for inspectors, but they have high capital and maintenance costs. UBITs are difficult to schedule since only a small number of them are in service in any given region. Other issues with UBIT inspections are potentially endangering the public and inspectors, adding additional weight to the bridge, congesting traffic lanes, and most important, UBIT inspections require skilled and qualified workers to operate them [15]. These indirect costs often result in considerably more burden to inspection agencies than the direct costs, making UBIT-free inspections very attractive to many DOTs.

Physical inspections are recommended when visual inspections are not sufficient for rating a certain region, in other words, uncertainty of defect presence or measurement requirements of a member or a defect. The most common practice for physical inspections of bridge slabs uses a sounding hammer and chain drag to locate delaminated regions by comparing the resonating sounds of the defected and undamaged areas [12].

Physical inspection of steel members includes finding under-paint defects to detect fatigue cracks, rust, and corrosion using wire brushes, grinding, and sand blasting. More comprehensive information on physical inspections can be found in the BIRM.

Advanced Inspections (NDE)

Practitioners and researchers recognized the shortcomings of visual and physical inspections in the 1990's. Rens et al. suggested the following demands for more accurate bridge assessments [16]:

- In-situ structural characteristic determinations

- Accurate evaluation of the current serviceability level

- Economic efficiency

- Degree of dependency on inspector skill or experience

To address these recommendations, Non-Destructive Evaluation (NDE) methods may be applied for bridge inspections. Based on the construction material, there are several NDE inspection methods suggested by BIRM for concrete bridges: Ultrasonic Testing (UT), Ground Penetration Radar (GPR), Impact Echo (IE), Infrared Thermography, Radiography Testing (RT), and Half-cell method; and for steel bridges: Acoustic Emission (AE), Dye Penetrant Testing (PT), Magnetic Testing (MT), Computed Tomography (CT), Eddy Current Testing (ET), and UT. The NDE methods provide essential information for bridge engineers and inspectors; however, these methods have not been practiced widely.

Rolander et al. conducted a survey to determine the state of the practice for high bridge inspection in the United States [17]. One of the questions on this survey was the

type and frequency of NDE methods practiced by each DOT at the time of the survey. Forty-one DOTs responded to this question. Chain drag, pachometers, rebound hammers, the half-cell method, GPR, and IE were used for concrete bridges by more than 10 DOTs. NDE methods were utilized more for steel bridges, most likely because most of them are related to fatigue inspections, which are difficult without some form of NDE. Thirty-four, thirty-four, and twenty-seven DOTs used PT, UT, and MT, respectively. This study concluded that DOTs used NDE methods more often than before (California DOT unpublished survey in 1993 was the base), but there was no information about the frequency of using these methods in bridge inspection. A more recent survey by Lee et al. indicated that out of thirty states with their own bridge inspection manuals only eight of them addressed using NDE methods in 2014 [8]. The most practiced NDE method for concrete bridge inspection was GPR, which was used at least once by 77.5% of surveyed state DOTs, while half of the surveyed states used AE during their inspections. All surveyed states used PT at least once for steel bridges. MT and UT were the second most frequently used NDE methods in steel bridges with a 95% exposure rate. The remaining NDE methods for steel bridges either were not used or were reported to be "very difficult" to use, suggesting that major changes in current NDE methods are necessary to minimize human involvement [18].

State DOTs considered visual inspection as the most frequent inspection method in the surveys [8,17]. As it will be explained later in the paper, UASs, an assistive tool for inspectors to perform visual inspections, can save time and money in DOTs. However, with the exception of visual sensors, the non-contact NDE techniques available for UASs, like various spectra cameras, may require time and effort for state DOT acceptance.

There is always a need for cost reductions and improvement to bridge inspection procedures as funding is always a constraint for bridge managers. This section has identified several techniques that can arguably provide more detailed data than traditional visual and physical inspections but may not be worth the time, effort, post-processing, and associated cost. This section also illustrated inspectors' reluctance to adopt new techniques. There is a need to reduce the inspection time and increase inspector and public safety all while decreasing inspection costs, which indicates a need for automated inspection. If unmanned inspection processes are going to replace current standard practices, then they must be robust and require similar time and effort to current practices. The following sections will investigate recent efforts to do so.

Unmanned/Automated Inspections

Visual and physical inspections are still considered the most reliable and common bridge inspection methods. In other industries (e.g., aerospace and automotive), the role of human errors in inspection have been scrutinized, evaluated, and limited for decades. Automated inspection devices equipped with software packages are now the routine inspection protocol in aviation industry [19]. Unmanned/Automated inspection and maintenance approaches in high-tech industries are the best choice to achieve minimum failure and optimum maintenance level [20]. However, as discussed in the previous section, few inspection agencies are interested in routine NDE use outside of a handful of fatigue crack detection techniques, which essentially augment the inspector's ability to visually identify cracks.

Unmanned/automated methods have the potential to improve and automate the

bridge inspection practice. On a small scale, these methods have been performed using either ground or airborne vehicles in the past. The first of robotic vehicles for bridge inspection were ground vehicles and were used for deck inspections. For example, the RABIT Bridge Deck Assessment Tool [21], is a multi-sensor robot used to detect surface and subsurface defects in a bridge deck. The onboard sensors mounted on RABIT were: impact echo, ultrasonic surface wave testing, GPR, electrical resistivity, and a high-resolution digital camera. The RABIT was able to collect data of bridge decks at a rate of 372 square meter per hour, longer than a typical visual inspection, but acquiring considerably more data [22]. RABIT was able to successfully characterize and detect the most common deterioration types in concrete decks including rebar corrosion, delamination, and concrete degradation [23].

Another example is a climbing robot to monitor reinforced concrete structures (under bridge). This robot is capable of detecting corrosion at early stages using electron bombardment [24]. The robot's movement is facilitated through movable suction cups, allowing inspection in hard-to-reach regions.

Lim et al. claimed that visual bridge deck inspections can be performed more accurately if they are performed autonomously [25]. A Robotic Crack Inspection and Mapping (ROCIM) robot was designed to replace human inspections and was capable of autonomous crack detection using a visual mounted camera and integrated edge detector software. In addition, a genetic-based path-planning algorithm was developed to locate turns and determine the traveling distance.

La et al. equipped the RABIT with an autonomous system for deck inspection using impact-echo, ultrasonic, and electrical resistivity [26]. The system was able to

navigate autonomously on a bridge deck, detecting cracks and delamination and evaluating the concrete modulus.

The above examples are the first generation of automated or semi-automated inspections with ground vehicles. Within the last decade, UASs have evolved and have obtained unprecedented capabilities and near ubiquity. Many sectors are taking advantage of these new capabilities to transform their industries. The capabilities of UASs and how they relate to bridge inspection are outlined in the following section. A recent review of the robotic infrastructure inspection can be found in [27]

UASs and Their Applications

Before moving on to current research on UAS based bridge inspections, a review of UAS definitions and applications is necessary. This review also includes a summary of UAS control and sensors.

UAS Definition

According to the Unmanned Aerial Vehicle System Association (UAVSA), a UAS is a combination of an Unmanned Aerial Vehicle (UAV), either fixed-wing aircraft, a multi-copter aircraft, the payload (what it is carrying), and the ground control system which is controlled by a human to some degree. UASs are generally defined as any aircraft or aerial device which is able to fly without an onboard human pilot. They are also known as remotely piloted aircrafts, remotely operated aircrafts, remotely piloted vehicles, drones, and remote controlled helicopters. Depending on the purpose for which the UAS is being used, their properties vary, including the number and weight of the mounted sensors, maximum flight altitude, maximum flight duration, etc. UAVs can be

fixed wing or vertical take-off and landing (VTOL) platforms.

Brief UAV History

The very first appearance of UASs in the United States goes back a century ago. Shortly after the first successful development of man-operated aircrafts as the United States entered World War I (WWI), automated unmanned aircrafts were designed to bomb enemy targets. However, this operation was canceled because of engine failure and consecutive setbacks. Also during WWI, the Germans developed an unmanned aircraft that performed one-way missions at a maximum speed of 650 km/h and an altitude of 300 m. At the beginning of the modern era, from 1959 to the present, the main use of UASs was exclusively military. UASs have played an important role in United States' victories and air superiority in different missions and threats [28]. The dominant market for UASs has been and still is military applications.

Within the last 20 years, UASs have found their way into civilian applications. Fig.2-3 shows an overview of UAS civilian applications and predicts the financial investments in this market until 2017 for each category in Europe [29]. Government applications were predicted to become the major market from 2014 onwards. The fire fighting and agriculture applications will be the second dominant market followed by the energy sector and earth observation until 2017. In addition, the government applications of UASs have been the most progressive market during the past five years of this study. Infrastructure maintenance programs (e.g. bridge inspections) are considered a sub-category of the government market and are just now beginning to be explored as an option for inspections.

UAS applications for civilian purposes have expanded significantly over the past decade and seem to be rising dramatically due to their low cost and tangible scientific improvements. Table 2-1 demonstrates the recent UAS applications in various fields. For each application, references have been provided for further reading.
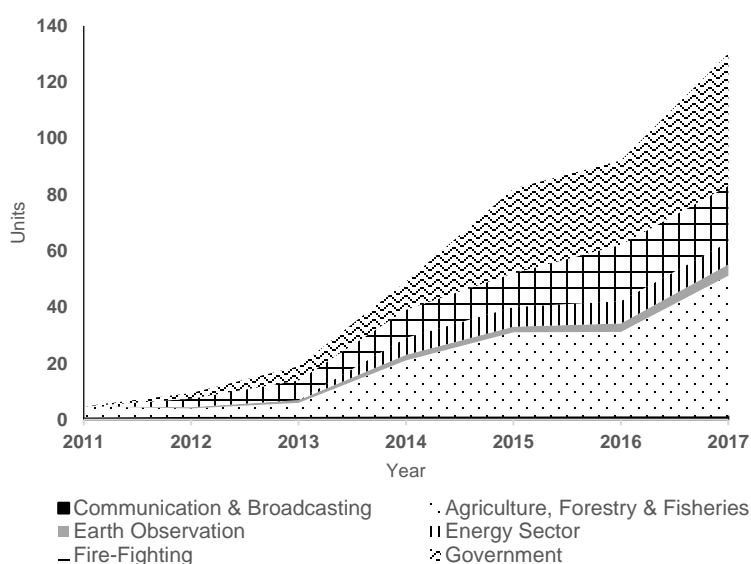
Fig. 2-3 The rising market of UASs for civilian application (Adapted from [29])

UAS Sensors

The type and number of sensors mounted on a UAS depends on the mission requirements. In most cases, the sensors on a UAS must be non-contact, significantly limiting the possible NDE techniques. The most popular sensors for evaluating the structure are visual and thermal cameras. There is also a suite of sensors available that are necessary to perform autopilot functions. This section introduces the most common sensors mounted on UASs and their applications.

Table 2-1 Variety of UASs applications

Application		Purpose	Reference
Military		Warfare	[28]
		Reconnaissance	[131]
		Intelligence	[28]
		Surveillance	[132]
		Anti-Terrorism	[133]
Civilian	Agriculture and Forestry	Crop Condition Monitoring	[134]
		Fertilization of Trails	[135]
		Properties of Plants	[136]
		Crops Treatment	[137]
		Nitrogen Emission	[138]
		Plant Detection	[139]
		Measurement of Tree Locations	[140]
		3D Mapping of Forest	[141]
	Disaster Monitoring and Management	Hurricane, Typhoons, and Tornados	[142]
		Earthquakes-Damage Evaluation With 3D Model	[143]
		Fire Detection	[144]
		Nuclear Leaks	[145]
		Oil Spill Detection	[146]
		Floods and Avalanches	[147]
		Rescue Missions	[148]
	Surveillance	Prevention of Un-Authorized Entry	[149]
	Environmental Monitoring	Soil Erosion	[150]
		Ground Surveys	[151]
	3D Mapping	Terrain Models	[152]
		Topographic Maps	[153]
		Mapping Landfill	[63]
		Building Models	[154,155]
		Shaded Objects Models	[156]
		Structure Models	[157]
		Archeologic Sites	[158]
	Atmospheric	Temperature Monitoring	[159]
	Wildlife Monitoring	Animal Behavior	[160]

Visual Cameras (Video/Image)

Visual sensors are the most common sensors and are widely used on UASs for

remote sensing purposes. The spectral range of these sensors is in the visible range, in other words, from wavelengths of 390 nanometers to 700 nanometers. Adverse temperatures, lighting conditions, high frequency engines and motors, significant vibrations, and sudden rotation of the UAS can affect the data acquisition process.

Thermal Infrared (TIR) Sensors

Thermal sensors are able to measure the emitted energy of a surface and convert that into temperature. There are two approaches used in infrared thermography: passive and active. The passive approach relies on the thermal properties of just the material and structures, which have a different temperature than the ambient temperature of the specimen. In active thermography, an external heat/cooling source is used to excite the material surface, allowing the TIR sensors to find the difference in thermal signature of specimens in different locations. However, in a bridge inspection situation, passive thermography using only the ambient heat generated by the sun is probably the only feasible option. Thermography is an established method for subsurface defect detection in concrete bridge decks and girders and can be used to generate a comprehensive thermal map [30,31].

Other Sensors

There are several other sensors available that a UAS could employ, which are currently limited due to sensors' weights and UASs' capabilities:

- *Light Detection and Ranging (LiDAR) sensors:* Measures distances and explores the scene by projecting light to the object of interest. These sensors can be used to reconstruct 3D models and maps from the object of interest or provide

information to the UAS regarding obstacle avoidance [32].

- *Multispectral and Hyperspectral Sensors:* The spectral bands visible to multispectral and hyperspectral sensors are greater than visual or thermal cameras because they cover a wider range of wavelengths [33].

- *Radio Detection and Ranging (RADAR)/Synthetic Aperture RADAR (SAR):* The installation of SAR on UASs was reported in several resources related or unrelated to bridge inspection [34-35]. The main application of RADAR and SAR is for underwater measurements, which could possibly provide information regarding bridge scour [36].

- *Sound Navigation and Ranging (SONAR):* In the past, these sensors have been used for surface mapping while flying UASs [37]. The current application for SONAR sensors is obstacle detection; however, SONAR use might be limited in a confined under-bridge space because of hard surfaces and bouncing sound waves.

- *Magnetic sensors:* These sensors can generate magnetic maps in great detail, identify various ferrous objects in the soil, and with enough power and accuracy could potentially generate defect maps in ferrous materials like steel girders [38].

- *Multi-sensors and Data Fusion:* Data acquired from different sensors can be combined using data fusion techniques. For instance, with the combination of a radiometer, visual camera, chemical sensor, and thermal infrared sensors, it is possible to measure relative humidity and temperature, CO_2, luminosity, and wind speed [39,40].

UAS Navigation

The purpose of this section is to introduce the basics of UAS navigation and the

associated sensors. The section explains the role of vital components of a UAS with

related references for a reader in the field of structural engineering. Using UASs for

infrastructure inspection and maintenance is a fast growing trend, but is often outside the

scope of most civil and infrastructure engineers' training, so the information provided

herein is intended to aid in comprehension of UAS navigation and limitations.

Nearly every UAS, through its autopilot computer and external sensors, comes

with some sort of autonomous control. Control and navigation are important issues in all

UAS applications, and most pilots are heavily reliant on basic stabilization routines and

GPS signals to maintain position. A 3D hold allows for safe control of a UAS in harsh

environmental conditions as well as stabilization for obtaining adequate images. In the

realm of bridge inspection, control and navigation issues have been reported to be

exceptionally problematic because of the challenges of bridge environments [41]. Several

algorithms and methods have been studied for UAS semi-autonomous control and

navigation.

UAS control and navigation is commonly carried out by GPS, Inertial Navigation

Sensors (INS), Inertial Measurement Units (IMU), Micro-Electro-Mechanical Systems

(MEMs), gyroscopes, accelerometers, and Altitude Sensors (AS) that are onboard the

UAS and used by the autopilot system [42]. GPS is a radio navigation system that allows

land, sea, and airborne users to determine their location and velocity [43]. INS is a

navigation aid device that uses a computer, a set of motion sensors, and a set of rotation

sensors that continuously calculate the position, orientation, and velocity (direction and

speed of movement) of a moving object through IMU without external references. MEMs are the technology used in microscopic devices, particularly those with moving parts [44].

The most common sensors employed for semi-autonomous UAS control are visual cameras due to their availability, ubiquity, and low-cost [45]. Image processing techniques can be employed to generate algorithms that identify certain points or objects, like key points, in a set of images as reference to either make a navigable map or hold a position. More information regarding cameras and algorithms used for this purpose are discussed in the following sections.

LiDAR, laser rangefinders, and ultrasonic sensors are often used by the autopilot to estimate the distance from the UAS to the ground or to close objects, allow mapping, and vertically or 3D hold the UAS. Other common sensors that can provide some help, but tend to be less accurate are magnetometers (i.e., compass [41]) and barometers, which sense the air pressure to estimate vertical position. Many of these sensors are highly valuable for navigation and control, but also have significant limitations, especially when used without GPS. For instance, barometers are affected by wind speed and can cause the UAS to drift and stereo vison systems can cause the UAS to follow the current and drift with the waves when used over water [46].

Autonomous Navigation

It may be possible to remove humans from routine inspection techniques in several years with the convergence of UAS platforms, sensors, and control improvements. The potential for automated inspections will improve when a combination

of sensors outlined in the previous section are used along with various types of navigation algorithms that often involve data fusion techniques [47,48]. For autonomous bridge or infrastructure inspections using self-navigated UASs, three fundamental problems need to be solved: mapping, localization, and path planning.

Mapping is the process where a UAS makes a map of its surroundings for navigational purposes using its onboard sensors [49]. Localization is the process of estimating a UAS's position based on a self-generated map, and path planning is the process of going from point A to B while avoiding obstacles [50,51]. When flying UASs near or under a bridge, GPS signals (an integral part of UAS control for most pilots) will be lost, likely resulting in loss of control and poor image quality. In such scenarios, a combination of IMU, cameras, and laser range finders can be used to simultaneously build a map of the environment and localize itself, however this has not yet been demonstrated as possible [46].

In recent navigational studies, a low-cost 5 MP monochrome or color visual camera set at 14-30 fps was found to be functional for navigational purposes [52,53]. Lemaire et al. proposed use of a monochrome camera that is able to operate at least at 60 fps and a 90-degree gimbal [54]. For proper controlling and navigation, a velocity of 30 fps was proposed to be sufficient in recent studies [45]. As a general rule, images larger than 0.3 Mega Pixel (MP) in size are not appropriate for image-processing techniques, like mapping and localization, because of excessive computational time for current on-board computer configurations [45].

One solution for localization and mapping in a GPS denied environment is called Simultaneous Localization and Mapping (SLAM). SLAM is a style of autonomous

navigation, which allows UASs to be controlled in a GPS-denied environment. During

the SLAM process, a UAS makes observations and measurements of the surrounding

environment using mounted sensors, then landmark recognition and positioning allows

the UAS to create a map of the structure and its surroundings [55]. SLAM has different

implementations depending on the integrated sensors on the UAS [56]. Implementation

of visual SLAM in absence of the GPS signals has drawn the attention of researchers in

recent years; however, most of them rely on data fusion acquired from several sensors,

such as monocular vision and barometer, and RGB-D cameras by providing color image

and per-pixel depth, and etc. [57,58]. Despite the successful implementation, none of

these methodologies have been used to navigate autonomously around complex structures

such as bridges.

This section discussed the potential for autonomous flights in GPS-denied

environments. Using just visual cameras for autonomous navigation and realtime

mapping is still an open problem. No actual bridge inspections have been carried out

using autonomous navigation and, as such, are severely limited by weather and pilot skill.

With current theoretical and software development, sensor technology, and commercial

availability, UASs cannot inspect a bridge without mostly manual control and therefore

UAS-assisted bridge inspections require skilled pilots [46].

3D Model Reconstruction

Useful 3D models of bridges could provide a permanent record of condition and

dimensions from one inspection to another and could also be used for navigation and

control purposes. Most of the work in this area has been on building inspection; however,

it should directly relate to bridge and infrastructure inspection.

A two dimensional (2D) image loses the scene depth during photography, but using the line of sight and camera positions from each image, depth can be restored and a 3D model can be constructed. Comparing features together can determine the correspondence level of each image. Development of robust feature detection algorithms is a fast moving research area in the computer science. There are several popular approaches for 3D image reconstruction, such as Structure-From-Motion (SFM) [59], and multi-view-stereo (MVS) [60]. All of which use some form of feature detection, which must be efficient enough to compare each of the images in a set made of possibly hundreds – or thousands in the case of infrastructure inspection – of images, which is computationally expensive. The features are traced back to a sequence of images to form the skeleton of the 3D model based on the feature movements.

To familiarize the reader with common terms in the computer vision area, some of the feature detectors are introduced along with references for further reading. One of the most popular feature detection algorithms is Scale-Invariant Feature Transform, or SIFT, which detects the maxima of Differences of Gaussian (DoG) [61]. SIFT also describes the detected feature, and for this reason it is more commonly called "feature descriptor." Speed Up Robust Features, or SURF, is another powerful feature detector and descriptor in the field of 3D model reconstruction [62]. Table 2-2 demonstrates some of the most important feature detectors used in image based 3D model reconstruction.

Table 2-2 Popular feature detectors and descriptors in 3D model reconstruction from 2D images

Feature Detector type	Name of the Method	Reference
Edge Detection	Canny, Sobel, Deriche, Differential, Prewitt, Cross	[73]
Corner Detection	Harris operator, Shi and Tomasi, Level curve curvature, Hessian, SUSAN, FAST	[161]
Blob Detection	Laplacian of Gaussian (LOG), DOG, Determinant of Hessian (DOH),	[162]
Ridge Detection	Hough Transformation, Structure Tensor	[163]
Feature Description	SIFT,SURF, Histogram of Oriented Gradient (HOG), Gradient Location and Orientation Histogram (GLOH)	[164]

A comprehensive summary of 3D model reconstruction studies that applies to structural inspections is shown in Table 2-3. This table demonstrates the evolution of 3D image reconstruction in civil infrastructure from 2004 (manual reconstruction) to 2017 (automated reconstruction). Furthermore, this table can be used as a starting point for future researchers to select methodologies and sensors for different applications. Useful visual cameras for 3D model reconstruction depend on the level of detail the model will require, and model accuracy can be improved through the use of LiDAR.

Generation of a detailed model for a bridge could be very tedious because of the complexity of the geometry. However, 3D models of bridges can be used for semi-autonomous inspections conducted by UASs [46]. Ideally, the 3D model can provide a virtual map for the UAS to navigate around the bridge and avoid obstacles.

Table 2-3 3D model reconstruction studies using UAS imagery for buildings

Ref.	Year	Object	Sensor's Type	Detector	Achievements	Shortcomings
[154]	2004	Buildings	Nikon D 100 Camera	Oblique Photogrammetry Camera Calibration	3D Model Reconstruction of Regular Buildings from single UAS image	Insufficient inspection detail, minimal potential for complex geometry
[165]	2009	Buildings	Integrated LiDAR Line Scan	Laser Scanner To Obtain The Depths	Regenerating 3D Model from LiDAR	Insufficient inspection detail, no details provided on computational time or accuracy
[97]	2009	Bridges	Visual	Manual Stitching	Generating Models for Under Bridge Elements	no details provided on computational time or accuracy
[156]	2010	Buildings, mapping	Video Camera	MVS Clustering	MVS Reconstruction at City Level of Several Buildings	Seven hour Run-time, insufficient inspection detail
[155]	2011	Mapping	Amateur or SLR Camera	Patch-Based MVS Software PCMS	3D surface mapping, possible use for birdge decks	Not applicable for under bridge inspection. No details provided on computational time or accuracy
[166]	2011	Buildings	High Resolution Panasoic Lumix GF1 camera LiDAR	SFM SIFT	3D Model of Buildings, Equal Level of Accuracy as LiDAR Model, accuracy was evaluated (1-3 cm)	No details provided on computational time. The accuracy of the model was not desirable for fine defect detection.
[167]	2012	Mapping	Digital SLR Camera-Canon 550D	MVS Georeferencing	3D Scene Modeling. Compared the Result of MSV to Terrestrial Data.	No details provided on computational time, not suitable for defect detection,
[168]	2012	Pavement	Canon EOS Digital Rebel Xti Camera	MVS SIFT	Pavement Damage Detection From 3D Model, 0.5 cm accuracy	No details provided on computational time, the accuracy computed based not on the defects but on targets
[63]	2012	Mapping	MK Hisight II Camera, Canon Digital Ixus 100 IS Camera	Off-The-Shelf Programs SIFT, PVMS, CMVS	A Comparison Between Available Software Packs for 3D Reconstruction	Position accuracy was not suitable for many defects (10-20 cm), No details provided on computational time
[169]	2013	Buildings	Canon SX230 Camera	Manual Stitching	UAS Review on Structural Health Monitoring and 2D Stitching	Manual model construciton

[65]	2014	Concrete Decks	DSLR Digital Camera	SFM	85% accuracy of crack detection, 3D model construction of the deck, max 0.3 cm difference in the 3D model (deck dimensions), 3 mm difference in detected cracks width	No field experiment, 10 hours of computational time to create the model, manual model development, noted sensitivity to lighting.
[64]	2014	Post-disaster	Visual Camera	SFM	3D model of Concrete specimens, small and full-scale, report the cracking area, 1 hour to create the model, 6 cm difference in specimen dimensions	Controleld lab experiment, manual model generation, no detection on cracks finer than 0.5 cm, no detection on vertical cracks (with respect to the camera), 0.15 cm difference in crack width
[66]	2014	Mapping, Complex Structures	12.3MP Olympus E-P1, Laser	SIFT ASIFT MVS Georreferencing	PW software development. Comparison between SIFT and ASIFT, 2 cm maximum difference,	Five hour processing time, not suitable for defect detection.

There are off-the-shelf or open-source programs available, either free or commercial, that can reconstruct 3D models. Microsoft Photosynth and Automatic Reconstruction Conduit (ARC3D) are free web services that can reconstruct 3D models from color images. Agisoft Photoscan is a popular commercial software product used to generate 3D models and has been used with some success by the authors [46]. However, generating a model of a 3 m long bridge mock-up autonomously using this software took nearly 8 hours, and the model's accuracy was unsuitable for navigation and inspection. Improvements could be made to that model, but not without considerable additional effort which state DOTs may not desire. As discussed in the NDE section, these advanced techniques need to be easy-to-implement if state DOTs are to use them routinely. Neitzel

and Klonowski generated 3D models based on 2D images acquired by UAS using several

of these programs and compared the results of these and other programs and also found

mixed results [63]. It seems that more developments need to be made in this area for 3D

models to be a truly feasible infrastructure inspection option.

Detailed 3D model of a bridge for purpose of damage identification has not been

constructed successfully yet. The proposed method by Torok et al. and Zheng have the

potential to be used for defect detection in bridges but neither of them had been examined

in the field [64,65]. Weather, sunlight, temperature, wind and other environmental

incidents would change the accuracy of the obtained model. In addition, the images used

in those studies were not from UASs. The models constructed from UAS images, in other

studies in Table 2-3, were not detailed enough for defect detection. The other issue with

3D model construction is the required time to create it. Five to 10 hours of model

construction time can be very long for bridge inspectors, especially when the goal of the

UAS inspection is replace visual inspection. Torok et al., stated the model was created in

1 hour [64]. However, the inspected object was small: 140 cm long column with a cross

section of 53 cm by 23 cm. A single pier in a small bridge would be considerably larger

and more complex, model reconstruction would likely take much longer. LiDAR seems

to be the best option to construct 3D models quickly, although the studies do not mention

the cost of using UAS equipped with a LiDAR sensor, which are typically heavy,

requiring a larger UAS. In addition, for the output data from LiDAR to become a 3D

model, skilled operators are required, which will add to the cost. Recent studies provided

their models' accuracy to the ground truth which ranged from 0.5 cm to 10 cm. For these

models to be effective in defect detection, an accuracy of a tenth of millimeter is

required, which was not provided by any of the investigated studies [46]. Therefore, at this time, the application of UASs for 3D model reconstruction of bridges is limited for navigation purposes rather than defect detection. For the modeling to be of use to navigation, processing times need to be decreased considerably, to near real time. In addition, either free or commercially available 3D software can only construct objects with simple geometries and does so without proper details and are time consuming. Recently developed methods can have better performances than the off-the-shelf software in construction of complex objects, such as Rodriguez-Gonzalvez et al. [66].

Automated Damage Detection

In order for automated inspections to become a reality, automated damage detection must also work with real time navigation and be able to obtain a condition assessment in a reasonable amount of time. Currently, the most promising bridge and infrastructure inspection method is visual image-based damage detection, which can be used with modified thermal or multi-spectral images. The requirements for these sensors are specific to their application, but sensor resolution needs to be fine enough to capture enough pixels of the defect and sound regions, and in the case of visual crack detection, the pixel intensity gradient must be large enough to distinguish the cracking from sound regions [67]. Thermal imaging has similar requirements, but camera sensitivity is paramount, especially since thermal UAS inspection is limited to passive thermography. Dorafshan et al., was able to detect fatigue cracks in the laboratory with a thermal camera, but only with a 0.2ºC sensitivity camera and a 1ºC sensitivity camera indicated nothing [46].

Image processing techniques are used to detect cracks, which are basically semi-linear objects, such as Canny, Sobel, Fourier transform, and Haar transform edge detectors [68]. Image segmentation techniques, percolation algorithms, and filtering operations are also common for concrete crack detection [69-71]. Sometimes, a combination of several image processing techniques are required for damage identification [72]. Vision based training can further improve defect detection using techniques such as neural networks, wavelet transforms, and fuzzy C-means clustering [73-76]. Mohan and Poobal wrote a critical review on concrete crack detection using image processing methods using visual, thermal, ultrasonic, and laser based images [77]. Autonomous image-based crack detection in steel members (fatigue cracks) is challenging because of their size (0.01-0.1 mm width) [67]. Xu et al. introduced an image-based fatigue crack identification framework using a restricted Boltzmann machine algorithm [78]. The authors proposed an image-based algorithm to find two known fatigue cracks on a steel bridge from UAS images in multiple controlled and uncontrolled conditions [67].

Subsurface defects, like reinforced concrete delaminations, can be identified through thermal imagery [79,80]. Other proven applications of infrared thermography for flaw detection are air blisters and crack propagation in FRP, voids in masonry and concrete members, flaws on painted steel members, rebar corrosion detection, and weld defect detections including lack of fusion, crack, nugget, expulsion, and porosity [81-86]. Two recent successful examples of using UAS-based thermography to find concrete delamination on bridge decks can be find in Omar and Nehdi and Wells and Lovelace [87,88]. Another promising area of use for automated inspections would be post-disaster

inspections where damage detection is necessary and many successful inspections have been carried out [89-95].

The above studies indicate the vast opportunities of visual and thermal data for defect detection using common UAS sensors, and many studies have been attempted in the past using UASs or other vehicles. Metni and Hammel developed some of the first real-time concrete crack detection algorithms [96]. In addition, Oh et al., was able to identify reinforced concrete cracks, aided by user input on a bridge in combination with image with an average error of 0.02 mm from a distance of 2.3 m with 96.7% accuracy [97]. Inspired by this robotic system proposed in [97], a semi-autonomous robotic system was proposed to inspect road and train bridges [98].

Recently, a combination of a 3D optical evaluation system and thermal infrared imagery was used to detect spalling and delamination in bridge decks, successfully detecting 4/7 defected areas when comparing to cores, but detected delamination in three sound regions (false positive) [99,100]. For comparison, chain drag reported 5 true positives (5/7) and 3 true negatives (3/3) for the same regions [31]. A canny edge detector combined with a Gaussian smoothing filter as part of pre-processing was programmed into the ROCIM robot and was reported to be successful but not applicable on UASs [101]. Zheng proposed a bridge deck crack detection and measurement technique based on the different normal vector orientation between sound and cracked surfaces, and crack dimensions could be detected within a 10% error from a reconstructed model [65].

Morgenthal and Hallermann assessed the quality of UAS-based structural inspections in different weather conditions on a 44 m tall church structure, a 100 m tall turbine machine house, and a 225 m high chimney [102]. Cracks, rust, spalling, and

surface degradation were detectable in the captured images; however, motion of the UAS

and wind speed affected the quality of images. Sankarasrinivasan et.al. proposed a top hat

transform and HSV threshold operation to identify concrete cracks in UAS images and

investigate the feasibility of real-time inspections [103]. Regions with spalls and cracks

were said to be successfully detected by this algorithm; however, the number of

examined images and number of true positives were not provided or compared to other

algorithms. Ellenberg et al., designed an experiment to assess UAS's image ability for

structural monitoring and damage quantification using digital image correlation and other

imaging, [104], techniques. Using a common 12 MP camera, deflection was estimated

within 0.1 mm, and simulated corrosion measurements using a K-means algorithm were

measured within 10-13% of error [105]. In addition, a combination of edge detectors,

filtering, threshold, and morphological operations were used to detect cracks with 88%

true positive and 69% true negative. Dorafshan et al., compared an algorithm based on

threshold morphological operations to another image-based crack detection method

suitable for UAS real-time detection [72,106]. The comparison showed an improved

crack detection accuracy of 41% and 48% and an increase in true negative rates of 46%

and 49% for defected and sound datasets. The proposed segmentation method was

examined on challenging datasets with irrelevant features in the images such as edges of

concrete members, surface clutter, paint stains, and background scenery lines that could

be confused with cracks by many image-processing techniques. Implementing Deep

Learning Convolutional Neural Networks (DLCNNs) in UAS-assisted inspections

showed promising results for concrete deck crack detection without human intervention.

The network was trained on a set annotated images (manually labeled as cracked or un-

cracked) taken by a point and shoot camera of several bridge decks (98% validation

accuracy). The trained network was then used to label new images taken by UAS of other

concrete structures autonomously with 88% accuracy [107].

Table 2-4 shows the summary of the above studies in addition to several new

research efforts from 2007 to 2017. Reviewing the literature shows that the largest

hurdles are probably a lack of a uniform assessment of accuracy and a baseline dataset

for easy comparisons among the different methods.

Table 2-4 UASs and damage identification

Ref.	Year	Defect	Sensor	Method	Achievements	Shortcomings
[96]	2007	Concrete Crack	10MP camera	Manual detection	Autonomous flight used	No autonomous damage detection. Success only on planar objects perpendicular to camera.
[97]	2009	Concrete Crack	Visual camera, Laser, Gyroscope	Noise removal, edge detection (Seed point method)	Integrated machine vision, and human aid, compares to Canny and Sobel edge detectors	Manual detection, no true positive and true negative reports.
[31]	2013	Concrete Spall	12.3MP DSLR camera,	3D optical bridge evaluation system (3DOBS)	Combining chain drag with infrared thermography, thermal and visual data fusion, destructive testing	3DOBS required close proximity to generate the 3D model, Chain drag more consistent and still requires lane closure. 3D model required surface preparation.
		Delamination	FLIR SC640 thermal camera	Passive thermography pattern recognition		
[65]	2014	3D model of concrete crack	DSLR Camera	Oriented thresholding operation	Crack detection and measurement on 3D model	Thresholding value was user-defined, no field experiments
[101]	2014	Bridge Deck	High resolution visual	LoG	Autonomous crack detection and mapping, realtime crack detection.	No under-bridge inspections, no true/false positive reports.

[102]	2014	Concrete Wall Cracks/Spalls, Steel Rust	Panasonic Lumix DMC TZ 22, 14.1MP and Sony NEX 5 14.2MP	Manual	Discussion of wind effect on UAS performance	Motion blur weakened the visual damage detection, no autonomous defect detection, no comparison to human inspection
		Concrete Wall Crack	Sony NEX 5 14.2MP	Automated computer-vision	probability of detection with clear and blurry images	Less successful crack detection in blurry images due to adverse weather
[103]	2015	Concrete Member Crack, Efflorescence, Surface Erosion	PAL 762*572 camera	Hat transformation, HSV and grey-scale thresholding	Detection of Concrete cracks and degradation	Accuracy not reported, user-defined parameters required, no comparison to human inspection.
[104]	2016	Concrete Member Crack, Beam Deformation, Steel Corrosion	10MP GoPro Hero 3	Median filtering, morphological operation, shape filtering, K-means segmentation.	Deflection measurement, crack detection, corrosion detection	Lab test, stationary camera, no comparison to human performance, accuracy not reported
[72]	2016	Concrete Pavement Crack	12MP Nikon camera	Median filtering, Sobel, HSV thresholding, morphological operations	Crack detection with 90% accuracy in less than 1 s per image, image segmentation using shape, UAS inspection	31% of false positive reports, user-defined values in the algorithm, no comparison to human inspection
[87]	2017	Concrete Delamin-ation	FLIR Vue Pro Thermal Camera	Histogram Equalization, Image Segmentation (K-mean clustering)	Delamination detection comparable to hammer sounding and half-cell potential, two full-scale inspections	No discussion on the effect of temperature, UAS's small payload, sensitive to weather
[46]	2017	Bridge Deck Cracks, Steel Fatigue Cracks	12MP Nikon, 12MP DJI Mavic, 12Mp GoPro Hero 4	Manual Detection, LoG Edge Detector	90% accuracy, Successful fatigue crack detection visually in UAS images, human comparison. Lab and outdoor detection.	Only two (movable) fatigue cracks in the dataset, cracks' size and location were know before inspection
[130]	2017	Bridge Deck Cracks	12MP Nikon	Sobel, Roberts, Gaussian Filter	Comparison between three edge detectors,	Images in the datasets had no irrelevant objects, shadows,

					Wide variety of images.	etc., No filed test or UAS information.
[67]	2017	Bridge Deck Cracks, Steel Fatigue Cracks	12Mp Nikon, 12MP DJI Mavic	LoG and Statistical Thresholding	92% accuracy, less than 1 second per image run time.	Images in concrete dataset were without irrelevant objects, The fatigue crack algorithm only tested on 2 images.
[76]	2017	Concrete cracks	4k Camera	Fuzzy C-means clustering	Detection fine cracks (0.3 mm width) from UAS Images, 90% true crack detection	No information about the camera, highly sensitive to image noise, 80% true negative reports, no comparison to human inspection.
[78]	2017	Steel fatigue cracks	4K Nikon D7000	Restricted Boltzmann machine	Detection of fatigue cracks with 90% accuracy	No UAS inspection,no field tests, user-defined parameters in the algorithm
[77]	2017	Concrete cracks	Visual, thermal, ultrasonic, laser.	Review	Comprehensive review on different methodologies and sensors for concrete crack detection	No discussion on the dataset, no output images for verification.
[107]	2018	Concrte cracks	12Mp Nikon, GoPro Hero 4, 12MP DJI Mavic	Deep Learning Convolutional Neural Networks (DLCNNs)	Successful implementation of DLCNNs trained on high quality images to detect concrete cracks in UAS images autonomously	Limited testing dataset, relative poor performance of the network on UAS images

In this section a review of possible applications of UASs for autonomous damage identification is provided. Past studies showed promising results in terms of finding concrete surface cracks and delamination in an autonomous manner. The performance of the implemented methods in terms of accuracy and time was tied to the cameras used in the inspection and the type of defects. Even though a few studies offered realtime defect detection, but the required framework and software, for bridge inspectors to actually use them, were not discussed. Another gap in the past studies was the lack of comparing

visual inspections performed by the inspectors to the ones performed using UASs and damage detection algorithms. However, there are studies comparing UAS to manned inspection, but the performance of the two methods was not compared to each other. The accuracy, cost, and time associated with autonomous defect detection may not be well-analyzed in the reviewed studies. Using these methods requires an extra personnel, familiar with how the algorithms were programmed, which will add costs to the inspections. Human inspection can be superior to autonomous defect detection in their current state since a trained inspector can detect variety of defects. Autonomous defect detection for fatigue cracks using UASs have either failed or had limited success in the past [46]. Performing certain inspections, such as in-depth inspection using some sort of NDE method or under-water inspection, can be either very challenging or impossible using UASs. Despite all the shortcomings, the autonomous defect detection can be helpful during a typical bridge inspection by providing an unbiased approach for conventional concrete defect [67].

UASs and Bridge Inspections

This chapter is dedicated to published studies and research about using UASs for DOT missions and is organized into two categories: bridge inspection and other applications. UAS applications in bridge inspection have become widespread with state DOTs. According to a survey performed by the American Association of State Highways and Transportation Officials (AASHTO) in 2016, seventeen state DOTs had researched and/or used UASs for certain transportation purposes [108].

The survey also indicated a growing number of state DOTs, either independently

or with the aid of one or more academic institutions, are studying UASs and developing

policies. Based on a literature search, there are more states involved in UAS research for

various purposes since the writing of Dorsey, including but not limited to North Carolina

and Utah. Fig.2-4 shows the states with current or past involvement with UASs for

different DOT missions [46].
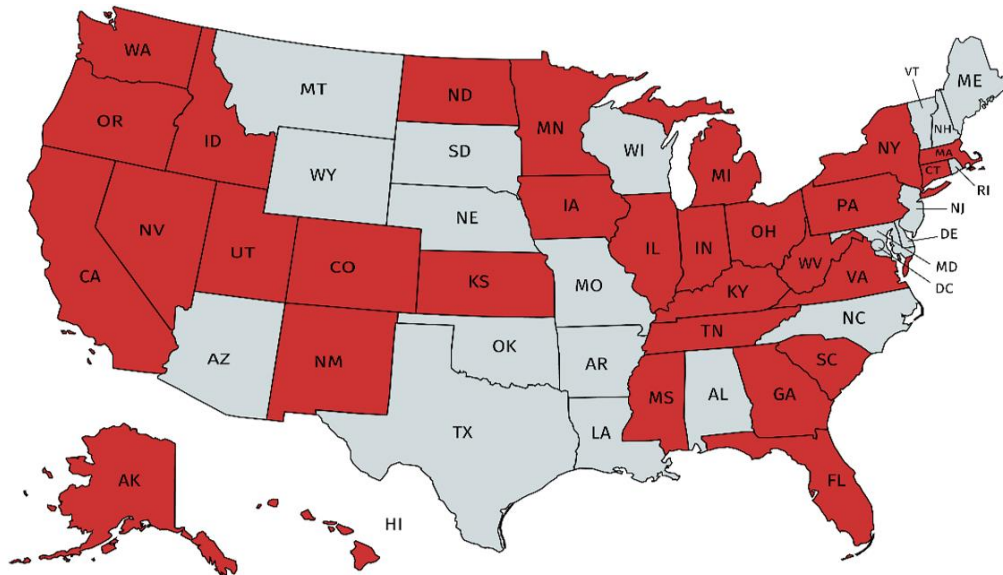
Fig.2-4 US Map with 34 red shaded states indicating current or past involvement with UAS research and applications (Adapted [46])

UASs and State DOTs

UASs have been used by departments of transportation for almost two decades

[46]. However, state DOTs have used UASs for different reasons. Currently, no DOTs

are using UASs for routine bridge inspections, but many are performing investigations in

this area. Many states are not investigating UAS assisted bridge inspections at all but are

performing some sort of feasibility investigations for evaluation of other infrastructure

like traffic, stockpile, and construction monitoring.

DOTs and UAS Bridge Inspections

California DOT

In 2008, California DOT and University of California at Davis published a report on aerial robot bridge inspection [41]. A custom UAS was designed to be tethered to the ground, and therefore was easier to control and conform to Federal Aviation Administration (FAA) regulations at the time. The onboard flight control computer was developed to provide a redundant high-speed communications link to manage the platform stability. However, the project was terminated because it did not result in a fully-deployable aerial vehicle due to the following problems: unreliable heading (compass), instability, especially in wind, and unsuccessful implementation of the altitude hold sensor. The California research project was one of the first research reports published by a DOT on utilizing UASs for bridge inspections.

Georgia DOT

As part of a joint research project with Georgia Institute of Technology in 2014, Georgia DOT published the results of twenty-four interviews with GDOT personnel in order to evaluate the economic and operational advantages and drawbacks of UASs within traffic management, transportation, and construction [109]. Five different UASs configurations, A through E, were investigated in the GDOT study. System A was a quad-motor UAS having FPV, VTOL, and a video camera suitable for monitoring operations such as and not limited to traffic monitoring. System B was an enhanced

version of System A, equipped with LiDAR. This system was recommended for any

mission that involved mapping. System C also expanded upon System A with emphasis

on prolonged environment/region monitoring, for example, construction sites. System D

was proposed as a platform for county-sized missions, whereas Systems A through C

were for regional missions. System D was a fixed winged aircraft with wingspan size of

2-6 m and capable of high-quality aerial photogrammetry. This system was suggested as

the proper candidate for post-disaster response missions and traffic monitoring. Finally,

System E configuration, which was recommended for bridge inspections, consisted of a

multi-rotor copter with 8 or more motors, potentially tethered, capable of VTOL, and

equipped with LiDAR and safety pilot mode.

Michigan DOT

Michigan DOT published the results of experiments on five main UAS platforms

with different sensors [100]. These UASs were equipped with a combination of visual,

thermal, and LiDAR sensors to assess critical infrastructures and their defects, for

example, bridges, confined spaces, traffic flow, and roadway assets. They concluded that

UASs are low-cost, flexible, and time-efficient tools that can be used for multiple

purposes: traffic control, infrastructure inspections, and 3D modeling of bridges and

terrain. Each platform was reported to be suitable for a certain task in Michigan DOT. A

VTOL, equipped with a thermal and a visual camera, proved to be the most appropriate

for high-resolution imaging of a bridge decks, but obtained mixed results when compared

to hammer sounding due to the poor surface quality of the deck. With regard to UAS

controls for bridge assessment, SLAM was proposed as a topic for future study with the

major challenge being UAS position accuracy.

Minnesota DOT (Phase 1)

Minnesota DOT initiated investigations into benefits and potentials of UAS

bridge inspection [15]. In this study, four bridges in Minnesota were inspected using

UASs to study the effectiveness of VTOL UASs. The first bridge inspection was a 26 m

long single span prestressted concrete bridge, and the UAS could not perform an under

bridge inspection due to low-clearance and lack of GPS signals. The human inspection

and the UAS inspection detected defects on a bridge deck such as spalls and cracking, but

the inspector detected missing anchor bolt nuts during the under-bridge inspection while

the UAS was unable to detect this defect. However, mild scour was only detectable in the

UAS images. The second bridge inspection was done on a 100 m long open spandrel

concrete arch bridge. The UAS was unable to survey the top of the bridge deck due to

traffic. Zoom lens provided reasonable visibility for some under-bridge items. In this

case, mild scour was not detectable in the UAS images, but the UAS inspection images

showed bearing deterioration that the human inspection report missed. On the third

structure, a five span steel underdeck truss, the UAS could investigate the truss

superstructure and substructure and excellent agreement was found between the human

and UAS inspection. The final bridge was approximately 850 m long with five truss arch

spans, and a UAS inspection was carried out on this bridge but was not compared to a

human inspection. It was concluded that UASs can be used in the field of bridge

inspection while posing minimum risk to the public and inspection personnel. In some

cases, UAS images provided a cost-effective way to obtain detailed information that may

not normally be obtained during routine inspections. FAA regulations prevented the UAS

from flying over traffic, negating the benefits of UAS inspections for the deck.

Florida DOT

In 2015, Florida DOT published a research report investigating the feasibility of

UAS-assisted inspection of bridges and high mast luminaires [110]. A UAS, equipped

with high-definition cameras was used in lieu of experienced inspectors to achieve the

following goals: reduce the cost of inspection, reduce the hazards to the inspector,

increase the public safety, and increase the inspection effectiveness through more

comprehensive data acquisition. Limitations were also identified, such as allowable

payloads, control and navigation in severe winds, and image quality in low-light

conditions. One aspect of this study was to select the main UAS components based on the

demands of the project. Weighted factor analyses were developed to provide a systematic

decision-making toolbox for each component, which led to the selection of three VTOL

UASs, four ground viewing stations, and three visual cameras. Finally, a dual camera

setup, and remote control gimbal were selected to perform the inspections. The selected

UAS was tested against wind to determine the required clearance from an object. This

clearance was estimated to be 0.3 m for wind speeds less than 11 km/h and wind gusts

less than 16 km/h; however, the required clearance is only valid for the tested UAS.

UASs were able to inspect a high mast luminaire in 8.5 minutes while providing adequate

pictures in acceptable details. Additionally, two preliminary field tests were performed

under controlled conditions where a pedestrian bridge and a wooden bridge were

inspected under 15 minutes and 10 minutes, respectively. The inspections indicated

moderate and severe rust and fine cracks. A field test with FDOT inspectors performed

the inspection in 10 minutes under 20 km/h wind speeds and 29 km/h wind gusts,

respectively. Rust, cracks through epoxy, bearing deformation, and deck and girder

separation were among the detected flaws. The other field test was performed on a steel

railroad drawbridge with wind speeds of 11 km/h and the wind gusts equal to 27 km/h.

Missing nuts and severely rusted bolts were detected. The third field inspection was

performed on a concrete and steel superstructure bridge in 10 minutes while the wind

speed was 27 km/h and the wind gusts were 40 km/h This inspection showed mild to

severe corrosion regions on a transverse girder bracing and a separation between the

girder and the deck in the images. A service and maintenance schedule was proposed for

UASs with a 25 hour of operation interval.

Idaho DOT

Idaho Transportation Department (ITD) in corporation with Utah State University

conducted a UAS bridge inspection with emphasis on damage detection in bridges with

Fracture Critical Members (FCM) [46]. Two aspects of remote sensing in bridge

inspections were investigated in this study: visual inspections and autonomous defect

detection, both using inspection data gathered by UASs. Several inspections conducted

on a lab made bridge using a 3DR Iris platform showing UASs can be used for deck

inspections and concrete crack detection in real time. An image processing algorithm was

also used to detect cracks automatically with 90% accuracy. The next phase of this study

was to determine the feasibility of fatigue crack detection using three UAS platforms:

3DR Iris, DJI Mavic, and a custom-made VTOL. A set of indoor and outdoor

experiments in GPS denied environments were carried out. The target of the inspections was to visually detect a real fatigue crack on a test-piece from UAS images in various situations to determine the minimum requirements in terms of clearance and lighting condition. The crack was not visible in the images captured by the 3DR Iris (with a GoPro Hero 4 camera) in any condition. DJI Mavic images were acquired without GPS and in dark lighting conditions (i.e., similar to that under a bridge), showing the fatigue crack. The custom VTOL struggled in GPS denied situations, but the optical zoom on its camera allowed for somewhat successful fatigue crack detection. An image-processing method for autonomous fatigue crack detection was developed which detected more than 80% of the crack length in DJI Mavic images. The DJI Mavic was recommended as a potentially suitable platform for under-bridge inspections due to reliance on a stereo-vision positioning system in absence of the GPS signals, a good quality camera, its small size for maneuvering between girders, and the camera's ability to function in low light conditions (manual exposure adjustment). This platform however did not perform properly over running water during inspection of an in-service fracture critical bridge in Idaho. Due to the absence of GPS signals under the bridge, the DJI Mavic relied mainly on its downward stereo vision positioning system for control and navigation. Therefore, the UAS did not hold neither did its altitude or its position when it was flown over the current. The performed field study was inconclusive with respect to fatigue crack detection, but was successful in detecting concrete and steel surface deterioration.

Minnesota (Phase 2)

Phase 2 of the Minnesota DOT study was completed in 2017 by inspecting 4 other

bridges throughout Minnesota [88]. The inspected bridges were longer than the ones

studied in the phase 1 [15]. The UAS performance for bridge inspection was compared to

standard hands-on inspection in terms of cost and time, access methods, and data

collection. Unlike the phase 1, UAS-based structural condition assessment of the bridges

was not compared to the hands-on results. A Sensefly Albris UAS, equipped with a

thermal and a visual camera, was used for the inspection. The platform was designed for

GPS-denied operation, inspection, and mapping. First, a 2,400 m long multi-span steel

bridge constructed in 1961 was inspected. The inspection of this bridge proved that the

UASs can successfully be used to navigate around large-scale bridges in severe weather

condition. However, the report does not define the severe weather. The UAS provided

data from under-bridge members yet, there was no actual indication of defect detection in

the report. With $20,000, UAS inspection was claimed to be 66% cheaper than the

traditional inspection ($59,000) which included four inspection vehicles, and a 25 m man

lift. However, the traditional inspection took 8 days to inspect the bridge while the UAS

finished the inspection in 5 days. The second inspected bridge was a 110 m long steel

high truss built in 1939. The main objective of this inspection was to detect deck

delamination using the integrated thermal camera on the UAS and compare the results to

chain dragging and handheld FLIR thermal camera. It was stated that "the onboard

thermal sensor was able to detect the deck delaminations with good accuracy", but this

was not quantified. A 3D model of this bridge was also constructed by processing UAS

images with Pix4D mapping software, however, no information regarding the

quality/accuracy of the model is presented. An 80 m long corrugated steel culvert was the

subject of the third inspection. The integrated headlight provided enough illumination to

capture usable images; however, UAS thrust kicked up dust, making the images not useful for inspection. The final inspection was done on an 86 years old 10-spanthrough truss bridge, one movable span, and three concrete spans. Reportedly this inspection helped the managers to decide to replace the railing based on the images captured by the UAS.

DOTs and Other UAS Applications

Virginia DOT

Virginia DOT cooperated with the National Consortium on Remote Sensing in Transportation to prove that it is possible to use UASs for traffic surveillance and monitoring [111]. The result of this cooperation showed that the UASs can reduce costs associated with traffic control by 50%.

Ohio DOT

Ohio DOT, in collaboration with Ohio State University in 2005, performed field experiments in Columbus, OH to collect data about freeway intersection movement, network paths, and parking lot monitoring. The outcome of the project provided quasi real-time space planning and distribution from the collected information by UASs to help travelers [112].

Florida DOT

Florida DOT (FDOT) began to investigate the applications of UASs in 2005 with the main focus on traffic management and road monitoring [113].

Washington State DOT

Washington State DOT and the University of Washington investigated the merits and challenges of using UASs to perform traffic surveillance and avalanche control [114]. They conducted experiments on two types of UASs: A fixed-wing aircraft and a VTOL rotary-wing aircraft (helicopter). The fixed-wing UAS was able to collect data from mountain slopes next to highways in case of an avalanche. The VTOL was found to be more suitable for urban area and traffic surveillance.

Utah DOT

Utah DOT in association with Utah State University studied the application of UASs for monitoring and documenting state roadway structures during a highway construction project [115]. Images were also taken to identify the species of wetland plant at Utah Lake wetland mitigation bank. The result of the inspection, after post-processing, was a mosaic model of the scene.

Idaho DOT

ITD initiated a preliminary investigation into UAS in 2014 to look into construction and stockpile monitoring. In this first investigation, visual and thermal images of bridge structures were taken, but were of limited use [46].

Summary of DOT investigations

Table 2-5 summarizes goals, achievements, and obstacles in each state DOT research project, organized chronologically by bridge inspection mission or non-bridge related. This table includes all state DOT studies on UASs that have been published or

cited by an article in research done between 2002 and 2017. Table 2-6 presents a

summary of the UAS platform and sensor specifications used in state DOTs and is

organized chronologically by bridge inspection mission or non-bridge related.

Table 2-5 UAS's progress and obstacles in state DOTs

Bridge Inspection				
State DOT	Ref.	Goals	Achievements	Shortcomings
California	[41]	Routine Bridge Inspection	Vertical takeoff, wind resistance up to 37 kmh, inspection images	Instability
Georgia	[109]	Determining proper UAS configuration for specific tasks	Proposition of five UAS configuration including the type of platform, vehicle, station and number and type of sensors.	No field inspections
Michigan	[100]	Initial Bridge Inspection, delamination detection	Successful construction of point cloud 3D models, defect detection (delamination)	Manual control, inconsistency between thermal and ground true in for delamination detection, inaccurate GPS
Minnesota (Phase 1)	[15]	Initial bridge inspection with off-the-shelf UASs	Structure mapping, thermal inspections, GPS assisted navigation, reasonable agreement between human and UAS inspection	FAA regulations prevented top bridge inspection, Loss of GPS signals prevented under bridge inspections,
Florida	[110]	Initial inspections of bridge and high mast luminaires	Similar image quality compared to human inspector, detection of concrete cracks down to 0.02 inches	FAA regulations prevented top bridge inspection, Loss of GPS signals prevented under bridge inspections, poor control in wind
Idaho	[46]	Fatigue crack detection (FCM inspection), GPS-denied navigation	Autonomous and visual bridge deck condition assessment, Autonomous and visual fatigue crack detection in mock inspections, field inspection	No crack detection in the field inspection, no over water flight due to sonar limitation,
Minnesota (Phase2)	[88]	GPS denied environment, initial inspection of large-scale bridges	Successful delamination detection using thermography, successful GPS-denied navigation, 3D model and mapping, cheaper and faster	No indication to weather effects, no comparison between UAS and human inspection.in terms of

			than traditional inspections for large-scale bridges	defect detection (except for delamination)
Non-Bridge Inspection				
State DOT	**Ref.**	**Goals**	**Achievements**	**Challenges**
Virginia	[111]	Traffic surveillance and road condition monitoring	Cost Saving	N/A
Florida	[113]	Recording data in less time consuming	FAA rule development, proof of concept	Manual control
Ohio	[112]	Freeway traffic assessment	quasi real-time space planning,	Manual control
Washington	[114]	Minimizing the highway avalanche closure and traffic control	Higher flight elevations up to 1500 feet, demonstrating need for flexible FAA regulations	Manual control, restrictive FAA regulations
Utah	[115]	Roadway construction and vegetation monitoring	Successful and high quality images	Manually controlled, inaccurate models of the site, insufficient image overlap

Table 2-6 UAS Mission Parameters in state DOTs

Bridge Inspection					
State DOT	**Year**	**Model/type**	**Sensors**	**Payload**	**Purpose**
California	2008	ES20-10	Visual Camera	4.5kg	Road Inspection
Michigan	2015	Bergen HexaCopter	Visual and Thermal Camera, LiDAR	5kg	Deck inspection, 3D modeling, roadway assets
		DJI Phantom	Visual camera	unknown	Bridge and construction monitoring
		BlackoutMini Quadcopter	Visual camera	unknown	Bridge structure imaging, confined space assessment
		Heli-Max 1 Si	Visual camera	unknown	Confined space assessment
		Walkera QR 100S	Visual camera	unknown	Confined space assessment
		FVPfactory Waterproof quadcopter	Visual Camera	"Half of vehicle weight"	Bridge structure imaging - undersides (For bridges over water)
		Blimp	Visual Camera	"Half of vehicle weight"	Traffic monitoring and maintenance
Minnesota (Phase 1)	2015	Ayeron Skyranger	Visual and Thermal Camera, Lights	Variable	Bridge inspection
Florida	2015	ArduPilot Mega 2.5 Micro Copter	Visual Camera	Variable	Bridge and high mast pole inspection
Idaho	2017	Custom-made (Goose)	Visual and thermal Camera	14.5kg	Bridge inspection
		DJI Mavic	Visual Camera	0.9kg	Bridge inspection
		3DR Iris	Visual Camera	0.4kg	Bridge inspection and fatigue crack detection
Minnesota (Phase 2)	2017	Sensefly Albris	Visual and Thermal Camera	1.8kg (including the UAS)	GPS-denied navigation, mapping, 3D model construction, bridge inspection.
Non-Bridge Inspection					
State DOT	**Year**	**Model/type**	**Sensors**	**Payload**	**Purpose**
Virginia	2002	ADAS	Visual Camera	-	Proof of concept
Ohio	2004	MLB BAT	Visual Camera	2.2kg	Traffic surveillance and road condition monitoring
Florida	2005	Aerosonde	Visual Camera	13kg	Traffic surveillance
Washington	2008	MLB-BAT R-Max	Visual Camera	2.2kg 29.5kg	Avalanche control, traffic supervision
Utah	2012	AggieAir	Visual Camera	0.9kg	Monitoring, Object detection
Idaho	2014	Sensfly eBee RTk	Visual and Thermal Cameras	0.73kg	Road monitoring

FAA Regulations on UASs

Current Regulations

There are two sets of rules for flying any aircraft: Visual Flight Rules (VFL) and
Instrument Flight Rules (IFR). According to the "Aeronautical Information Manual," a
controlled airspace is defined as "…an airspace of defined dimensions within which air
traffic control service is provided to both IFR and VFR flights in accordance with its
classifications" [116]. In the United States, the controlled airspaces are designated as in
Table 2-7.

Table 2-7 Designated Airspaces in United States (Adapted from [116])

Name of the class	Definitions
Class A	From 5,500m mean sea level (MSL) up to and including Flight Level[1] 600.
Class B	From the surface to 3000m MSL.
Class C	From the surface to 1,200 m (4,000-foot) above the airport elevation.
Class D	From the surface to 760m from the airport elevation.
Class E	An airspace that is not classified as A, B, C, and D
Class G	Uncontrolled airspace with no IFR operation.

[1.] Flight Level (FL) are described by a nominal altitude in hector-feet while being a multiple of 500-foot. FL 600 is equal to 18,200 m (60,000-foot)

The FAA was established after the Federal Aviation Act in 1958 and was called
the "Federal Aviation Agency" at first, until it became a part of the DOT and took on its
present name in 1967. One of the responsibilities of this administration was and is to
provide safety regulations for flying UASs. FAA recognizes two categories for UAS use:
"Fly for fun" and "Fly for work/business." The former does not require permission from
FAA, but the vehicle should be registered through the FAA website. The "Fly for

work/business" category is restricted by FAA. The latest version of the FAA rules was published on the FAA website on June 21, 2016. Some of these regulations are as follows:

- The total weight of the unmanned aircraft should be less than 25 kg (vehicle and payload).

- The vehicle must remain within the visual line-of-sight of the remote pilot in command, the person manipulating the flight controls, and the visual observer during the flight.

- The aircraft must not operate over any persons that are not directly participating in the operation, are not placed under a covered structure, and are not inside of a covered stationary vehicle.

- Flight is only permitted during day-light or civil twilight with appropriate anti-collision lighting.

- The sole use of a first person view camera does not satisfy the "see-and-avoid" requirements.

- The maximum altitude is 133 m above ground level (AGL) or within 133 m of a structure.

- The maximum speed of the UAS must not exceed 160 km/h.

- No person may act as a remote pilot or visual observer for more than one UAS at the same time.

- The UAS operator must either hold a remote pilot airman certificate or be under the direct supervision of a certificate holder.

- UASs must be registered and certified by the FAA.

- The UAS must not be flown within 8 km of an airport without prior authorization from the airport operators.

- The UAS must not be flown from a moving vehicle.

Pilots requirements are:

- Must be at least 16-years old

- Must pass an initial aeronautical knowledge test at an FAA-approved knowledge testing center

- Must be vetted by the Transportation Safety Administration (TSA)

- Must pass a recurrent aeronautical knowledge test every 24 months.

Registered aircraft must have an application form (AC Form 5050-1) and evidence of UAS ownership. After submitting these documents, the UAS is registered and a Certificate of Authorization (COA) can be requested. The following information is required to submit the COA application form: concept of operation and type of missions, operation location, altitude, communications, and flight procedures [109]. After submission, FAA conducts a comprehensive operational and technical review on the application to ensure the UAS can operate safely with other airspace users. As of 2018, the wait time to complete the application is 60 days. The COA application also requires proof of airworthiness for the UAS. This proof can be obtained either by submitting an Airworthiness Statement or through FAA's Certificate of Airworthiness. As a new interim policy, FAA has been speeding up COA, also known as Certificate of Waiver in section 333 for certain commercial UASs. Section 333 exemption holders now are

automatically granted with "blanket 200 foot," which allows them to fly anywhere in the

country except for restricted airspaces, as long as they are below 61 m (200 feet) and the

platform is not heavier than 24 kg. The part 107 regulations provide a flexible

framework; however, more opportunities have been provided by FAA to omit these

regulations. Table 2-8 demonstrates the summary of the regulations for flying UASs and

micro UASs (weight less than or equal to 2 kg).

Table 2-8 UAS and micro UAS regulations (adapted from [110])

Provision	UAS	Micro UAS
Maximum Weight (platform plus payload)	24 kg	2 kg
Airspace confinements	Class G, and Class B, C, D, E with Air Traffic Center permission	Only Class G
Distance from people and structures	No operation over any person not involved and uncovered	No limitation
Autonomous operations	Yes	No
Required aeronautical knowledge	Knowledge test	Self-certification
FPV	Permitted; if visual line of sight is satisfied	Not permitted
Visual observer training	Not required	Not required
Operator training	Not required	Not required
Operator certificate	Required with knowledge test	Required without knowledge test
Preflight safety assessments	Required	Required
Operation within 8 km of an airport	Prohibited	Prohibited
Operate in congested region	Permitted	Permitted
Liability insurance	Not required	Not required
Night operation	Prohibited	Prohibited

FAA Restriction to UAS Bridge Inspection

The previous section illustrated the current FAA regulation on using UASs. These regulations pose limitations on the certain aspects of UAS bridge inspection which will be discussed in this section.

- FAA mandates the pilot has a line-of-sight to the vehicle during the inspection. However, one of the advantages of using UASs is to access to locations that are difficult to reach without a UBIT [46,117,118]. Maintaining the line-of-sight becomes impossible for certain terrain and topographical situations, severely limiting inspection. It may be possible to obtain a waiver for these situations.

- Past studies indicate bridge deck inspection is one of the strength of UASs over human inspector in terms of cost and time of inspection [31,88]. However, the current FAA regulations prohibit UASs over passing traffic, requiring lane closure. Waivers for flight over traffic are possible, however, the proximity to said traffic will be a deciding factor.

- One of the proven techniques for deck delamination detection in using thermal inertia which requires taking thermal image of a surface in two different ambient temperatures with maximum possible temperature gradient, i.e., daytime and nighttime [80], yet the FAA limits the UAS operation to daytime.

- According to FAA regulations, the maximum flight altitude is 133 m. Therefore, any bridge elevated more than 133 m cannot be inspected while one of the merits of using UASs is to provide data on bridges that are challenging such as tall bridges. There are almost 150 bridges with the height of 133 m or more and

average age of 59 years which cannot be inspected by UASs. Again, a waiver is likely possible to relax this restriction.

Synthesis of UAS Bridge Inspections and Future Needs

The previous sections have outlined applications of UASs in different fields, including bridge inspection, and discussed the current capabilities related to automated inspections (i.e., 3D modeling, damage detection, and controls). UAS-assisted bridge inspections have had success throughout the United States that have resulted in successful routine inspections of easily accessible locations when UASs had access to GPS, and autopilot features. The compiled literature on these topics is informative about the future path of UASs for bridge inspection by recognition of current challenges and benefits. DOT research with UAS-based bridge inspections is relatively scarce and involved mostly off-the-shelf solutions and focused on feasibility. Proving that a UAS can be an alternative to visual inspections would very valuable in bridge inspection practice, but current studies have focused on case studies. This section compiles the current main benefits and drawbacks of UASs as an alternative to visual inspections and the future potential for automated inspections.

Immediate UAS Inspection Potential

As mentioned in before, the most interesting aspect of using UASs for state DOTs and bridge inspection agencies were visual inspections. The following sections investigate the possible advantages of using UASs for bridge inspections.

Safer Inspection

One of the major advantages of UASs in this field is the higher degree of safety. According to the engineer of maintenance and operation at Michigan DOT, "…using UAVs provides a mechanism to keep the crew out of high risk situations" [100]. UASs can obtain photos from under-bridge regions without requiring manlifts and potentially road closures, allowing for increased inspector and public safety, while the acquired data by UASs have similar qualities as visual inspections [88]. Fig.2-5a shows a UAS during a targeted visual inspection to detect fatigue cracks. If an inspector was to perform the visual inspection (for location shown Fig.2-5a), it would require rappelling or a UBIT [46]. Fig.2-5b shows the inspection image of a possible fatigue crack taken by UAS. Inspection of high mast poles and cable-stayed members are other scenarios where UASs can provide a safer situation [15,110].

(a)   (b)

Fig. 2-5 (a) A UAS inspecting girders bridge under a bridge, (b) an image of a fatigue crack taken by a UAS from a bridge girder with fatigue crack

Additionally, safety risks and costs may decrease because there may be fewer people involved (Table 2-9). According to current FAA rules, having a certified pilot and

a spotter is considered legally adequate to fly UASs; whereas, an inspection will typically

involve at one to four people in the visual inspection.

Table 2-9 Manual and drone cost comparison (adapted from [108])

Method of inspection	Time spent	Lane closure	People involved	Money spent
Visual Inspection	8hour	Yes	4	$4600 U.S.
UAS Inspection	1hour	Yes	2	$250 U.S.

Faster Inspection

The time required to inspect a complex bridge or obtain photos of a hard-to-reach

location, like Fig.2-5, can be decreased considerably with UASs. For example, Yang et

al. stated that it only took 42 minutes to complete an entire bridge inspection using a

UAS: 25 minute set up time, 10 minute first flight, and 7 minute second flight. The

inspected bridge was 240 m long and 8 m wide, but bridges are likely to be highly

variable depending on the structure type [119]. In this case, public advertisement of the

closure and set-up time for closing down the road can also be eliminated when the UAS

is not visible to traffic. Note that the work by Yang et al. was a survey of the structure

and was not of quality for a true inspection (i.e., detecting defects), which would take

considerably longer. Table 2-9 is adapted from an AASHTO report, for deck inspection

claiming UAS inspection reduce the deck inspection cost [108]. The size and condition of

the inspected deck, and also the objective of this inspection were not mentioned in this

report. Assuming both inspections were performed to get similar information of the deck, the UAS was faster by 8 times. There have been scenarios during the inspection where having a UAS sped up the inspection process, however, more comprehensive experiments and inspections need be carried out to determine when and how UASs can decrease the inspection time and by how much.

Economical Inspections

In addition to the safety and time reductions, there is also a documented cost reduction; many of the cost reductions are associated with the safety and time reductions. If UASs are used instead of manned inspection, cost for just the deck inspection can decrease from $4600 to $250 [108,123]. The itemized cost of the inspection, according the Dorsey, is shown in Table 2-9 [108]. This survey did not address many of the assumptions about costs associated with span length, age of the bridge, location of the bridge, etc. In addition, the current FAA regulation prohibits using UASs over the traffic, so the cost of lane closure, estimated to be $3,000, should also be added to the cost of UAS inspection. A more detailed study for under-bridge inspection showed a more realistic cost estimation for visual versus UAS-based inspection, as shown in Table 2-10 [120]. This table shows that the inspection costs of a two span bridge can be reduced by more than one third. However, there are hidden costs that are commonly ignored in these studies, such as cost of renting a pilot and UAS. For many DOTs, the inspection of a simple bridge (e.g., no fatigue details, relatively easy access, low traffic) may take only 20-30 minutes and require only a single inspector with a camera and binoculars [12]. In these cases, UAS bridge inspection will not improve the cost or time associated. For a

large-scale bridge (2,400 m long), a 2017 cost analysis showed that UAS-inspection was

37% faster and 66% cheaper than the traditional inspection [88]. However, details

regarding this calculation and inspection performance was neither reported or compared.

Table 2-10 The cost of visual and UAS inspections for under bridge (adapted [120])

Method of inspection	Cost of traffic control	Cost of UBIT	Cost of Inspectors	Total
Visual Inspection	$640	$2000	$1200	$3840
UAS Inspections	$320	0	$750	$1070

As a case study, a bridge with FCMs was inspected using hands-on and UAS-

assisted methods. The bridge is located in Ashton, Idaho, and carries Ashton-Flagg

Ranch road traffic over the Fall River (ITD Bridge Key 21105). The full details of this

inspection can be found in [46,118]. The bridge consisted of two main longitudinal

frames on the Northern and Southern sides (West-East orientation). Hands-on inspection

was carried out using a UBIT in four hours to inspect the whole bridge. The total cost of

the inspection was $391 per hour, including UBIT costs, of inspection ($1,564 for four

hours) which is itemized in Table 2-11. Separately, a DJI Mavic Pro UAS was used to

inspect the bridge (costs are per hour). The UAS followed the water current without

pilots control making inspection over the water impossible (refer to Idaho DOT section,

for more details). Due to this issue, only a quarter of the fatigue prone locations were

inspected using UAS which included 12 susceptible connections in four floor beams, two

girder splices, a girder web, a concrete barrier, and bottom flange two girders. The UAS-

assisted inspection identified the presence of fatigue cracks in two floor beam

connections. These cracks have previously been detected marked through hands-on

inspections. The images from these fatigue cracks show the marker lines, but not the

actual cracks (Fig. 2-6a). In addition, the UAS-assisted inspection ruled out the presence

of fatigue cracks in other inspected regions (Fig. 2-6b). Other defects such as concrete

delamination and efflorescence, and steel rust were detected in the UAS-assisted

inspection. The UAS-assisted inspection took 4.5 hours with a net flight time of 1.5 hours

(90 minutes). The inspection cost in this case was $200 per hour. Considering a quarter of

the bridge was inspected in 4.5 hours, the inspection costs extrapolated to whole bridge

using the UAS would be $1800. This case study shows the hourly cost of UAS inspection

is almost half of the hourly cost of UBIT inspection, which agrees with previous studies

[88, 120]. However, the extrapolated UAS inspection time was longer than the actual

UBIT assisted hands-on inspection. The additional time made UAS-assisted inspection

15% more expensive than the hands-on inspection. It should be noted that the time and

cost associated with using UASs is different for various situations as outlined in other

places in this paper.

Other Benefits

An indirect benefit of UAS-assisted inspection may be lessened traffic

congestion. Road closures and time required for a particular traffic disturbance can be

limited, which is particularly important for high traffic bridges. Sometimes the objective

of the inspection is to check the general integrity of the structure, such as checking if

large items are missing or large areas are defected, for instance, a 330 m long barrier

railing was inspected using a UAS in less than 3 hours, enabling to the designers to make

an informed decision to ultimately replace the railing [88,110].

Table 2-11 The cost of hands-on and UAS-assisted inspections for FCM inspection [46]

Method of inspection	UBIT	Support Truck	UBIT Operator	Inspector	Pilot and UAS	Total	Full Bridge (total)
Hands-on	$200	$16	$75	$100	-	$391	$1564
UAS	-	-	-	$100	$100	$200	$1800
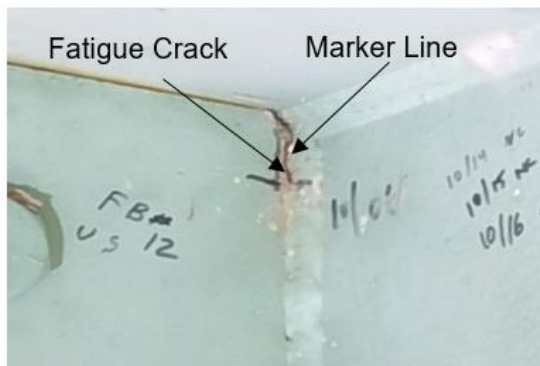
(a)   (b)

Fig. 2-6 (a) UAS-assisted FCM inspection (a) a location with fatigue crack, (b) a location without fatigue crack

UAS Inspection Challenges

The advantages mentioned in previously are possible under relatively ideal

conditions. Ideal conditions include a skilled pilot, no software and hardware

malfunctions, an appropriate UAS, and no adverse weather conditions. Currently, there

are many challenges associated with bridge inspections. Some challenges are due to the

availability of this emerging technology, and some are due to the regulations associated with governing bodies such as the FAA and state DOTs.

Regulations

Current FAA restrictions are not too burdensome for an agency to perform inspections, but provide enough restrictions to limit use in some situations. Regulations will relax over time, as in the past, as public perception, UAS reliability, and autonomous controls continue to improve. Currently, FAA regulations will allow UASs to inspect bridges if the they are not visible to traffic. Thus, for any inspection process that involves UASs being exposed to traffic, such as UAS bridge deck inspections, cable stay towers, above grade trusses, or even high mast luminaries, the traffic will need to be modified. Furthermore, FAA regulations mandate that the pilot is in visual contact with the UAS at all times, even if using first person view (FPV), which gives the pilot a live feed of the flight from a camera on the UAS. This mandate severely limits some difficult to access bridges which may still have inaccessible locations for the UAS due to this restriction.

Flight Control

Probably the largest hurdle to fully automated inspections is the GPS-denied environment under the bridge. Most pilots, skilled or unskilled, will have excessive difficulty without significant aid from the autopilot, the most useful and reliable of which comes from GPS signals. Coupled with the fact that most pilots own their own UASs, which will be used on multiple jobs, the risk of losing a UAS in a waterway or simply crashing it may deter many pilots from under-bridge inspections. UASs rely on GPS signals for autopilot features and stability. Under a bridge, these signals are either very

weak or non-existent and UASs cannot be controlled properly [15]. Thus, claiming that

UASs are a feasible alternative to UBIT visual bridge inspections, as some studies have

indicated, is not accurate [108,120]. Zink and Lovelace handled this issue by using high-

definition cameras with zoom capabilities, but the applicability of these techniques is

limited [15]. Many new off-the-shelf UASs have indicated that they have additional

sensors (SONAR, LiDAR) that can aid in GPS-denied environments, but there is little

proof of feasibility at this time for bridge inspection [15,88]. Without the benefit of GPS,

control under a bridge is very limited, especially in high wind situations, risking

catastrophic damage to the UAS and sensors and even posing a safety hazard to the pilot,

inspector, spectators, and motorists. There are many promising control possibilities to

automate the inspection process, like SLAM outlined above, but the harsh environment

and difficult scenarios limit the current generation of UAS controls packages.

A skilled pilot is necessary, especially in a complicated situation like a bridge

inspection where there are potentially harsh environments. Pilot needs to have substantial

navigation skills to capture stable images while still be able to complete the inspection

without imposing damage to the UAS. A skilled pilot can aid in a successful under or

over-bridge inspection, and DOTs are likely to mandate some specific level of skill.

Presence of a pilot (COA/333 or Part 107) is also legally mandatory for any type of non-

recreational activity in the outdoors. Wages for an accomplished pilot can be

considerable and variable. According to an informal survey of UAS pilots available in the

authors' area, costs can be as high as $1200/day but as low as $650/day, plus travel

expenses. Based on the above findings, there is a major need for improvements in the

areas of UAS controls, navigation, and image processing in order to maintain

effectiveness.

Time

If for a typical structure a typical inspector will only require 30 minutes of onsite time to arrive at an appropriate condition rating, a UAS inspection will need to meet or exceed this to become viable. Considerable time and money could be spent on data post-processing if thermal images are desired as well as any semi-automated damage detection. Inspectors need a way to arrive at a condition onsite and move onto the next bridge without creating an additional level of analysis. Part of this will come with future automation of the inspection process, but currently, image-processing techniques for damage detection and 3D modeling are not at the level required for even a semi-automated real-time inspection. Whether for image modifications like removing image distortion or for intelligent feature detection algorithms like image-based crack detection, the post-processing operations have been commonly used for UAS bridge inspection research, but are still not time or cost effective for most bridges at this time [100,117]. Performing these complex operations is costly and requires professional and highly trained staff, which are inaccessible to most DOTs [110]. Post-processing operations also need time to perform on the order of a few minutes to a few hours. As such, there is a major need for automated or semi-automated tool development for bridge inspection that will make UAS bridge inspections feasible.

Weather

Weather will continue to play a major role in UAS bridge inspections. Unfortunately, if there is a bad weather day, an inspection cannot always be rescheduled

due to the many demands placed on a bridge inspection program. Inspections are often scheduled many months out without the possibility of returning due to tight DOT and private inspector schedules, although inspection dates can become more flexible when a UBIT is not involved. The quality of the UAS flight and the acquired data can decrease due to adverse weather [102,117]; furthermore, captured images or videos may not be clear due to the variable lighting conditions underneath a bridge. High wind speeds will significantly increase the allowable clearance between the UASs and the object of interest because of the risk for damaging sensitive mechanical equipment or even the structure itself [110,118]. UASs have several vulnerable components, especially the propellers, but also sensors. The pilot needs to be very cautious near a structure while trying to obtain the best resolution possible, and the complex geometry of bridge structures further complicates the situation. Many newer commercial UASs contain some obstacle avoidance software integrated into the autopilot; however, these options have not been evaluated in any known research. These options have the potential to help, but depending on the settings they could also hinder the inspection if the UAS gets too close to a point of interest [46]. One of the greatest tools a UAS pilot or spotter has for real-time defect detection is live streaming of visual data to the ground crew. However, due to the distance from the UAS to the receiver, interference, and bad weather, this can be compromised, making post-processing mandatory [46]. For a smaller bridge, a setback like this can eliminate the time and cost benefits of using UASs for inspections.

Functionality

UAS inspections can only replace visual inspections and are unlikely to be able to

perform physical inspections anytime in the foreseeable future, but UASs can perform

some limited NDE. Many times during an inspection, an inspector must remove rust,

nests or droppings from an area to observe a defect. UASs cannot prepare the surface for

defect detection without major advances in robotics and control. UASs are limited to non-

contact NDE methods (e.g., visual, thermal) to assess the condition, whereas with a UBIT

inspection, nearly all options for bridge inspection are available. Currently, an inspector

can measure the size of a defect in real time, whereas a UAS can only provide this

function on a limited basis with additional sensors and significant post-processing, most

of which would not be off-the-shelf. The application of UASs are restricted to visual

inspection, and if the inspectors decide a region requires more investigation, a UBIT must

be used, which may still allow for a more robust inspection and cost reduction.

A functional UAS requires constant tuning and maintenance on the platform and

all the components, e.g., motors, propellers, sensors, ground station unites, and

controlling joy sticks [110]. UASs require skilled mechanical and electrical engineers to

retune their system after replacing or upgrading a broken or out-of-date component.

Without proper tuning, the autopilot functions can be less effective, resulting in less

effective or dangerous inspections. However, the cost of individual components on UASs

are continuously decreasing. Even full off-the-shelf system costs are rapidly dropping

while their functionality are improving.

Gaps in Industry

To select a suitable UAS for inspection, one needs to consider various parameters.

For bridge inspection these parameters are varied based on inspection type and owner

needs [46,118]. If the bridge inspection industry wishes to move in the direction of UAS assisted inspections for the long term, these needs must be formalized and this chapter is a first step to this.

The bridge inspection programs for each state can be very different. Each state relies on a combination of consultants and state employees to perform their required bridge inspections. Many consultants, eager to win more business, are pressing DOTs to allow UAS-assisted inspections. DOTs are grappling with this change and desire to develop standards and training protocols to ensure inspection quality. The recent popularity of UAS in civil infrastructure health monitoring and inspection has created the opportunity for private companies to perform UAS-based inspection professionally. AETOS, Empire Unmanned, Microdrones, BDI and TechCorr are among companies providing UAS-based inspection services; however, bridge owners are not usually among their clients. Most of the inspections conducted by these companies have been on tanks, pipe and power lines, and industrial sites (e.g. power plants) which are not as complicated as bridge inspections. DOTs may wish to train internal UAS pilots for bridge inspection. As of 2018, the cost of UAS registration for commercial UAS is $25. The pilot has to obtain a remote pilot license which costs $165. The pilot can acquire field-training through academic aviation credits (e.g., $500 at Utah State University for one semester). The cost of UAS varies from $500 to several thousand dollars; however, a DJI Mavic Pro, or a DJI Mavic Air are around $1,000 and are suitable for bridge inspections. For a DOT, the total cost for training an employee as a UAS pilot can be as low as $2,000.

Future Needs

This chapter has outlined several current capabilities and proof of concept investigations for UAS bridge inspections as well as shortcomings of using UASs and areas in need of improvement. The following section outlines the areas of improvement that will enhance the capabilities of UASs and improve and automate infrastructure inspection.

Autonomous Control

Overall, each study which investigated unmanned inspections, whether bridge inspections or another application, used some form of autonomous control. Equipping the platform with some form of autonomous control algorithm(s) and appropriate sensors such as cameras (with image processing), LiDAR, and SONAR can help the UAS to autonomously record or avoid features or even simply hold altitude in GPS-denied environments; this would vastly improve bridge inspections. Some of these features are being implemented to various extents on a smaller scale in next-generation off-the-shelf platforms [15,46,118]. However, current limitations on UAS autonomous control ties the flight and inspection performance to the skills of the pilot. If fully autonomous control is to ever be achieved, the UASs can be operated by the bridge inspectors themselves, assuming FAA regulations allow it.

Additionally, in order to have widespread augmentation of human inspections, the inspection of all bridge types must improve, posing cost, time, and sensing challenges. Self-navigated UASs are the solution for achieving more efficient and reliable bridge inspection; however, no studies have been carried out to assess the feasibility of self-

navigated UASs in bridge inspection. However, the breakthroughs in UAS technology have made them considerably more functional. For instance, the size and weight of UASs and sensors have been decreasing while the allowable altitude, control range, and payload capacity are increasing.

Sensors

Visual and thermal cameras are the most common UAS sensors available for inspection purposes. These technologies still provide significant opportunities in the field of 3D modeling and defect detection. However, UASs are severely limited to non-contact only sensors, eliminating the most popular and proven NDE technologies with which bridge owners are comfortable. Improvements are occurring rapidly in non-contact sensing like infrared thermography and high resolution visual imagery; however, these are not well used or accepted by DOTs [31, 46,72,104,102]. Probably the most difficult hurdle to improving sensing of bridge structures is widespread acceptance of non-contact NDE by DOT engineers. This will likely require significant research to improve accessibility, training, and political improvements for this conservative group of engineers. Image processing techniques, specifically those in the thermography area, have shown promising results. These results are mostly validated in the laboratory, but not in the challenging environments in which bridges reside [46,85,87,117,121,122]. One major area of impact for UAS bridge inspection will be FCM inspections, which require a disproportionate amount of the operations and maintenance budget. FCM inspections are usually manned, arms-length inspection that uses some form of contact NDE along with a UBIT. The FCM inspections are often done on a large structure and are exceptionally

expensive [118]; however, UAS based inspection are not as successful as hand-on inspections in finding fatigue cracks (often much less than 0.5 mm wide) [46,117,118]. In addition, UAS-assisted FCM inspections are required to have some sort of self-navigation for GPS-denied operations which has not been resolved yet [46,118].

3D Model Reconstruction

Many previous studies illustrated the possibility of creating 3D models of a bridge from UAS-captured images. The ability to create a 3D model that includes enough detail to observe defects, support settlement, or structural members displacements could be invaluable to bridge management engineers. However, with off-the-shelf software and with current algorithms this is very time-consuming, not accurate enough, and not at a high enough resolution. With the improvement of LiDAR and even SONAR sensors, 3D models can also be constructed from LiDAR information, but only with skilled post-processing. There is potential for this with current sensor fusion techniques that combine several types of information, increased functionality, and accuracy [124-126]. With current inspection requirements, 3D models may be redundant for the average bridge, which takes only 30 minutes to inspect, but future work may make them more feasible and useful. Combining a 3D reconstructed model with Bridge Information Modeling may prove to be highly valuable, especially for older structures that do not have plans or need a detailed load or condition rating [127].

In addition to a detailed model suitable for inspection, an accurate model would be a major step toward autonomous inspections and self-navigated UASs. The SIFT and SURF algorithms have proven to be the most efficient way for feature detection in the

realm of 3D reconstruction; however, it is expected that the future focus of visual sensing

should be on generating efficient algorithms for real-time 3D model reconstruction that

align with DOT inspection needs.

Automatic Damage Detection

There are several ways damage can be detected using a UAS-assisted inspection.

The simplest way is to have a trained inspector view a live feed of video during the

inspection and manually identify damage as if the inspector was near the damage. This

option works well but is limited by the quality of the view-screen, which is limited to

1080p resolution, or in some cases, 4k resolution. Furthermore, this style of inspection is

hampered by inspector bias and human error. As many other industries attempt to limit

human inspections, it is likely that human influence will eventually be reduced through

some form of augmented or automated damage detection. Currently, a significant issue

with autonomous damage detection is the expense of post processing. Some recent

techniques have been developed that can provide a near real-time augmentation for crack

detection, but more robust tools are needed that fit within the current inspection

framework [72]. If additional sensors are employed, like LiDAR or thermal imaging,

damage detection techniques will require a skilled investigator to evaluate for accuracy

and/or very generic algorithms need to be developed [66]. A normal human inspection

results in a handful of images that are used for record keeping purposes while UAS

inspections result in thousands of images, increasing storage demand, and off-site

inspector time, which is unlikely to reduce costs.

Furthermore, the accuracy of all damage detection techniques depends on the

quality of the raw data, which is unlikely to be recollected if post-processing must be done off site. Because adverse weather and vibration of the platform can cause blurry images, shadow contrast, and lack of observable heat flux, care must be taken to use the appropriate sensor and platform for the situation. More intelligent post-processing algorithms used to detect smaller defects are also in demand but will always be tied to the raw data accuracy. The ability to automatically detect and separate irrelevant objects in the images, such as shadows and background scenery lines, is a current hot topic in crack detection algorithms. In the case of thermal imagery, it is important to select a proper time to capture thermal images. The proper time depends on the depth of the defects, the material, and the weather temperature [128,129]. More sensitive and higher resolution thermal cameras can help, but good thermal measurements are more likely to be affected by how the inspector pre-planned the inspection process. It is anticipated that more standard procedures, like ASTM D4788-03, which focuses on bridge deck delamination detection using thermography, will be developed for surface and subsurface defects and for various materials in the future [31].

Regulation

Current rules that apply to UASs are much more relaxed than in the past, but still represent significant restrictions. Since the applications of UASs in structural inspection and maintenance are being developed in conjunction with government agencies (state DOTs), more flexible regulations are predicted to be sanctioned in the near future. These new regulations will likely reflect public perception of UAS safety as well as the improvements on UAS control and platform reliability. With respect to infrastructure

inspection, the rules that hinder inspection the most are the visual line-of-sight necessity, required visual observers, and limit of a single UAS controlled by a single pilot.

Available UASs for Bridge Inspections

In this section, available off-the-shelf UAS platforms are presented with their suitability for different types of bridge inspections. The recommended UASs in this section are based on the authors experience and do not represent the whole UAS market. Due to lack of definitive guidelines to help with the selection of UASs, sensors, and other equipment, this can be challenging for DOTs to successfully start a UAS inspection program. Table 2-12 shows several UASs along with their general specifications, price (as of April 2018), and the potential bridge inspection applications. The price of a UAS for bridge inspection varies significantly, depending on the purpose of the inspection, quality and quantity of the integrated sensors, and computing capabilities. Integrating thermal cameras with the existing visual sensors can increase the price of the UAS up to three times. If a requirement of inspection is 3D model reconstruction, the size and the price of the UAS increases dramatically. Neither of these options may be necessary to complete most types of bridge inspection. On the other hand, in the case of under-bridge inspections, the UAS must have an auxiliary positioning system, vision system, to compensate with lack of GPS signals, in order to have a successful mission. The potential applications mentioned in this table are not without the limitations and challenges discussed throughout this paper; however, the content of this table guides the bridge owners and inspectors when purchasing a UAS and provides a variety of commercial options. Furthermore, the table does not suggest that the entire bridge inspection can be

performed using only the recommended UASs. The possible challenges during each UAS

bridge inspection are expected to vary significantly since published inspection reports

with UASs are limited.

Table 2-12 General specifications for UAS-assisted bridge inspections

UAS	Sensors	Positioning System	Size (cm)	Maximum Flight Time (min)	Price Range ($)	Potential Bridge Inspection Applications
Parrot BEBOP 2	Visual	GPS	32.8 by 38.2	25	500-700	Over-bridge, visual detection of macroscale surface cracks (thicker than 0.8 mm), routine inspection, checking the bridge structural integrity
3DR Iris[1]	Visual	GPS	63 by 38	20	600-800	
3DR Solo[1]	Visual	GPS	40 by 40	20	800-1000	
DJI Mavic Air	Visual	GPS, Vision System	21.3 (diagonal)	20	800-900	Over and under-bridge, visual detection of surface cracks (as thin as 0.04 mm), routine inspection, FCM inspection, checking the bridge structural integrity
DJI Mavic Pro	Visual	GPS, Vision System	33.5 (diagonal)	27	1000-1200	
DJI Phantom 4 Pro	Visual	GPS and Vision System	35 (diagonal)	30	1800-2000	
	Visual and Thermal				5500-8000	Over and under-bridge, visual detection of surface cracks (as thin as 0.04 mm), subsurface defect detection
DJI Mavic Air	Visual and Thermal	GPS, Vision System	21.3 (diagonal	20	4000-6000	

DSLR Pros Law Enforcement	Visual and Thermal	GPS and Vision System	64.3 (diagonal)	17	13000-15000	(delamination), routine inspection, FCM inspection, checking the bridge structural integrity
Albris SenseFly	Visual and Thermal	GPS	56 by 80	20	30000-35000	Over-bridge inspection, autonomous 3D model reconstruction, microscale defect detection (thinner than 0.02 mm),
Altus LRX	Visual, Thermal, LiDAR	GPS	140 (diagonal)	20	40000-50000	Over and under-bridge inspection, autonomous 3D model reconstruction, microscale defect detection (thinner than 0.02 mm), subsurface defect detection

[1] No integrated camera

Conclusions

This chapter has outlined the state-of-the-art for bridge inspections and UAS technology with the aim of educating and informing academics and decision makers about the current and future capabilities of UAS-assisted or automated bridge inspections. The current state of practice for bridge inspections, especially in United States, is heavily tied to visual inspections with minimal use of NDE. Bridge owners have demonstrated reluctance to accept NDE methods unless they are absolutely required for bridge evaluations. UAS-assisted bridge inspections have the potential to not only decrease

costs, but to also improve the adoption of NDE technologies, potentially increasing inspection accuracy, however UAS inspections face major hurdles.

UASs have shown promising results in civilian applications as well as civil engineering purposes, and many state DOTs have performed feasibility studies and found significant limitations, but also successes. The most common UAS applications in DOTs were traffic monitoring and surveillance, road condition assessment, and mapping; however, significant effort has been put into bridge structure inspection with varying degrees of success. The perception of UAS effectiveness for bridge inspection is tied to several variables, including DOT expectations, pilot skill, weather condition, and off-the-shelf limitations. It was shown that, ideally, UASs can provide less expensive and less time-consuming inspections for under bridge regions without traffic closure, but not in all situations and there are obstacles to overcome. FAA regulations have recently relaxed, but impose significant limitations, including required line of sight and UAS certification. Using advanced NDE sensors or even visual images can become too burdensome to be effective for routine inspections. Current autopilot controls have become a severe limitation for under bridge inspections due to the loss of GPS signals, causing a UAS to rely on a vision positioning system or a suite of other sensors which are questionably useful in the severe under-bridge environment.

The literature identified two major potential functions for UAS based inspections: 3D model reconstruction and autonomous damage identification. Unfortunately, these functions face major implementation limitations in order to be functional for complex – or even routine – inspections. Programs capable of generating 3D reconstructed bridge models, from either SFM or MVS, using feature detectors and feature descriptors such as

SIFT and SURF have been used for 3D model reconstructions of building, sites, and objects, but are very time consuming and require highly skilled technicians. These models have promising applications for UAS navigation but are unlikely to be accurate enough for bridge inspections without significant advancements. Autonomous defect detection methods are another promising advantage for UAS-assisted bridge inspections. Surface defect detection, for example, cracks, spalls, and surface degradation, have been successfully detected from visual images. Delaminated regions have been located and measured using thermal imagery on concrete bridge decks. A major hurdle to the adoption of these methods for UAS bridge inspection is resistance from bridge owners that have historically not implemented NDE technologies.

Based on the synthesis of this state-of-the-art review of bridge inspection and UASs, the following conclusions can be made:

1. The review of current bridge inspection practices makes it clear that there is a need for continuous improvement of bridge inspection procedures and cost reductions. Several NDE technologies were identified that can provide a better inspection but, based on DOT surveys, may not be worth the time, effort, post-processing, and cost associated with them [46,124]. UAS sensors may also fall within this category. Improvements should take the form of reduced inspection time and increased inspector and public safety, as well as decreased inspection costs, all of which indicate the need for automated inspections [27]. If automated inspection processes are going to replace standard practice, then they must be robust and require a similar amount time and effort to current bridge inspections techniques in order to gain widespread adoption.

2. The recent advances of UASs and UAS have the potential to shift the bridge inspection paradigm by providing low cost options to gather previously difficult or expensive images [108,120,].

3. UASs have increased in popularity and functionality for many applications, but the challenging nature of bridge inspections has reduced their effectiveness in this area [15,28,41,46]. UASs can also decrease the allocated time and budget for large-scale bridge inspections by providing inspection data comparable to hands-on method [88,117,118].

4. There have been mixed successes for UAS-assisted bridge inspections throughout the United States that have resulted in successful inspections of easily accessible locations where the UAS has access to GPS, the most reliable and effective tool for UAS autopilots (see Table 2-5).

5. There is a major need for improvements in the areas of UAS controls, navigation, and image processing in order to maintain effectiveness [46,100,110].

6. Weather currently plays too big of a role in UAS flight success, which is a very significant barrier for many state agencies with very tight inspection schedules [46,110,102]. This can be mitigated with continued improvement of autopilot controls in GPS-denied environments. UAS controls need to improve such that a pilot can safely and effectively obtain stable images of every part of the bridge in any reasonable weather.

7. For UAS inspections to become commonplace and cost-effective, automated inspection may need to become a reality, or at least, vast improvements will need to be made on autopilot controls [41,43,44,97]. Based on the above syntheses, full

automation during a bridge inspection is not possible given current technology and environmental challenges.

8. Image processing techniques (3D mapping or damage detection) that can detect defects are a significant advantage of a UAS inspection [107,131], but without the possibility of a real-time inspection will not become a routine part of any bridge inspection soon due to the level of detail required [46,118].

9. Bridge owners must learn to accept and become comfortable with the non-contact NDE techniques unique to UAS inspections for the full potential of UAS bridge inspection to be realized [8,129]. This places the burden on industry and researchers to develop accurate, generic algorithms for post-processing that can facilitate a real-time inspection or fit within existing local bridge inspection constraints [55,69,70,71].

10. Current FAA restrictions are not too burdensome for an agency to perform some inspections, but provide significant challenges to be useful in all situations [46,110]. Regulations will relax over time, as public perception, UAS reliability, and autonomous controls continue to improve [44,46,110].

References

[1] FHWA (2015). Deficient Bridges by Highway System. https://www.fhwa.dot.gov/bridge/nbi/no10/defbr15.cfm#a. Accessed 19 April 2018.

[2] ASCE (2017). Infrastructure Report Card. https://www.infrastructurereportcard.org/americas-grades/. Accessed 19 April 2018.

[3] Chang, M., Maguire, M., & Sun, Y. (2017). Framework for mitigating human

bias in selection of explanatory variables for bridge deterioration modeling. *Journal of Infrastructure Systems*, *23*(3), 04017002. https://doi.org/10.1061/(ASCE)IS.1943-555X.0000352

[4] Chang, M., and Maguire, M., (2016). Developing Deterioration Models for Wyoming Bridges. Wyoming Department of Transportation, Cheyenne. http://www.dot.state.wy.us/files/live/sites/wydot/files/shared/Planning/Research/RS0421 4%20Bridge%20Deterioration.pdf

[5] Lichtenstein, A. G. (1993). The silver bridge collapse recounted. *Journal of performance of constructed facilities*, *7*(4), 249-261. https://doi.org/10.1061/(ASCE)0887-3828(1993)7:4(249)

[6] Chong, K. P., Carino, N. J., & Washer, G. (2003). Health monitoring of civil infrastructures. *Smart Materials and structures*, *12*(3), 483-493. https://doi.org/10.1177/1475921703036169

[7] Swenson, D. V., & Ingraffea, A. R. (1991). The collapse of the Schoharie Creek Bridge: a case study in concrete fracture mechanics. International journal of fracture, 51(1), 73-92. DOI: 10.1007/BF00020854.

[8] Lee, S., & Kalos, N. (2014). Non-destructive testing methods in the US for bridge inspection and maintenance. KSCE Journal of Civil Engineering, 18(5), 1322-1331. DOI:10.1007/s12205-014-0633-9.

[9] Thompson, P. D., Small, E. P., Johnson, M., & Marshall, A. R. (1998). The Pontis bridge management system. *Structural engineering international*, *8*(4), 303-308. https://doi.org/10.2749/101686698780488758

[10] Tarighat, A., & Miyamoto, A. (2009). Fuzzy concrete bridge deck condition

rating method for practical bridge management system. Expert Systems with

Applications, 36(10), 12077-12085. https://doi.org/10.1016/j.eswa.2009.04.043

[11] Khan, M. S. (2000). Bridge-management systems past, present and

future. *Concrete International*, *22*(8), 53-56.

[12] Ryan, T. W., R. A. Hartle, J. E. Mann, and L. J. Danovich. 2012. "Bridge

inspector's reference manual." FHWA NHI 03-001, FHWA, U.S. Department of

Transportation. https://www.fhwa.dot.gov/bridge/nbis/pubs/nhi12049.pdf

[13] FHWA (2018). Archived: Highway Bridges by Deck Structure Type 2016.

https://www.fhwa.dot.gov/bridge/nbi/no10/deck16.cfm. Accessed 19 April 2018.

[14] Dekelbab, W., Al-Wazeer, A., & Harris, B. (2008). History lessons from the

national bridge inventory. Public Roads, Publication Number: FHWA-HRT-08-004.

https://www.fhwa.dot.gov/publications/publicroads/08may/05.cfm

[15] Zink, J., & Lovelace, B. (2015). Unmanned aerial vehicle bridge inspection

demonstration project (No. MN/RC 2015-40).

www.dot.state.mn.us/research/TS/2015/201540.pdf

[16] Rens, K. L., Wipf, T. J., & Klaiber, F. W. (1997). Review of nondestructive

evaluation techniques of civil infrastructure. Journal of performance of constructed

facilities, 11(4), 152-160. DOI: http://dx.doi.org/10.1061/(ASCE)0887-

3828(1997)11:4(152)

[17] Rolander, D., Phares, B., Graybeal, B., Moore, M., & Washer, G. (2001).

Highway bridge inspection: State-of-the-practice survey. *Journal of the Transportation

Research Board*, (1749), 73-81. https://doi.org/10.3141/1749-12

[18] Vaghefi, K., Oats, R. C., Harris, D. K., Ahlborn, T. T. M., Brooks, C. N.,

Endsley, K. A., ... & Dobson, R. (2011). Evaluation of commercially available remote sensors for highway bridge condition assessment. Journal of Bridge Engineering, 17(6), 886-895. DOI: http://dx.doi.org/10.1061/(ASCE)BE.1943-5592.0000303

[19] Latorella, K. A., & Prabhu, P. V. (2000). A review of human error in aviation maintenance and inspection. International Journal of Industrial Ergonomics, 26(2), 133-161. DOI: 10.1016/S0169-8141(99)00063-3

[20] Prieto, F., Redarce, T., Lepage, R., & Boulanger, P. (2002). An automated inspection system. The International Journal of Advanced Manufacturing Technology, 19(12), 917-925. DOI: 10.1007/s001700200104

[21] FWHA (2014). RABIT Bridge Inspection Tool. https://www.fhwa.dot.gov/research/tfhrc/programs/infrastructure/structures/ltbp/ltbpresearch/rabit/index.cfm. Accessed 19 April 2018.

[22] Gucunski, N., Boone, S. D., Zobel, R., Ghasemi, H., Parvardeh, H., and Kee, S.-H. (2014). "Nondestructive evaluation inspection of the Arlington Memorial Bridge using a robotic assisted bridge inspection tool (RABIT)." Nondestructive characterization for composite materials, aerospace engineering, civil infrastructure, and homeland security, Vol. 9063, SPIE, Bellingham, WA. doi: 10.1117/12.2063963

[23] Gucunski, N., Kee, S. H., La, H., Basily, B., Maher, A., & Ghasemi, H. (2015, April). Implementation of a fully autonomous platform for assessment of concrete bridge decks RABIT. In Structures Congress 2015 (pp. 367-378). Reston, VA, DOI: http://dx.doi.org/10.1061/9780784479117.032

[24] Leibbrandt, A., Caprari, G., Angst, U., Siegwart, R. Y., Flatt, R. J., and Elsener, B. (2012). "Climbing robot for corrosion monitoring of reinforced concrete

structures." 2nd Int. Conf. on Applied Robotics for the Power Industry (CARPI), IEEE, New York, 10–15. https://doi.org/10.1109/CARPI.2012.6473365

[25] Lim, R. S., La, H. M., Shan, Z., & Sheng, W. (2011, May). Developing a crack inspection robot for bridge maintenance. In IEEE International Conference on Robotics and Automation (ICRA), pp. 6288-6293. Shanghai. DOI: 10.1109/ICRA.2011.5980131

[26] La, H. M., Gucunski, N., Dana, K., & Kee, S. H. (2017). Development of an autonomous bridge deck inspection robotic system. 34 (8), 1489-1504. *Journal of Field Robotics*. https://doi.org/10.1002/rob.21725

[27] Lattanzi, D., & Miller, G. (2017). Review of robotic infrastructure inspection systems. *Journal of Infrastructure Systems*, *23*(3), 04017004 (1-16). https://doi.org/10.1061/(ASCE)IS.1943-555X.0000353

[28] Cook, K. L. (2007, March). The silent force multiplier: the history and role of UAVs in warfare. In IEEE Aerospace Conference, pp. 1-7. Big Sky, MT. https://doi.org/10.1109/AERO.2007.352737

[29] European Commission (2009). Study Analysing the Current Activities in the Field of UAV. Enterprise and Industry Directorate-General. "Where are we today – the industrial/economical/political situation in Europe and the international interdependencies". https://ec.europa.eu/docsroom/documents/1707/attachments/1/translations/en/renditions/pdf

[30] ASTM, A. D. (2013). 4788: Standard Test Method for Detecting Delaminations in Bridge Decks using Infrared Thermography. ASTM International, West

Conshohocken, Pennsylvania.

[31] Vaghefi, K., Ahlborn, T. T. M., Harris, D. K., & Brooks, C. N. (2015). Combined imaging technologies for concrete bridge deck condition assessment. Journal of Performance of Constructed Facilities, 29(4), 04014102. DOI: http://dx.doi.org/10.1061/(ASCE)CF.1943-5509.0000465

[32] Whitehead, K., & Hugenholtz, C. H. (2014). Remote sensing of the environment with small unmanned aircraft systems (UASs), part 1: a review of progress and challenges. *Journal of Unmanned Vehicle Systems*, *2*(3), 69-85. http://dx.doi.org/10.1139/juvs-2014-0007

[33] Jensen, R. R., Hardin, A. J., Hardin, P. J., & Jensen, J. R. (2011). A new method to correct pushbroom hyperspectral data using linear features and ground control points. GIScience & Remote Sensing, 48(3), 416-431. DOI: 10.2747/1548-1603.48.3.416

[34] Gonzalez-Partida, J. T., Almorox-Gonzalez, P., Burgos-Garcia, M., & Dorta-Naranjo, B. P. (2008). SAR system for UAV operation with motion error compensation beyond the resolution cell. Sensors, 8(5), 3384-3405. https://doi.org/10.3390/s8053384

[35] Remy, M. A., de Macedo, K. A., & Moreira, J. R. (2012, July). The first UAV-based P-and X-band interferometric SAR system. Paper presented at the 2012 IEEE international geoscience and remote sensing symposium (IGARSS), pp. 5041-5044. Munich, Germany. DOI: 10.1109/IGARSS.2012.6352478

[36] Colomina, I., & Molina, P. (2014). Unmanned aerial systems for photogrammetry and remote sensing: A review. ISPRS Journal of Photogrammetry and Remote Sensing, 92, 79-97. https://doi.org/10.1016/j.isprsjprs.2014.02.013

[37] Sa, I., Hrabar, S., & Corke, P. (2014, September). Inspection of pole-like

structures using a vision-controlled VTOL UAV and shared autonomy. In *IEEE/RSJ International Conference on Intelligent Robots and Systems (IROS 2014),* (pp. 4819-4826). IEEE. Chicago, IL. https://doi.org/10.1109/IROS.2014.6943247

[38] Pajares, G. (2015). Overview and current status of remote sensing applications based on unmanned aerial vehicles (UAVs). *Photogrammetric Engineering & Remote Sensing*, *81*(4), 281-329. https://doi.org/10.14358/PERS.81.4.281

[39] Vierling, L. A., Fersdahl, M., Chen, X., Li, Z., & Zimmerman, P. (2006). The Short Wave Aerostat-Mounted Imager (SWAMI): A novel platform for acquiring remotely sensed data from a tethered balloon. Remote sensing of environment, 103(3), 255-264. https://doi.org/10.1016/j.rse.2005.01.021

[40] Roldán, J. J., Joossen, G., Sanz, D., del Cerro, J., & Barrientos, A. (2015). Mini-UAV based sensory system for measuring environmental variables in greenhouses. Sensors, 15(2), 3334-3350. https://doi.org/10.3390/s150203334

[41] Moller, S. (2008). CALTRANS Bridge Inspection Aerial Robot. CA08-0182, Final Report. Division of Research and Innovation, California Department of Transportation. Sacramento, CA. www.dot.ca.gov/newtech/researchreports/reports/2008/08-0182.pdf

[42] Valavanis, K. P., & Vachtsevanos, G. J. (2015). Future of unmanned aviation. In: Valavanis, K. P., Vachtsevanos, G. J. (Eds.) Handbook of unmanned aerial vehicles. Springer, Dordrecht, Netherlands. http://dx.doi.org/10.1007/978-1-4020-6114-1

[43] Kerns, A. J., Shepard, D. P., Bhatti, J. A., & Humphreys, T. E. (2014). Unmanned aircraft capture and control via GPS spoofing. Journal of Field Robotics, 31(4), 617-636. https://doi.org/10.1002/rob.21513

[44] Miller, B. M., Stepanyan, K. V., Popov, A. K., & Miller, A. B. (2017). UAV navigation based on videosequences captured by the onboard video camera. *Automation and Remote Control*, *78*(12), 2211-2221. https://doi.org/10.1134/S0005117917120098

[45] Máthé, K., & Buşoniu, L. (2015). Vision and control for UAVs: A survey of general methods and of inexpensive platforms for infrastructure inspection. Sensors, 15(7), 14887-14916. https://doi.org/10.3390/s150714887

[46] Dorafshan, S., Maguire, M., Hoffer, N., and Coopmans, C., (2017). Fatigue Crack Detection Using Unmanned Aerial Systems in Under-Bridge Inspection. RP 256. Final Report. Boise: Idaho Department of Transportation. http://apps.itd.idaho.gov/apps/research/Completed/RP256.pdf

[47] Zhou, G., & Reichle, S. (2010). UAV-based multi-sensor data fusion processing. International Journal of Image and Data Fusion, 1(3), 283-291. http://dx.doi.org/10.1080/19479832.2010.497343

[48] Fasano, G., Accardo, D., Moccia, A., Carbone, C., Ciniglio, U., Corraro, F., & Luongo, S. (2008). Multi-sensor-based fully autonomous non-cooperative collision avoidance system for unmanned air vehicles. *Journal of aerospace computing, information, and communication*, *5*(10), 338-360. https://doi.org/10.2514/1.35145

[49] Thrun, S., Burgard, W., & Fox, D. (2000). A real-time algorithm for mobile robot mapping with applications to multi-robot and 3D mapping. *n Proceedings of the IEEE International Conference on Robotics and Automation (ICRA2000)*, San Francisco, CA, 2000, vol.1. pp. 321-328. DOI: 10.1109/ROBOT.2000.844077

[50] Se, S., Lowe, D., & Little, J. (2002). Mobile robot localization and mapping with uncertainty using scale-invariant visual landmarks. *The international Journal of*

robotics Research, *21*(8), 735-758. https://doi.org/10.1177/027836402761412467

[51] Goerzen, C., Kong, Z., & Mettler, B. (2010). A survey of motion planning algorithms from the perspective of autonomous UAV guidance. *Journal of Intelligent and Robotic Systems*, *57*(1), 65-100. https://doi.org/10.1007/s10846-009-9383-1

[52] Flores, G., Zhou, S., Lozano, R., & Castillo, P. (2014). A vision and GPS-based real-time trajectory planning for a MAV in unknown and low-sunlight environments. Journal of Intelligent & Robotic Systems, 74(1-2), 59-67. https://doi.org/10.1007/s10846-013-9975-7

[53] Stephen, J., & Lachapelle, G. (2001). Development and testing of a GPS-augmented multi-sensor vehicle navigation system. *The journal of navigation*, *54*(2), 297-319. https://doi.org/10.1017/S0373463301001357

[54] Lemaire, T., Berger, C., Jung, I. K., & Lacroix, S. (2007). Vision-based slam: Stereo and monocular approaches. *International Journal of Computer Vision*, *74*(3), 343-364. https://doi.org/10.1007/s11263-007-0042-3

[55] Kim, J., & Sukkarieh, S. (2007). Real-time implementation of airborne inertial-SLAM. *Robotics and Autonomous Systems*, *55*(1), 62-71. https://doi.org/10.1016/j.robot.2006.06.006

[56] Bachrach, A., He, R., & Roy, N. (2009). Autonomous flight in unknown indoor environments. *International Journal of Micro Air Vehicles*, *1*(4), 217-228. https://doi.org/10.1260/175682909790291492

[57] Urzua, S., Munguía, R., & Grau, A. (2017). Vision-based SLAM system for MAVs in GPS-denied environments. *International Journal of Micro Air Vehicles*, 9(4), 283-296. https://doi.org/10.1177/1756829317705325

[58] Fuentes-Pacheco, J., Ruiz-Ascencio, J., & Rendón-Mancha, J. M. (2015). Visual simultaneous localization and mapping: a survey. *Artificial Intelligence Review*, *43*(1), 55-81. https://doi.org/10.1007/s10462-012-9365-8

[59] Westoby, M. J., Brasington, J., Glasser, N. F., Hambrey, M. J., & Reynolds, J. M. (2012). 'Structure-from-Motion'photogrammetry: A low-cost, effective tool for geoscience applications. *Geomorphology*, *179*, 300-314. https://doi.org/10.1016/j.geomorph.2012.08.021

[60] Pons, J. P., Keriven, R., & Faugeras, O. (2007). Multi-view stereo reconstruction and scene flow estimation with a global image-based matching score. *International Journal of Computer Vision*, *72*(2), 179-193. http://dx.doi.org/10.1007/s11263-006-8671-5

[61] Lowe, D. G. (2004). Distinctive image features from scale-invariant keypoints. International journal of computer vision, 60(2), 91-110. https://doi.org/10.1023/B:VISI.0000029664.99615.94

[62] Bay, H., Ess, A., Tuytelaars, T., & Van Gool, L. (2008). Speeded-up robust features (SURF). *Computer vision and image understanding*, *110*(3), 346-359. https://doi.org/10.1016/j.cviu.2007.09.014

[63] Nex, F., & Remondino, F. (2014). UAV for 3D mapping applications: a review. *Applied geomatics*, *6*(1), 1-15. https://doi.org/10.1007/s12518-013-0120-x

[64] Torok, M. M., Golparvar-Fard, M., & Kochersberger, K. B. (2013). Image-based automated 3D crack detection for post-disaster building assessment. Journal of Computing in Civil Engineering, 28(5), A4014004. DOI: http://dx.doi.org/10.1061/(ASCE)CP.1943-5487.0000334

[65] Zheng, P. (2014). *Crack Detection and Measurement Utilizing Image-Based Reconstruction*. Research Report. Blacksburg: Virginia Polytechnic Institute and State University. https://vtechworks.lib.vt.edu/bitstream/handle/10919/48963/crack_detection_and_measurement_utilizing_image_based_reconstruction.pdf?sequence=1&isAllowed=y

[66] Rodriguez-Gonzalvez, P., Gonzalez-Aguilera, D., Lopez-Jimenez, G., & Picon-Cabrera, I. (2014). Image-based modeling of built environment from an unmanned aerial system. Automation in Construction, 48, 44-52. https://doi.org/10.1016/j.autcon.2014.08.010

[67] Dorafshan, S., Maguire, M., (2017). Autonomous Detection of Concrete Cracks on Bridge Decks and Fatigue Cracks on Steel Members. Digital Imaging 2017 (pp. 33-44), ASNT, Mashantucket, CT. https://ndtlibrary.asnt.org/2017/AutonomousDetectionofConcreteCracksonBridgeDecksandFatigueCracksonSteelMembers

[68] Abdel-Qader, I., Abudayyeh, O., & Kelly, M. E. (2003). Analysis of edge-detection techniques for crack identification in bridges. Journal of Computing in Civil Engineering, 17(4), 255-263. https://doi.org/10.1061/(ASCE)0887-3801(2003)17:4(255)

[69] Abdel-Qader, I., Pashaie-Rad, S., Abudayyeh, O., & Yehia, S. (2006). PCA-based algorithm for unsupervised bridge crack detection. Advances in Engineering Software, 37(12), 771-778. https://doi.org/10.1016/j.advengsoft.2006.06.002

[70] Yamaguchi, T., Nakamura, S., Saegusa, R., & Hashimoto, S. (2008). Image-Based Crack Detection for Real Concrete Surfaces. *IEEJ Transactions on Electrical and Electronic Engineering*, 3(1), 128-135. https://doi.org/10.1002/tee.20244

[71] Nishikawa, T., Yoshida, J., Sugiyama, T., & Fujino, Y. (2012). Concrete crack detection by multiple sequential image filtering. Computer-Aided Civil and Infrastructure Engineering, 27(1), 29-47. https://doi.org/10.1111/j.1467-8667.2011.00716.x

[72] Dorafshan, S., Maguire, M., and Qi, Xi. "Automatic Surface Crack Detection in Concrete Structures Using OTSU Thresholding and Morphological Operations" (2016). *Civil and Environmental Engineering Faculty Publications*. Paper 1234. https://digitalcommons.usu.edu/cgi/viewcontent.cgi?article=2232&context=cee_facpub

[73] Gonzalez, R. C., & Woods, R. E. (2007). Image processing. Digital image processing (Second Edition), Prentice Hall, Upper Saddle River, New Jersey 07458. ISBN 10: 0201508036.

[74] Moon, H. & Kim, J. (2011), Intelligent crack detecting algorithm on the concrete crack image using neural network, in *Proceedings of the 28th ISARC*, Seoul, Korea, 1461–1467.

[75] Hutchinson, T. C., & Chen, Z. (2006). Improved image analysis for evaluating concrete damage. *Journal of Computing in Civil Engineering*, *20*(3), 210-216. https://doi.org/10.1061/(ASCE)0887-3801(2006)20:3(210)

[76] Noh, Y., Koo, D., Kang, Y. M., Park, D., & Lee, D., (2017) "Automatic crack detection on concrete images using segmentation via fuzzy C-means clustering," In: *2017 IEEE International Conference on Applied System Innovation (ICASI)*, Sapporo, 2017, pp. 877-880. DOI: 10.1109/ICASI.2017.7988574

[77] Mohan, A., & Poobal, S. (2017). Crack detection using image processing: A

critical review and analysis. *Alexandria Engineering Journal*.

https://doi.org/10.1016/j.aej.2017.01.020

[78] Xu, Y., Li, S., Zhang, D., Jin, Y., Zhang, F., Li, N., & Li, H. (2018).

Identification framework for cracks on a steel structure surface by a restricted Boltzmann

machines algorithm based on consumer-grade camera images. *Structural Control and*

Health Monitoring, *25*(2), e2075. https://doi.org/10.1002/stc.2075

[79] Gaydeckp, P. A., & Burdekin, F. M. (1998). Nondestructive testing of

reinforced and pre-stressed concrete structures. *Nondestructive Testing and*

Evaluation, *14*(6), 339-392. https://doi.org/10.1080/10589759808953058

[80] DelGrande, N., & Durbin, P. F. (1999, February). "Delamination detection in

reinforced concrete using thermal inertia", In Proc. SPIE 3587, Nondestructive

Evaluation of Bridges and Highways III, https://doi.org/10.1117/12.339924

[81] Tashan, J., & Al-Mahaidi, R. (2012). Investigation of the parameters that

influence the accuracy of bond defect detection in CFRP bonded specimens using IR

thermography. *Composite Structures*, *94*(2), 519-531.

https://doi.org/10.1016/j.compstruct.2011.08.017

[82] Clark, M. R., McCann, D. M., & Forde, M. C. (2003). Application of

infrared thermography to the non-destructive testing of concrete and masonry bridges.

Ndt & E International, 36(4), 265-275. https://doi.org/10.1016/S0963-8695(02)00060-9

[83] Edis, E., Flores-Colen, I., & de Brito, J. (2014). Passive thermographic

detection of moisture problems in façades with adhered ceramic cladding. *Construction*

and Building Materials, *51(1)*, 187-197.

https://doi.org/10.1016/j.conbuildmat.2013.10.085

[84] Omar, M., Hassan, M. I., Saito, K., & Alloo, R. (2005). IR self-referencing thermography for detection of in-depth defects. Infrared physics & technology, 46(4), 283-289. https://doi.org/10.1016/j.infrared.2004.04.005

[85] Aggelis, D. G., Kordatos, E. Z., Soulioti, D. V., & Matikas, T. E. (2010). Combined use of thermography and ultrasound for the characterization of subsurface cracks in concrete. Construction and Building Materials, 24(10), 1888-1897. https://doi.org/10.1016/j.conbuildmat.2010.04.014

[86] Runnemalm, A., Broberg, P., & Henrikson, P. (2014). Ultraviolet excitation for thermography inspection of surface cracks in welded joints. *Nondestructive Testing and Evaluation*, *29*(4), 332-344. https://doi.org/10.1080/10589759.2014.941842

[87] Omar, T., & Nehdi, M. L. (2017). Remote sensing of concrete bridge decks using unmanned aerial vehicle infrared thermography. *Automation in Construction*, *83*, 360-371. https://doi.org/10.1016/j.autcon.2017.06.024

[88] Wells, J., & Lovelace, B. (2017). Unmanned Aircraft System Bridge Inspection Demonstration Project Phase II (No. MN/RC 2017-18). http://dot.state.mn.us/research/reports/2017/201718.pdf

[89] Murphy, R. R., Steimle, E., Griffin, C., Cullins, C., Hall, M., & Pratt, K. (2008). Cooperative use of unmanned sea surface and micro aerial vehicles at Hurricane Wilma. *Journal of Field Robotics*, *25*(3), 164-180. https://doi.org/10.1002/rob.20235

[90] Giordan, D., Manconi, A., Remondino, F., & Nex, F. (2017). Use of unmanned aerial vehicles in monitoring application and management of natural hazards. *Journal of Geomatics, Natural Hazards and Risk, 8(1),* 1-4. https://doi.org/10.1080/19475705.2017.1315619

[91] Qi, J., Song, D., Shang, H., Wang, N., Hua, C., Wu, C., ... & Han, J. (2016). Search and Rescue Rotary-Wing UAV and Its Application to the Lushan Ms 7.0 Earthquake. *Journal of Field Robotics*, *33*(3), 290-321. https://doi.org/10.1002/rob.21615

[92] Adams, S. M., Levitan, M. L., & Friedland, C. J. (2013). High resolution imagery collection utilizing unmanned aerial vehicles (UAVs) for post-disaster studies. In *ATC & SEI Conference on Advances in Hurricane Engineering: Learning from Our Past, Miami, Florida, USA,* (pp. 777-793). https://doi.org/10.1061/9780784412626.067

[93] Dai, F., Dong, S., Kamat, V. R., & Lu, M. (2011). Photogrammetry assisted measurement of interstory drift for rapid post-disaster building damage reconnaissance. Journal of Nondestructive Evaluation, 30(3), 201-212. https://doi.org/10.1007/s10921-011-0108-6

[94] Xu, Z., Yang, J., Peng, C., Wu, Y., Jiang, X., Li, R., ... & Tian, B. (2014). Development of an UAS for post-earthquake disaster surveying and its application in Ms7. 0 Lushan Earthquake, Sichuan, China. *Computers & Geosciences*, *68*, 22-30. https://doi.org/10.1016/j.cageo.2014.04.001

[95] Vetrivel, A., Gerke, M., Kerle, N., & Vosselman, G. (2016). Identification of structurally damaged areas in airborne oblique images using a visual-Bag-of-Words approach. Remote Sensing, 8(3), 231-253. https://doi.org/10.3390/rs8030231

[96] Metni, N., & Hamel, T. (2007). A UAV for bridge inspection: Visual servoing control law with orientation limits. Automation in construction, 17(1), 3-10. https://doi.org/10.1016/j.autcon.2006.12.010

[97] Oh, J. K., Jang, G., Oh, S., Lee, J. H., Yi, B. J., Moon, Y. S., ... & Choi, Y. (2009). Bridge inspection robot system with machine vision. Automation in Construction,

18(7), 929-941. https://doi.org/10.1016/j.autcon.2009.04.003

[98]Sutter, B., Lelevé, A., Pham, M. T., Gouin, O., Jupille, N., Kuhn, M., ... & Rémy, P. (2018). A semi-autonomous mobile robot for bridge inspection. *Automation in Construction*, *91*, 111-119. https://doi.org/10.1016/j.autcon.2018.02.013

[99] Escobar-Wolf, R., Oommen, T., Brooks, C. N., Dobson, R. J., & Ahlborn, T. M. (2017). Unmanned Aerial Vehicle (UAV)-Based Assessment of Concrete Bridge Deck Delamination Using Thermal and Visible Camera Sensors: A Preliminary Analysis. *Research in Nondestructive Evaluation*, 1-16. https://doi.org/10.1080/09349847.2017.1304597

[100] Brooks, C., Dobson, R. J., Banach, D. M., Dean, D., Oommen, T., Wolf, R. E., ... & Hart, B. (2015). Evaluating the Use of Unmanned Aerial Vehicles for Transportation Purposes (No. RC-1616). Michigan Tech Research Institute, Ann Arbor, Michigan. https://www.michigan.gov/documents/mdot/RC1616_Part_C_488517_7.pdf

[101] Lim, R. S., La, H. M., & Sheng, W. (2014). A robotic crack inspection and mapping system for bridge deck maintenance. IEEE Transactions on Automation Science and Engineering, 11(2), 367-378. https://doi.org/10.1109/TASE.2013.2294687

[102] Morgenthal, G., & Hallermann, N. (2014). Quality assessment of unmanned aerial vehicle (UAV) based visual inspection of structures. Advances in Structural Engineering, 17(3), 289-302. https://doi.org/10.1260/1369-4332.17.3.289

[103] Sankarasrinivasan, S., Balasubramanian, E., Karthik, K., Chandrasekar, U., & Gupta, R. (2015). Health Monitoring of Civil Structures with Integrated UAV and Image Processing System. Procedia Computer Science, 54(2015), 508-515. https://doi.org/10.1016/j.procs.2015.06.058

[104] Krishna, K., & Murty, M. N. (1999). Genetic K-means algorithm. IEEE Transactions on Systems, Man, and Cybernetics, Part B (Cybernetics), 29(3), 433-439. DOI:10.1109/3477.764879

[105] Ellenberg, A., Kontsos, A., Moon, F., & Bartoli, I. (2016). Bridge related damage quantification using unmanned aerial vehicle imagery. *Structural Control and Health Monitoring*, *23*(9), 1168-1179. https://doi.org/10.1002/stc.1831

[106] Talab, A. M. A., Huang, Z., Xi, F., & HaiMing, L. (2016). Detection crack in image using Otsu method and multiple filtering in image processing techniques. Optik-International Journal for Light and Electron Optics, 127(3), 1030-1033. https://doi.org/10.1016/j.ijleo.2015.09.147

[107] Dorafshan, S., Coopmans, C., Thomas, R., Maguire, M. (In Press). Deep Learning Neural Networks for sUAS-Assisted Structural Inspections: Feasibility and Application, ICUAS18. IEEE. Dallas Marriot City Center, Dallas.

[108] Dorsey (2016), AASHTO Special Report (fact sheet AASHTO created to accompany the survey report) https://indd.adobe.com/view/78d3b1d3-13c3-42c0-8bf2-75ea8c534d1a. Accessed 19 April 2018.

[109] Irizarry, J., & Johnson, E. N. (2014). Feasibility study to determine the economic and operational benefits of utilizing unmanned aerial vehicles (UAVs). FHWA-GA-1H-12-38. Georgia Institute of Technology. https://smartech.gatech.edu/handle/1853/52810?show=full

[110] Otero, L. D., Gagliardo, N., Dalli, D., Huang, W. H., & Cosentino, P. (2015). Proof of concept for using unmanned aerial vehicles for high mast pole and bridge inspections (No. BDV28 TWO 977-02). Florida Institute of Technology.

https://rosap.ntl.bts.gov/view/dot/29176/dot_29176_DS1.pdf?

[111] Kanistras, K., Martins, G., Rutherford, M. J., & Valavanis, K. P. (2015). Survey of unmanned aerial vehicles (UAVs) for traffic monitoring. In *Handbook of unmanned aerial vehicles* (pp. 2643-2666). Springer Netherlands.

[112] Coifman, B., McCord, M., Mishalani, M., and Redmill, K. (2004). "Surface transportation surveillance from unmanned aerial vehicles." Proc., 83rd Annual Meeting of the Transportation Research Board. pp 11-20

[113] Srinivasan, S., Latchman, H., Shea, J., Wong, T., & McNair, J. (2004, October). Airborne traffic surveillance systems: video surveillance of highway traffic. In *Proceedings of the ACM 2nd international workshop on Video surveillance & sensor networks*. (pp. 131-135). New York.

[114] McCormack, E. D., & Trepanier, T. (2008). The use of small unmanned aircraft by the Washington State Department of Transportation (No. WA-RD 703.1). Research Report, Washington State Department of Transportation. Olympia, Washington. https://www.wsdot.wa.gov/research/reports/fullreports/703.1.pdf

[115] Barfuss, S. L., Jensen, A., & Clemens, S. (2012). Evaluation and development of unmanned aircraft (UAV) for UDOT needs (No. UT-12.08). Salt Lake City, UT. https://www.udot.utah.gov/main/uconowner.gf?n=10710706202834543

[116] FAA (2017). Aeronautical Information Manual: Official Guide to Basic Flight Information and ATC Procedures. U.S. Department of Transportation. https://www.faa.gov/air_traffic/publications/media/AIM_Basic_dtd_10-12-17.pdf. Accessed 19 April 2018.

[117] Dorafshan, S., Maguire, M., Hoffer, N. V., & Coopmans, C. (2017, June).

Challenges in bridge inspection using small unmanned aerial systems: Results and lessons learned. In *2017 IEEE International Conference on Unmanned Aircraft Systems (ICUAS17),* (pp. 1722-1730). Miami, FL. DOI: 10.1109/ICUAS.2017.7991459

[118] Dorafshan, S., Thomas, R., Maguire, M., Fatigue Crack Detection Using Unmanned Aerial Systems in Fracture Critical Inspection of Steel Bridges (In Press). ASCE Journal of Bridge Engineering. Special Collection on Non-contact Sensing Technologies for Bridge Structural Health Assessment. DOI:10.1061/(ASCE)BE.1943-5592.0001291

[119] Yang, C. H., Wen, M. C., Chen, Y. C., & Kang, S. C. (2015, January). An Optimized Unmanned Aerial System for Bridge Inspection. ISARC. Proceedings of the International Symposium on Automation and Robotics in Construction, Volume 32, 1-6,

[120] Chan, B., Guan, H., Jo, J., & Blumenstein, M. (2015). Towards UAV-based bridge inspection systems: a review and an application perspective. Structural Monitoring and Maintenance, 2(3), 283-300. DOI: 10.12989/smm.2015.2.3.283

 [121] Broberg, P. (2013). Surface crack detection in welds using thermography. *NDT & E International*, *57(2013)*, 69-73. https://doi.org/10.1016/j.ndteint.2013.03.008

[122] Rodríguez-Martín, M., Lagüela, S., González-Aguilera, D., & Martínez, J. (2016). Thermographic test for the geometric characterization of cracks in welding using IR image rectification. *Automation in Construction*, *61*, 58-65. https://doi.org/10.1016/j.autcon.2015.10.012

[123] Connor, R. J., Dexter, R. J., & Mahmoud, H. (2005). NCHRP Synthesis 354: Inspection and management of bridges with fracture-critical details. Volume 354,

Washington D C: Transportation Research Board. https://doi.org/10.17226/13887

[124] Haghighat, M. B. A., Aghagolzadeh, A., & Seyedarabi, H. (2011). A non-reference image fusion metric based on mutual information of image features. Computers & Electrical Engineering, 37(5), 744-756. https://doi.org/10.1016/j.compeleceng.2011.07.012

[125] Xiong, N., & Svensson, P. (2002). Multi-sensor management for information fusion: issues and approaches. Information fusion, 3(2), 163-186. https://doi.org/10.1016/S1566-2535(02)00055-6

[126] Gross, G. A., Nagi, R., Sambhoos, K., Schlegel, D. R., Shapiro, S. C., & Tauer, G. (2012, July). Towards hard+ soft data fusion: Processing architecture and implementation for the joint fusion and analysis of hard and soft intelligence data. In *2012 15th International Conference on Information Fusion (FUSION). IEEE*, pp. 955-962. Singapore.

[127] Shen, Z., & Jensen, W. (2015). Integrated 3D Bridge-Condition Visualization (BCV) to Facilitate Element-Based Bridge Condition Rating (EBCR). Nebraska Department of Roads Research Reports. Report M004. Lincoln, NE. http://digitalcommons.unl.edu/ndor/168/.

[128] Maldague, X. (2001). Theory and practice of infrared technology for nondestructive testing. John Wiley and Sons, INC. New York. ISBN: 978-0-471-18190-3.

[129] Lee, S., & Kalos, N. (2015). Bridge inspection practices using non-destructive testing methods. Journal of Civil Engineering and Management, 21(5), 654-665. http://dx.doi.org/10.1061/9780784413517.132

[130] Dorafshan S., Maguire, M., and Chang, M., (2017). Comparing Automated Image-Based Crack Detection Techniques in Spatial and Frequency Domains, 26th ASNT Research Symposium, Jacksonville, Florida.

[131] Werrell, K. P. (1998). Dark eagles: A history of top secret US aircraft programs. *The Journal of Military History*, *62*(1), 225-226.

[132] McDaid, H., & Oliver, D. (1997). Smart weapons: Top secret history of remote controlled airborne weapons. New York: Barnes & Noble.

[133] Bone, E., & Bolkcom, C. (2003, April). Unmanned aerial vehicles: Background and issues for congress. Library of Congress. Washington DC Congressional Research Service.

[134] Bendig, J., Yu, K., Aasen, H., Bolten, A., Bennertz, S., Broscheit, J., ... & Bareth, G. (2015). Combining UAV-based plant height from crop surface models, visible, and near infrared vegetation indices for biomass monitoring in barley. *International Journal of Applied Earth Observation and Geoinformation*, *39(2015)*, 79-87. https://doi.org/10.1016/j.jag.2015.02.012

[135] Urbahs, A., & Jonaite, I. (2013). Features of the use of unmanned aerial vehicles for agriculture applications. *Aviation*, *17*(4), 170-175. https://doi.org/10.3846/16487788.2013.861224

[136] Grenzdörffer, G. J., & Niemeyer, F. (2011). UAV based BRDF-measurements of agricultural surfaces with PFIFFikus. International Archives of the Photogrammetry, Remote Sensing and Spatial Information Sciences, 38, 229-234.

[137] Huang, Y., Hoffmann, W. C., Lan, Y., Wu, W., & Fritz, B. K. (2009). Development of a spray system for an unmanned aerial vehicle platform. Applied

Engineering in Agriculture, 25(6), 803-809. doi:10.13031/2013.29229

[138] Li, J., Zhang, F., Qian, X., Zhu, Y., & Shen, G. (2015). Quantification of rice canopy nitrogen balance index with digital imagery from unmanned aerial vehicle. Remote Sensing Letters, 6(3), 183-189. http://dx.doi.org/10.1080/2150704X.2015.1021934

[139] T Torres-Sánchez, J., Peña, J. M., De Castro, A. I., & López-Granados, F. (2014). Multi-temporal mapping of the vegetation fraction in early-season wheat fields using images from UAV. *Computers and Electronics in Agriculture*, *103*, 104-113. https://doi.org/10.1016/j.compag.2014.02.009

[140] Wallace, L., Lucieer, A., Watson, C., & Turner, D. (2012). Development of a UAV-LiDAR system with application to forest inventory. *Remote Sensing*, *4*(6), 1519-1543. DOI:10.3390/rs4061519

[141] Dandois, J. P., & Ellis, E. C. (2013). High spatial resolution three-dimensional mapping of vegetation spectral dynamics using computer vision. Remote Sensing of Environment, 136, 259-276. https://doi.org/10.1016/j.rse.2013.04.005

[142] Klemas, V. V. (2015). Coastal and environmental remote sensing from unmanned aerial vehicles: An overview. *Journal of Coastal Research*, *31*(5), 1260-1267.

[143] Recchiuto, C.T., Sgorbissa, A., (2017). Post-disaster assessment with unmanned aerial vehicles: A survey on practical implementations and research approaches. *J Field Robotics*. https://doi.org/10.1002/rob.21756

[144] Ambrosia, V. G., Wegener, S., Zajkowski, T., Sullivan, D. V., Buechel, S., Enomoto, F., ... & Hinkley, E. (2011). The Ikhana unmanned airborne system (UAS) western states fire imaging missions: from concept to reality (2006–2010). *Geocarto*

International, *26*(2), 85-101. http://dx.doi.org/10.1080/10106049.2010.539302

[145] Han, J., Xu, Y., Di, L., & Chen, Y. (2013). Low-cost multi-UAV technologies for contour mapping of nuclear radiation field. *Journal of Intelligent & Robotic Systems*, *70*(1-4), 401-410. https://doi.org/10.1007/s10846-012-9722-5

[146] Liu, P., Li, X., Qu, J. J., Wang, W., Zhao, C., & Pichel, W. (2011). Oil spill detection with fully polarimetric UAVSAR data. *Marine Pollution Bulletin*, *62*(12), 2611-2618. https://doi.org/10.1016/j.marpolbul.2011.09.036

[147] Tamminga, A. D., Eaton, B. C., & Hugenholtz, C. H. (2015). UAS-based remote sensing of fluvial change following an extreme flood event. *Earth Surface Processes and Landforms*, *40*(11), 1464-1476. https://doi.org/10.1002/esp.3728

[148] Bernard, M., Kondak, K., Maza, I., & Ollero, A. (2011). Autonomous transportation and deployment with aerial robots for search and rescue missions. *Journal of Field Robotics*, *28*(6), 914-931. https://doi.org/10.1002/rob.20401

[149] Desikan, P., Karunakaran, K., & Gokulnath, G. (2013). Design of an aquatic park and salvation of endangered aquatic species in its natural habitat. *APCBEE procedia*, *5*, 197-202. https://doi.org/10.1016/j.apcbee.2013.05.035

[150] d'Oleire-Oltmanns, S., Marzolff, I., Peter, K. D., & Ries, J. B. (2012). Unmanned aerial vehicle (UAV) for monitoring soil erosion in Morocco. *Remote Sensing*, *4*(11), 3390-3416.

[151] de Haas, T., Ventra, D., Carbonneau, P. E., & Kleinhans, M. G. (2014). Debris-flow dominance of alluvial fans masked by runoff reworking and weathering. Geomorphology, 217, 165-181. https://doi.org/10.1016/j.geomorph.2014.04.028

[152] Martin, P. G., Payton, O. D., Fardoulis, J. S., Richards, D. A., & Scott, T. B.

(2015). The use of unmanned aerial systems for the mapping of legacy uranium mines. *Journal of environmental radioactivity*, *143*, 135-140.

[153] Shahbazi, M., Théau, J., & Ménard, P. (2014). Recent applications of unmanned aerial imagery in natural resource management. *GIScience & Remote Sensing*, *51*(4), 339-365. https://doi.org/10.1080/15481603.2014.926650

[154] Jizhou, W., Zongjian, L., & Chengming, L. (2004). Reconstruction of buildings from a single UAV image. In Proc. International Society for Photogrammetry and Remote Sensing Congress (pp. 100-103). Hannover, Germany.

[155] Koutsoudis, A., Vidmar, B., Ioannakis, G., Arnaoutoglou, F., Pavlidis, G., & Chamzas, C. (2014). Multi-image 3D reconstruction data evaluation. Journal of Cultural Heritage, 15(1), 73-79. https://doi.org/10.1016/j.culher.2012.12.003

[156] Jin, H., Cremers, D., Wang, D., Prados, E., Yezzi, A., & Soatto, S. (2008). 3-d reconstruction of shaded objects from multiple images under unknown illumination. International Journal of Computer Vision, 76(3), 245-256. https://doi.org/10.1007/s11263-007-0055-y

[157] Furukawa, Y., Curless, B., Seitz, S. M., & Szeliski, R. (2010, June). Towards internet-scale multi-view stereo. In Computer Vision and Pattern Recognition (CVPR), 2010 IEEE Conference on (pp. 1434-1441). IEEE. San Francisco, CA. http://dx.doi.org/10.1109/CVPR.2010.5539802

[158] Siebert, S., & Teizer, J. (2014). Mobile 3D mapping for surveying earthwork projects using an Unmanned Aerial Vehicle (UAV) system. *Automation in Construction*, *41*, 1-14. https://doi.org/10.1016/j.autcon.2014.01.004

[159] Rogers, K., & Finn, A. (2013). Three-dimensional UAV-based atmospheric

tomography. *Journal of Atmospheric and Oceanic Technology*, *30*(2), 336-344. https://doi.org/10.1175/JTECH-D-12-00036.1

[160] Dunham, K. M. (2012). Trends in populations of elephant and other large herbivores in Gonarezhou National Park, Zimbabwe, as revealed by sample aerial surveys. African Journal of Ecology, 50(4), 476-488. https://doi.org/10.1111/j.1365-2028.2012.01343.x

[161] Mehrotra, R., Nichani, S., & Ranganathan, N. (1990). Corner detection. Pattern Recognition, 23(11), 1223-1233. https://doi.org/10.1016/0031-3203(90)90118-5

[162] Remondino, F., & El-Hakim, S. (2006). Image-based 3D modelling: a review. The Photogrammetric Record, 21(115), 269-291. https://doi.org/10.1111/j.1477-9730.2006.00383.x

[163] Lindeberg, T. (1998). Edge detection and ridge detection with automatic scale selection. International Journal of Computer Vision, 30(2), 117-156. https://doi.org/10.1023/A:1008097225773

[164] Chandrasekhar, V., Chen, D. M., Lin, A., Takacs, G., Tsai, S. S., Cheung, N. M., ... & Girod, B. (2010, September). Comparison of local feature descriptors for mobile visual search. In *17th IEEE International Conference on Image Processing (ICIP)* (pp. 3885-3888). Hong Kong.

[165] Wang, L., & Chu, C. H. H. (2009, October). 3D building reconstruction from LiDAR data. In IEEE International Conference on Systems, Man and Cybernetics, (SMC 2009). pp. 3054-3059. San Antonio, TX. DOI: 10.1109/ICSMC.2009.5345938

[166] Bruno, S., De Fino, M., & Fatiguso, F. (2018). Historic Building Information Modelling: performance assessment for diagnosis-aided information

modelling and management. *Automation in Construction*, *86*, 256-276.

https://doi.org/10.1016/j.autcon.2017.11.009

[167] Harwin, S., & Lucieer, A. (2012, August). An accuracy assessment of georeferenced point clouds produced via multi-view stereo techniques applied to imagery acquired via unmanned aerial vehicle. In ISPRS (International Archives of the Photogrammetry, Remote Sensing and Spatial Information Sciences), ISPRS Congress (pp. 475-480). Melbourne, Australia. https://doi.org/10.5194/isprsarchives-XXXVIII-1-C22-183-2011

[168] Zhang, C., & Elaksher, A. (2012). An Unmanned Aerial Vehicle-Based Imaging System for 3D Measurement of Unpaved Road Surface Distresses. Computer-Aided Civil and Infrastructure Engineering, 27(2), 118-129. DOI: 10.1111/j.1467-8667.2011.00727.x

[169] Kuo, C. H., Leber, A., Kuo, C. M., Boller, C., Eschmann, C., & Kurz, J. (2013, September). Unmanned robot system for Structure health monitoring and Non-Destructive Building Inspection, current technologies overview and future improvements. In *Proc. of the 9th International Workshop on SHM, Stanford Univ., Stanford/CA, USA*

CHAPTER III

FATIGUE CRACK DETECTION USING UNMANNED AERIAL SYSTEMS IN

FRACTURE CRITICAL INSPECTION OF STEEL BRIDGES

Abstract

Many state agencies are investigating the use of Unmanned Aerial Systems

(UAS) for bridge inspections. Some agencies are receiving pressure from consultants and

their own administrations to implement UAS inspections with limited knowledge of their

efficacy. This chapter studies the feasibility of using UAS for fatigue crack detection in

bridges with fracture critical members (FCM) through real-time and post-flight visual

inspection. The effects of surface illumination on the minimum crack-to-camera (MCC)

distance at which a fatigue crack can be detected was investigated in the laboratory.

Mock field inspections evaluated the achievable crack-to-platform (ACP) distance in

GPS-denied and windy environments, and determine if known cracks can be identified at

achievable standoff distances. Finally, two FCM inspections demonstrated the field

performance of UAS in identifying fatigue cracks. Results highlight the importance of

camera specifications and surface illumination in determining the required standoff

distance of crack detection. Furthermore, the results demonstrate the difficulties in

obtaining clear images with unstable UAS in GPS-denied or windy environments.

Nevertheless, the best performing platform tested in this study exhibited performance

comparable to the average of 30 human inspectors at a fatigue crack identification

training structure. The limited results presented here proved the feasibility of using UAS

for fatigue crack detection in FCM inspections of steel bridges, but highlighted the

shortcomings of UAS for this type of hands-on inspection.

Introduction

According to the National Bridge Inventory, there are more than 200,000 in-service steel bridges in the United States (NBI, 2017). About 22,000—or 11 percent—of these are designated fracture critical (Pham et al., 2016). The American Association of State Highway Transportation Officials (AASHTO) defines a fracture critical member (FCM) as a "component in tension whose failure is expected to result in the collapse of the bridge or the inability of the bridge to perform its function" (AASHTO 2016). Fracture critical bridges are prone to fatigue cracking, which has historically led to structural failure (Lichtenstein 1993; Biezma and Schanack 2007). Fatigue is the tendency of a member to fail at a stress level below the elastic limit when subjected to cyclic loading.

Federal regulations mandate FCM inspections every 24 months (FHWA, 2017). FCM inspections are hands-on—requiring the inspector to be in close proximity to the FCM—and may include NDE for crack detection (Hearn 2007). When visual inspection is inconclusive in terms of fatigue crack detection, a suitable NDE method can verify the presence of a fatigue crack. A number of NDE techniques exist for crack detection in steel structures, including acoustic emission, smart paint, dye penetration, magnetic particles, radiography, and ultrasonic testing (Lee et al., 2014). FCM inspections do not require hands-on inspection of all structural members. Instead, the inspector identifies components and regions susceptible to fatigue cracks—either through experience or based on results of previous inspections—and performs a targeted inspection.

FCM inspections are more costly and time consuming than other types of inspections; a 2005 survey of bridge owners revealed that FCM inspections cost 200–500% more than other inspection types (Connor et al., 2005). Dorafshan et al., (2017a) reported the following reasons for increased cost and time involved in FCM inspections:

- May require specialized equipment, operators, and training (e.g. under-bridge inspection trucks (UBIT) and operators);

- May require non-destructive evaluation (NDE) to detect cracks; and

- May require traffic control and lane closure.

Many state agencies are investigating potential application of unmanned aerial systems (UAS) for bridge inspections. Some agencies are receiving pressure from consultants and their own administrations to implement UAS inspections with limited knowledge of their efficacy and currently few studies exist that investigate UAS use for FCM inspections. The authors hypothesize that FCM bridge inspections can be performed with UAS, thus obviating the above cost-increasing considerations. For the last decade, state Departments of Transportation (DOTs) have used UAS for a variety of missions, including traffic control, mapping, and surveillance (Dorafshan et al., 2017a). However, bridge inspection is a relatively new application of UAS. Michigan DOT reported the first successful UAS-assisted bridge inspection in 2015 (Brooks et al., 2015). A UAS equipped with visual, thermal, and light detection and ranging (LIDAR) sensors was used for routine bridge inspections in Michigan. Using UAS data, researchers constructed a three-dimensional (3D) model of a bridge and identified delamination in the deck (Brooks et al., 2015).

Minnesota DOT initiated a multi-phase feasibility study regarding UAS-assisted bridge inspections. The first phase involved initial inspections of four Minnesota bridges using UAS (Zink and Lovelace, 2015). The UAS inspection results were comparable to human inspections of those bridges, providing valuable inspection images in a low-cost and safe manner. The second phase involved UAS inspection of four additional Minnesota bridges (Wells and Lovelace, 2017). The researchers were able to construct 3D bridge models and delamination maps (from thermal images). Furthermore, they were successful in inspecting large-scale initial inspections of bridges and inspections of culvert bridges in GPS-denied environments. Despite the successful detection of a known fatigue crack in mock inspections, UAS images did not show any cracks during the inspection of an in-service bridge (Wells and Lovelace, 2017).

A Florida DOT report discussed the use of UAS in lieu of experienced inspectors for inspection of bridges and high mast luminaires (Otero et al., 2015). The intent of the study was to provide a safer and cheaper initial inspection. Results from mock inspections suggested that concrete cracks of width 0.5 mm were detectable in UAS images.

Previous DOT studies demonstrate successful implementation of UAS for initial inspections where the objective is to gather general information from a bridge. UAS provides inspectors real time visual access to structural components without physically accessing the structure. However, a recent Idaho Transportation Department (ITD) report outlined the state of the art of UAS-assisted bridge inspection and identified several associated challenges, with emphasis on fatigue crack detection (Dorafshan et al., 2017b). These challenges include:

- UAS camera must be in close proximity to detect cracks;

- Photographic quality diminishes in poorly-lit under-bridge environment;

- UAS navigation in poorly-lit and GPS-denied under-bridge environment is difficult; and

- UAS cannot clear debris or other obstructions from FCM.

There nevertheless exists precedent for UAS damage detection, suggesting significant potential for their use in fatigue crack detection (Oh et al., 2009). Metni et al. (2007) used UAS to detect cracks in concrete bridge decks. Similarly, Morgenthal and Hallermann (2014) used UAS for visual detection of concrete wall cracks. Several authors demonstrate autonomous detection of concrete cracks (Jahanshahi et al., 2009; Sankarasrinivasan et al., 2015; Dorafshan et al., 2016; Dorafshan et al., 2017c; Dorafshan, and Maguire, 2017), steel cracks (Yeum and Dyke 2015), post disaster inspections (Adams et al., 2011), bridge 3-dimensional modeling and inspections (Lattanzi and Miller 2014 and Gillins et al., 2016), and autonomous detection of concrete deck delamination (Omar and Nehdi 2017). However, the application of UAS for detection of fatigue cracks during FCM inspections has not yet been demonstrated. The performance of UAS in terms of accuracy and time is tied to the type of cameras used in the inspection and the type of defects. Implementing Deep Learning Convolutional Neural Networks (DLCNNs) in UAS-assisted inspections showed promising results for concrete deck crack detection without human intervention. The network was trained on a set annotated images (manually labeled as cracked or un-cracked) taken by a point and shoot camera of several bridge decks. The trained network was then used to label new

images taken by UAS of other concrete structures autonomously with 88% accuracy (Dorafshan et al., 2018a). A gap in the past studies was the lack of comparing visual inspections performed by the inspectors to the ones performed using UASs and non-contact damage detection methods (Dorafshan and Maguire 2018, Dorafshan et al., 2018b). This chapter addresses these research needs. This study is the first one focusing on fatigue crack detection in bridges using UASs. The location of fatigue cracks, under-bridge members, and their small size impose unique challenges to UAS-assisted bridge inspections including but not limited to the absence of GPS signals, navigation in a semi-confined location, absence of natural light, smaller required clearance between UAS and the cracks, intensified wind and gust speed, flying over water, and debris cluttering the cracks.

The intent of this chapter is to: (1) demonstrate the feasibility of UAS-assisted FCM inspections of steel bridges; and (2) identify some of the remaining challenges and research needs in this area. This chapter has the following sections. Specifications of the studied UASs and their cameras, determination of minimum requirements for visual fatigue crack detection using three studied cameras through a set of laboratory experiments, fatigue crack detection in controlled and uncontrolled environments to evaluate the performance of the studied UASs, results of a FCM bridge inspection using UAS, results of the FCM inspection at Purdue university laboratory, and finally conclusions.

UAS

Three UASs, shown in Fig. 3-1, were used for fatigue crack detection in this

study. Two UAS (DJI Mavic and 3DR Iris) were low-cost commercial models. A third

UAS (The Goose) was custom made to carry heavier payloads (i.e. a standalone digital

camera). UAS specifications are listed in Table 3-1. The cost of each platform is included

in the table; even though costs will vary significantly with time, this information is

included to set up a comparison of the relative cost of the three platforms tested here.

  The cameras on the DJI Mavic was integrated on the platform by the DJI. In case

of the 3DR Iris, the camera had to be light and small due to the limited payload. The

GoPro Hero 4 was therefore selected to be mounted on the 3DR Iris. The Goose was

capable of carrying a significant payload so a conventional digital camera, Nikon

COOLPIX L830, was selected. Table 3-2 lists camera specifications. The cameras in this

study had similar sensor type and size and comparable resolutions. Furthermore, these

cameras represent similar off-the-shelf cameras that would be selected by inspectors

using low-cost UAS for bridge inspections.

Fig. 3-1 Three UAS used for FCM inspections

Table 3-1 UAS specifications

Specification	Goose	DJI Mavic	3DR Iris
Cost (USD)	5,000	1,000	< 500
Weight (kg)	11.40	0.74	1.28
Type	Coaxial Octocopter	Quadcopter	Quadcopter
Flight time (minutes)	27	27	16-22
Payload (kg)	14.40	0.90	0.40
First person view	No	Yes	Yes
Camera adjustments	No	Yes	No
Altitude measurement	Barometer, GPS	Sonar, GPS	GPS

Table 3-2 Camera Specifications

Specification	Nikon COOLPIX L830	DJI Camera	GoPro Hero 4
Weight (g)	508	NA	174
Resolution (max)	4068×3456 (16 MP)	4000×3000 (12 MP)	4000×3000 (12 MP)
Sensor type	CMOS	CMOS	CMOS
Lens aperture	F3-5.9	F2.2	F2.8
Sensor size (in)	1/2.3	1/2.3	1/2.3
ISO (max)	3200	1600	6400
Field of view* (mm)	22.5-765	28	17.2

* equivalent focal lengths in 35mm

Minimum Requirements for UAS Fatigue Crack Detection

Experiment Description

Indoor laboratory experiments were performed in order to determine the maximum distance at which UAS cameras could identify a known fatigue crack under varying lighting conditions. To keep constant the physical size of each pixel in the indoor experiment, each camera was used to take a picture at a standard clearance as measured

from a 200 mm reference bar. In pictures taken by DJI Mavic and the GoPro cameras, the physical horizontal dimension captured was 210 mm. The field of view for the Nikon camera is different than the other cameras; however, same field of view is achieved by adjusting the camera's optical zoom to capture 210 mm physical horizontal dimension. After calibration in this manner, the zoom remained constant through the office experiment.

Using this test setup, the camera clearance to a 43-mm diameter steel coupon provided by Idaho Transportation Department (ITD) was changed until a fatigue crack could be identified. The identified maximum distance is reported as the maximum crack-to-camera distance (MCC). Fig. 3-2 shows the known fatigue crack, in the coupon. The crack length was approximately 14 mm and the crack width was approximately 0.04 mm (measured by a microscope). This specimen was provided by ITD.

Fig. 3-2 Test piece with fatigue crack in 2-o'clock position

Three illumination levels were selected to simulate the range of lighting

conditions encountered during a bridge inspection. The first, *dark*, corresponds to under-bridge conditions on a cloudy day. This condition is similar to deep twilight with illumination in the range 0–10.8 lx (Woo and Wong, 1979). The second, *normal*, corresponds to an intermediate lighting condition with illumination in the range 100–150 lx (Illumination, 2009). The third, *bright*, corresponds to under-bridge conditions using an artificial light source with illumination in excess of 200 lx. Surface illumination was provided by two light sources (450 and 750 lx). Light sources were adjusted to provide the correct illumination for each condition, as verified by a Digi-Sense datalogging light meter with NIST traceable calibration (the light was measured on the surface of the test-piece).

MCC for each UAS camera was determined under each lighting condition. The UAS camera was first positioned at a distance of 1.2 m from the fatigue crack specimen (Fig. 3-2) and an image was recorded. The starting distance 1.2 m was selected because it is an easily achievable clearance for most commercial UAS. The operator observed the image and qualitatively evaluated if the known crack was visible. If the crack was not detectable at 1.2 m, MCC distance was reduced by 0.1 m. This procedure was repeated until the crack became visible in the recorded image. The distance at which the crack became visible to the operator under a specific lighting condition is reported as the MCC distance. This measurement is obviously subjective because it relied on the visual acuity of the operator. Furthermore, the operator was aware of both the presence and location of the crack. A single operator performed all of the tests in order to minimize variability (the same operator was also the inspector in mock and field inspections throughout this study). In addition to MCC, normalized MCC to pixel size was identified for each

lighting condition and camera. Pixel size to MCC values were computed by dividing the MCC to the pixel size of the image MCC was calculated from. These values were divided by a factor of 1,000 for better presentation. Higher values for normalized MCC to pixel size represent greater clearance and smaller pixel size which provide a better condition for visual detection. Images were recorded while UAS cameras were stationary, i.e. not during fight. Auto exposure mode was used in the cameras during this experiment except for the Mavic, which was altered in real time. This type of real time adjustment was not possible using the Nikon and GoPro cameras on the other UAS platforms. Because of this adjustment it seems that the conditions constituting bright, normal and dark changes, but this is due to the changes in exposure settings.

Results

Nikon L830 (The Goose)

Fig. 3-3 presents images taken at the MCC distance in each lighting condition by the Nikon L830 camera. The change in the captured images are due to the lighting conditions. The crack was located at the 3 o'clock position in these picture. The MCC distance for dark lighting was 0.3 m (Fig. 3-3a). The MCC distance increased to 0.8 m under normal lighting (Fig. 3-3b). Under bright lighting, the MCC distance increased to 1.0 m (Fig. 3-3c). For comparison, observation at less than one meter is typically considered "hands-on". The normalized MCC to pixel size was greatest for Nikon images, with 3.97, 4.03, and 4.09, in dark, normal, and bright lighting conditions, respectively.
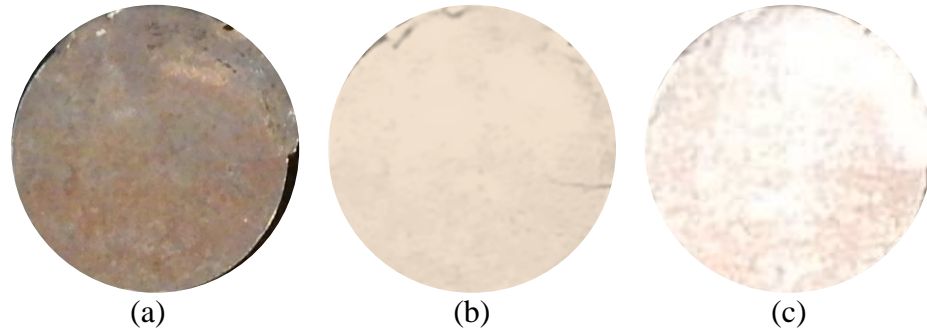
Fig. 3-3 Nikon L830 images taken at MCC distances of (a) 0.3 m in dark, F3, ISO1600, (b) 0.8 m in normal, F3, ISO 640, and (c) 1.0 m in bright, F3, ISO 280

GoPro Hero 4 (Iris)

Fig. 3-4 presents images taken at the MCC distance in each lighting condition taken by the GoPro camera from the Iris. The MCC distance in dark lighting was 0.2 m (Fig. 3-4a). The MCC distance tripled to 0.6 m in normal lighting (Fig. 3-4b). The MCC distance did not improve when bright lighting was provided; the MCC distance under bright lighting was also 0.6 m (Fig. 3-4c). The normalized MCC to pixel size values were smallest among the studied cameras with 1.76, 1.70, and 1.70 in, normal, and bright lighting condition, respectively.

DJI Camera (Mavic)

Fig. 3-5 presents images taken at the MCC distance in each lighting condition by the DJI camera from the Mavic. The MCC distance in dark lighting was 0.4 m (Fig. 3-5a). In normal lighting, the MCC distance more than doubled to 0.9 m (Fig. 3-5b). Under bright lighting, the MCC distance increased to 1.1 m the maximum value recorded during the experiment (Fig. 3-5c). The normalized MCC to pixel size values in DJI images were

close to the Nikon camera values with 4.03, 3.40, and 3.11 in dark, normal, and bright

lighting conditions, respectively.
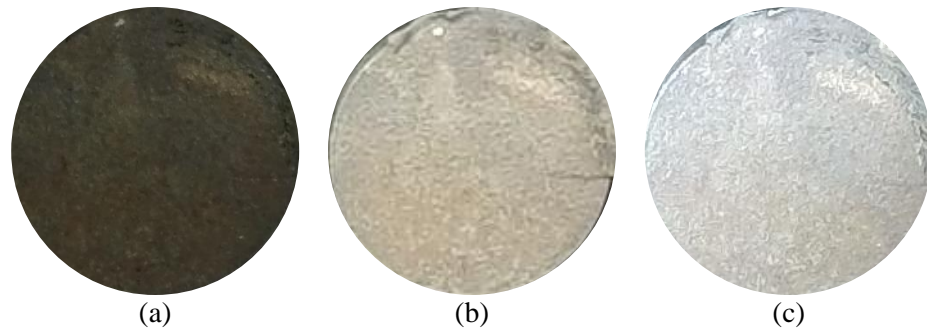
Fig. 3-4 GoPro images taken at MCC distances of (a) 0.2 m in dark, F2.8, ISO 400, (b) 0.6 m in normal, F2.8, ISO 400, and (c) 0.6 m in bright, F2.8, ISO 400.
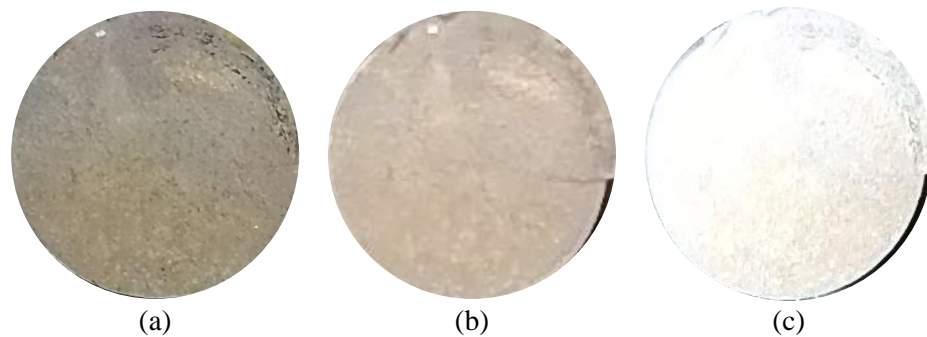
Fig. 3-5 DJI images taken at MCC distances of (a) 0.4 m in dark, F2.2, ISO 1600, (b) 0.9 m in normal, F2.2, ISO 617, and (c) 1.10 m in bright, F2.2, ISO 483

Summary

MCC distances and normalized MCC to pixel size values for each of the three

cameras and lighting conditions are summarized in Table 3-3. Note the values in this

table are only valid for the described condition of the laboratory experiments. As

expected, decreased surface illumination reduced the distance at which the crack could be detected. MCC distances increased from 0.2 m (GoPro) and 0.4 m (DJI) in dark lighting condition to 0.6 m (GoPro) and 1.10 m (DJI) in bright lighting condition. These results demonstrate the importance of lighting in UAS-assisted bridge inspection, particularly when the intent is to detect small features like fatigue cracks. However, since the change in MCC between normal and bright lighting conditions was small (less than 20% for each camera), the normal lighting condition was deemed acceptable for the remainder of the experiments. The ability of the camera to increase the ISO sensitivity for low lighting conditions improved the visual crack detection. As seen in Fig. 3-3 and Fig. 3-5, Nikon and DJI Mavic cameras was set the ISO sensitivity differently automatically for each lighting condition, between 280 to 1600 for Nikon and between 480 to 1600 for DJI Mavic; whereas, the ISO sensitivity for the GoPro images, shown in Fig. 3-4, were always 400. The normalized pixel size to MCC is maximum in the Nikon pictures (around 4.0 for all lighting conditions). The DJI Mavic camera has the second largest values between 3.11 (bright) and 4.03 (dark) which means this camera takes better pictures for fatigue crack detection in low light condition. The pictures taken by GoPro camera have the least normalized pixel size to MCC values (approximately 1.70 in all lighting conditions) which means this camera is not as suitable for fatigue crack detection as the others.

Mock FCM Inspections

Experiment Description

Indoor and outdoor mock field inspections were performed to determine if known fatigue cracks could be identified in controlled and uncontrolled environments using

UAS images. The MCC experiments detailed in the previous section showed that cracks could be identified with stationary cameras in a variety of lighting conditions. The intent of the experiment detailed in this section was to determine if cracks could be identified in-flight in field conditions.

Table 3-3 MCC distance (m) and normalized MCC to pixel size for UAS cameras in dark, normal, and bright conditions

Lighting Condition	MCC (m)			Normalized MCC to pixel size (mm/1000 mm)		
	Nikon L830 (Goose)	GoProHero4 (Iris)	DJI Camera (Mavic)	Nikon L830 (Goose)	GoProHero4 (Iris)	DJI Camera (Mavic)
Dark	0.3	0.2	0.4	3.96	1.76	4.03
Normal	0.8	0.6	0.9	4.03	1.70	3.40
Bright	1.0	0.6	1.10	4.09	1.70	3.11

Two types of inspections were performed in each of two conditions. *Real-time* inspections required the operator to identify fatigue cracks through a 12-cm first person view (FPV) monitor while the UAS was in flight. Post-flight inspections required the operator to identify fatigue cracks on a full size computer monitor following the conclusion of the inspection flight. Real-time and post-flight inspections were performed in a controlled environment (indoors) and an uncontrolled environment (outdoors). The controlled environment was inside of the Systems, Materials, and Structural Health Laboratory (SMASH Lab) at Utah State University (USU), a 500-m^2 indoor testing facility in Logan, UT. The intent of testing in the controlled environment was to evaluate the effects of flying in a GPS denied environment on fatigue crack detection distance. Such effects include vibration, unstable flight, and difficulty navigating in confined spaces. The uncontrolled environment was under a single-span steel girder bridge located

at the Utah Water Research Laboratory (UWRL) at USU in Logan, UT. The intent of

testing in the uncontrolled environment was to evaluate the effects of environmental

variables (most notably, wind), in addition to the GPS-denied operation, on the UAS

flights and consequently on the MCC distance.

The inspection team included a pilot and an inspector; the same inspection team

performed all inspections. The fatigue-cracked specimen shown previously in Fig. 3-2

was positioned in various locations within each environment. The minimum distance that

the pilot achieved between the UAS and the fatigue-cracked specimen was reported as

the achieved crack-to-platform (ACP distance). The inspector estimated the ACP distance

visually. Upon viewing the resulting image, whether in real-time or post-flight, the

inspector qualitatively evaluates whether the crack is detectable.

Controlled Environment

The fatigue-cracked specimen shown in Fig. 3-2 was adhered to a steel test frame

at an elevation of 3 m in the SMASH Lab at USU. The normal lighting condition was

provided and verified in the same manner as discussed previously.

The Goose was unable to hold a stable position during flight due to the absence of

GPS signal, which negatively affected image quality. The ACP distance in normal

lighting in the controlled environment was 0.7 m, which was 0.2 m shorter than the MCC

distance. Fig. 3-6a shows the resulting image, in which the crack is barely visible. Since

the Goose does not allow for FPV imaging, this result is based only on post-flight

inspection. No real-time inspection results were obtainable.

The Iris also suffered in the GPS-denied environment. It could not hold a stable

position long enough to detect the fatigue crack without GPS-reliant obstacle avoidance or altitude hold features. The ACP distance was 0.5 m, which was 0.1 m shorter than the MCC distance. Even at this distance, the crack was not detectable in either real-time or post-flight inspections. Fig. 3-6b shows the image collected by the Iris at the ACC distance of 0.5 m, in which no crack can be observed.

The Mavic is equipped with stereo-vision positioning system and sonar altitude hold; thus, the pilot was able to maintain a stationary position in the GPS-denied controlled environment. Stereo-vision positioning uses the overlapping view of the two cameras to find the position of the UAS. More details on how this system works can be found in Mustafa et al., (2012). The pilot was able to achieve an ACP distance of 0.25 m, close to the MCC distance in the normal lighting. Fig. 3-6c shows the image taken by the Mavic, in which the crack is clearly observable. The crack was detectable in both real-time and post-flight inspections using the Mavic at the ACP distance of 0.25 m. However, it is interesting to note that the crack is still visible in Fig. 3-6a despite having almost 3 times greater ACP distance (0.7 m) than the Fig. 3-6c which is taken with Mavic at ACP distance of 0.25 m. It seems that the higher resolution of the Nikon camera compared to the DJI Mavic and image stabilization feature compensated for the Goose instability and vibrations.
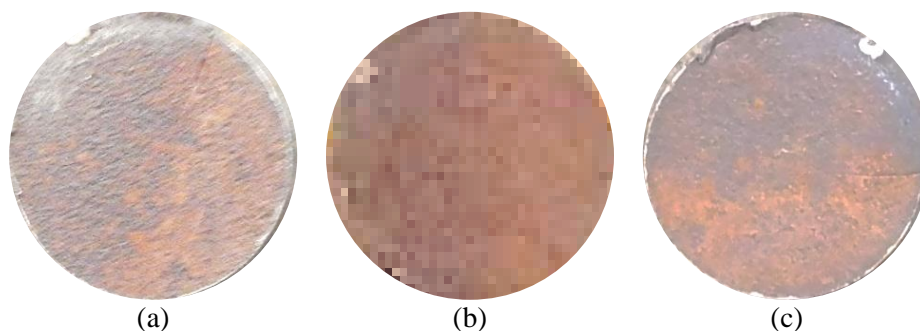
Fig. 3-6 Fatigue crack images taken at ACP distances in controlled, GPS denied environment; (a) Goose (0.7 m), (b) Iris (0.5 m), (c) Mavic (0.25 m)

Table 3-4 summarizes the results of mock FCM inspections in normal lighting conditions in a controlled, GPS denied environment. Note the values in this table are only valid for the described conditions of the mock inspection in the controlled environment.

Table 3-4 Summary of crack detection results for UAS in normal lighting conditions in controlled, GPS denied environment

Result	Goose	Iris	Mavic
ACP distance (m)	0.7[a]	0.5	0.25
Realtime	N/A	No detection	detection
Post-flight	Detection	No detection	detection

[a]with 10× zoom

Uncontrolled Environment

Where the controlled (indoor) mock inspection elucidated the effects of flight in the absence of a GPS signal (e.g., vibration, GPS denied operation), the uncontrolled (outdoor) mock inspection elucidates the additional effects of wind and navigation in a

confined space. The fatigue-cracked specimen shown in Fig. 3-2 was adhered to a girder

under the UWRL bridge in Logan, UT. The inspection was performed on the morning of

January 10, 2017. KUTLOGAN25 weather station (located 5.5 km from the test location)

reported that the wind speed was approximately 11 m/s (25 mph) at the time of testing

(Weather 2017a). The maximum bridge clearance was approximately 2 m, which was

deemed too narrow for access by the Goose. Therefore, inspections in the uncontrolled

environment were only completed with the Mavic and the Iris.

The pilot achieved an ACP distance of 0.6 m with the Iris. This was 0.1 m longer

than the achieved ACP distance in the controlled environment. The increase in ACP is

attributed to the wind speeds during testing. The inspector was unable to detect the crack

during real-time or post-flight inspections in normal lighting conditions.

Despite the wind, the pilot was able to achieve the same ACP distance with the

Mavic as achieved in the controlled environment (0.25 m). The crack was readily visible

in real-time inspections with normal or bright lighting, and in post-flight inspections in all

lighting conditions. Representative images are shown in Fig. 3-7a through Fig. 3-7c.

Following this success, the fatigue-cracked specimen was repositioned to sit facing the

earth on the bottom flange of a girder in order to determine the effects of camera angle on

the crack detection. As shown in Fig. 3-7d, the inspector was able to detect the fatigue

crack even at an oblique angle. This is significant, considering the maximum tilt angle of

the Mavic camera is 30 degrees. The brightness was varied and fit within the bounds of

the definitions for bright, normal, and dark as measured by the lightmeter. Unlike the

laboratory experiments, the exposure of the DJI camera is adjusted in Fig. 3-7 to most

clearly capture the crack. Greater values of exposure were set on the camera as the

lighting condition got darker minimizing apparent differences in image brightness in this figure. The blurriness in the figures could have been due to combination of factors including adequate exposure control, GPS-denied operation, and UAS vibrations.

(a)   (b)

(c)   (d)
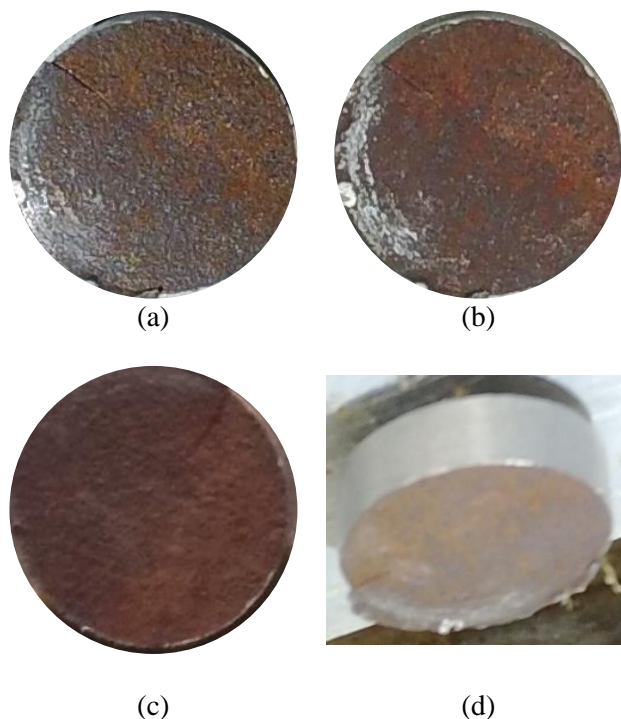
Fig. 3-7 Fatigue crack images taken by Mavic in (a) bright, (b) normal, and (c) dark lighting; and (d) at oblique angle (bright)

Table 3-5 summarizes the results of mock FCM inspections in an uncontrolled outdoor environment with wind speeds of approximately 11 m/s. The results demonstrate the ability of the Mavic to detect fatigue cracks at realistic ACP distances in the field. Note the values in this table are only valid for the described conditions of the mock inspection in the uncontrolled environment. The mock inspections also show having auxiliary positioning system, such as stereo-vision on DJI Mavic, is crucial in UASs,

especially for navigating under a bridge where the GPS signals are either weak or non-existent.

Table 3-5 Summary of crack detection results for UAS in uncontrolled outdoor environment

Result	Mavic			Iris
	Lighting			
	Dark	Normal	Bright	Normal
ACP distance (m)	0.25			0.6
Real-time	Detection	Detection	Detection	No detection
Post-flight	No detection	Detection	Detection	No detection

FIELD FCM INSPECTIONS

Following successful detection of known cracks in a variety of conditions using the Mavic, the authors selected that UAS for field inspections. Two rounds of field inspections were completed. The first was a deck arch bridge over Fall River in Ashton, ID (ITD Bridge Key 21105). Previous FCM inspections of the Fall River Bridge by ITD revealed several fatigue cracks. The intent of the first field inspection was to determine if these previously identified fatigue cracks could be detected with the Mavic in real-time or post-flight inspections. However, the exact locations of the cracks were not revealed to the inspection team. The second field inspection was completed at the Steel Bridge Research, Inspection, Training, and Engineering (S-BRITE) Center at Purdue University in Lafayette, IN. This training structure includes several known fatigue cracks, unknown to the inspection team, and is used to train FCM inspectors. The intent of the second field inspection was to (1) determine if the known fatigue cracks could be detected with the

Mavic in real-time or post-flight inspections, and (2) compare the results of UAS-assisted

FCM inspection with those of human FCM inspection and with the ground truth (i.e., the

known number of fatigue cracks in the structure).

Fall River Bridge FCM Inspection

Fig. 3-8 shows plan and perspective views of the Fall River Bridge. The bridge

comprises two main longitudinal frames in East-West orientation and fifteen

perpendicular transverse floor beams. The floor beams are connected to the girder webs

by gusset plates. Inspection of the Fall River Bridge commenced at 11:30 AM on March

22, 2017. The nearest weather station, KIDASH08, was 35 km from the inspection site

and reported a maximum wind speed of 7 m/s (16 mph) during the 90-minute inspection

flight (Weather 2017b). However, the inspection team estimated that the wind gust

speeds at the inspection location were considerably more. The inspection team was

located at the Southern side of the bridge on the Eastern bank of the Fall River, shown on

the right hand side of Fig. 3-8a as the ground station.

In the GPS-denied under-bridge environment, the Mavic tended to follow the

river current without the pilot's control. The visual positioning system—the dominant

sensor in absence of GPS signal—caused this by picking up the river current. To mitigate

this issue, the inspection team only inspected the first four Eastern floor beams, which

were above solid ground. The pilot flew the UAS under the bridge, inspecting 12

locations on the floor beams, two girder splices, the Southern girder web, the Southern

concrete barrier, the bottom flange connection to the web on the Southern girder, and the

bottom flange of the Southern girder, as shown in Fig. 3-9a. Two of these inspection

points—11 and 12—are known to include fatigue cracks based on previous FCM

inspections by ITD. The inspector and pilot knew which girders had fatigue cracks but

the exact locations of fatigue cracks were not revealed to them. The inspection team

verified that fatigue cracks were not present at inspection points 1–10 during both real-

time (on 12-cm FPV monitor) and post-flight (on 60-cm computer monitor) inspections.

Fig. 3-10 shows representative inspection images from inspection points 3 and 4, which

clearly show that no fatigue cracks exist in those locations. Fig. 3-11 shows images taken

at inspection points 11 and 12. It is impossible to detect fatigue cracks in the original

images (Fig. 3-11a and 3-11b). With magnification (Fig. 3-11c and 3-11d) it is still

difficult to identify the location of cracks, even though they are marked from previous

inspections. This is due in part to the limited APC distance and camera resolution.

Markings made by ITD inspectors during previous inspections also obscured the cracks,

(i.e. black marker along crack length) making them more difficult to identify (Fig. 3-11c).

b shows the FPV view of Mavic flying under the bridge and approaching a fatigue crack

susceptible location. Marks from previous inspections indicating the presence of a fatigue

crack are visible in the figure. The handheld spotlight, held by the inspector, served a

dual purpose during the inspection: as a pointer to guide the pilot to the locations of

interest, and to provide illumination. The ACP distance in the field condition was

approximately 0.5 m, double that achieved during the mock inspections. During wind

gusts, the ACP distance increased to 0.75 m.

(a)   (b)

Fig. 3-8 Aerial (a) plan and (b) perspective view of Fall River Bridge in Ashton, ID (Images courtesy of Dan Robinson, AggieAir.)

(a)   (b)
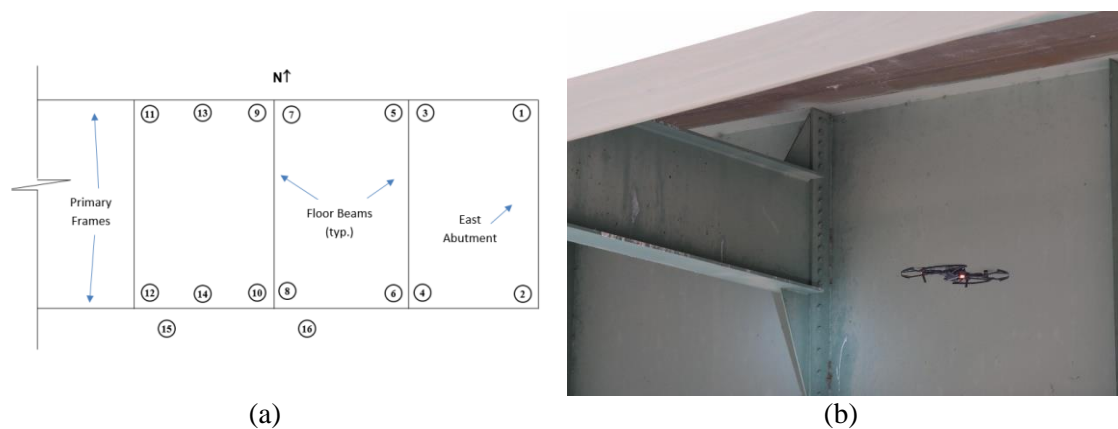
Fig. 3-9 (a) Inspection points on Fall River Bridge; (b) view of Mavic on approach to inspection points

The inspection team verified that fatigue cracks were not present at inspection points 1–10 during both real-time (on 12-cm FPV monitor) and post-flight (on 60-cm computer monitor) inspections. Fig. 3-10 shows representative inspection images from

inspection points 3 and 4, which clearly show that no fatigue cracks exist in those

locations. Fig. 3-11 shows images taken at inspection points 11 and 12. It is impossible to

detect fatigue cracks in the original images (Fig. 3-11a and 3-11b). With magnification

(Fig. 3-11c and 3-11d) it is still difficult to identify the location of cracks, even though

they are marked from previous inspections. This is due in part to the limited APC

distance and camera resolution. Markings made by ITD inspectors during previous

inspections also obscured the cracks, (i.e. black marker along crack length) making them

more difficult to identify (Fig. 3-11c).

(a)   (b)

Fig. 3-10 Inspection images from Fall River Bridge points (a) 3 and (b) 4 showing no fatigue cracks

The inspector detected several other items of interest, including corrosion in the

bottom flange of the Southern girder, efflorescence, concrete cracks, possible

delamination in Southern barrier, and minor corrosion on the splice plate of the Southern

girder in real-time. Real-time and post-flight inspection images were of sufficient quality

to rule out the presence of fatigue cracks in locations 1 through 10. However, the FCM

inspection was inconclusive because of the presence of the marker lines on the cracks.
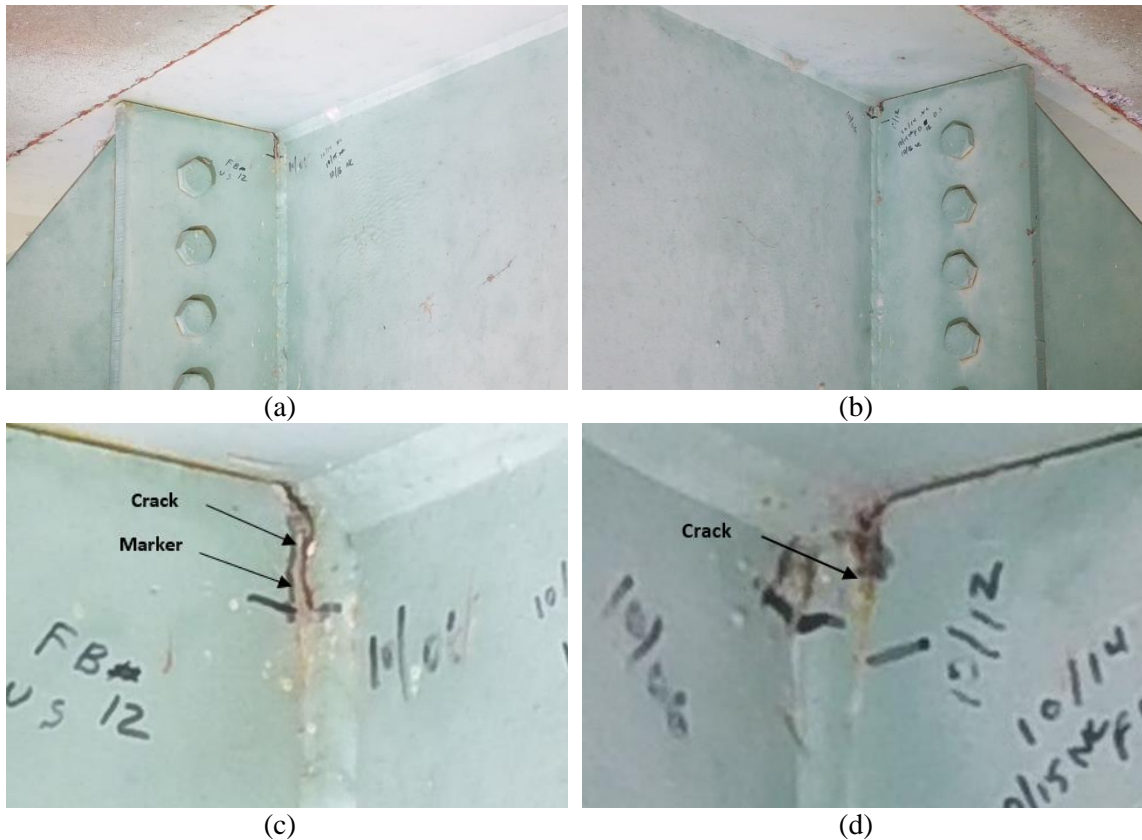
Fig. 3-11 Inspection images from Fall River Bridge points (a) 11 and (b) 12; and magnified inspection images from points (c) 11 and (d) 12

The Fall River field inspection revealed a significant drawback in UAS-assisted FCM inspections. It is not acceptable in practice to perform an inspection and report inconclusive results, which could easily happen if the local weather under the bridge is less than ideal, as was the case with this inspection. Lack of the GPS signals, combined with wind gusts, made the flight impossible for large portions of the time on-site. Lastly, in order to comply with federal aviation administration regulations, the pilot had to

maintain a line of sight with the UAS which severely limited UAS accessibility to all the members under the bridge. Future UASs for FCM bridge inspections are suggested to have small sizes, more reliable positioning systems in lieu of GPS signals, wind and turbulence resistivity, clearance measurement capability (laser range finder), 360-degree gimbal, onboard adjustable light source, and on-the-fly adjustable camera setting for exposure and optical zoom). As of now, a commercial UAS that meets these requirements does not exist (Dorafshan and Maguire 2018). DJI Mavic family UASs satisfy some of the requirements making them an adequate candidate for UAS-assisted FCM inspections.

S-BRITE Center FCM Inspection

Fig. 3-12 shows the Probability of Detection (POD) training structure at the S-BRITE Center at Purdue University. This structure is primarily used for visual inspection research and inspector training. The POD structure is intended to mimic a 120 m, two-span, highway bridge with three girder lines elevated approximately 8 m above the ground. Each girder spans approximately 12 m and the girder lines are spaced 3 m apart. The test frame supports three types of test specimens: (1) plate girders and wide flange specimens, (2) welded cover plate specimens, and (3) riveted plate specimens. The plate girder and wide flange specimens are suspended from the frame beams, and the welded cover plates are attached to the bottom flanges. Riveted cover plates are attached to the frame columns. Each specimen can have one fatigue crack, multiple fatigue cracks or no fatigue cracks. Inspectors are evaluated based on their ability to correctly locate the fatigue cracks and distinguish cracks from surface defects (scratches, corrosion, debris,

etc.). In total, the inspection team examined 72 girder specimens, 19 welded cover plate specimens, and 8 riveted plate specimens. A facility proctor joined the inspection team.
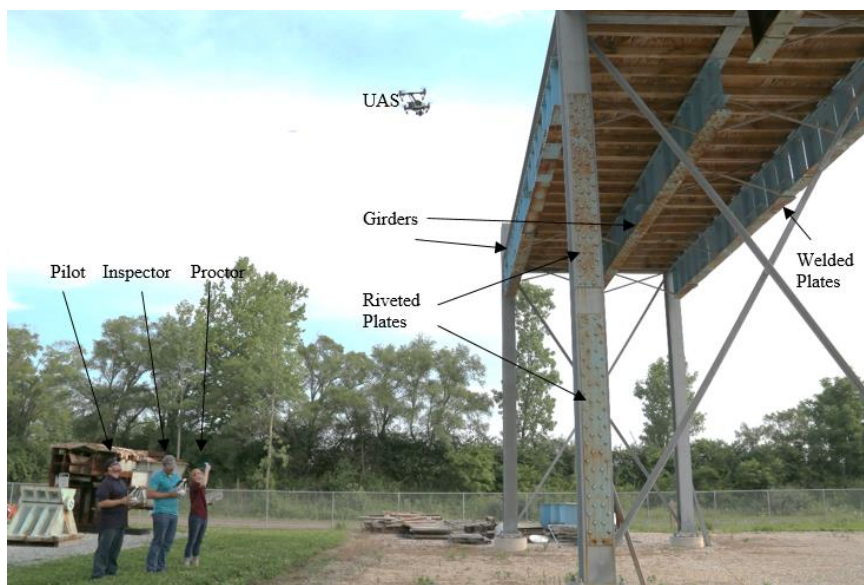
Fig. 3-12 Training POD frame at S-BRITE center, Purdue University

The inspection team used the Mavic—the same UAS used in the Fall River Bridge field inspection—and two additional UAS—a DJI Inspire 1 and a DJI Phantom 3—for the S-BRITE Center field inspection. Multiple similar platforms provided redundancy in the case of equipment failure and allowed one UAS to be used for inspection while the remaining two were charging. Fig. 3-13 shows the three UAS and Table 3-6 lists relevant specifications. The on-board cameras were of comparable quality and specification as it is shown in Table 3-7. The flight time varied based on the weight of the platform. Each UAS was equipped with FPV image streaming (using a 25-cm FPV monitor), downward sonar sensors, vision system, and barometers. The Mavic was the only one equipped with stereo-vision positioning in this experiment. The FPV monitor

used in the S-BRITE Center field inspection was upgraded from that used in the previous field inspection; in addition to a larger viewing area, the new FPV monitor allowed remote gimbal control, zoom, and exposure adjustments in real-time. The S-BRITE Center inspection took place on July 5–6, 2017. Inspections were performed between 10:00 AM and 8:30 PM on July 5 and between 9:00 AM and 5:00 PM on July 6. Maximum recorded wind speeds according to the KLAF weather station at the Purdue University airport were approximately 4 m/s (9 mph), which is much calmer than the wind speeds experienced during the mock inspections and the Fall River Bridge inspection (Weather 2017c and Weather 2017d).

| (a) | (b) | (c) |
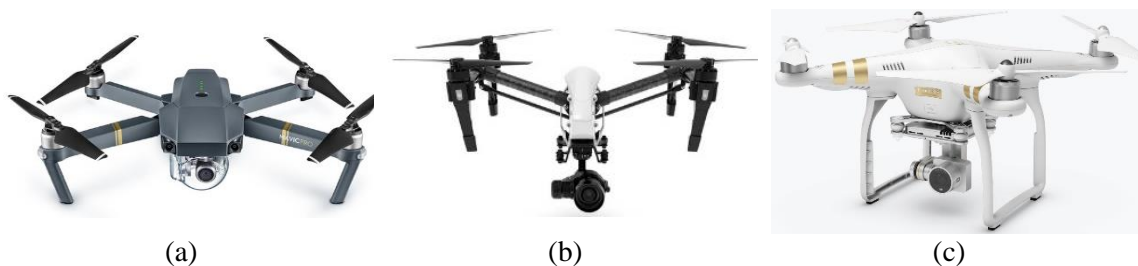
Fig. 3-13 (a) DJI Mavic, (b) DJI Inspire, and (c) DJI Phantom UAS used in S-BRITE inspection

Table 3-6 UAS specifications for S-BRITE center inspection

Specification	Mavic	Inspire	Phantom
Weight (kg)	0.7	3.4	1.3
Camera resolution (MP)	12	12	12
Flight time (min)	27	15	23
Vision system	Stereo	Downward	Downward

Table 3-7 Camera Specifications used in S-BRITE center

Specification	DJI Mavic	DJI Inspire	DJI Phantom
Resolution (max)	4000×3000 (12 MP)	4000×3000 (12 MP)	4000×3000 (12 MP)
Sensor type	CMOS	CMOS	CMOS
Lens aperture	F2.2	F2.8	F2.8
Sensor size (in)	1/2.3	1/2.3	1/2.3
ISO (max)	1600	1600	1600
Field of view (mm)	20	24-30	20

Table 3-8 summarizes the inspections. 72 Seventy-two girder specimens were inspected using the Mavic. Eighteen of these were also inspected using the Inspire in order to compare platforms. Twenty welded plate specimens were inspected using the Inspire, and eight riveted plate specimens were inspected using the Phantom. The post-flight inspections were carried out by the same inspector involved in real-time inspections. An S-BRITE Center proctor analyzed the inspection results. For each reported crack or *call*, the proctor recorded a true positive (hit) or a false positive (fallout). The proctor also reported the number of false negatives (misses). The hit-to-call ratio is the number of hits divided by the number of calls. The true positive rate (TPR) is the number of hits to the sum of hits and misses (in percent). The false positive rate (FPR) is the number of false positives divided by the number of calls (in percent). The proctor also reported the average performance of thirty hands-on inspections (using human inspectors) for comparative purposes. Table 3-9 summarizes the inspection results in terms of calls, inspection time, TPR, FPR, and hit to call ratio.

Table 3-8 UAS inspection locations and statistics

UAS	Specimen Type	ACP Distance (cm)	No of Pictures	Inspection Time (min)	Post-flight (min)
DJI Mavic	Girders	25-50	990	241	31
DJI Inspire	Girder, Welded Plates	75-100	992	74	70
DJI Phantom	Riveted Plates	75	107	52	24

Table 3-9 Comparison of UAS and human inspection performance

Realtime						
UAS	Member (No)	Calls	Time (min)	TPR (%)	FPR (%)	Hit/Call (%)
Mavic	G (72)	159	241	64	89	11
	G (18)	34	27	33	91	9
Inspire	G (18)	32	57	44	88	13
	WP (20)	26	17	75	88	12
Phantom	RP (8)	68	52	89	88	12
Post-flight						
UAS	Member (No)	Calls	Time (min)	TPR (%)	FPR (%)	Hit/Call (%)
Mavic	G (72)	61	116	61	72	28
	G (18)	16	22	33	81	19
Inspire	G (18)	14	31	44	71	29
	WP (20)	15	24	0	100	0
Phantom	RP (8)	45	69	78	84	16
Hands-on (average of 30)						
UAS	Member (No)	Calls	Time (min)	TPR (%)	FPR (%)	Hit/Call (%)
Mavic	G (72)	82	144	61	79	21
	G (18)	19	27	44	79	21
Inspire	G (18)	19	27	44	79	21
	WP (20)	11	No Data	75	73	27
Phantom	RP (8)	10	17	89	20	80

Girder Specimens

A 241-minute real-time inspection of 72 girder specimens using the Mavic

resulted in 159 calls. Eighteen of these were hits for a hit-to-call ratio of 11% and a FPR

of 89%. The proctor reported 10 misses, for a TPR of 64%. Fig. 3-14 shows examples of

true positive, false negative, and false positive images from the Mavic girder inspection.

Fig. 3-14a shows a 9.2-cm fatigue crack that the inspector detected. Fig. 3-14b shows a

2.7-cm fatigue crack that the inspector missed, and Fig. 3-14c shows a spot of rust

staining that the inspector erroneously identified as a fatigue crack.

(a)   (b)   (c)
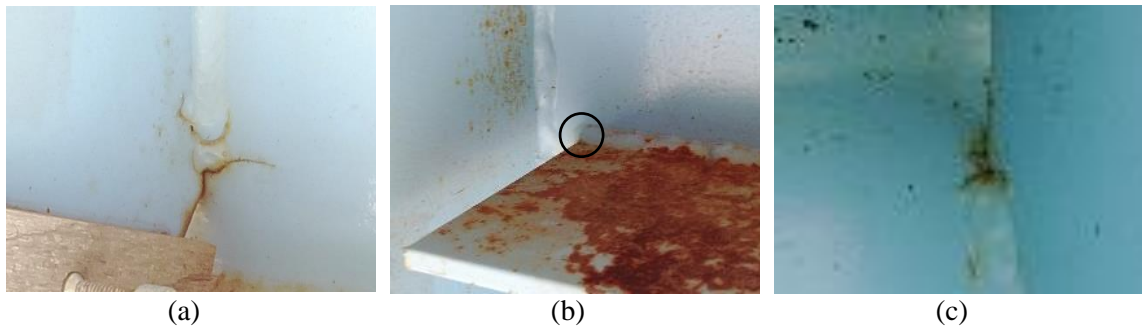
Fig. 3-14 Girder inspection images: (a) true positive (hit), (b) false negative (miss), and (c) false positive

Eighteen girder specimens on the exterior girder line of the POD frame were

inspected using both the Mavic and the Inspire. The 27-minute real-time inspection with

the Mavic produced 34 calls with 3 hits, 31 false positives, and 6 misses. The 57-minute

real-time inspection with the Inspire produced two fewer calls but one more hit. Despite

requiring more than double the inspection time, the Inspire had a greater hit-to-call ratio

(13% vs. 9%), greater TPR (44% vs. 33%), and lower FPR (88% vs. 91%) than the

Mavic. The Inspire is a larger UAS with a better camera, however, it was less

maneuverable and stable than the Mavic. Also, the optical focusing for the Inspire was

not as efficient, requiring more flight time to obtain a reading by the inspector, which explains the increased inspection time and lower image quality.

Welded Cover Plate Specimens

A 17-minute real-time inspection of 20 welded plate specimens using the Inspire resulted in 26 calls. Three of these calls were hits, for a hit-to-call ratio of 12%. However, the inspector missed only one crack for a TPR of 75%. Fig. 3-15 shows examples of true positive, false negative, and false positive images from the welded cover plate inspection. Fig. 3-15a shows a 12.8-cm fatigue crack that the inspector detected. Fig. 3-15b shows a 5-cm crack that the inspector did not detect. Fig. 3-15c shows a rust line that the inspector erroneously reported as a crack. The inspection performance in this task suffered greatly because the pilot was unable to achieve stable flight in the GPS-denied under-structure environment. Image quality suffered due to UAS instability and also the underslung cameras had limited ability to inspect the overhead cover plates due to the camera upward rotation limitations. Thus, the ACP distance was relatively large and the images were less clear. Furthermore, the inspector had less experience detecting the cracks present in the welded cover plate details.

Riveted Plate Specimens

A 52-minute real-time inspection of eight riveted plate specimens using the Phantom produced 68 calls, of which 8 (12%) were hits. Again, the inspector missed only one crack, giving a TPR of 89%. Fig. 3-16 shows examples of true positive, false negative, and false positive images from the riveted plate inspection. Fig. 3-16a shows a 2-cm fatigue crack that the inspector detected. Fig. 3-16b shows a 4-cm crack that the

inspector did not detect. Fig. 3-16c shows a rust line that the inspector erroneously

reported as a crack.

| (a) | (b) | (c) |

Fig. 3-15 Welded plate inspection images: (a) true positive (hit), (b) false negative (miss), and (c) false positive

| (a) | (b) | (c) |
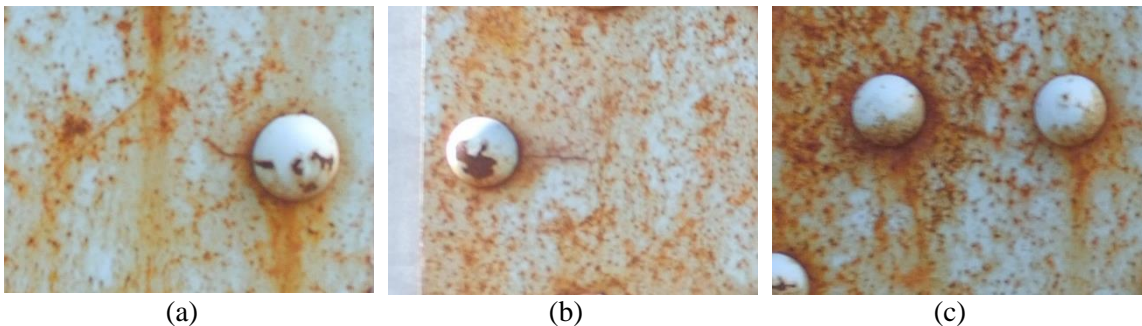
Fig. 3-16 Riveted plate inspection images: (a) true positive (hit), (b) false negative (miss), and (c) false positive

Overall, the real-time UAS inspections performed reasonably well for this

inspection category. Again, false positives were an issue, as the average hit-to-call ratio

was about 12%, meaning that about one in 8 calls corresponded to an actual crack. The

TPR varied across the board. In the best case, the inspector identified 89% of fatigue

cracks in eight riveted plate specimens. In the worst case, the inspector identified only a

third of the fatigue cracks present in 18 exterior girder specimens. The inspector had trouble labeling cracks due to the complexity of the riveted specimens, which might explain some of the true positive variability.

Post-Flight Inspections

Post-flight inspections produced mixed results. On average, the number of calls was about half that of real-time inspections of the same specimen sets. For example, while the real-time inspection of 72 girder specimens with the Mavic produced 159 calls, the post-flight inspection produced only 61. The post-flight inspection typically extended the inspection time by 50–130%. The hit-to-call ratio was improved over the real-time inspection in all but one case. Post-flight inspection of 20 welded plates using the Inspire produced zero hits. This was mainly due to the location of the specimens which required an upward camera and lack of stability of the DJI Inspire. Excluding that data point, the average hit-to-call ratio during post-flight inspections was about 18%, a significant improvement over the 12% average hit-to-call ratio during real-time inspections. However, the post-flight TPR was the same or worse than the real-time TPR in all cases. In the case of the welded plate inspection, the inspector correctly identified 3 of the 4 cracks during the real-time inspection, but none during the post-flight inspection.

Interestingly, calls made during the real-time and post-flight inspections were not always identical. Real-time inspections with the Mavic produced 160 calls. Post-flight inspections with the Mavic produced 61 calls, of which only 59 corresponded to identical real-time calls. Similarly, real-time inspections with the Phantom produced 68 calls. Post-flight Phantom inspections produced 45 calls, of which only 7 corresponded to identical

real-time calls. The Inspire was an exception to this trend; real-time inspections produced 58 calls and post-flight inspections produced 29, all of which corresponded to identical real-time calls. While post-flight inspections resulted in a fewer number of false positives than real-time inspections, they did not result in additional true positives. This, combined with the greatly increased inspection time, calls into question the utility of post-flight inspections; but the hit-to-call ratio improved in the post-flight inspections. In this experiment, the real-time and post-flight inspections were considered separately. In practice, however, they can be used together to have more accurate crack detections because in real-time the inspector was more concerned about missing a crack than reporting false positives. As such, it is difficult to question the utility of post-flight inspections in practice. Furthermore, post-flight inspections require the storage of vast amounts of data and considerable time in excess of the actual inspection flight. These requirements may not be palatable to bridge owners, both of which would increase costs above the UAS inspection, even though FPRs decrease. In general, false positives were greatly decreased (up to 17%) and improved hit-to-call ratio significantly (up to 17%). With the inspection of the DJI Inspire images from the welded cover plates.

Comparison to Human Hands-On Inspection

At worst, hands-on inspections took as long as real-time UAS inspections. For example, the average hands-on inspection time of 18 exterior girder specimens lasted 27 minutes. Real-time inspection of the same 18 exterior girder specimens using the Mavic also took 27 minutes, but real-time inspection using the Inspire took more than twice as long. On average, hands-on inspection of all 72 girder specimens took 144 minutes,

which was over 1.5 hours shorter than the time required for real-time inspection of the same 72 girders using the Mavic. In the case of riveted plates, hands-on inspection was more than three times faster than real-time UAS inspection using the Phantom. When the additional inspection time associated with the post-flight inspection was considered, hands-on inspection was 1.8–7 times faster than UAS inspection.

Hands-on inspections of the 72 girder specimens produced almost 50% fewer calls than real-time UAS inspections but more calls than post-flight UAS inspections. The average hands-on inspector correctly located 17 fatigue cracks for a hit-to-call ratio of 21% or about one in five. The real-time UAS inspection identified 18 cracks but the hit-to-call ratio was only about one in ten. The hit-to-call ratio for the post-flight inspection was improved at 28%, but the TPR matched the hands-on average.

The average hands-on inspector made 11 calls during inspection of the 20 welded plate specimens. About one in four calls was a correctly identified crack (hit). On average, hands-on inspectors correctly identified 3 of 4 cracks, which matched the performance during the real-time UAS inspection. However, the real-time UAS inspection made more than double the number of calls as the average hands-on inspector. Thus, the hit-to-call ratio was much worse (12% vs. 27%). Interestingly, the post-flight UAS inspection produced 15 calls but zero hits, due to the poor quality of the images and the inspector's inexperience with fatigue cracks in on the welded cover plates.

Hands-on inspections of riveted plates produced excellent results. The average inspection time was only 17 minutes and inspectors identified 8 of 9 total cracks. Of ten calls, eight were hits and only two were false positives. The TPR from real-time UAS inspection of the same eight riveted plates was the same as the hands-on average, but the

UAS inspection made 68 calls, of which 60 (88%) were false positives.

Summary of S-BRITE inspection

In summation, UAS-assisted inspections were longer in duration than human-only hands-on inspections. Real-time inspections resulted in a much larger number of calls than hands-on inspections, but the number of hits was not significantly higher. Post-flight inspections produced fewer false positives, but did not improve the TPR. These results show that the performance of UAS in FCM inspections can approach the quality of hands-on inspections, although the inspection time and number of false positives are likely to be more than hands-on inspection. The non-contact nature of the UAS-assisted inspection provides an opportunity for less labor-intensive inspections; but, it would also cause more false positive reports. As such, UAS inspection may be of most utility in cases where hands-on inspection is unsafe or impossible. As discussed previously, the hands-on inspection metrics represent the average performance of thirty human inspectors. As such, some human inspectors perform much better, and some much worse. Similarly, the results presented here should not be construed to describe the performance of all UAS, pilots, inspectors, camera platforms, etc., especially since only a single inspector and pilot tandem was used for the UAS assisted inspection. However, these results clearly indicate UAS assisted FCM inspections can perform similar to humans, but the DOT should be prepared for increased false positives, and it is not recommended that UAS assisted inspections replace FCM human inspection without further investigation. Based on the results of this study, the inspection time of the UAS-assisted FCM inspection is more than the average manned inspection; however, the S-BRITE

POD frame is not a very challenging bridge in terms of accessibility. Inspection of

bridges with more difficulty in accessibility, can benefit more from UASs as long as the

pilot has a visual line of sight to the UAS.

CONCLUSIONS AND FUTURE STUDIES

Previous literature demonstrates the application of UAS for initial inspection of

bridges, visual and autonomous detection of delamination or cracking in concrete, and

checking the surface condition of structures. This chapter investigated the application of

UAS for detection of fatigue cracks in steel bridges during FCM inspections.

Laboratory investigations revealed the importance of camera quality and surface

illumination on the maximum crack-to-camera (MCC) distance at which fatigue cracks

can be detected. Observed MCC distances with stable cameras (fixed, not in flight)

ranged from 0.3 m for the worst performing platform in dark lighting to 1.1 m for the best

performing platform in bright light. Mock FCM inspections demonstrated the difficulties

in detecting known cracks in GPS-denied or windy environments. Some platforms were

unstable in GPS-denied indoor environments and thus clear images were not obtainable.

The best performing platform has an achievable crack-to-platform (ACP) distance that

was far smaller than the previously determined MCC distance, meaning it was easily able

to obtain clear enough images for crack detection. This was true for both real-time

(inspection from FPV monitor during flight) and post-flight (inspection of recorded

images after flight) inspections. Note the results in this study do not cover all scenarios in

FCM bridge inspection and are valid for the described conditions of the mock inspection.

Nevertheless, the findings can serve as a guideline for bridge inspectors in order to

perform more successful UAS-assisted FCM inspections.

Two FCM inspections of structures with known fatigue cracks demonstrated the ability of the UAS platform to identify fatigue cracks in the field. The first, at Fall River Bridge in Ashton, ID, was inconclusive due to marker obscuring the potential fatigue cracks. The inspector was able to rule out the presence of fatigue cracks in several inspection locations. However, the inspector was unable to identify fatigue cracks in locations that were known to contain them. This was mainly due to limited ACP distances in gusting winds and obscuration of the cracks by markings from previous inspections. The Falls River inspection also indicated that GPS denied navigation, combined with the 10 m/s (22 mph) wind gusts made controlled flight near impossible. Also, the stereo-vision positioning, which enables some control in when GPS-denied, causes significant instability over water and FAA line of sight requirements eliminated accessibility to nearly half of the structure due to sight conditions.

The second field inspection, at the S-BRITE Center training facility at Purdue University, compared the performance of UAS inspections and human inspections. UAS inspection was comparable to hands-on inspection in terms of the number of real cracks that were identified. However, UAS inspections took far longer and resulted in a much higher number of false positives. In general, the results of this laboratory and field study show that fatigue crack identification during FCM inspections is promising using UAS, however challenges exist and more research is needed prior to routine use of UAS for fatigue crack detection.

Moving from manned to unmanned inspections, particularly for bridges with Fracture Critical Members (FCM), requires using Unmanned Aerial Systems (UASs)

with auxiliary positioning systems to compensate with the lack of GPS signals. The results of this study suggest that using UAS that rely heavily on GPS signals for navigation is very difficult and unlikely to produce fatigue crack detection. The stability of many systems in the GPS denied environment poses a risk to the UAS, pilot and mission. UAS pilots may not wish to risk their UAS in such situations until better autonomous position control is available. Among studied UASs, inspection using the DJI Mavic Pro was more successful than the others due to stereo-vision positioning system; however, this system causes instability when the UAS is over a current like a river (a common situation during FCM inspections). Future UASs for FCM bridge inspections are required to have small sizes, more reliable positioning systems in lieu of GPS signals, wind and turbulence resistivity, clearance measurement capability (laser range finder), 360-degree gimbal, onboard adjustable light source, and adjustable camera setting for exposure and optical zoom. As of now, a commercial UAS that meets these requirements does not exist. DJI Mavic family UASs satisfy some of the requirements making them a proper candidate for UAS-assisted FCM inspections. The results presented in this chapter are based on limited number of inspections which definitely does not mimic all possible inspection scenarios. More UAS-assisted FCM inspections are required to draw a comprehensive conclusion on the performance of UASs in terms of accuracy, hits, and inspection time.

References

AASHTO (2016), Manual for Bridge Evaluation 2nd Edition, 2016 Interim Revisions. *Washington, D.C. :American Association of State Highway and Transportation Officials*

Adams, S. M., & Friedland, C. J. (2011, September). A survey of unmanned aerial vehicle (UAV) usage for imagery collection in disaster research and management. In 9th International Workshop on Remote Sensing for Disaster Response (p. 8).

Aggieair (2017), "A Remote Sensing Unmanned Aerial System for Scientific Applications". <http://aggieair.usu.edu/> (April 12, 2017).

Biezma, M. V., & Schanack, F. (2007). Collapse of steel bridges. Journal of Performance of Constructed Facilities, 21(5), 398-405.

https://doi.org/10.1061/(ASCE)0887-3828(2007)21:5(398)

Brooks, C., Dobson, R. J., Banach, D. M., Dean, D., Oommen, T., Wolf, R. E., ... & Hart, B. (2015). Evaluating the Use of Unmanned Aerial Vehicles for Transportation Purposes (No. RC-1616). Michigan Tech Research Institute, Ann Arbor, Michigan. https://www.michigan.gov/documents/mdot/RC1616_Part_C_488517_7.pdf

Conner, R. J., Dexter, R. J., & Mahmoud, H. (2005). Inspection and management of bridges with fracture-critical details: a synthesis of highway practice (Vol. 354). Transportation Research Board. www.trb.org/publications/nchrp/nchrp_syn_354.pdf

Dorafshan, S., Coopmans, C., Thomas, R., Maguire, M. (2018a). Deep Learning Neural Networks for sUAS-Assisted Structural Inspections: Feasibility and Application, ICUAS18. IEEE. Dallas Marriot City Center, Dallas.

Dorafshan, S., & Maguire, M. (2017, June). Autonomous Detection of Concrete Cracks on Bridge Decks and Fatigue Cracks on Steel Members. In Digital Imaging 2017 (pp. 33-44), Foxwoods Resort and Casino in Mashantucket, CT.

Dorafshan S and Maguire M., (2018). Bridge Inspection: Human Performance, Unmanned Aerial Vehicles and Automation, Submitted to Journal of Civil Structural Health Monitoring.

Dorafshan S., Maguire, M., and Chang, M., (2017). Comparing Automated Image-Based Crack Detection Techniques in Spatial and Frequency Domains, 26th ASNT Research Symposium, Jacksonville, Florida. https://ndtlibrary.asnt.org/2017/AutonomousDetectionofConcreteCracksonBridgeDecksandFatigueCracksonSteelMembers.

Dorafshan, S., Maguire, M., Hoffer, N., and Coopmans, C., (2017a). Fatigue

Crack Detection Using Unmanned Aerial Systems in Under-Bridge Inspections. Final

Report. Idaho Transpiration Department. Boise. ID.

http://apps.itd.idaho.gov/apps/research/Completed/RP256.pdf

Dorafshan, S., Maguire, M., Hoffer, N., & Coopmans, C., (2017b, June).

Challenges in bridge inspection using small unmanned aerial systems: Results and

lessons learned. In Unmanned Aircraft Systems (ICUAS), 2017 International Conference

on (pp. 1722-1730). IEEE. DOI: 10.1109/ICUAS.2017.7991459.

Dorafshan, S., Maguire, M., Hoffer, N., and Coopmans, C., (2018b). Unmanned

Aerial Vehicle Augmented Bridge Inspection Feasibility Study. Final Report. Center for

Advanced Infrastructure and Technology. CIAT-UTC-NC31, Final Report. Piscatway,

NJ.

Dorafshan, S., Maguire, M., and Qi, Xi., (2016). Automatic Surface Crack

Detection in Concrete Structures Using OTSU Thresholding and Morphological

Operations, UTC Report 01-2016, Aug. 2016.

http://digitalcommons.usu.edu/cgi/viewcontent.cgi?article=2232&context=cee_facpub

FHWA (2017) "FAPG 23 CFR 650C, National Bridge Inspection

(Standards." https://www.fhwa.dot.gov/legsregs/directives/fapg/cfr0650c.htm (Aug. 15,

2017).

Gillins, M. N., Gillins, D. T., & Parrish, C. (2016). Cost-Effective Bridge Safety

Inspections Using Unmanned Aircraft Systems (UAS). In Geotechnical and Structural

Engineering Congress 2016 (pp. 1931-1940).

https://doi.org/10.1061/9780784479742.165

Hearn, G. (2007). Bridge inspection practices (Vol. 375). Transportation Research

Board. https://www.nap.edu/read/14127/chapter/6#27

Illumination (2009) "Regulations (Standards - 29 CFR). Occupational Safety and Health Administration, US Dept. of Labor. " https://web.archive.org/web/20090508051301/https://www.osha.gov/pls/oshaweb/owadis p.show_document?p_table=STANDARDS&p_id=10630 < (Aug. 15, 2017).

Jahanshahi, M. R., Kelly, J. S., Masri, S. F., & Sukhatme, G. S. (2009). A survey and evaluation of promising approaches for automatic image-based defect detection of bridge structures. Structure and Infrastructure Engineering, 5(6), 455-486.

Lattanzi, D., & Miller, G. R. (2014). 3D scene reconstruction for robotic bridge inspection. Journal of Infrastructure Systems, 21(2), 04014041. https://doi.org/10.1061/(ASCE)IS.1943-555X.0000229

Lee, S., & Kalos, N. (2014). Non-destructive testing methods in the US for bridge inspection and maintenance. KSCE Journal of Civil Engineering, 18(5), 1322-1331. https://doi.org/10.1007/s12205-014-0633-9

Lichtenstein, A. G. (1993). The silver bridge collapse recounted. Journal of performance of constructed facilities, 7(4), 249-261. https://doi.org/10.1061/(ASCE)0887-3828(1993)7:4(249)

Metni, N., & Hamel, T. (2007). A UAV for bridge inspection: Visual servoing control law with orientation limits. Automation in construction, 17(1), 3-10. https://doi.org/10.1016/j.autcon.2006.12.010

Morgenthal, G., & Hallermann, N. (2014). Quality assessment of unmanned aerial vehicle (UAV) based visual inspection of structures. Advances in Structural Engineering, 17(3), 289-302. DOI: 10.1260/1369-4332.17.3.289

Mustafah, Y. M., Azman, A. W., & Akbar, F. (2012). Indoor UAV positioning using stereo vision sensor. *Procedia Engineering*, *41*, 575-579. https://doi.org/10.1016/j.proeng.2012.07.214

NBI (2017), "National Bridge Inventory. " https://www.fhwa.dot.gov/bridge/britab.cfm (Jan. 16, 2018).

Oh, J. K., Jang, G., Oh, S., Lee, J. H., Yi, B. J., Moon, Y. S., ... & Choi, Y. (2009). Bridge inspection robot system with machine vision. Automation in Construction, 18(7), 929-941. https://doi.org/10.1016/j.autcon.2009.04.003

Omar, T., & Nehdi, M. L. (2017). Remote sensing of concrete bridge decks using unmanned aerial vehicle infrared thermography. Automation in Construction. https://doi.org/10.1016/j.autcon.2017.06.024

Otero, L. D., Gagliardo, N., Dalli, D., Huang, W. H., & Cosentino, P. (2015). Proof of Concept for Using Unmanned Aerial Vehicles for High Mast Pole and Bridge Inspections. Contract BDV28, 977-02. https://ntl.bts.gov/lib/55000/55400/55430/FDOT-BDV28-977-02-rpt.pdf

Parr, M. J., Connor, R. J., & Bowman, M. (2009). Proposed method for determining the interval for hands-on inspection of steel bridges with fracture critical members. Journal of Bridge Engineering, 15(4), 352-363. https://doi.org/10.1061/(ASCE)BE.1943-5592.0000057

Pham, H., Gull, J., Mohammadi, A., & Azizinamini, A. (2016). Managing Florida's Fracture Critical Bridges-Phases I & II. www.fdot.gov/research/Completed_Proj/Summary.../FDOT-BDV29-977-17-rpt.pdf

Sankarasrinivasan, S., Balasubramanian, E., Karthik, K., Chandrasekar, U., &

Gupta, R. (2015). Health Monitoring of Civil Structures with Integrated UAV and Image

Processing System. Procedia Computer Science, 54, 508-515.

https://doi.org/10.1016/j.procs.2015.06.058

Weather (2017a)"Weather History For Logan, UT | Weather Underground".

2017. Wunderground.Com.

https://www.wunderground.com/history/airport/KLGU/2017/1/10/DailyHistory.html?req

_city=Logan&req_state=UT&req_statename=&reqdb.zip=84321&reqdb.magic=1&reqdb

.wmo=99999 (Jan. 10, 2017)

Weather (2017b). "Weather History for Ashton, ID | Weather Underground".

https://www.wunderground.com/personal-weather-

station/dashboard?ID=KIDASHTO8#history/s20170322/e20170322/mdaily (March 22,

2017).

Weather (2017c). "Weather History for Lafayette, IN | Weather Underground".

https://www.wunderground.com/history/airport/KLAF/2017/7/5/DailyHistory.html?req_c

ity=West+Lafayette&req_state=IN&req_statename=&reqdb.zip=47907&reqdb.magic=1

&reqdb.wmo=99999 (July 5, 2017)

Weather (2017d)"Weather History for Lafayette, IN | Weather Underground".

https://www.wunderground.com/history/airport/KLAF/2017/7/5/DailyHistory.html?req_c

ity=West+Lafayette&req_state=IN&req_statename=&reqdb.zip=47907&reqdb.magic=1

&reqdb.wmo=99999 (July 6, 2017)

Wells, J., & Lovelace, B. (2017). Unmanned Aircraft System Bridge Inspection

Demonstration Project Phase II (No. MN/RC 2017-18).

http://dot.state.mn.us/research/reports/2017/201718.pdf

Woo, G. C. S., & Long, W. F. (1979). Recommended light levels for clinical procedures. Optom. Monthly, 70, 722-725. Woo, G. C. S., & Long, W. F. (1979). https://www.noao.edu/education/QLTkit/ACTIVITY_Documents/Safety/LightLevels_outdoor+indoor.pdf

Yeum, C. M., & Dyke, S. J. (2015). Vision-based automated crack detection for bridge inspection. Computer-Aided Civil and Infrastructure Engineering, 30(10), 759-770. 10.1111/mice.12141

Zink, J., & Lovelace, B. (2015). Unmanned aerial vehicle bridge inspection demonstration project (No. MN/RC 2015-40). www.dot.state.mn.us/research/TS/2015/201540.pdf

CHAPTER IV

FRACTURE CRITICAL INSPECTIONS IN STEEL BRIDGES: HUMAN

PERFORMANCE AND UNMANNED AERIAL SYSTEMS COMPARISON IN

FATIGUE CRACK DETECTION

Abstract

The chapter investigates the use of Unmanned Aerial Systems (UASs) for the inspection of bridges with fracture critical members to find fatigue cracks. The research team had four inspectors inspecting a probability of detection (POD) training structure at the at the Steel Bridge Research, Inspection, Training, and Engineering (S-BRITE) center at Purdue University to locate the fatigue crack(s) on the POD frame specimens. The results of these inspections were compared to results of 30 hands-on inspections of the same specimens in terms of hit rate, hit to call ratio, inspection time, and length of the largest crack missed (LCM). In general, the desk inspections and the field inspections had comparable hit rates and hit to call ratios; however, the type and location of the inspected specimens significantly affected the results of the UAS-assisted inspections. The results indicated the superiority of hands-on inspections to UAS-assisted inspections in terms of hit rate, hit to call ratio, and inspection time; however, the UAS-assisted inspections matched or exceeded the hands-on results in certain scenarios (out of plane specimens). In addition, the desk inspections resulted in detecting cracks 8% smaller than the field inspections and 11% smaller than the hands-on inspections. Regardless, the results can be considered satisfactory since none of the inspectors had previous UAS-assisted inspection training or experience.

Introduction

It was not until the deadly 1967 bridge collapse in West Virginia (Silver Bridge Collapse) that fatigue cracking was introduced to bridge engineers due to the evaluation and implementation of systematic bridge inspection programs (Lichtenstein, 1993). It took the bridge engineering community in the U.S. a few years to incorporate the new requirements into practice, addressing the need to build fatigue resistant bridges in 1980 in terms of materials, design, and construction (Connor, et al., 2005). However, looking at the national bridge inventory (NBI), almost 70% of the steel bridges, more than 120,000 bridges, were built before 1980 (FHWA, 2013), which makes them prone to fatigue cracking. Fatigue crack(s) can cause structural collapse if the bridge does not have enough redundancy, e.g. the Silver Bridge. According to AASHTO LRFD bridge design and specifications, a "component in tension whose failure is expected to result in the collapse of the bridge" is called a fracture critical member (FCM). It is estimated that almost 10% of the in service U.S. bridges are categorized as FCM (Parr, et al., 2009). In the national bridge inspection standards, Federal regulations mandate special inspections, i.e. FCM inspections, for FCM bridges with a maximum interval between inspections of 24-months (FHWA, 2017). The FCM inspections include an inspector within arms-length (hands-on) of the locations susceptible to fatigue cracks, which in addition to visual inspection allows them to perform non-destructive evaluation (NDE) techniques if necessary (Hearn, 2007). According to a survey, the FCM inspections were two to five times more expensive than the non-FCM inspections (Connor, et al., 2005). In addition to the cost associated with the NDE techniques, FCM inspections require specialized equipment, trained operators, under-bridge inspection trucks, traffic control, and lane

closure, which increases cost (Dorafshan et al., 2017a and b).

California, Michigan, Minnesota, and Florida have used Unmanned Aerial Systems (UASs) for bridge inspections in the past (Dorafshan & Maguire, 2018). Due to their non-contact nature, UAS-assisted inspections can result in safer and less time-consuming inspections without the need for traffic control. In addition, UASs can record the inspection data, e.g. visual images and videos, which can be used for further manned or unmanned post processing. Unmanned processing can include applying image processing techniques on the inspection data to detect concrete cracks (Dorafshan et al., 2017c) or fatigue cracks (Dorafshan and Maguire, 2017). Defect detection can be done in a fully automated manner after the flight by applying deep convolutional neural networks on UAS images (Dorafshan, et al., 2018b), which are superior to edge detectors (Dorafshan et al., 2018c). However, the first FCM inspection performed using UASs was in Idaho (Dorafshan et al., 2017a) and had limited success in the field. Researchers conducted a study to determine the minimum requirements to achieve desirable results in UAS-assisted FCM inspections in terms of camera, UAS platform, and distance to the region of interest (Dorafshan, et al., 2018a). UAS inspection was successful in mock inspections performed in controlled and un-controlled GPS-denied environments. Dorafshan et al. (2018a) also conducted a series of UAS inspections on a probability of detection (POD) training structure at the Steel Bridge Research, Inspection, Training, and Engineering (S-BRITE) center at Purdue University to locate the fatigue crack(s) on the POD frame specimens in two approaches. The first approach was a realtime inspection where an inspector was asked to identify the fatigue crack(s) for each specimen on the inspection forms while a pilot was flying a commercial UAS. The inspector used a 25-cm

First Person View (FPV) monitor that was connected to the UAS wirelessly during the inspection to detect the crack(s). The FPV monitor allowed the inspector to change the point of view, exposure, and zoom of the UAS camera (DJI Mavic). The inspector detected between 64% and 89% of the cracks on the POD frame for different specimens, which matched or exceeded the average results of 30 hands-on inspections; however, the average number of calls required to detect a crack, hit-to-call ratio, in realtime UAS inspection was almost twice that of the average hands-on inspection. The inspector also reviewed the UAS inspection data after the inspection, which did not improve the hit rate; however, in the post-flight inspection, the average hit-to-call ratio was improved by 12% compared to the realtime inspection.

The main focus of the study done by Dorafshan et al. (2018a) was to evaluate UAS performance during an FCM inspection that did not consider the effects of different inspections scenarios. This study aims to address the followings:

1. Establish the effectiveness of unmanned aerial system (UAS) inspection for identifying cracks in steel bridges;

2. Evaluate the practicality of performing bridge inspections from the office using video captured with a UAS;

3. Establish methods for improving UAS inspection of steel bridges;

4. Identify the strengths and weaknesses of UAS inspection of steel bridges.

To compare the inspectors' performance to each other, the research team asked all the inspectors to fill out a questionnaire designed by the research team. To determine the work load associated with both types of inspections, inspectors were asked to fill out the official national aeronautics and space administration task load index (NASA TLX) in the

middle of the inspection (Hart & Staveland, 1988). The inspectors were asked to complete a standard vision test, Snellen eye chart (Ferris III, et al., 1982), contrast sensitivity test, Pelli Robson Chart (Pelli & Robson, 1988), near visual acuity test, and Jaeger chart (Khurana, et al., 2014) by viewing videos/images of the charts recorded by the UAS.

Experimental Program

 This section describes the experimental program carried out for this study, which includes the UAS platform, a brief introduction to the inspected specimens mounted on the POD frame at the S-BRITE center, a routine field inspection for the realtime fatigue crack detection, a routine desk inspection for the post-flight fatigue crack detection, an inspector survey, a NASA TLX, and vison tests.

UAS Platform

 A commercial DJI Mavic Pro was used to perform the field inspections and record inspection data for the desk inspections. Some of the technical specifications of the platform and its onboard camera are shown in Table 4-1. This platform was selected since it provided the best results in the previous FCM inspections (Dorafshan, et al., 2018a).

 Specimens

 The inspected POD frame is shown Fig. 4-1. The specimens mounted on the POD frame were produced at the Bowen laboratory at Purdue University. The POD structure is intended to mimic a 120 m, two-span highway bridge with three lines of girders elevated approximately 8 m above the ground. Each girder spans approximately 12 m with 3 m of

transverse spacing. The locations and sizes of the fatigue cracks on these specimens were only known to the S-BRITE center staff (not to the inspectors or the pilot). As seen in the figure, three types of specimens were mounted on the POD frame: out of plane girder (OOP), riveted cover plates (RCP), and welded cover plates (WCP) specimens.

Table 4-1 DJI Mavic Pro specifications

Platform			
Weight (g)	Type	Flight Time (min)	Diagonal Size, Propellers Excluded (mm)
740	Quadcopter	27	335
Camera			
Sensor Type	Sensor Size (mm)	Video Frame Rate	Camera Adjustment through FPV monitor
CMOS	7.66	30	Zoom, Exposure, and Gimbal

Fig. 4-1 Three types of specimens mounted on the POD frame located at Purdue University

Field Inspections

Four bridge inspectors performed the field inspections of the POD frame between December 18th and December 21st, 2018. A pilot from Utah State University and a proctor from Purdue University accompanied the inspectors on each inspection day. Each field inspection started with a 30-minute inspection tutorial that taught the inspector how to use a 12-cm FPV monitor for recording and camera adjustments. The proctor provided a binder of blank inspector sheets for each specimen. For each specimen, the inspector marked the crack(s) on the corresponding specimen sheet (or indicated that the specimen did not have any cracks) while the pilot flew the UAS near the inspected specimen. Fig. 4-2 and Fig. 4-3 show the typical setup for the field inspections. The wind speeds during the filed inspection days were obtained from KLAF weather station at the Purdue University airport (Weatherunderground, 2017) and are presented in Table 4-2. This table also reports a start time (including the tutorial) and an end time for each day of inspections. As seen in Table 4-2, the inspection time varied each day due to either the loss of sunlight or the inspector's unavailability in the afternoons. In addition to the filled inspection forms, the inspectors were asked to complete the questionnaire, NASA TLX, and vision tests forms, as well.

Desk Inspections

For the desk inspection, videos of 54 specimens of the POD frame were selected including 32 OOP, 14 WCP, and 6 RCP specimens. The research team reviewed the inspection videos from each day to find the corresponding video for each selected specimen (Table 4-3).

Fig. 4-2 The setup for the field inspections
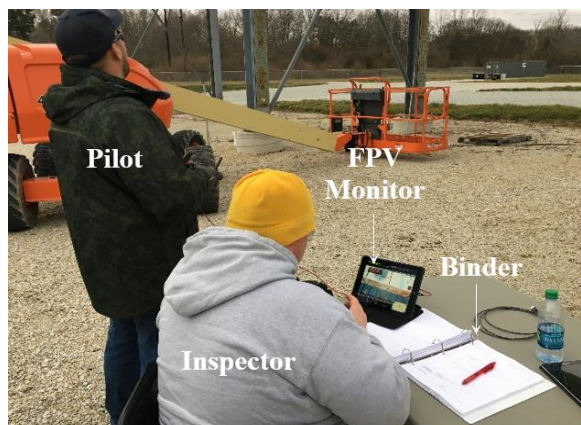
Fig. 4-3 FPV monitor and blank binders

Table 4-2 Field inspections

Day	Start	End	Wind Speed (kmh)		
			Min	Mean	Max
December 18th	8:45	16:27	12	17	24
December 19th	8:05	17:11	11	15	20
December 20st	10:10	16:18	9	14	20
December 21st	8:15	15:47	7	13	20

Then the videos of each inspection day were shared with 33 bridge inspectors working for DOTs or private contractors (19 inspectors returned the results as seen in Table 4-3). The inspectors were asked to review the videos and fill out the inspection forms, along with the questionnaire, NASA TLX, and vison tests (similar to the field inspection). The desk inspection time limit was 480 min (eight hours) to finish inspecting all the specimens, and the choice of review hardware, e.g. monitor, software, and media player, was left to the inspectors. The research team suggested using VLC media player because it is free to use and allows zooming and other adjustments.

Table 4-3 The videos for desk inspection

Day	No of Inspectors	Specimen	No of Specimens	Video Duration (min)
December 18th	4	OOP	36	46
		WCP	16	14
		RCP	0	15
		Total	**52**	**75**
December 19th	6	OOP	54	60
		WCP	16	26
		RCP	8	17
		Total	**78**	**103**
December 20st	4	OOP	54	70
		WCP	16	44
		RCP	15	11
		Total	**85**	**125**
December 21st	4	OOP	36	141
		WCP	16	23
		RCP	0	18
		Total	**52**	**182**

NASA TLX

NASA TLX was introduced in 1988 to quantify the workload of one or more

individuals when performing or immediately after performing cognitive and manual

control tasks, complex laboratory and supervisory control tasks, and aircraft simulations

(Hart & Staveland, 1988). Despite being designed for aviation and flight simulations, the

NASA TLX has been used to determine and compare the workload of other tasks as well

(Hart, 2006) in terms of the following::

- Mental Demand (low/high): How much mental and perceptual activity
  was required (e.g., thinking, deciding, calculating, remembering, looking,
  searching, etc.)? Was the task easy or demanding, simple or complex,
  forgiving or exacting?

- Physical Demand (low/high): How much physical activity was required
  (e.g., pushing, pulling, turning, controlling, activating, etc.)? Was the task
  easy or demanding, slow or brisk, slack or strenuous, restful or laborious?

- Temporal Demand (low/high): How much time pressure did you feel due
  to the rate or pace at which the tasks or task elements occurred? Was the
  pace slow and leisurely or rapid and frantic?

- Performance (good/poor): How successful do you think you were in
  accomplishing the goals of the task set by the experimenter (or yourself)?
  How satisfied were you with your performance in accomplishing these
  goals?

- Effort (low/high): How hard did you have to work (mentally and
  physically) to accomplish your level of performance?

- Frustration Level (low/high): How insecure, discouraged, irritated,

stressed, and annoyed versus secure, gratified, content, relaxed, and

complacent did you feel during the task?

Raw ratings and their associated weight for each factor were calculated based on

the inspectors' answers to six individual ratings and 15 pairwise comparisons questions.

The pilot was also asked to complete a NASA TLX form. The final score, which is the

weighted average of the raw ratings, shows the workload: 0 for no workload, 100 for high

workload.

Vision Tests

The charts associated with the Snellen eye test (Ferris III, et al., 1982), Pelli

Robson test (Pelli & Robson, 1988), and Jaeger test (Khurana, et al., 2014) were installed

on the POD frame. The inspectors were asked to complete the form for each test based on

the realtime streaming (for field inspections) or the recording of the chart (for desk

inspections). Inspectors were allowed to use any available hardware and software to

improve the results. Fig. 4-4shows images taken by the DJI Mavic of the vision test

charts used in this study along with their dimensions. As seen in Fig. 4-4a, there are 11

lines with letters in the Snellen chart. The quantity of letters increases and the size

decreases when going from the top to the bottom. The number of the last line from the

top that the inspectors identified correctly was considered the score for the Snellen test.

Fig. 4-4b shows the Pelli Robson chart were the contrast decreased for each group of

three letters. The score depended on the line where the inspector missed more than one

letter in a group of letters (0-2.25). In the Jaeger test (Fig. 4-4c), score is based on the

smallest readable paragraph in the visual images and in the vision video (1 for the

smallest fonts to 11 for the largest fonts).

| (a) | (b) | (c) |
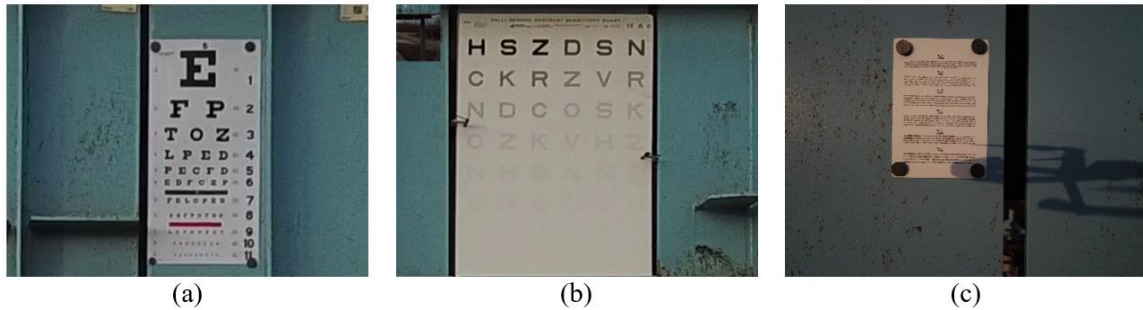
Fig. 4-4 Charts used for the vision tests, (a) Snellen 558.8 mm × 279.4 mm, (b) Pelli Robson 825.5 mm × 596.9 mm, (c) Jaeger 177.8 mm × 120.65 mm

Results

The inspection forms including the specimens, vision tests, NASA TLX, and questionnaires were gathered by the research team for both field and desk inspections. The locations of the fatigue cracks were known to the Proctor at Purdue University. For each specimen, the inspector may have one, several, or zero calls for cracks. If the call is correct, it is a "hit"; otherwise, it is a false positive. The ratio of number of hits to the total number of cracks is called the hit ratio. In addition, the hit to call ratio is defined as the required number of calls to make one hit, which is obtained by dividing the number of hits by the sum of the hits and false positives.

Field Inspection Results

The demographic of the field inspectors are shown in Table 4-4, and Table 4-5 shows the summary of the field inspection results in terms of inspection time (T), hit rate (HR), hit to call ratio (HCR), length of largest crack miss (LCM), and video length for

different types of specimens. The results of the vision and NASA TLX tests are shown in

Table 4-6. The inspection time in the table refers to the length of the UAS flight in

minutes. As seen in Table 4-5, the inspection time was 38-64% of the total field time,

which was mostly due to charging time of the equipment. The metrics of the inspection,

hit rate, hit to call ratio, and LCM were not affected by the inspector's demography.

However, it seems that the younger inspectors had the best overall hit rate of 60% on Dec

21st and the highest hit to call ratio of 46% on Dec 20th. Table 4-5 also shows that the

inspectors detected 58% to 67% of the cracks on the OOP specimens, whereas two

inspectors did not detect any of the cracks on the WCP specimens. Hit rate and hit to call

ratio on Dec. 19th were 67% and 86, respectively and on Dec. 20th were 56% and 45%,

respectively. In addition, the most accurate crack detection happened when the inspector

performed better in the vision tests on December 21st (Table 4-6). The NASA TLX

results showed that frustration was the governing factor for the inspectors while mental

demand had the highest score for the pilot.

In the inspection surveys, two inspectors indicated that the UAS-assisted

inspection required similar effort compared to their typical inspection. The warmup

training helped the inspectors as it somewhat to fully prepared them for the inspection;

however, all inspectors reported that the UAS-assisted inspection provided worse quality

than the hands-on inspection.

Desk Inspection

The demographic information of the desk inspectors is shown Table 4-7. For each

inspector, a random ID was generated that started with the date of the inspection day.

Two of these inspectors also participated in the field inspections, 18BN-82 and 21BN-85.

Table 4-7 includes the inspectors' employers, year of experience, type of engineering

license, such as Professional Engineer (PE) or Structural Engineer (SE), their obtained

educational degree, age, and number of inspections in the past 12 months including

routine, routine for steel bridges, and hands-on.

Table 4-4 Demographic of the field inspectors

Day	Years of Experience	Age	No of Routine Insp. (last year)	No of Routine in Steel Insp. (last year)	No of Hands-on Insp. (last year)
18th	16.5	47	800	280	25
19th	16	50	340	51	15
20st	7	31	35	17	10
21st	5	35	25	18	8

Table 4-5 Results of the field inspection

Day	Inspection Time (min)	Field T (min)	Type	HR (%)	HCR (%)	LCM (mm)	Video Length (min)
18th	125	328	OOP	67	18	72	46
			WCP	0	0	108	14
			RCP	NA	NA	NA	15
			All	**50**	**13**	**108**	**75**
19th	199	375	OOP	67	52	133	60
			WCP	0	0	108	26
			RCP	67	86	38	17
			All	**58**	**46**	**133**	**103**
20th	145	224	OOP	50	24	125	44
			WCP	33	25	108	11
			RCP	56	45	32	15
			All	**48**	**27**	**125**	**70**
21st	201	315	OOP	60	15	74	141
			WCP	60	16	108	23
			RCP	NA	NA	NA	17
			All	**60**	**15**	**108**	**181**

Table 4-6 Vision tests and NASA TLX results for the field inspections

Test		18th	19th	20th	21st	Pilot (Avg.)
Snellen		NA	3	5	5	NA
Pelli Robson		NA	1.65	1.5	1.65	NA
Jaeger		NA	NA	11	9	NA
TLX	Score	69	82	47	73	67
	Factor	Frustration	Frustration	Frustration	Mental Demand	Mental Demand

Table 4-8 presents the results of the Snellen (SN), Pelli Robson (PR), and Jaeger

(Ja) vision tests and the NASA TLX for the desk inspections. The SN results had the

highest coefficient of variation (COV) at 35% while the PR results had the lowest COV

at 11% among different inspectors. The vision tests between each set of inspection videos

produced comparable results, as seen in Fig. 4-5. As for the TLX, the average score for

each set of inspection videos varied from 58% and 64%, with the most reported

governing factor being mental demand (12 out of 19).

Table 4-7 Demographic of the desk inspectors

ID	Agency	Experience	Licensure	Education Level	Age	No. of Routine Inspections	No. of Routine Inspection (Steel)	No. of Hands-on Inspection
18BN-82	Private	18	PE (Civil)	Bachelor	48	1,000	200	25
18RW-82	Private	NG	NG	NG	NG	NG	NG	NG
18SD-87	Private	5	PE (Civil)	Bachelor	29	100	NG	50
18WJ-84	DOT	5	None	High School	35	132	NG	12
19AS-85	DOT	14	None	Associate	39	15	7	8
19HG-80	DOT	10	PE (Civil)	Master	65	30	7	5
19KU-89	DOT	8	None	Associate	42	110	16	17
19RT-88	Private	12	PE (Other)	Bachelor	51	300	45	15
19SG-83	Private	20	PE, SE (Civil)	Master	57	200	NG	10

19YD-89	Private	34	PE (Civil)	Master	56	49	31	57
20OD-89	Private	20	PE (Civil)	Master	46	60	48	80
20RJ-83	Private	21	PE, SE (Civil)	Bachelor	44	2	0	0
20HQ-83	DOT	1	None	High School	43	130	39	6
20YF-86	Private	8	PE, SE (Civil)	Master	30	35	20	20
21DF-85	DOT	8	PE (Civil)	Bachelor	39	50	25	25
21JG-81	DOT	11	None	Trade	52	500	250	22
21EH-80	DOT	7	SE	Master	65	180	54	10
21BN-85	DOT	6	PE (Civil)	Master	36	25	18	8
21ET-84	Private	4	PE (Civil)	Master	29	200	70	9

Table 4-8 Vision tests and NASA TLX results for the desk inspectors

ID	SN	PR	Ja	TLX	
				Score	Factor
18BN-82	7	1.05	7	72	Frustration
18RW-82	3	1.5	9	82	Frustration
18SD-87	5	1.5	9	42	Mental Demand
18WJ-84	10	1.5	9	58	Mental Demand
19AS-85	5	1.65	7	64	Effort
19HG-80	11	1.65	7	65	Mental Demand
19KU-89	9	1.65	7	63	Mental Demand
19RT-88	5	NG	8	69	Mental Demand
19SG-83	5	1.65	9	68	Mental Demand
19YD-89	5	1.35	11	47	Mental Demand
20OD-89	6	1.65	7	58	Mental Demand
20RJ-83	5	1.8	7	59	Frustration
20HQ-83	7	1.65	7	67	Mental Demand
20YF-86	5	1.65	7	NG	NG
21DF-85	6	1.35	11	54	Mental Demand
21JG-81	5	1.65	7	66	Mental Demand
21EH-80	8	1.5	9	27	Frustration
21BN-85	11	1.65	11	78	Frustration
21ET-84	8	1.35	7	64	Mental Demand
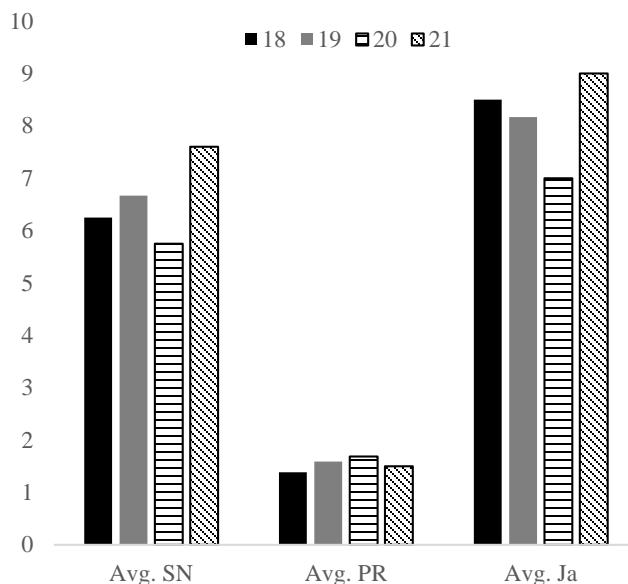
Fig. 4-5 Average of vision tests scores for each set of inspection videos

Dec. 18the Videos

Table 4-7 shows the metrics of the desk inspections for the videos taken on the Dec. 18th. The inspectors had the highest average HR of 56% and HCR of 65%, for the RCP specimens. The average HCR dropped to 19% in the OOP specimens, while the average HR for the OOP specimens was comparable to the RCP specimens (50%). The inspectors scored poorly for the WCP specimens with the average HR of 5% and HCR of 2%. The UAS used for the field inspections had a tilt-angle of 30-degrees, which limited both the pilot and the inspector's ability to capture proper inspection videos of WCP specimens. The WPC specimens governed the LCM values in three out of the four desk inspections, with LCM equal to 108 mm; however, the greatest LCM value was 132 mm, which was for OOP specimens. The greatest T values were recorded while inspecting the OOP specimens; however, this was due to the fact that there were more OOP specimens

(32) inspected than other specimens (20). To have a better perception of the inspection time, time ratio (TR) was introduced. TR was obtained by dividing T by the video length, which was previously reported in Table 4-5. The TR values were between 2 and 5 for WPC specimens, which were the highest values among specimens in three desk inspections out of the four.

Table 4-9 Results of the desk inspection on Dec. 18th videos

ID	Type	HR (%)	HCR (%)	LCM (mm)	T (min)	TR
18BN-82	OOP	40	13	92	126	2.7
	WCP	0	0	108	67	*4.8*
	RCP	78	88	38	25	1.7
	All	**45**	**19**	**108**	**218**	**2.9**
18RW-82	OOP	53	11	72	88	1.9
	WCP	0	0	108	29	*2.1*
	RCP	67	67	21	23	1.5
	All	**48**	**15**	**108**	**140**	**1.9**
18SD-87	OOP	33	38	132	82	1.8
	WCP	0	0	108	28	*2.0*
	RCP	11	50	38	17	1.1
	All	**21**	**40**	**132**	**127**	**1.7**
18WJ-84	OOP	73	13	72	290	6.3
	WCP	20	8	108	70	*5.0*
	RCP	67	55	38	45	3.0
	All	**62**	**16**	**108**	**405**	**5.4**

Dec. 19th Videos

Table 4-10 shows the metrics of the desk inspections for the videos taken on the 19th. The inspectors had the highest average HR of 69% and HCR of 74%, for the RCP specimens. The average HCR dropped to 24% in the OOP specimens while the average HR for the OOP specimens was close to that of the RCP specimens (68%). The

inspectors scored poorly for the WCP specimens, with the average HR of 13% and HCR of 3.5%. The WPC specimens governed the LCM values in five out of the six desk inspections with 108 mm and 106 mm; however, the greatest LCM value was 132 mm, which was for OOP specimens. The highest TR values occurred during the desk inspections of the OOP specimens (4.7).

Dec. 20th Videos

Table 4-10 shows the metrics of the desk inspections for the videos taken on the 20th. The inspectors had the highest average HR of 78% and HCR of 75%, for the RCP specimens. The average HR and HCR dropped to 56% and 19%, respectively, in the OOP specimens. The inspectors scored relatively good for the WCP specimens with an average HR of 45% and HCR of 15%. The WPC specimens governed the LCM values for all desk inspections, with the largest value equal to 108 mm. The highest TR values were between 2.7 and 5.5 for WPC specimens and were the governing case in all four desk inspections.

Dec. 21st Videos

Table 4-12 shows the metrics of the desk inspections for the videos taken on the 21st. The inspectors had the highest average, HR of 79% and HCR of 82%, for the RCP specimens. The average HR and HCR dropped to 59% and 17%, respectively, in the OOP specimens. The inspectors scored relatively well for the WCP specimens with the average HR equal to 36% and HCR equal to 22%. The WPC specimens governed the LCM values for all desk inspections, with the largest value of 108 mm. No type of specimen controlled in terms of greatest TR. However, the maximum TR value among all

specimens was 2.6, which was for the WPC specimens.

Table 4-10 Results of the desk inspection on Dec. 19th videos

ID	Type	HR (%)	HCR (%)	LCM (mm)	T (min)	TR
19AS-85	OOP	80	36	74	279	4.7
	WCP	20	11	108	83	3.2
	RCP	78	88	21	65	3.8
	All	**69**	**40**	**108**	**427**	**4.1**
19HG-80	OOP	67	15	72	158	2.6
	WCP	20	4	106	59	2.3
	RCP	78	58	19	32	1.9
	All	**62**	**17**	**106**	**249**	**2.4**
19KU-89	OOP	73	10	132	242	4.0
	WCP	40	6	108	66	2.5
	RCP	89	42	19	39	2.3
	All	**72**	**13**	**132**	**347**	**3.4**
19RT-88	OOP	53	44	87	95	1.6
	WCP	0	0	108	34	1.3
	RCP	11	100	38	26	1.5
	All	**31**	**45**	**108**	**155**	**1.5**
19SG-83	OOP	60	14	72	161	2.7
	WCP	0	0	108	56	2.2
	RCP	67	75	21	32	1.9
	All	**52**	**19**	**108**	**249**	**2.4**
19YD-89	OOP	73	27	72	111	1.9
	WCP	0	0	108	39	1.5
	RCP	89	80	12.7	29	1.7
	All	**66**	**35**	**108**	**179**	**1.7**

Discussion

In order to investigate all the results together, the effect of several parameters on the inspection metrics, i.e. HR, HCR, LCM, and TR, are discussed in this section.

The Effect of the Inspection Videos

The inspection metrics were different for each inspection day. Comparing the HR values for all specimens in Table 4-9 through Table 4-12 showed that the inspectors with

videos from the 20th and 21st detected a greater number of cracks (average HR of 63%)

than the inspectors reviewing videos from the first two inspection days (average HR of

51%). In addition, the average LCM for the last two days was 104 mm compared to 113

mm in the first two days. This can be justified by the environmental factors. As seen in

Table 4-2, at the first two days of the inspections, the wind speed was higher than that of

the last two days. Higher wind speed compromises UAS stability heavily in GPS-denied

environments which led to lower quality recordings.

Table 4-11 Results of the desk inspection on Dec. 20th videos

ID	Type	HR (%)	HCR (%)	LCM (mm)	T (min)	TR
20OD-89	OOP	67	23	72	80	1.8
	WCP	20	20	108	30	2.7
	RCP	67	75	32	21	1.4
	All	**59**	**30**	**108**	**131**	**1.9**
20RJ-83	OOP	73	29	74	105	2.4
	WCP	60	11	108	38	3.5
	RCP	100	100	0	27	1.8
	All	**79**	**31**	**108**	**170**	**2.4**
20HQ-83	OOP	47	17	87	216	4.9
	WCP	40	22	108	61	5.5
	RCP	56	100	32	35	2.3
	All	**48**	**25**	**108**	**312**	**4.5**
20YF-86	OOP	73	8	27	117	2.7
	WCP	60	7	108	57	5.2
	RCP	89	24	25	84	5.6
	All	**76**	**10**	**108**	**258**	**3.7**

Table 4-12 Results of the desk inspection on Dec. 21ˢᵗ videos

ID	Type	HR (%)	HCR (%)	LCM (mm)	T (min)	TR
21DF-85	OOP	53	11	74	207	1.5
	WCP	0	0	108	32	1.4
	RCP	78	100	21	22	1.3
	All	**52**	**15**	**108**	**261**	**1.4**
21JG-81	OOP	53	17	87	184	1.3
	WCP	0	0	108	26	1.1
	RCP	56	100	25	31	1.8
	All	**45**	**25**	**108**	**241**	**1.3**
21EH-80	OOP	67	6	72	189	1.3
	WCP	40	4	90	60	2.6
	RCP	89	32	13	35	2.1
	All	**69**	**9**	**90**	**284**	**1.6**
21BN-85	OOP	40	29	133	190	1.3
	WCP	60	50	108	34	1.5
	RCP	78	88	38	43	2.5
	All	**55**	**43**	**108**	**267**	**1.5**
21ET-84	OOP	80	24	22	144	1.0
	WCP	80	57	89	58	2.5
	RCP	78	88	21	31	1.8
	All	**79**	**35**	**89**	**233**	**1.3**

The Effect of Type of Specimens

The desk inspection results were affected significantly by the type of specimens in all inspection videos, as seen in Fig. 4-6. The desk inspection of the RCP specimens resulted in the lowest HR and HCR. In addition, the inspectors spent more time on the RCP specimens considering the video length (higher TR). On the other hand, the inspectors were the most successful with the RCP specimens. The HCR values were less than the HR values for OOP and HCR, whereas HCR exceeded or matched the HR for RCP specimens. The greatest value of LCM was obtained when the inspectors reviewed

the RCP specimens (LCM equal to 108 mm) except for the 18SD-87 and 19KU-89

inspectors who missed a 132 mm crack on the OOP specimens.
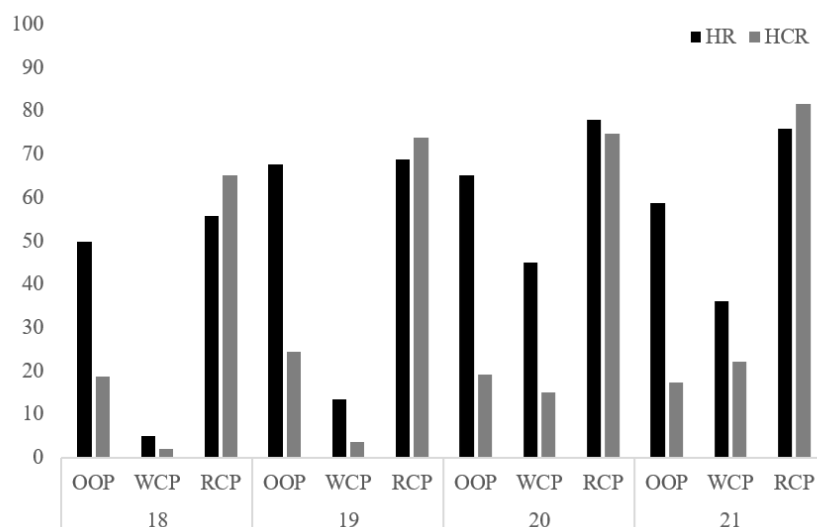
Fig. 4-6 A summary of the average HR and HCR for each set of inspection videos

The Effect of the Inspectors

The average HR for the desk inspections was 57%. Ten inspectors exceeded the

average, with the highest HR being 79% among all specimens. The HCR values were

consistently lower than the HR values with an average of 25%. Eight inspectors scored

higher HCR than the average HCR, with the greatest being 45%. Fig. 4-7 indicates the

inspector's HR and HCR scores, with lines representing the average values. The average

TLX scores for all inspectors was 61%, whereas the inspectors with higher than average

HR scores had lower TLX scores (average of 56%). A similar trend can be seen for the

inspectors with higher than average HCR scores; they had TLX scores with a mean of

59%. These trends can be seen in Fig. 4-8a as the higher TLX scores resulted in lower

HR and HCR. The average of SN and PR vision tests for the ten inspectors was higher

than average for all inspectors. In addition, the eight inspectors with HCR scores greater

than the average scored better in the Ja tests. However, as seen in Fig. 4-8b through Fig.

4-8d, there was not a consistency between the vision test results and the metrics. The ten

inspectors with higher HR and the eight with higher HCR than the average had more

years of experience, 13.1 and 14.5, respectively, than the average years of experience of

the inspectors,11.8, which is reflected in Fig. 4-8e, especially for the HR values.

However, the above-average inspectors performed less routine inspections and more

hands-on inspections than the rest in the 12-month period before the desk inspection. The

number of hands-on inspections is not consistent with the HR and HCR values, as seen in

Fig. 4-8f. The results also indicate that the inspectors working as private contractors had

higher HCR and lower TR than the ones employed by DOTs; however, the DOT

inspectors were slightly better in terms of HR (Table 4-13).
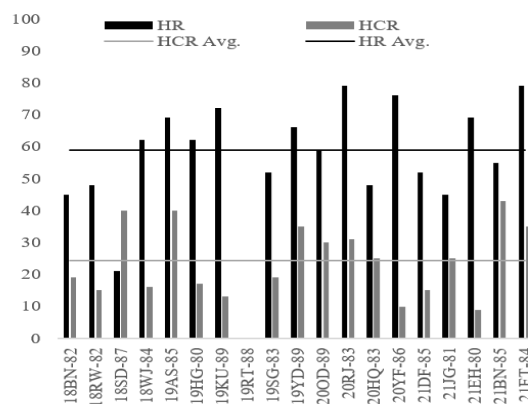
Fig. 4-7 Average HR and HCR for each desk inspector on all specimens
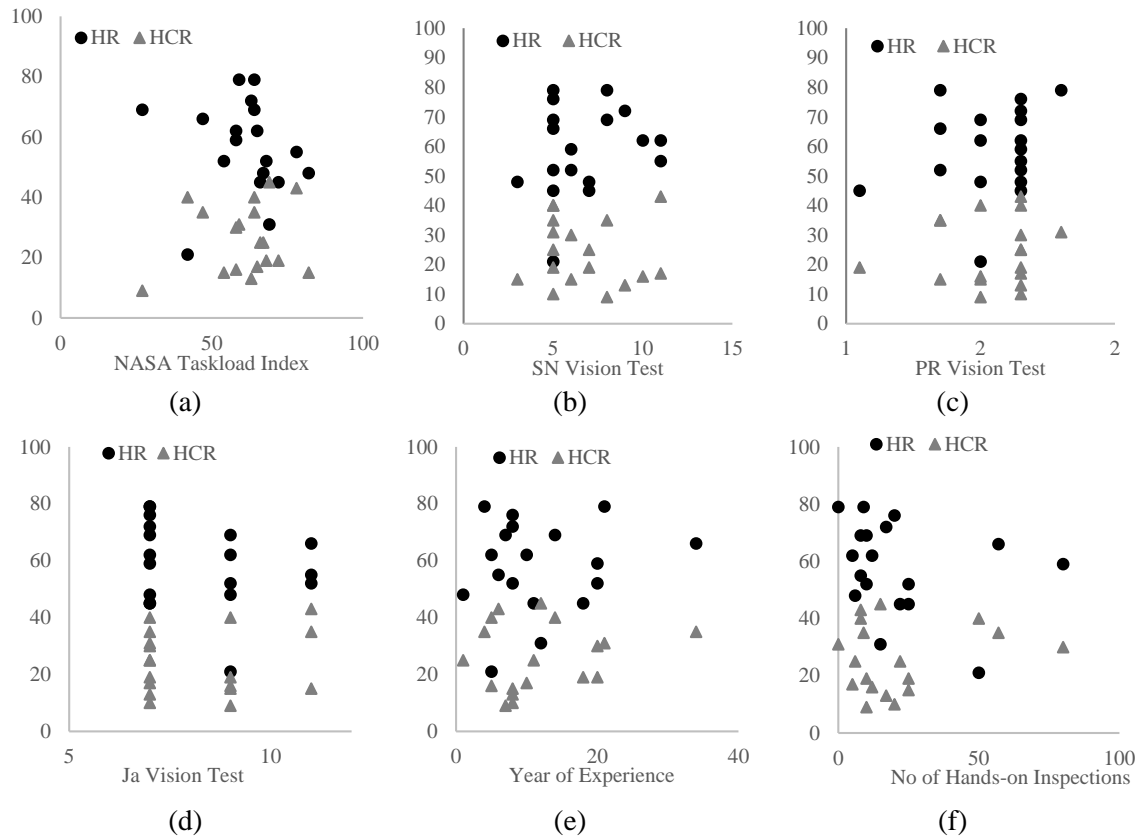
Fig. 4-8 HR and HCR versus (a) NASA TLX scores, (b) SN vision test, (c) PR vision test, (d) Ja Vision test, (e) year of experience, (f) number of hands-on inspections

Table 4-13 The effect of the agency on the inspection metrics

Agency	HR (Avg.)	HCR (Avg.)	LCM (Avg.)	TR (Avg.)
DOT	58%	22%	108	2.85
Private	56%	28%	108	2.14

The Effect of Review Software and Hardware

Due to the nature of the desk inspections, it is important to investigate the effects

of software and hardware used in the inspections on the results. For software, i.e. the

media player used to review the inspection videos, the research team suggested VLC

media player. This player is free and allows the user to adjust zoom and brightness while

the video is playing. Fourteen inspectors used the VLC media player, two used Windows Media Player (WMP), and three did not specify. Nine of the ten inspectors with higher than average HR and seven out of eight inspectors with higher than average HCR used the VLC media player. The inspectors were asked to identify whether they used a certain feature of the media player, and if they did, score that feature on the scale of one to five according to its usefulness. Table 4-14 shows the features, how many inspectors used them during the desk inspections (frequency), and the average usefulness score. Pause and rewind aside, zooming had the highest usefulness score and was used by all 14 inspectors that used VLC media player. In addition, the ability to change the brightness of the video was used by all the VLC users and scored 3.93, making, on average, this feature also very important. The zoom and brightness adjustment improved the quality of the desk inspections by allowing the inspectors to see more details in the videos (Fig. 4-9). Nine of the ten inspectors with higher HR than average and six out of eight inspectors with higher HCR than average used VLC media player and its features during the desk inspections.

In terms of hardware, the inspectors were asked to provide the specifications of their monitors. The most successful inspectors used a 508-mm monitor or larger. The videos recorded by the DJI Mavic had resolutions of 3840×2160, while the highest resolution in the monitors used by the inspectors was only 1920×1080. Using a monitor with the same resolution as the videos could improve the results of the desk inspections.

Table 4-14 Feature scores for the media player

Feature	Frequency	Score (Avg.)
Pause	17	4.76
Rewind	16	4.75
Fast forward	15	3.67
Decrease the speed of the video	10	3.3
Increase the speed of the video	10	2.1
Zoom	14	4.36
Brightness adjustment	14	3.93
Still photo from the video	8	3.6
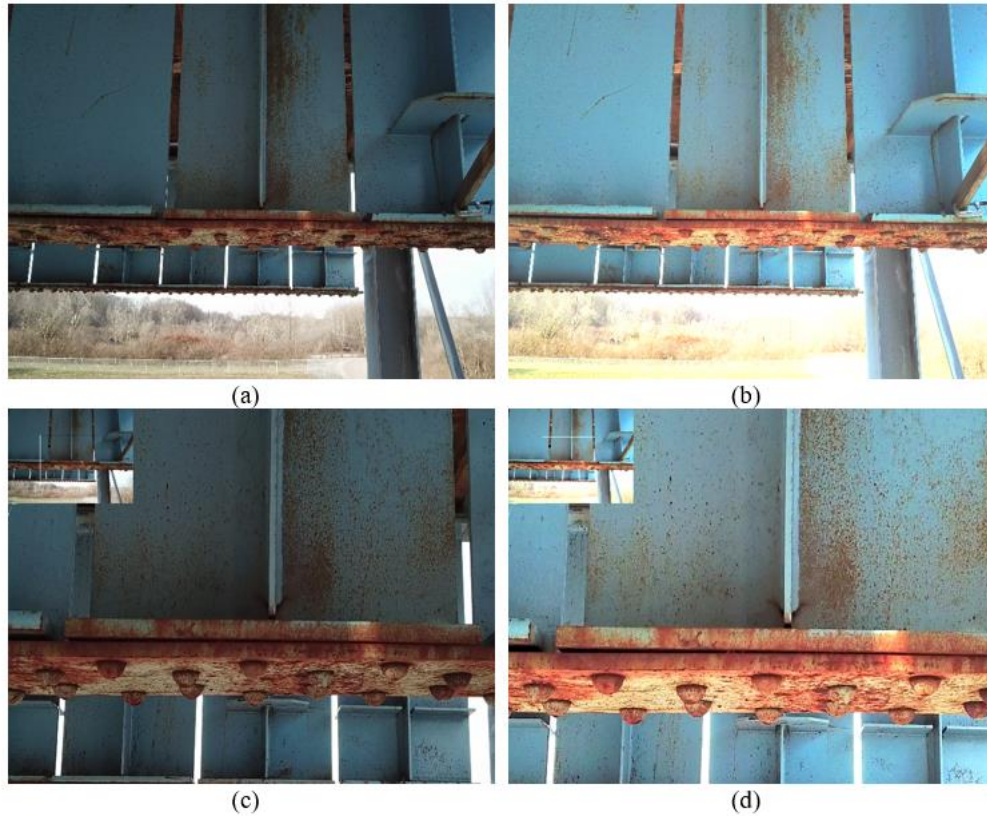
Fig. 4-9 Still image from a video of an OOP specimen, (a) original, (b) adjusted brightness, (c) zoomed on a susceptible region, (d) zoomed on a susceptible region with brightness adjustment

Inspectors Assessment

The inspectors were asked the following four questions:

- How did your effort-level during the desk inspection compare to your effort-level during a typical bridge inspection? (less, similar, more)

- How did your focus-level during the desk inspection compare to your focus level during a typical bridge inspection? (less, similar, more)

- The desk inspection videos provided (worse, similar, better) quality as compared to a UAS inspection performed live in the field.

- The desk inspections provided (worse, similar, better) quality as compared to an arm's length inspection.

Fig. 4-10 presents the answers given by the inspectors. In terms of the effort-level, seven inspectors indicated more compared to a typical inspection. However, ten inspectors claimed the desk inspections required similar or less effort to perform than typical bridge inspections, which suggests the possible acceptance of the UAS technology along with the desk inspection setups in the bridge community. In addition, 15 inspectors required similar or less focus level than during typical bridge inspections, which suggests that desk inspections could improve bridge inspection practice. Almost 63% of the inspectors reported that the desk inspection videos provided similar or better quality than the field inspections. Therefore, it is practical for the inspectors to capture the inspection videos and review them later rather than detect the cracks in the field. Finally, a majority of the inspectors preferred hands-on inspection over desk inspection. This could be due to the remote nature of the UAS inspections; however, the quality of the desk inspections can be improved by using higher resolution cameras and monitors and more stable UAS platforms as was suggested in previous studies (Dorafshan & Maguire, 2018; Dorafshan,

et al., 2018a).
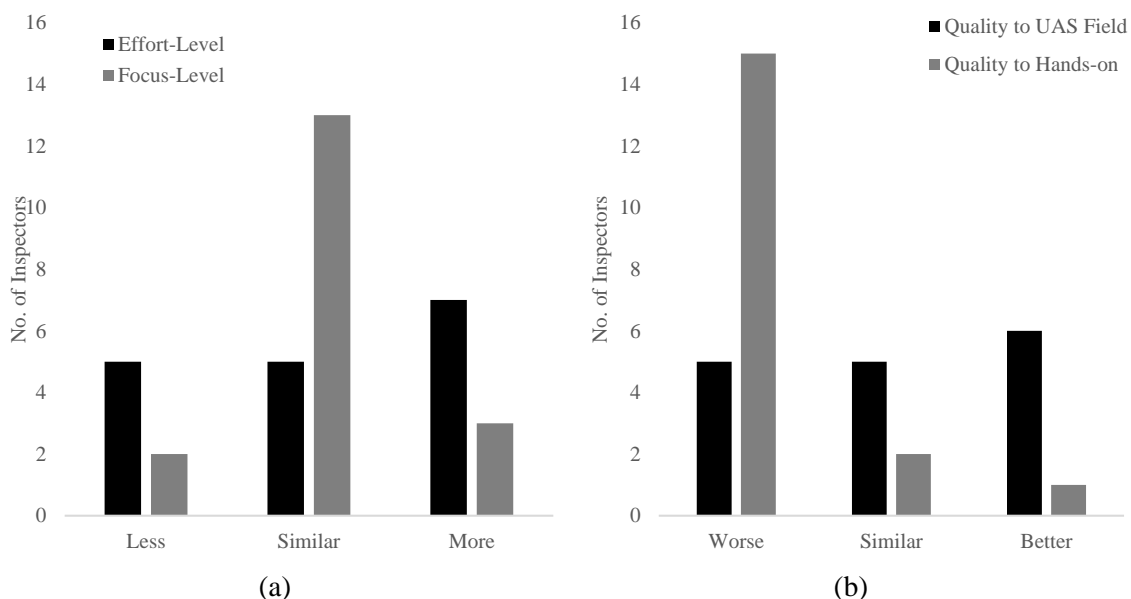
Fig. 4-10 Inspector assessments of the desk inspections (a) effort and focus levels compared to the typical bridge inspection, (b) quality compared to UAS field and hands-on inspections

Comparison to the Hands-on Inspections

The S-BRITE center offers training programs for bridge inspectors, including hands-on inspections on the POD frame. A set of 30 hands-on inspections performed on the same specimens investigated in this study are collected from the S-BRITE center as shown in Table 4-15. The results of the UAS-assisted field inspection and the average of the desk inspections for each inspection day is presented in Table 4-16.

Fig. 4-11 shows the HR and HCR for each type of specimen for desk, field, and hands-on inspections. As seen, for OOP and RCP specimens, the desk and field inspections provided comparable HR and HCR scores. As for the WCP, the results of the desk and field inspections were considerably lower than the hands-on inspections. This is mainly due to the location of the WCP specimens, which created a more challenging

scenario during the flight. The inspectors required more clearance between the DJI Mavic

and the WCP specimens, which prevented them from capturing proper videos.

Table 4-15 The average of the hands-on inspections

Type	HR (%)	HCR (%)	LCM (mm)	T (min)
OOP	65	25	133	86
WCP	57	27	108	20
RCP	84	81	38	17
All	**70**	**34**	**133**	**122**

Table 4-16 The average of UAS inspections

Day	Type	Desk Inspection Result (Avg.)				Field Inspections Results			
		HR (%)	HCR (%)	LCM (mm)	T (min)	HR (%)	HCR (%)	LCM (mm)	T (min)
18	OOP	50	19	92	147	67	18	72	-
	WCP	5	2	108	49	0	0	108	**-**
	RCP	56	65	34	28	NA	NA	NA	**-**
	All	**44**	**23**	**114**	**223**	**50**	**13**	**108**	**125**
19	OOP	68	24	85	174	67	67	133	-
	WCP	13	4	108	56	0	0	108	**-**
	RCP	69	74	22	37	NA	86	38	**-**
	All	**59**	**28**	**112**	**268**	**50**	**46**	**133**	**199**
20	OOP	65	19	65	130	50	24	125	-
	WCP	45	15	108	47	33	45	108	**-**
	RCP	78	75	22	42	56	46	32	**-**
	All	**66**	**24**	**108**	**218**	**48**	**46**	**125**	**145**
21	OOP	59	17	78	183	60	15	74	-
	WCP	36	22	101	42	60	16	108	**-**
	RCP	76	82	24	32	NA	NA	NA	**-**
	All	**60**	**25**	**101**	**257**	**60**	**27**	**108**	**201**
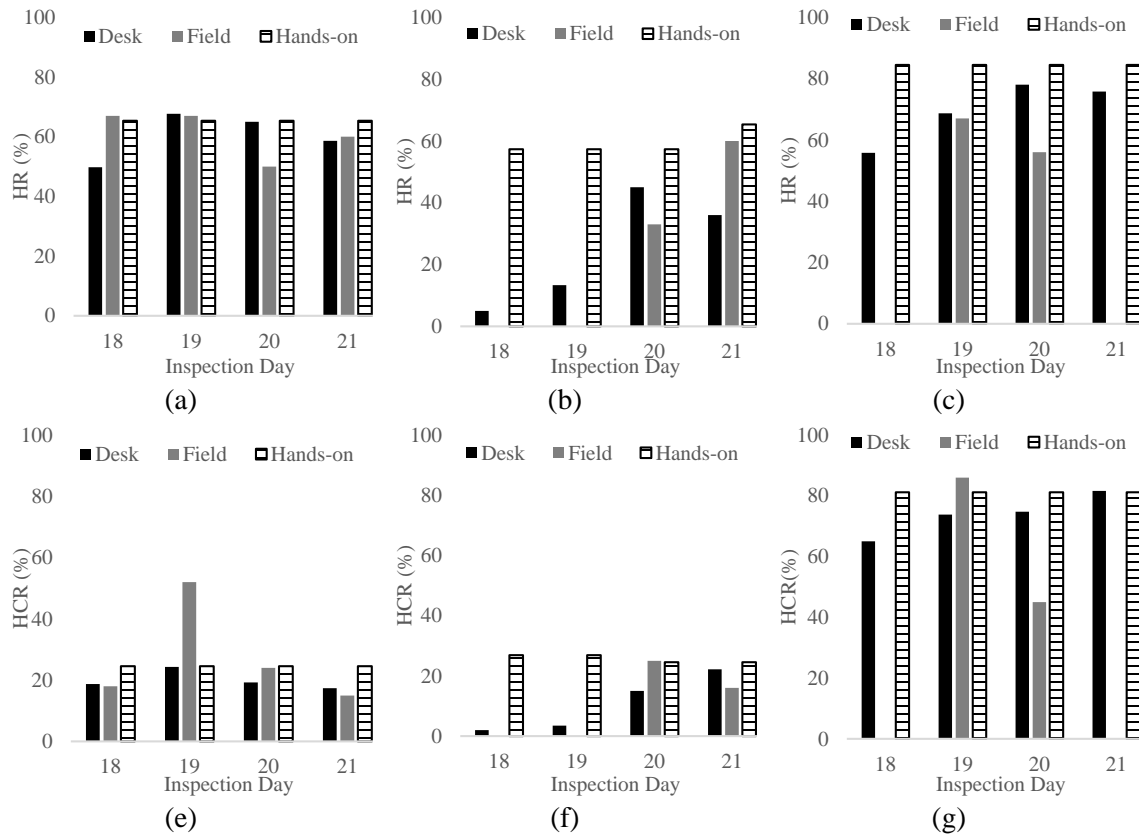
Fig. 4-11 Comparing the UAS-assisted inspections to the hands-on inspections, (a) HR for OOP, (b) HR for WCP, (c) HR for RCP, (d) HCR for OOP, (e) HCR for WCP, and (f) HCR for RCP

In terms of T, the desk inspections were the most time-consuming, as can be seen in Fig. 4-12a. The average T for the field inspections was 168 min and for the desk inspections was 241 min, which were 38% and 98% more than the average T of the hands-on inspections, respectively. Considering none of the inspectors have participated in UAS-assisted inspections before expect for two field inspectors who also performed two of the desk inspections, more allocated time was expected. In addition, the desk inspections do not get considerably more expensive or frustrating as the inspection time increases since they happened after the field inspections. Therefore, the inspectors had the ability to dedicate more time without worrying about wasting money. Fig. 4-12b

shows the LCM values for each type of inspection. The average LCM for the desk inspections was 109 mm, which was 11% and 8% less than the hands-on and field inspections, respectively.
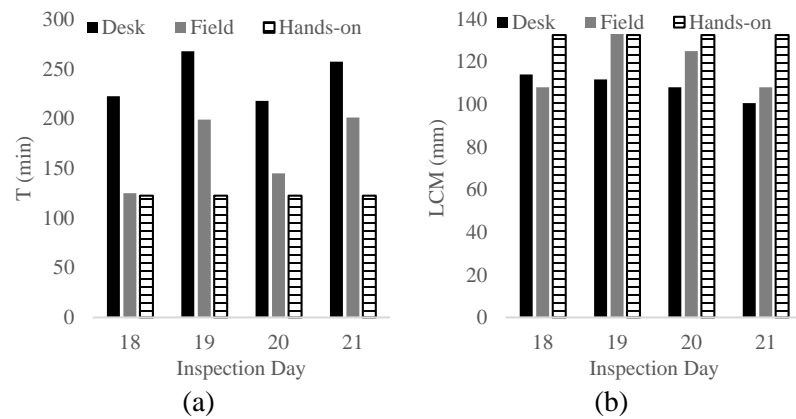
Fig. 4-12 Comparing the UAS-assisted inspection to the hands-on inspections, (a) T, (b) LCM

Conclusions and Future Work

Inspection of bridges with fracture critical members (FCM) is among the most challenging tasks for the bridge community to perform since these bridges are susceptible to fatigue cracks. The current practice for FCM inspection is hands-on inspection with application of some sort of non-destructive evaluation (NDE) method if necessary. Successful applications of Unmanned Aerial Systems (UASs) in state departments of transportation (DOTs) in the past make them an interesting option for FCM inspections; however, there are no studies investigating the factors for an effective UAS-assisted FCM inspection.

The research team conduct four UAS-assisted inspections on a probability of

detection (POD) training structure at the Steel Bridge Research, Inspection, Training, and Engineering (S-BRITE) center at Purdue University to locate the fatigue crack(s). Each inspection included a different inspector, accompanied by a pilot flying a DJI Mavic UAS, inspecting different types of the specimens on the POD frame through a first person view (FPV) monitor. The video streamed to the FPC monitor was also recorded and stored for another phase of the study. The inspectors marked the location of cracks on a binder that was used to evaluate their performance. The metrics of this study were hit rate (HR), hit to call ratio (HCR), length of the largest crack missed (LCM), and inspection time (T). The inspection videos of 54 specimens for each day of inspection were shared with 19 bridge inspectors to perform desk inspections by reviewing them and marking the cracks. The selected specimens included the three types of specimens on the POD frame: out of plane (OOP), welded cover plate (WCP), and riveted cover plate (RCP). Based on the results, the following remarks can be made:

- Inspectors with more hands-on inspections performed better in the desk inspections.
- Inspectors who performed better in the vision tests performed better in the desk inspections
- Wind speed had a noticeable effect on the metrics of both field and desk inspection. (results were better for the days with lower wind speeds)
- Inspectors performed considerably better on the OOP and RCP specimens than the WCP specimens due to the locations of WCP specimens and limited upward tilt-angle of the DJI Mavic.

- Lower workload experienced by the inspectors resulted in better inspection metrics.

- Inspectors employed by private agencies performed marginally better than the DOT inspectors.

- Using a media player with zoom and brightness adjustment improves the desk inspections.

- The hands-on inspections had better metrics than the UAS-assisted inspections for all specimens; however, the UAS-assisted inspections produced similar metrics, except for T, to the hands-on inspections for OOP and RCP specimens.

- The LCM was the only metric that was better in the desk inspections

- The desk inspections and the field inspections were 98% and 38% more time-consuming than the hands-on inspections, respectively.

This study shows the potential of implementing UAS-assisted inspections for future FCM inspections. Considering none of the inspectors were trained or participated in UAS inspections before, the results are promising. The authors recommend the following for future work to improve the inspection results:

- Performing the inspections using a UAS with at least a 90-degree tilt-angle.

- Providing UAS-assisted training sessions for the inspectors before the inspection.

- Preforming the desk inspections on similar monitors with equal or higher

resolution than the videos.

References

Connor, R. J., Dexter, R. J. & Mahmoud, H., 2005. *Inspection and management of bridges with fracture-critical details: a synthesis of highway practice,* Washington, D.C.: Transportation Research Board.

Dorafshan, S., Coopmans, C., Thomas, R. & Maguire, M., 2018b. *Deep Learning Neural Networks for sUAS-Assisted Structural Inspections: Feasibility and Application.* Dallas, IEEE.

Dorafshan, S. & Maguire, M., 2017d. *Autonomous detection of concrete cracks on bridge decks and fatigue cracks on steel members.* Mashantucket, CT, Digital Imaging.

Dorafshan, S. & Maguire, M., 2018. Bridge inspection: human performance, unmanned aerial systems and automation. *Journal of Civil Structural Health Monitorng ,* 8(3), pp. 443-476.

Dorafshan, S., Maguire, M. & Chang, M., 2017c. *Comparing automated image-based crack detection techniques in spatial and frequency domains.* Jacksonville, FL, 26th ASNT Research Symposium.

Dorafshan, S., Maguire, M., Hoffer, N. & Coopmans, C., 2017a. *Challenges in bridge inspection using small unmanned aerial systems: Results and lessons learned.* New York: IEEE., International Conference on Unmanned Aircraft Systems (ICUAS17).

Dorafshan, S., Maguire, M., Hoffer, N. & Coopmans, C., 2017b. *Fatigue Crack Detection Using Unmanned Aerial Systems in Under-Bridge Inspection,* Boise, ID: Idaho

Transportation Department.

Dorafshan, S., Thomas, J. R. & Maguire, M., 2018c. Comparison of Deep Convolutional Neural Networks and Edge Detectors for Image-Based Crack Detection in Concrete. *Construction and Building Materials,* Volume 186, pp. 1031-1045.

Dorafshan, S., Thomas, R. & Maguire, M., 2018a. Fatigue Crack Detection Using Unmanned Aerial Systems in Fracture Critical Inspection of Steel Bridges. *Journal of Bridge Engineering,* 23(10), p. 04018078.

Ferris III, F. L., Kassoff, A., Bresnick, G. H. & Bailey, I., 1982. New visual acuity charts for clinical research. *American journal of ophthalmology,* 94(1), pp. 91-96.

FHWA, 2013. [Online]
Available at: https://www.fhwa.dot.gov/bridge/nbi/no10/yrblt_yrreconst13.cfm#b
[Accessed 02 08 2018].

FHWA, 2017. *National bridge inspection standards. 23 CFR 650C,* Washington DC: FHWA.

Hart, S. G., 2006. *Nasa-Task Load Index (NASA-TLX); 20 Years Later.* Los Angeles, the human factors and ergonomics society annual meeting, Sage Publications..

Hart, S. G. & Staveland, L. E., 1988. Development of NASA-TLX (Task Load Index): Results of empirical and theoretical research. *Advances in psychology,* Volume 52, pp. 139-183.

Hearn, G., 2007. *Bridge Inspection Practices. NCHRP synthesis 375.* Washington, DC: Transportation Research Board.

Khurana, A. K., Khurana, A. K. & Khurana, B., 2014. *Theory and practice of optics and refraction.* 3rd ed. s.l.:Elsevier India.

Lichtenstein, A. G., 1993. The Silver Bridge Collapse Recounted. *Journal of Performance of Constructed Facilities,* 7(4), pp. 249-261.

Parr, M. J., C. R. J. & Bowman, M., 2009. Proposed method for determining the interval for hands-on inspection of steel bridges with fracture critical members. *Journal of Bridge Engineering,* 15(4), pp. 352-363.

Pelli, D. G. & Robson, J. G., 1988. The design of a new letter chart for measuring contrast sensitivity. *Clinical Vision Sciences,* Volume 2, pp. 187-199.

Weatherunderground, 2017. *Weather History for Purdue Univ, IN.* [Online]
Available at:
https://www.wunderground.com/history/weekly/us/in/lafayette/KLAF/date/2017-12-18
[Accessed 18-21 12 2017].

CHAPTER V

IMAGE PROCESSING ALGORITHMS FOR CRACK DETECTION IN CONCRETE

STRUCTURES

Abstract

This chapter discusses image processing algorithms for detection of defects in concrete. Such algorithms are useful for improving the accuracy of crack detection during autonomous inspection of bridges and other structures. The authors propose a generic image processing algorithm for crack detection, which includes the major steps of filter design, edge detection, image enhancement, and segmentation. The edge detection was carried out by six filters in the spatial (Roberts, Prewitt, Sobel, and Laplacian of Gaussian) and frequency (Butterworth and Gaussian) domains. These algorithms are applied to fifty images each of defected and sound concrete and an inspector attempted to identify cracks in binary images. The performance of the six filters is compared in terms of accuracy, precision, minimum detectable crack width, computational time, and noise-to-signal ratio. In general, frequency domain techniques were slower than spatial domain methods due to computational intensity of the Fourier and inverse Fourier transformations used to move between the spatial and frequency domains. Frequency domain methods also produced noisier images than spatial domain methods. Crack detection in the spatial domain using the Laplacian of Gaussian filter proved to be the fastest, most accurate, and most precise method, and resulted in the finest minimum detectable crack width.

Introduction

The United States is home to more than 600,000 bridges, more than one-third of which include a concrete superstructure or wear surface [1]. These bridges require a variety of periodic inspections in accordance with federal regulations [2]. The most common inspection type is the routine inspect, wherein the inspector scans the bridge deck to identify surface degradation or surface cracking. Such inspections are costly [3], time-consuming [4], and labor intensive [5]. Autonomous inspection [5] [6] [7] [8] [9] may be a cost-effective solution to these problems if the accuracy of human inspection can be matched. Image-based inspection for cracks [10, 11], spalls [12, 13], delaminations [13, 14, 15], and corrosion [16] using unmanned aerial systems (UAS) have proven effective based on previous literature.

Image-based autonomous inspections still require human inspectors to review images. The number of images collected depends on a number of factors, but is commonly in the hundreds of thousands [5]. Manual identification of flaws in such large images sets is time consuming and prone to inaccuracy due to inspector fatigue or human error. Image processing algorithms can improve the accuracy and efficiency of autonomous inspections by either (a) enhancing images to improve ease of human detection of defects or (b) autonomously identifying defects. This chapter discusses the former.

Cracks in a two-dimensional (2D) image are classified as edges, and thus existing edge detection algorithms are likely candidates for crack identification. 2D images are represented mathematically by matrices (one matrix, in the case of greyscale images, or three matrices in the case of red/green/blue color images). An ideal edge is defined as a

discontinuity in the greyscale intensity field. Crack detection algorithms can emphasize edges by applying filters in either the spatial or frequency domain. The use of a wide variety of edge detection filters or transformations for crack detection has been demonstrated in the literature [11, 17-33] but there is little guidance on the best methods.

Save two noteworthy exceptions, most research focuses on developing new methods for crack detection rather than comparing the performance of existing methods. Abdel-Qader et al. [18] compared the performance of the fast Haar transform, Fourier transform, Sobel filter, and Canny filter for crack detection in 25 images of defected concrete and 25 images of sound concrete. The fast Haar transform was the most accurate method, with overall accuracy of 86%, followed by the Canny filter (76%), Sobel filter (68%), and the Fourier transform (64%). The processing time was not considered. Mohan and Poobal [34] reviewed a number of edge detection techniques for visual, thermal, and ultrasonic images, but the information presented was from several studies that considered vastly different data sets, and so the results are not directly comparable. This chapter presents a direct comparison of the performance of four common edge detection methods in the spatial domain (Roberts, Prewitt, Sobel, and Laplacian of Gaussian) and two in the frequency domain (Butterworth and Gaussian) by applying them to a dataset of fifty sound and fifty defected images of concrete.

Analytical Program

Fig. 5-1 shows a generic image analysis algorithm developed for this study. The generic algorithm includes three main steps: Edge detection, edge image enhancement, and segmentation. Edge detection in the spatial domain involves greyscale conversion

and application of a filter. Edge detection in the frequency domain requires additional steps to transform the image from the spatial domain to the frequency domain before application of the filter, and the inverse operation to transform the filtered image back to the spatial domain. This section details the particulars of each step in the generic image processing algorithm.
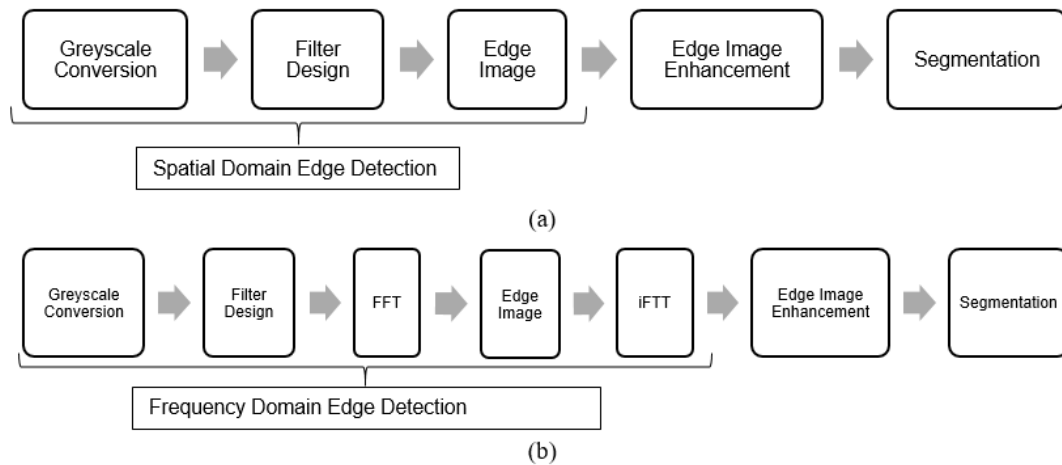
Fig. 5-1 The steps in the proposed crack detection algorithm, (a) the spatial domain, (b) the frequency domain

Greyscale conversion

Edge detection algorithms perform best with greyscale images [35], so the first step in the image analysis procedure is greyscale conversion of color images. The original color image comprises a matrix of pixels, each with a defined red, green, and blue intensity. Greyscale conversion follows Equation 5-1, where $I(x, y)$ is the grayscale intensity of pixel (x, y), and $R(x, y)$, $G(x, y)$, and $B(x, y)$ are the red, green, and blue pixel intensities of the same, respectively.

$$I(x,y) = 0.2989R(x,y) + 0.5870G(x,y) + 0.1140B(x,y) \tag{5-1}$$

Edge detection in the spatial domain

In general, edge detection in images requires filtering by one of several common methods that are discussed in detail below. Filters are applied as a small matrix of values called a kernel through a mathematical operation known as convolution. In general form, the convoluted image O is the sum of the element-by-element products of the image intensity matrix I and the kernel K in every position in which K fits fully inside I. Equation 5-2 describes this in plainer terms for image size $M \times N$ and kernel size $m \times n$.

$$O(i,j) = \sum_{k=1}^{m} \sum_{\ell=1}^{n} I(i+k-1, j+\ell-1)K(k,\ell) \tag{5-2}$$

The convoluted image O will be of size $(M - m + 1) \times (N - n + 1)$. The kernel typically includes both x and y components; the convoluted images E_x and E_y obtained from the x and y components of the filter emphasize vertical and horizontal edges, respectively. The final edge image E is the square root of the sum of the squared component images, i.e.

$$E(x,y) = \sqrt{E_x^2(x,y) + E_y^2(x,y)} \tag{5-3}$$

Common edge detecting filters in the spatial domain include Roberts, Prewitt, and Sobel. Equations 5-4 through 5–6 give the x and y kernels for the Roberts (R_x and R_y), Prewitt (P_x and P_y), and Sobel (S_x and S_y) filters. These filters compute the gradient between neighboring pixels in the x and y directions and intensify areas of high gradient (i.e., edges). Filters are constructed such that the components are of opposite sign and the sum of all components is zero. The Roberts filter (Equation 5-4) is a compact kernel, which could lead to very fast processing times. The Prewitt (Equation 5-5) and Sobel

(Equation 5-6) filters use larger 3×3 kernels nad are therefore more powerful but likely require extended computation times. The Prewitt is a first-order filter (the largest magnitude component is one); the second-order Sobel filter will likely produce an image with more intensified edges.

$$R_x = \begin{bmatrix} 1 & 0 \\ 0 & -1 \end{bmatrix} \qquad\qquad R_y = \begin{bmatrix} 0 & 1 \\ -1 & 0 \end{bmatrix} \tag{5-4}$$

$$P_x = \begin{bmatrix} -1 & 0 & 1 \\ -1 & 0 & 1 \\ -1 & 0 & 1 \end{bmatrix} \qquad P_y = \begin{bmatrix} 1 & 1 & 1 \\ 0 & 0 & 0 \\ -1 & -1 & -1 \end{bmatrix} \tag{5-5}$$

$$S_x = \begin{bmatrix} -1 & 0 & 1 \\ -2 & 0 & 2 \\ -1 & 0 & 1 \end{bmatrix} \qquad S_y = \begin{bmatrix} 1 & 2 & 1 \\ 0 & 0 & 0 \\ -1 & -2 & -1 \end{bmatrix} \tag{5-6}$$

Another popular edge detection method in the spatial domain is the Laplacian of Gaussian (LoG) function. When applied to an image with intensities $I(x, y)$, the Laplacian operator $\nabla^2 = \frac{\partial^2 I}{\partial x^2} + \frac{\partial^2 I}{\partial y^2}$ emphasizes both edges and noise or artifact. The influence of noise can be reduced by first applying the Gaussian smoothing filter given by Equation 5-7, where x and y are the spatial coordinates within the Gaussian kernel and σ is the standard deviation.

$$G(x, y) = \frac{1}{\sqrt{2\pi\sigma^2}} exp\left(-\frac{x^2+y^2}{2\sigma^2}\right) \tag{5-7}$$

Equation 5-8 gives the Lapalacian of the Gaussian, which can be preallocated for a given filter size $m \times n$ and standard deviation σ.

$$LoG = \nabla^2\big(G(x, y)\big) = \frac{x^2+y^2-2\sigma^2}{4\sigma^4} exp\left(-\frac{x^2+y^2}{2\sigma^2}\right) \tag{5-8}$$

Iterative optimization of the parameters m, n, and σ is possible on an image-by-

image basis, but it is convenient to predefine both the size and standard deviation. For the purposes of this study, the LoG kernel is defined as a square matrix with size equal to 0.5% of the maximum image dimension and the standard deviation is defined as one-fourth the maximum image dimension. At first glance, it would appear that the larger 13×13 LoG filter would be more computationally intensive than the smaller Roberts, Prewitt, and Sobel filters discussed previously. However, the LoG filter does not include x and y component kernels. Thus only one convolution operation (Equation 5-2) is required, and there is no need for the component transformation (Equation 5-3).

Edge detection in the frequency domain

Edge detection in the frequency domain requires transformation from the spatial domain to the frequency domain. This is quickly accomplished using the fast Fourier transform (FFT), which transforms the greyscale image intensities $I(x, y)$ into the frequency components $F(u, v)$. Unlike in the spatial domain, where the filter kernel is of arbitrary size, the filter kernel in the frequency domain is the same size as the image. The edge image $E(u, v)$ in the frequency domain is the element-by-element product of the filter kernel $K(u, v)$ and the frequency domain image $F(u, v)$, i.e.,

$$E(u, v) = K(u, v) \odot F(u, v) \tag{5-9}$$

where $\odot$ denotes element-wise multiplication. Inverse fast Fourier transformation (iFFT) of the frequency domain edge image $E(u, v)$ gives the edge image in the spatial domain $E(x, y)$.

The two most common frequency domain edge detection filters include Butterworth [36] and Gaussian [37] high pass filters. High pass filters attenuate

frequencies above some defined cutoff frequency D_0. Equation 5-10 gives the general

form of the nth-order Butterworth filter kernel $K_B(u, v)$, where $D(u, v)$ is the distance

between the pixel (u, v) and the origin of the frequency (the center of the $M \times N$ image)

as defined by Equation 5-11.

$$K_B(u, v) = 1 - \frac{1}{1 + \left[\frac{D(u,v)}{D_0}\right]^{2n}} \qquad (5\text{-}10)$$

$$D(u, v) = \sqrt{\left[u - \left(\frac{M}{2} + 1\right)\right]^2 + \left[v - \left(\frac{N}{2} + 1\right)\right]^2} \qquad (5\text{-}11)$$

Similarly, Equation 5-12 gives the general form of the Gaussian high pass filter

kernel $K_G(u, v)$, where $D(u, v)$ is again the distance between the pixel (u, v) and the

frequency origin and σ is the assumed standard deviation of the frequency distribution.

$$K_G(u, v) = 1 - e^{\frac{-D^2(u,v)}{2\sigma^2}} \qquad (5\text{-}12)$$

For the purposes of this study, a fourth order $(n = 4)$ Butterworth filter was

constructed with cutoff frequency $D_0 = M/10$. The Guassian filter was constructed with

standard deviation $\sigma = M/10$. Fig. 5-2 presents a graphical representation of the

Butterworth and Gaussian filters.

Edge image enhancement

Edge images $E(x, y)$ resulting from spatial or frequency domain edge detection

filters contain a range of pixel intensities that require scaling. The scaling function given

by Equation 5-13 converts the edge image pixel intensities $E(x, y)$ to linearly scaled edge

image pixel intensities $E_{sc}(x, y)$ such that $0 \leq I_{sc}(x, y) \leq 1$.

$$E_{sc}(x, y) = [E(x, y) - \min(E)] \left[\frac{1}{\max(E) - \min(E)}\right] \qquad (5\text{-}13)$$

(a)   (b)
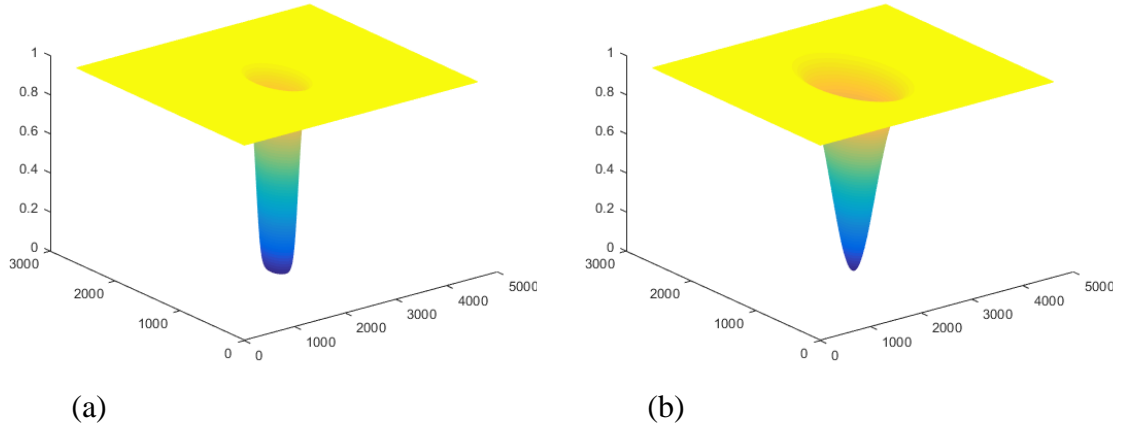
Fig. 5-2 (a) Butterworth ($n = 4$, $D_0 = 259$) and (b) Gaussian ($\sigma = 59$) filters for edge detection in the frequency domain

The scaled edge image $E_{sc}(x, y)$ requires contrast adjustment to improve edge clarity. Equation 5-14 transforms the scaled edge image $E_{sc}(x, y)$ into the enhanced edge image $E_e(x, y)$, where $\mu_{E_{sc}}$ and $\sigma_{E_{sc}}$ are the mean and standard deviation of the scaled edge image pixel intensities, respectively.

$$E_e(x, y) = [E_{sc}(x, y) - \min(E_{sc})] \left[\frac{2\sigma_{E_{sc}}}{\max(E_{sc}) - \min(E_{sc})} \right] + \mu_{E_{sc}} \qquad (5\text{-}14)$$

Segmentation

Segmentation is the final step in the proposed image analysis algorithm. This process converts the edge image to the binary image, in which pixels belonging to a crack take an intensity value of one and the remaining pixels take an intensity value of zero. Selection of an appropriate threshold intensity—above which a pixel is classified as a crack and below which it is not—is critical. If the threshold intensity is too high, cracks

go undetected. If it is too low, the image becomes noisy and it is difficult to differentiate cracks from noise. This work considered two threshold operations for segmentation: pixel threshold and area threshold.

The pixel threshold operation follows Equation 5-15, where $B_1(x, y)$ is the first-level binary image and T_1 is the pixel threshold value.

$$B_1(x, y) = \begin{cases} 0, & E_e(x, y) < T_1 \\ 1, & E_e(x, y) \geq T_1 \end{cases} \qquad (5\text{-}15)$$

T_1 can be selected using Otsu's method [38] or other intuitive/adaptive approaches [31]. In this study, T_1 was selected based on the statistical properties of pixel intensities in the enhanced edge image $E_e(x, y)$. Equation 5-16 defines T_1, where μ_{E_e} and σ_{E_e} are the mean and standard deviation of the enhanced edge image pixel intensities.

$$T_1 = \mu_{E_e} + 3\sigma_{E_e} \qquad (5\text{-}16)$$

Similarly, the area threshold operation follows Equation 5-17, where $B_2(x, y)$ is the second-level binary image and T_2 is the area threshold value.

$$B_2(x, y) = \begin{cases} 0, & B_1(x, y) < T_2 \\ 1, & B_1(x, y) \geq T_2 \end{cases} \qquad (5\text{-}17)$$

Equation 5-18 defines T_2 according to the area of each connected component A_{cc}, where $\sigma_{A_{cc}}$ is the standard deviation of the areas of connected components in B_1.

$$T_2 = \sigma_{A_{cc}} \qquad (5\text{-}18)$$

The area of connected components A_{cc} is determined according to eight-neighbor connectivity, which considers pixel connectivity in the vertical, horizontal, or diagonal directions, such that pixel (x, y) is connected to all pixels $(x \pm 1, y \pm 1)$. A_{cc} could alternatively be defined according to four-neighbor connectivity, which is a stricter

definition that only considers connectivity in the vertical and horizontal directions, such that pixel (x, y) is connected to pixels $(x \pm 1, y)$ and $(x, y \pm 1)$. For the purposes of this research, the more relaxed eight-neighbor definition of connectivity was adopted.

The second-level binary image B_2 is the final product of the proposed crack detection algorithm.

Experimental Program

In order to test the crack detection algorithm discussed above, researchers gathered fifty images of sound concrete and fifty images of cracked concrete from several previously tested concrete panels at the Systems, Materials, and Structural Health Laboratory (SMASH Lab) at Utah State University [39]. Images were taken with a 12 MP digital camera with focal length of 35 mm. The distance between the lens and the surface was 1.0 m. The surface illumination, as verified by a Digi-Sense data logging light meter with NIST traceable calibration, was 150–250 lx. The image resolution was 2592×4608 px and the approximate field size was 1.0×1.2 m. RGB images were saved in JPEG format. Image processing was performed in MATLAB on a 64-bit operating system with 32 GB memory and 3.40 GHz processor. Fig. 5-3 shows representative images of defected and sound concrete. Images were processed in six iterations, corresponding to the four spatial domain edge detectors and two frequency domain edge detectors.

Following image processing, an inspector reviewed the second-level binary images resulting from each of the six iterations in random order and classified each image as cracked or sound. The inspector reviewed only the second-level binary images and was

not privy to the original images or images from intermediate steps in the crack detection algorithm. The same inspector inspected all of the images. The team then compared the results of each inspection to the ground truth, i.e., the known classification of each image as defected or sound based on physical inspection of the concrete surface aided by a crack microscope. The team then recorded the number of true positives (TP or hits), true negatives (TN or specificity), false positives (FP or fallout), and false negatives (FN or misses) for each iteration of the crack detection algorithm. A TP is a defected image in which the inspector accurately identifies the defect. A TN is a sound image that the inspector accurately identifies as sound. A FP is a sound image within which the inspector inaccurately identifies a defect. A FN is a defected image that the inspector inaccurately identifies as sound. A hit required the inspector to identify at least half of the actual crack length in a defected image. Fallout occurred when the inspector identified a crack in the noise or artifact of the second-level binary image.

(a)

(b)

Fig. 5-3 Representative images of (a) defected and (b) sound concrete

The performance of each iteration of the proposed algorithm was evaluated in terms of accuracy, precision, processing time, and minimum detectable crack width (MDCW). Accuracy is the sum of the number of hits and the specificity divided by the total number of images. Precision is the ratio of hits to the sum of hits and fallout. Processing time is the time required for execution of the crack detection algorithm using a particular edge detector. MDCW is the width of the narrowest crack detected in each iteration of the algorithm for cracks with widths of 0.08, 0.10, 0.40, 0.80, and 1.00 mm, as verified by a crack width microscope with 0.02 mm resolution. The algorithms are also compared in terms of the pixel intensity range in the enhanced edge images and the noise-to-signal ratio (N/S). A wider range of pixel intensities suggests a sharper contrast between defects and sound regions. The N/S describes the level of noise or artifact in the image and is defined as the ratio of lit pixels (ones) to the total number of pixels in

the second-level binary image B_2. The N/S is only computed for the sound dataset, because any lit pixels are known to be noise and not defects. A lower N/S is obviously preferred because defects become more difficult to resolve when the image is noisy.

Results

Table 5-1 summarizes the results of the six iterations of the proposed crack detection algorithm.

Spatial domain, Roberts filter

Crack detection in the spatial domain using Roberts filter resulted in the lowest number of hits (64%), but also resulted in the lowest fallout (10%). Thus, while the Roberts filter was the least accurate (77%), its precision (86%) was among the highest. The minimum detectable crack width was 0.4 mm, the largest of the six edge detectors evaluated. The processing time (1.67 s per image) was near the median of the six methods evaluated. Fig. 5-4 shows representative edge, enhanced edge, first-level binary, and second-level binary images from spatial domain edge detection of an image from the defected set (Fig. 4-3a) using Roberts filter.

Spatial domain, Prewitt filter

Crack detection in the spatial domain using Prewitt filter resulted in the second lowest number of hits (82%) and the highest fallout (18%). The Prewitt filter was the second least accurate and the least precise of the six methods evaluated. The minimum detectable crack width was 0.2 mm, which was comparable to four of the six methods. The processing time (1.40 s per image) was among the shortest. Fig. 5-5 shows

representative edge, enhanced edge, first-level binary, and second-level binary images

from spatial domain edge detection of an image from the defected set using Prewitt filter.

Table 5-1 Performance of different edge detectors in the proposed crack detection algorithm

Domain	Edge Detector	TP (%)	TN (%)	FP (%)	FN (%)	Accuracy (%)	Precision (%)	MDCW (mm)	Time (s)
Spatial	Roberts	64	90	10	36	77	86	0.4	1.67
Spatial	Prewitt	82	82	18	18	82	82	0.2	1.4
Spatial	Sobel	86	84	16	14	85	84	0.2	1.4
Spatial	LoG	98	86	14	2	92	88	0.1	1.18
Frequency	Butterworth	80	86	14	20	83	85	0.2	1.81
Frequency	Gaussian	80	88	12	20	84	87	0.2	1.92

(a) (b)

(c) (d)

Fig. 5-4 (a) Edge, (b) enhanced edge, (c) first-level binary, and (d) second-level binary images; defected dataset, spatial domain, Roberts filter
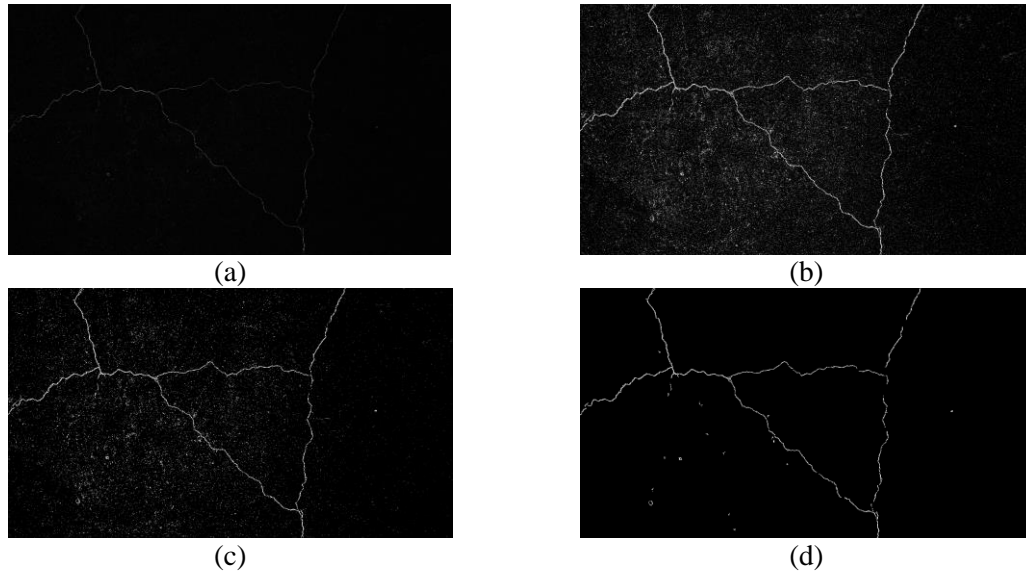
Fig. 5-5 (a) Edge, (b) enhanced edge, (c) first-level binary, and (d) second-level binary images; defected dataset, spatial domain, Prewitt filter

Spatial domain, Sobel filter

Crack detection in the spatial domain using Sobel filter resulted in the second highest number of hits (86%) and the second highest fallout (16%). Thus, while the Sobel filter was among the most accurate (85%) it was also among the least precise (84%). The minimum detectable crack width was 0.2 mm and the processing time (1.4 s per image) was among the shortest. Fig. 5-6 shows representative edge, enhanced edge, first-level binary, and second-level binary images from spatial domain edge detection of an image from the defected set using Sobel filter.

(a)   (b)

(c)   (d)
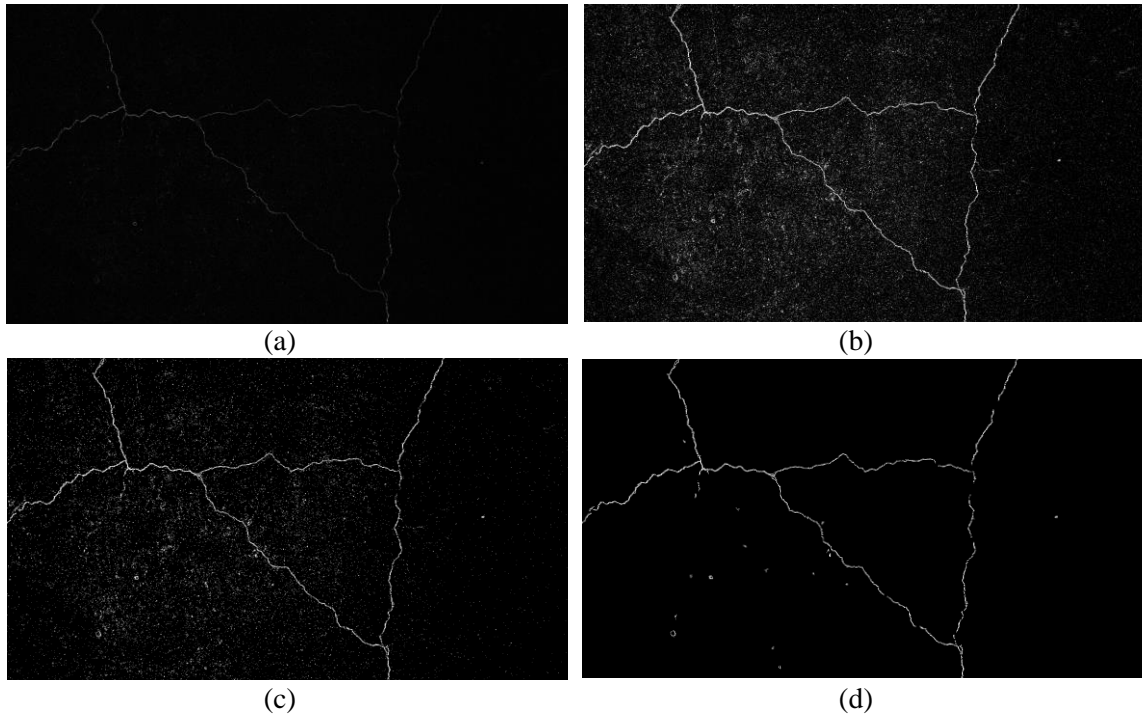
Fig. 5-6 (a) Edge, (b) enhanced edge, (c) first-level binary, and (d) second-level binary images; defected dataset, spatial domain, Sobel filter

Spatial domain, LoG filter

Crack detection in the spatial domain using the LoG filter resulted in the highest number of hits (98%), with only one miss in fifty defected images. The fallout (14%) was near the median for the six methods evaluated. Nevertheless, the LoG filter was the most accurate (92%) and the most precise (88%). Furthermore, the LoG method has the narrowest minimum detectable crack width (0.1 mm) and the shortest processing time (1.18 s per image). Fig. 5-7 shows representative edge, enhanced edge, first-level binary, and second-level binary images from spatial domain edge detection of an image from the defected set using LoG filter.
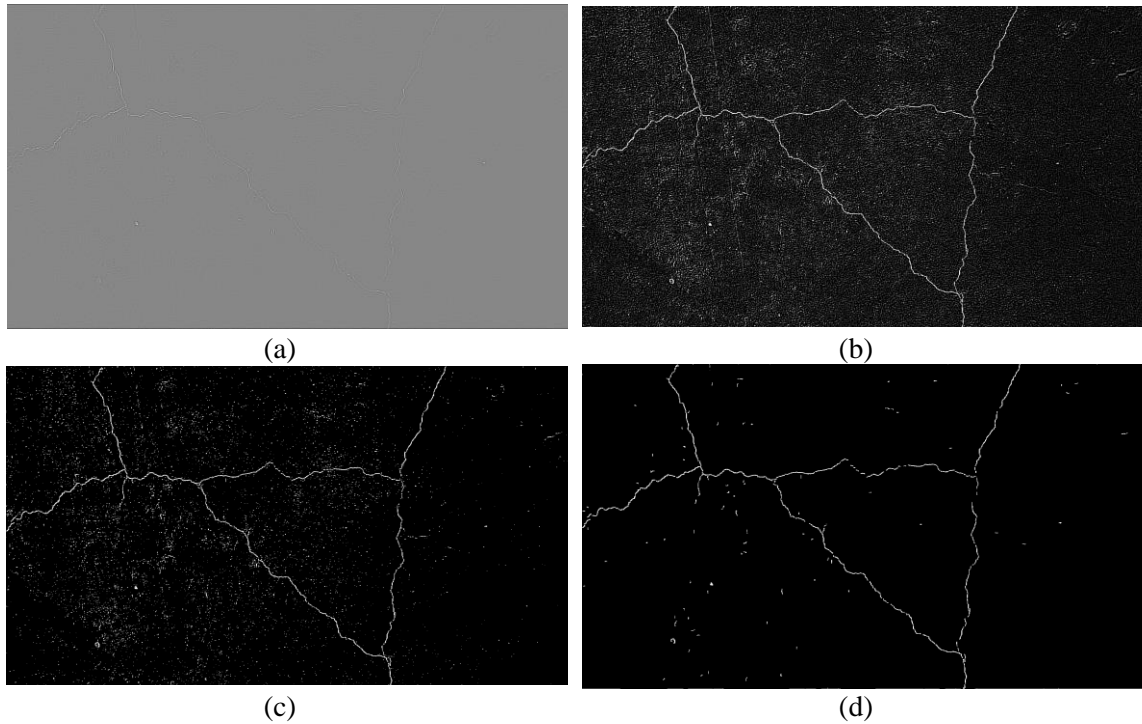
Fig. 5-7 (a) Edge, (b) enhanced edge, (c) first-level binary, and (d) second-level binary images; defected dataset, spatial domain, LoG filter

Frequency domain, Butterworth filter

Crack detection in the frequency domain using Butterworth filter resulted in the median number of hits (80%) and the median fallout (14%). The accuracy (83%) and precision (85%) were also near the median of the six methods evaluated. The minimum detectable crack width was again 0.2 mm and the processing time (1.81 s per image) was the second longest of the six methods. Fig. 5-8 shows representative edge, enhanced edge, first-level binary, and second-level binary images from frequency domain edge detection of an image from the defected set using Butterworth filter.

(a)
(b)

(c)
(d)
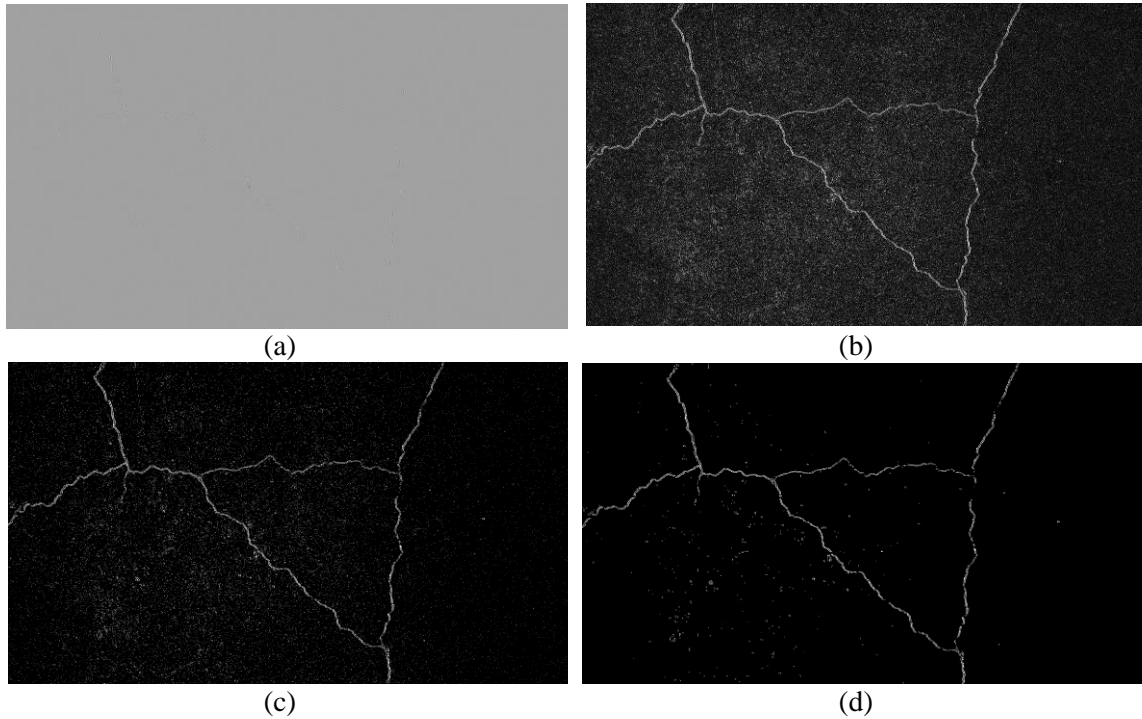
Fig. 5-8 (a) Edge, (b) enhanced edge, (c) first-level binary, and (d) second-level binary images; defected dataset, frequency domain, Butterworth filter

Frequency domain, Gaussian filter

Crack detection in the frequency domain using Gaussian filter resulted in the median number of hits (80%) and the second lowest fallout (12%). The accuracy (84%) was also near the median value but the precision (87%) was the second highest. The minimum detectable crack width was again 0.2 mm. The processing time (1.92 s per image) was the longest of the six methods evaluated. Fig. 5-9 shows representative edge, enhanced edge, first-level binary, and second-level binary images from frequency domain edge detection of an image from the defected set using Gaussian filter.
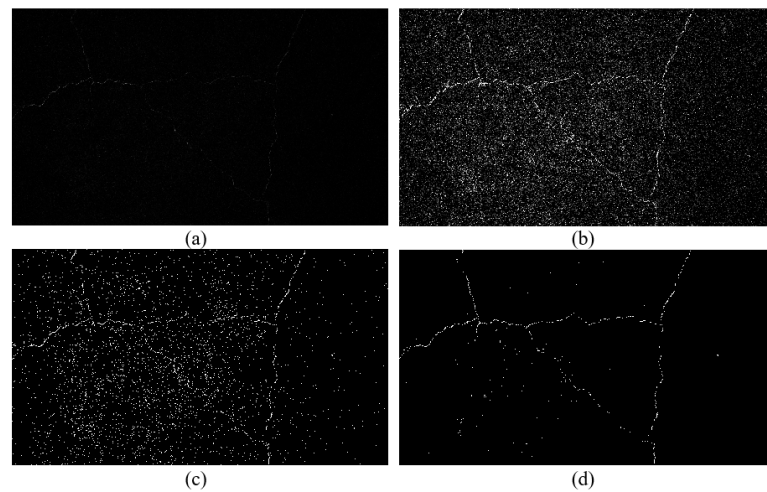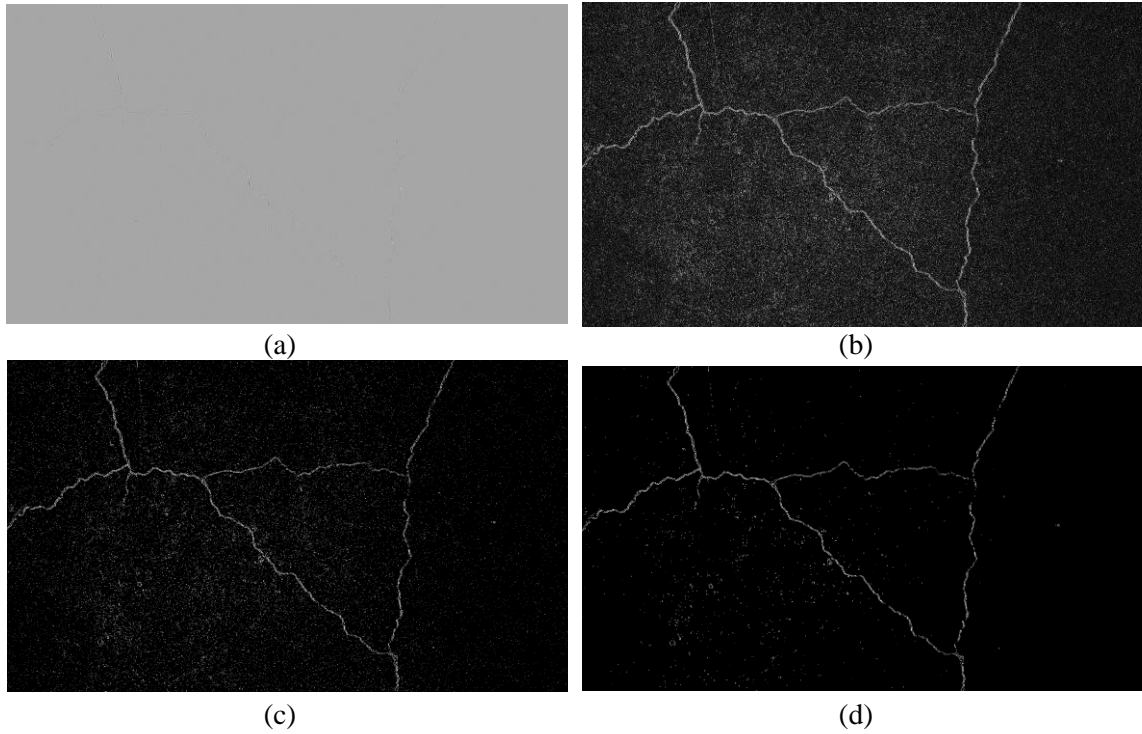
Fig. 5-9 (a) Edge, (b) enhanced edge, (c) first-level binary, and (d) second-level binary images; defected dataset, spatial domain, Gaussian filter

Comparison

Table 5-2 presents a comparison of the range of pixel intensities in the enhanced edge image E_e, the pixel thresholds T_1 and T_2 used for construction of the first- and second-level binary images B_1 and B_2, and the noise-to-signal ratio N/S observed in sound dataset using the six edge detection methods. Fig. 5-10 presents a direct comparison of second-level binary images from analysis of the image in Fig 3-5a, a member of the defected dataset. Similarly, Fig. 5-11 shows a direct comparison of the second-level binary images from analysis of the image in Fig. 5-3b, a member of the sound dataset.

Edge detection in the spatial domain using LoG filter was the fastest of the six

crack detection methods evaluated. The frequency domain methods were expected to be

the fastest because the element-wise product (Equation 5-9) requires far fewer floating-

point operations than the iterative convolution operation (Equation 5-2). However, the

computational intensity of the Fourier and inverse Fourier transformations used to move

between the spatial and frequency domains greatly increased processing time. The

frequency domain methods took an average of 1.87 seconds per image, while the spatial

domain methods took on average of 1.41 seconds per image. The LoG filter was expected

to be computationally efficient in comparison with the other methods despite its

comparatively large size (13×13). The computational efficiency of this method results

from the fact that LoG uses only one kernel, as opposed to x and component kernels as

in the other spatial domain methods. This reduces the number of convolution operations

(Equation 5-2) from two to one and obviates the use of Equation 5-3. The computational

efficiency of the other spatial domain methods did not follow the expected trend. It was

expected that the processing time would increase with the kernel size, and that the 3×3

Prewitt and Sobel filters would require longer computational time than the 2×2 Roberts

filter. In fact, the opposite was true. Processing time for the Roberts filter was 20% longer

than for the Prewitt or Sobel. The reader will recall the output image from Equation 5-2 is

of dimension $(M - m + 1) \times (N - n + 1)$ for image size $M \times N$ and kernel size $m \times n$.

Thus, a smaller kernel actually produces a larger edge image. This explains, at least in

part, the increased computational time for the smaller Roberts filter. The LoG filter was

also both the most accurate and precise of the six methods tested. The LoG method

resulted in 98% hits with only one miss among the fifty images in the defected dataset.
The next most accurate method recorded 7 misses. The remaining methods all recorded
ten or more misses. Thus, the accuracy of LoG (92%) was significantly higher than the
other five methods (77–85%). The precision of LoG (88%), which also considers fallout,
was much closer to that of the other five methods (82–87%). The LoG method recorded 7
false positives in the fifty images in the sound dataset. The Roberts filter, with 18 misses,
was by far the least accurate (77%). However, with only five false positives, it was
among the most precise (86%). Prewitt was the least precise with 9 misses, 9 false
positives, and 82% precision.

The LoG filter resolved the finest cracks with MDCW of 0.1 mm. Most of the
other methods were only able to resolve cracks 0.2 mm or wider. The Roberts filter could
only detect cracks 0.4 mm or wider. Considering the image size used in this study, one
pixel is equivalent to 0.2 mm. Thus, the LoG filter was useful in detecting cracks that are
about 1 pixel wide, while Roberts could only resolve cracks that are 2 pixels wide.

The contrast adjustment ranges, segmentation thresholds T_1 and T_2, and noise-to-
signal ratios N/S listed in Table 5-2 give some context to the performance metrics
discussed above. The contrast adjustment ranges, J_1 and J_2 represent the range of pixel
intensities in the enhanced edge image E_e. A wider range of contrast values (J_2- J_1)
corresponds to more intensification of edges within the image. Thus, cracks should be
more easily detected when the contrast adjustment range is large. The Roberts filter,
which performed poorly according to the performance metrics discussed above, exhibited
the smallest range. The LoG filter, which arguably exhibited the best performance, had

one of the widest contrast adjustment ranges. Furthermore, the contrast adjustment range

for the LoG filter was quite different between the defected and sound datasets. This

resulted from a large number of pixels with high intensities in the defected image.

The noise-to-signal ratio N/S was evaluated only for the sound dataset for the

simple reason that the noise in sound images was more well defined. In the perfectly ideal

case, no pixels should be lit in the second-level binary image from the sound dataset.

Thus, any lit pixels are by default noise. In the defected dataset, the distinction between

signal and noise is ill defined. In general, the spatial domain methods exhibited lower

N/S than the frequency domain methods. The lowest N/S were observed for the Prewitt

and Sobel filters, with N/S of 0.32 and 0.33, respectively. The Roberts filter exhibited

only slightly more noise ($N/S = 0.41$). In comparison, the LoG filter produced a fairly

noisy edge image ($N/S = 0.90$).

Increased noise in the frequency domain manifests as an increase in the standard

deviation σ_{E_e} of the pixel intensities of the enhanced edge image E_e. Following Equation

5-16, this causes an increase in the pixel threshold T_1. While pixel thresholds were higher

in the frequency domain, area thresholds were lower. This results from reduced

continuity of cracks in the frequency domain.

It was expected that the LoG method, which was the most successful in terms of

the performance metrics—accuracy, precision, MDCW, and processing time—would

also exhibit the least noise. Instead, the noise-to-signal ratio in the LoG images was

among the highest observed. This can be explained in part by the images shown in Fig. 5-

10 and Fig. 5-11. The presence of cracks in even the noisiest of images in Fig.5-10e and f

is clear. Similarly, even in the sound images with the highest N/S (Fig. 5-11e and Fig. 5-11f), it is easy to see that no cracks are present. Despite the large number of lit pixels, no pattern of connectivity is apparent and thus the inspector can reasonably conclude that he or she is observing noise and not a defect. These images represent only a single data point for each method from the defected and sound dataset. However, they suggest that the level of noise in the binary image is not the only factor affecting the inspector's ability to detect cracks. The continuity of cracks in the binary image is also important, especially considering that the inspector needed to identify at least half of the crack in order to register a hit.

The value of the area threshold T_2 gives some idea of the continuity of cracks in the defected images. T_2 was defined in Equation 5-18 as the standard deviation $\sigma_{A_{cc}}$ of the areas of connected components A_{cc}. When the continuity of cracks in the binary image is poor (i.e., the cracks are discontinuous), $\sigma_{A_{cc}}$ is small. Conversely, when the cracks in the binary image are highly continuous, $\sigma_{A_{cc}}$ increases. Thus, higher values of T_2 imply a higher degree of continuity of cracks in the binary image. Additionally, when the cracks are highly continuous in binary images from the defected dataset, the value of T_2 will be much higher for the defected dataset than for the sound dataset. Such is the case for the Prewitt, Sobel, and LoG filters. The same is also true, but to a lesser degree, for the Butterworth and Gaussian filters. The values of T_2 for the sound and defected datasets using the Roberts filter are similar. This suggests poor continuity of the cracks in the binary images, which is confirmed in Fig. 5-10a. Considering that the Roberts filter was among the worst methods tested here, this result is not at all surprising. The cracks in

the rest of the binary images form the defected dataset (Fig. 5-10b–Fig. 5-10f) are visibly more continuous.

The results presented here have some significant implications for future work in the realm of automated detection without human inspectors. For all of the evaluated methods, the pixel segmentation threshold T_1 was higher for the defected dataset than for the sound dataset. The same was true for the area segmentation threshold T_2. For the LoG method, the contrast adjustment ranges were also much different for the defected dataset than for the sound dataset. Future research could consider these differences as indicators of the likelihood that a particular processed image includes a defect.

Table 5-2 The average range and threshold value for each method in defected and sound datasets

Method	Defected Dataset				Sound Dataset				
	J_1	J_2	T_1	T_2	J_1	J_2	T_1	T_2	Average N/S (%)
Roberts	0.204	0.251	0.70	25	0.21	0.25	0.64	21	0.41
Prewitt	0.232	0.290	0.66	76	0.23	0.29	0.59	53	0.32
Sobel	0.230	0.291	0.67	75	0.23	0.29	0.59	53	0.33
LoG	0.534	0.590	0.71	58	0.62	0.69	0.63	32	0.90
Butterworth	0.581	0.631	0.89	10	0.57	0.64	0.93	6	1.74
Gaussian	0.594	0.640	0.89	8	0.58	0.64	0.93	5	1.76

Conclusions

This study proposed a generic image-processing algorithm for detection of defects

in concrete for the purpose of comparing different edge detection algorithms. The proposed algorithm involved edge detection, edge image enhancement, and segmentation. Edge detection was completed in the spatial domain using Roberts, Prewitt, Sobel, and LoG filters; and in the frequency domain using Butterworth and Gaussian filters. Fifty images of defected concrete and fifty of sound concrete were analyzed by the proposed algorithm in six iterations making use of the six aforementioned edge detection strategies). An inspector reviewed the resulting binary images from each iteration and identified cracks. The inspection results were compared to the ground truth, and the six edge detection methods were compared based on accuracy, precision, minimum detectable crack width, and processing time per image. Edge detection in the spatial domain using LoG filter yielded the highest accuracy (92%) and precision (88%), the finest minimum detectable crack width, and the fastest processing time (1.18 s per image). All but one of the remaining methods (edge detection in the spatial domain using Roberts filter) yielded greater than 80% accuracy and were able to detect cracks as fine as 0.2 mm. While crack detection in the spatial domain using Roberts filter yielded the lowest accuracy (77%), it also yielded the fewest false positives (10%) and its precision (86%) was among the highest. In general, the processing time was longer for crack detection in the frequency domain (1.8–1.9 s per image) than in the spatial domain (1.2–1.7 s per image). Additionally, the second-level binary images (the final product of the image processing algorithm) were much noisier in the frequency domain. According to these results, crack detection in the spatial domain using LoG filter yields the best and fastest results for detecting defects in concrete structures.

Fig. 5-10 Second-level binary images from defected dataset obtained by crack detection in the spatial domain using (a) Roberts, (b) Prewitt, (c) Sobel, and (d) LoG; and in the frequency domain using (e) Butterworth and (f) Gaussian
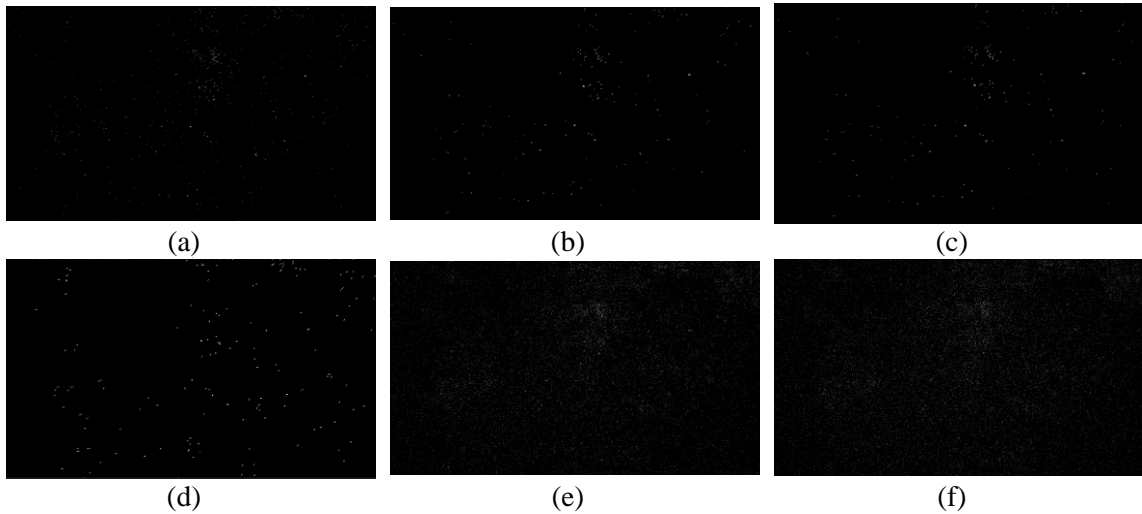
Fig. 5-11 Second-level binary images from sound dataset obtained by crack detection in the spatial domain using (a) Roberts, (b) Prewitt, (c) Sobel, and (d) LoG; and in the frequency domain using (e) Butterworth and (f) Gaussian

References

[1]   Federal Highway Administration, "National Bridge Inventory," FHWA, McLean, VA, 2017.

[2]   Federal Highway Administration, "National Bridge Inspection Standards (FHWA–FAPG 23 CFR 650C)," FHWA, McLean, VA, 2017.

[3]   B. Chan, H. Guan, J. Jo and M. Blumenstein, "Tuwards UAV-based bridge inspection systems: A reivew and an application perspective," Structural Monitoring and Maintenance, vol. 2, no. 3, p. 283–300, 2015.

[4]   C. H. Yang, M. C. Wen, Y. C. Chen and S. C. Kang, "An optimized unmanned aerial system for bridge inspection," in Proceedings of the International Symposium on Automation and Robotics in Construction, Vilnius, Lithuania, 2015.

[5]   S. Dorafshan, M. Maguire, N. Hoffer and C. Coopmans, "Fatigue Crack Detection Using Unmanned Aerial Systems in Under-Bridge Inspection," Idaho Transportation Department, Boise, ID, 2017.

[6]   S. Dorafshan, M. Maguire, N. Hoffer and C. Coopmans, "Challenges in bridge inspection using small unmanned aerial systems: Results and lessons learned," in Proceedings of the 2017 International Conference on Unmanned Aircraft Systems, Miami, FL, 2017.

[7]   N. Gucunski, S. H. Kee, H. M. La, B. Basily and A. Maher, "Delamination and concrete quality assessment of concrete bridge decks using a fully autonomous RABIT platform," International Journal of Structural Monitoring and Maintenance, vol. 2, no. 1, p. 19–34, 2015.

[8]   R. S. Lim, H. M. Lag and W. Sheng, "A robotic crack inspection and

mapping system for bridge deck maintenance," ICCC Transactions on Automation Science and Engineering, vol. 11, no. 2, p. 367–378, 2014.

[9]   N. Gucunski, S. H. Kee, H. La, B. Basily, A. Maher and H. Bhasemi, "Implementation of a fully autonomous platform for assessment of concrete bridge decks RABIT," in Structures Congress 2015, Portland, OR, 2015.

[10]   N. Metni and T. Hamel, "A UAV for bridge inspection: Visual servoing control law with orientation limits," Automation in Construction, vol. 17, no. 1, p. 3–10, 2007.

[11]   S. Dorafshan, M. Maguire and X. Qi, "Automatic Surface Crack Detection in Concrete Structures using OTSU Thresholding and Morphological Operations (UTC 01-2016)," Utah Transportation Center, Logan, UT, 2016.

[12]   S. German, I. Brilakis and R. DesRoches, "Rapid entropy-based detection and properties measurement of concrete spalling with machine vision for post-earthquake safety assessments," Advanced Engineering Informatics, vol. 26, no. 4, p. 846–858, 2012.

[13]   K. Vaghefi, T. T. M. Ahlborn, D. K. Harris and C. N. Brooks, "Combined imaging technologies for concrete bridge deck condition assessment," Journal of Performance of Constructed Facilities, vol. 29, no. 4, 2013.

[14]   H. Sohn, D. Dutta, J. Y. Yang, M. DeSimio, S. Olson and E. Swenson, "Automated detection of delamination and disband from wavefield images obtained using a scanning laser vibrometer," Smart Materials and Structures, vol. 20, no. 4, 2011.

[15]   T. Omar and M. L. Nehdi, "Remote sensing of concrete bridge decks using unmanned aerial vehicle infrared thermography," Automation in Construction, vol. 83, p. 360–371, 2017.

[16]   A. Ellenberg, A. Kontsos, F. Moon and I. Bartoli, "Bridge related damage quantification using unmanned aerial vehicle imagery," Structural Control and Health Monitoring, vol. 23, no. 9, p. 1168–1179, 2016.

[17]   J. Kittler, R. Marik, M. Mirmehdi, M. Petrou and J. Song, "Detection of defects in colour texture surfaces," in IAPR Workshop on Machine Vision Applications, Kawasaki, 1994.

[18]   I. Abdel-Qader, P. Abudayyeh and M. E. Kelly, "Analysis of edge-detection techniques for crack identification in bridges," Journal of Computing in Civil Engineering, vol. 17, no. 4, p. 255–263, 2003.

[19]   I. Abdel-Qader, S. Pashaie-Rad, P. Abudayyeh and S. Yehia, "PCA-based algorithm for unsupervised bridge crack detection," Advances in Engineering Software, vol. 37, no. 12, p. 771–778, 2006.

[20]   T. Yamaguchi, S. Nakamuran, R. Saegusa and S. Hashimoto, "Image-based crack detection for real concrete surfaces," IEEJ Transactions on Electrical and Electronic Engineering, vol. 3, no. 1, p. 128–135, 2008.

[21]   J. K. Oh, G. Jang, S. Oh, J. H. Lee, B. J. Yi, Y. S. Moon, J. S. Lee and Y. Choi, "Bridge inspection robot system with machine vision," Automation in Construction, vol. 18, no. 7, p. 929–941, 2009.

[22]   H. Moon and J. Kim, "Intelligent crack detecting algorithm on the concrete crack image using neural network," in Proceedings of the 28th International Symposium on Automation and Robotics in Construction, Seoul, 2011.

[23]   H. Wang, Z. Chen and L. Sun, "Image preprocessing methods to identify micro-cracks of road pavement," Optics and Photonics Journal, vol. 3, no. 2, p. 99, 2013.

[24]   P. Zheng, "Crack Detection and Measurement Utilizing Image-Based Reconstruction," MS Thesis. Virginia Polytechnic Institute, Blacksburg, VA, 2014.

[25]   R. S. Lim, H. M. La and W. Sheng, "A robotic crack inspection and mapping system for bridge deck maintenance," IEEE Transactions on Automation Science and Engineering, vol. 11, no. 2, p. 367–378, 2014.

[26]   J. W. Kim, S. B. Kim, J. C. Park and J. W. Nam, "Development of crack detection system with unmanned aerial vehicles and digital image processing," in Advances in Structural Engineering and Mechanics (ASEM15), Incheon, 2015.

[27]   A. Rimkus, A. Podviezko and V. Gribniak, "Processing digital images for crack localization in reinforced concrete members," Procedia Engineering, vol. 122, p. 239–243, 2015.

[28]   S. Sankararinivasan, E. Balasubramanian, K. Karthik, U. Chandrasekar and R. Gupta, "Health monitoring of civil structures with integrated UAV and image processing system," Procedia Computer Science, vol. 54, p. 508–515, 2015.

[29]   A. M. A. Talab, Z. Huang, F. Xi and L. HaiMing, "Detection crack in image using Otsu method and multiple filtering in image processing techniques," Optik-International Journal for Light and Electron Optics, vol. 127, no. 3, p. 1030–1033, 2016.

[30]   S. Dorafshan, M. Maguire and M. Chang, "Comparing automated image-based crack detection techniques in spatial and frequency domains," in Proceedings of the 26th American Society of Nondestructive Testing Reseach Symposium, Jacksonville, FL, 2017.

[31]   S. Dorafshan and M. Maguire, "Autonomous detection of concrete cracks on bridge decks and fatigue cracks on steel members," in Digital Imaging 2017,

Mashantucket, CT, 2017.

[32]   Y. Noh, D. Koo, Y. M. Kang, D. Park and D. Lee, "Automatic crack detection on concrete images using segmentation via fuzy C-means clustering," in Proceedings of the 2017 International Conference on Applied System Innovation, Sapporo, 2017.

[33]   H. Kim, E. Ahn, S. Cho, M. Shin and S. H. Sim, "Comparative analysis of image binarization methods for crack identification in concrete structures," Cement and Concrete Research, vol. 99, p. 53–61, 2017.

[34]   A. Mohan and S. Poobal, "Crack detection using image processing: A critical review and analysis," Alexandria Engineering Journal, vol. In press., 2017.

[35]   R. C. Gonzalez and R. E. Woods, Digital image processing, Upper Saddle River, NJ: Prentice Hall, 2002.

[36]   S. Butterworth, "On the theory of filter amplifiers," Wireless Engineer, vol. 7, no. 6, p. 536–541, 1930.

[37]   H. Blinchikoff and H. Krause, Filtering in the time and frquency domains, The Institution of Engineering and Technology, 2001.

[38]   N. Otsu, "A threshold selection method from gray-level histograms," IEEE Transactions on Systems, Man, and Cybernetics, vol. 9, no. 1, p. 62–66, 1979.

[39]   S. Xing, "Structural Identification and Damage Identification using Output-Only Vibration Measurements," http://digitalcommons.usu.edu/etd/1067, 2011.

[40]   G. Hearn, Bridge inspection practices, Transportation Research Board, 2007.

[41]   D. Pines and A. E. Aktan, "Status of structural health monitoring of long-

span bridges in the United States," Progress in Structural Engineering and Materials, vol. 4, no. 4, p. 372–380, 2002.

[42]   M. R. Jahanshahi, J. S. Kelly, S. F. Masri and G. S. Sukhatme, "A survey and evaluation of promising approaches for automatic image-based defect detection of bridge structures," Structures and Infrastructure Engineering, vol. 5, no. 6, p. 455–486, 2009.

CHAPTER VI

COMPARISON OF DEEP CONVOLUTIONAL NEURAL NETWORKS AND EDGE

DETECTORS FOR IMAGE-BASED CRACK DETECTION IN CONCRETE

Abstract

This chapter compares the performance of common edge detectors and deep

convolutional neural networks (DCNN) for image-based crack detection in concrete

structures. A dataset of 19 high definition images (3420 sub-images, 319 with cracks and

3101 without) of concrete is analyzed using six common edge detection schemes

(Roberts, Prewitt, Sobel, Laplacian of Gaussian, Butterworth, and Gaussian) and using

the AlexNet DCNN architecture in fully trained, transfer learning, and classifier modes.

The relative performance of each crack detection method is compared here for the first

time on a single dataset. Edge detection methods accurately detected 53–79% of cracked

pixels, but they produced residual noise in the final binary images. The best of these

methods was useful in detecting cracks wider than 0.1 mm. DCNN methods were used to

label images, and accurately labeled them with 99% accuracy. In transfer learning mode,

the network accurately detected about 86% of cracked images. DCNN methods also

detected much finer cracks than edge detection methods. In fully trained and classifier

modes, the network detected cracks wider than 0.08 mm; in transfer learning mode, the

network was able to detect cracks wider than 0.04 mm. Computational times for DCNN

are shorter than the most efficient edge detection algorithms, not considering the training

process. These results show significant promise for future adoption of DCNN methods

for image-based damage detection in concrete. To reduce the residual noise, a hybrid

method was proposed by combining the DCNN and edge detectors which reduced the
noise by a factor of 24.

Introduction

At least a third of the more than 600,000 bridges in the United States include a
concrete superstructure or wearing surface [1]. Routine inspections of concrete bridges
are conducted periodically to assess overall condition and to identify surface cracking or
other degradation [2]. Manned inspections of this type are costly, time consuming, and
labor intensive [3] [4] [5]. Unmanned and autonomous inspections are a potentially
viable alternative to manned inspections [5] [6] [7] [8] [9] [10]. Inspections performed by
robots or unmanned aerial systems (UAS) are typically image-based, meaning that the
inspection platform takes images that are then processed and/or reviewed by an inspector.
Previous literature demonstrates several successful applications of image-based
inspections to detect cracks [11, 12], spalls [13, 14], delaminations [14, 15, 16], and
corrosion [17] in concrete bridges.

Image-based inspections of this type can be performed in three general ways: Raw
image inspection, image enhancement, or autonomous image processing. Raw image
inspection means that the inspector views the images taken during the inspection without
any additional processing [5, 18]. The number of images collected depends on a number
of factors, but is commonly in the hundreds of thousands [5, 18]. Manual identification of
flaws in such large images sets is time consuming and prone to inaccuracy due to
inspector fatigue or human error. Enhanced image inspection refers to the use of some
image processing algorithm to make it easier to identify flaws in inspection images. This

is typically performed using one of several edge detection algorithms, which greatly magnify the visibility of cracks within images. In doing so, the aforementioned problems with inspector fatigue can be mitigated to some degree. Finally, autonomous image processing refers to the use of an algorithm that detects cracks within images. This is typically accomplished using machine learning algorithms or other artificial intelligence schemes.

This chapter discusses the latter two approaches and compares their performance. Image enhancement methods includes the application of a variety of image processing techniques on visual images to detect cracks including but not limited to morphological operations [19], digital image correlation [20, 21], image binarization [22, 23], percolation model [24], wavelet transforms [25], and edge detectors [12] [27] [29] [33] [34] [36] [37] [38] [36]. The autonomous approach for crack detection on the other hand requires a set of training images to learn the features of cracks. Similarly, several researchers have shown the feasibility of autonomous crack detection in visual images using combined image processing techniques and artificial neural networks [30, 40]. Deep convolutional neural networks (DCNNs) have been recently used for concrete crack detection [41, 42, 43].

Despite the abundance of image-based crack detection studies, direct comparisons between these methods is a gap. Save two noteworthy exceptions, most research focuses on developing new methods for crack detection rather than comparing the performance of existing methods. Abdel-Qader et al. [27] compared the performance of the fast Haar transform, Fourier transform, Sobel filter, and Canny filter for crack detection in 25 images of defected concrete and 25 images of sound concrete. The fast Haar transform

was the most accurate method, with overall accuracy of 86%, followed by the Canny

filter (76%), Sobel filter (68%), and the Fourier transform (64%). he processing time was

not considered in the analysis and the criteria for recoding true of false positives in the

binary images were not clear. Lack of definition for metrics such as true positive has seen

in the past studies. Mohan and Poobal [44] reviewed a number of edge detection

techniques for visual, thermal, and ultrasonic images, but the information presented was

from several studies that considered vastly different data sets, and so the results are not

directly comparable. A comparison between two edge detectors, Canny and Sobel, and a

convolutional neural network is done in [42]. However, the comparison was performed

on four images. In addition, the edge detectors were used without pre-processing which is

not a very common practice. Another shortcoming of the comparison in [42] is the lack of

accuracy definition of the edge detector results. This chapter compares image processing

and deep learning techniques together as a reference for future study. which includes a

direct comparison of the performance of four common edge detection methods in the

spatial domain (Roberts, Prewitt, Sobel, Laplacian of Gaussian) and two in the frequency

domain (Butterworth and Gaussian) and an AlexNet-based DCNN in three modes of

training (fully trained, transfer learning, and no-training) by applying them to an

annotated dataset designated for crack detection.

Dataset

The dataset used in this study consisted of 100 images of concrete panels that

simulated reinforced concrete bridge decks for the purpose of verifying various non-

destructive testing. These panels were constructed previously in Systems, Materials, and

Structural Health laboratory (SMASH Lab) at Utah State University. Images are collected with a 16 MP digital single lens reflex camera with 35 mm focal length and no zoom. The target was normal to the axis of the lens at a distance of approximately 0.5 m. The background illumination was in the range 400–1000 lx, as measured by a NIST traceable digital light meter purchased new just prior to measurement. The finest crack width was approximately 0.04mm and the widest was 1.42mm. The original image size was 2592×4608 px and the field of view was approximately 0.3×0.55 m. Images were stored as JPEG with average file size near 5 MB. In order to comply with the architecture of the DCNN, each original image was divided into 180 sub-images with size of 256×256 px. The sub-images were labeled in two categories, 1,574 sub-images with cracks and 16,426 sub-images without cracks. Fig. 6-1Fig. illustrates the studied dataset with one example of high-resolution image, a sub-image labeled as C from the original image if it had a crack, and a sub-image labeled as U from the original image if it did not. For DCNN applications, this dataset was divided into training dataset, validation dataset, and testing dataset as shown in Table 6-1. The testing dataset was selected randomly from 100 original images. The images in this dataset are a portion of the bridge deck images of the structural defect dataset (SDNET2017 [45]). The sub-images in the testing dataset have also been segmented in the pixel-level as Cp and Up for semantic comparison where Cp stands for pixels with cracks and Up stands for sound pixels. The results of the pixel-level segmentation on the testing dataset are presented in Table 6-2. In this table, the Cp ratio stands for the number of pixels in each image labeled as crack to total number of pixels in that image.

100 Original High-resolution Image

Concrete Edge

Concrete Cracks

18,000 sub-images

1,574 Sub-images Labeled C   ~Half-million Pixels Labeled C   16,426 Sub-images Labeled U
                              (Only for testing Dataset)
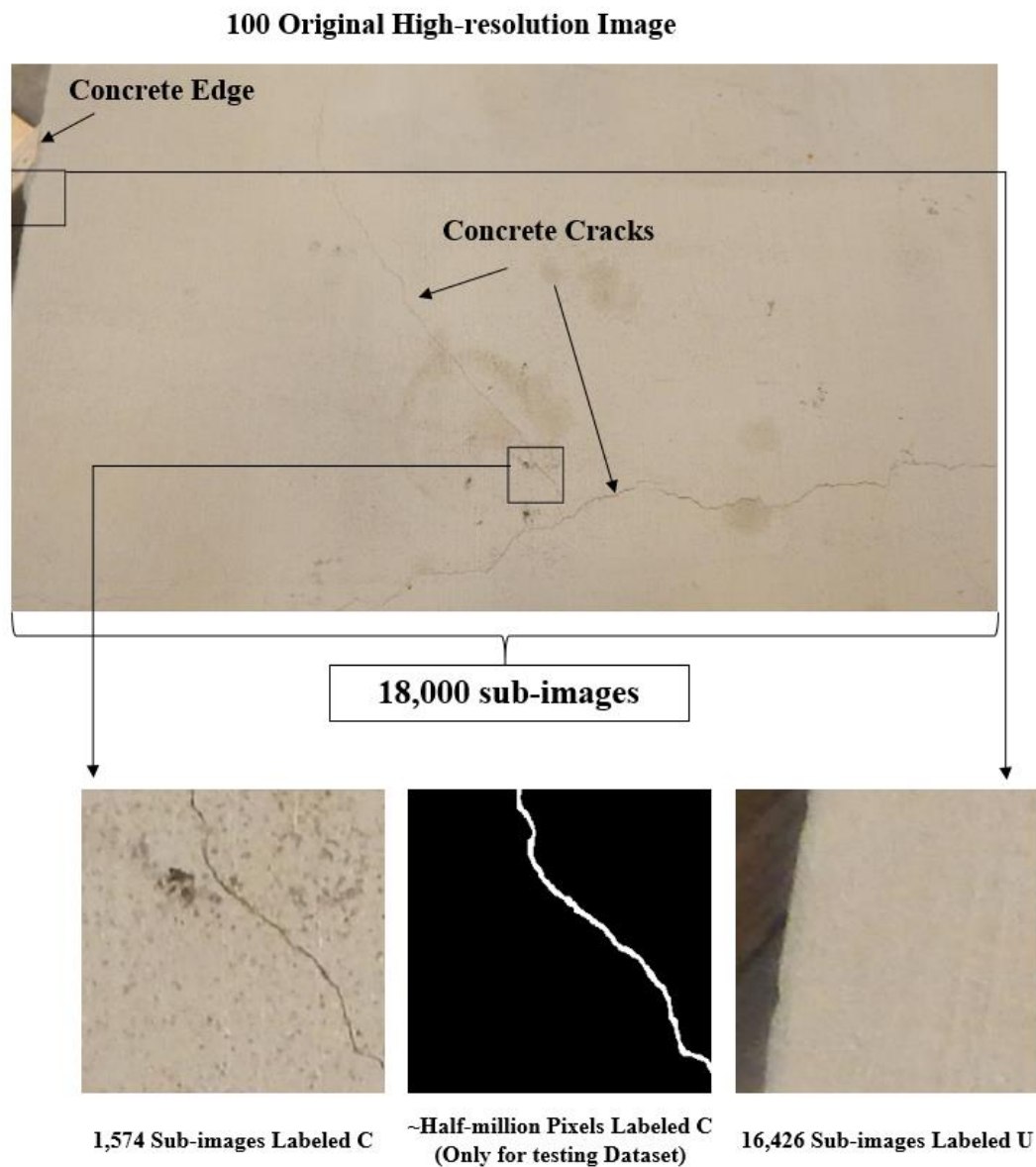
Fig. 6-1 Illustration of the dataset

Table 6-1 Number of cracked and sound sub-images in training, validation, and testing datasets

Dataset	No of Original Images	C	U	Total
Training	81	1129	11680	12809
Validation		125	1646	1771
Testing	19	319	3101	3420

Table 6-2 Number of Cp and Up pixels in the testing dataset

Dataset	Cp	Up	Cp Ratio (%)
im1	18835	11777645	0.16
im2	13952	11782528	0.12
im3	67548	11728932	0.57
im4	13472	11783008	0.11
im5	46192	11750288	0.39
im6	46372	11750108	0.39
im7	46658	11749822	0.40
im8	37572	11758908	0.32
im9	42675	11753805	0.36
im10	88321	11708159	0.75
im11	2693	11793787	0.02
im12	1264	11795216	0.01
im13	3336	11793144	0.03
im14	0	11796480	0.00
im15	5995	11790485	0.05
im16	4203	11792277	0.04
im17	0	11796480	0.00
im18	4953	11791527	0.04
im19	1304	11795176	0.01

Edge Detection

In this paper, edge detection refers to the use of filters (edge detectors) in an image processing algorithm for the purpose of detecting or enhancing the cracks in an image such that they can be more easily and efficiently located within a large image dataset. Cracks in a two-dimensional (2D) image are classified as edges, and thus existing edge detection algorithms are likely candidates for crack identification. 2D images are represented mathematically by matrices (one matrix, in the case of greyscale images, or three matrices in the case of red/green/blue color images). An ideal edge is defined as a

discontinuity in the greyscale intensity field. Crack detection algorithms can emphasize edges by applying filters in either the spatial or frequency domain. Edge detection algorithms purport to make manual crack detection more reliable. In general, such image processing algorithms follow three steps: (1) edge detection, (2) edge image enhancement, and (3) segmentation (sometimes called binarization or thresholding). Edge detection involves the application of various filters in either the spatial or frequency domain to a grayscale image in order to emphasize discontinuities. Edge image enhancement scales the image and adjusts contrast to improve edge clarity. Segmentation transforms the enhanced edge image into a binary image of cracked and sound pixels.

In the spatial domain, the convoluted image E is the sum of the element-by-element products of the image intensity I and the kernel K in every position in which K fits fully in I. For $I_{M \times N}$ (image dimension $M \times N$) and $K_{m \times n}$ (kernel size $m \times n$):

$$E(i,j) = \sum_{k=1}^{m} \sum_{\ell=1}^{n} I(i+k-1, j+\ell-1) K(k, \ell) \qquad (6\text{-}1)$$

E is of size $(M - m + 1) \times (N - n + 1)$. Filters kernels may include x and y components (corresponding to image spatial dimension in horizontal and vertical dimensions), K_x and K_y, in which case the edge image E is the hypotenuse of E_x and E_y.

Four edge detector filters in the spatial domain were employed in this study: Roberts in x and y directions, denoted as K_{Rx} and K_{Ry} in Eq. 6-2, Prewitt in x and y directions, denoted as K_{Px} and K_{Py} in Eq. 6-3, Sobel in x and y directions, denoted as K_{Sx} and K_{Sy} in Eq. 6-4, and Laplacian-of-Gaussian (LoG) denoted as K_{LoG} in Eq. 6-5. A 10×10 LoG filter was employed here with standard deviation of $\sigma = 2$.

$$K_{Rx} = \begin{bmatrix} 1 & 0 \\ 0 & -1 \end{bmatrix} \qquad\qquad K_{Ry} = \begin{bmatrix} 0 & 1 \\ -1 & 0 \end{bmatrix} \qquad (6\text{-}2)$$

$$K_x = \begin{bmatrix} -1 & 0 & 1 \\ -1 & 0 & 1 \\ -1 & 0 & 1 \end{bmatrix} \qquad K_{Py} = \begin{bmatrix} 1 & 1 & 1 \\ 0 & 0 & 0 \\ -1 & -1 & -1 \end{bmatrix} \qquad (6\text{-}3)$$

$$K_{Sx} = \begin{bmatrix} -1 & 0 & 1 \\ -2 & 0 & 2 \\ -1 & 0 & 1 \end{bmatrix} \qquad K_{Sy} = \begin{bmatrix} 1 & 2 & 1 \\ 0 & 0 & 0 \\ -1 & -2 & -1 \end{bmatrix} \qquad (6\text{-}4)$$

$$K_{LoG} = \nabla^2\big(G(x,y)\big) = \frac{x^2+y^2-2\sigma^2}{4\sigma^4} exp\left(-\frac{x^2+y^2}{2\sigma^2}\right) \qquad (6\text{-}5)$$

Edge detection in the frequency domain requires transformation of the spatial

domain image I into the frequency domain image F by fast Fourier transform (FFT). The

edge image E is the element-wise product of the filter kernel K and the frequency domain

image F:

$$E(u,v) = K(u,v) \odot F(u,v) \qquad (6\text{-}6)$$

where u and v are the dimensions of the transformed image in the frequency

domain. Two edge detector filters in the frequency domain were employed in this study:

Butterworth denoted as K_B in Eq. 6-7 and Gaussian denoted as K_G in Eq. 6-8.

$$K_B(u,v) = 1 - \frac{1}{1+\left[\frac{D(u,v)}{D_0}\right]^{2n}} \qquad (6\text{-}7)$$

$$K_G(u,v) = 1 - e^{\frac{-D^2(u,v)}{2\sigma^2}} \qquad (6\text{-}8)$$

where $D(u,v)$ is the distance between the pixel (u,v) and the origin of the

frequency (the center of the $M \times N$ image) as defined by Eq. 6-9, D_0 and n are the user-

defined parameters to define the order and cut-off frequency in the Butterworth filter; and

σ is the user-defined parameter to define the standard deviation of the Gaussian filter.

$$D(u, v) = \sqrt{\left[u - \left(\frac{M}{2} + 1\right)\right]^2 + \left[v - \left(\frac{N}{2} + 1\right)\right]^2} \qquad (6\text{-}9)$$

and $\boldsymbol{K}_B$, and $\boldsymbol{K}_G$, are Butterworth and Gaussian filters.

The scaled edge image $\boldsymbol{E}_{sc}$ is $\boldsymbol{E}$ scaled such that $0 \leq \boldsymbol{E}_{sc} \leq 1$. The enhanced edge image is then:

$$\boldsymbol{E}_e(x, y) = [\boldsymbol{E}_{sc}(x, y) - \min(\boldsymbol{E}_{sc})] \left[\frac{2\sigma_{E_{SC}}}{\max(\boldsymbol{E}_{sc}) - \min(\boldsymbol{E}_{sc})}\right] + \mu_{\boldsymbol{E}_{sc}} \qquad (6\text{-}10)$$

where $\min(\boldsymbol{E}_{sc})$, $\max(\boldsymbol{E}_{sc})$, $\sigma_{E_{sc}}$, and $\mu_{\boldsymbol{E}_{sc}}$ are minimum, maximum, standard deviation, and mean of the scaled edge image, respectively. Edge enhancement is a crucial part of the proposed method by improving the segmentation of pixels with cracks from the background pixels. Fig2 shows an example of the effect of edge enhancement on the final binary image of the proposed algorithm (Sobel edge detector).

| (a) | (b) | (c) |
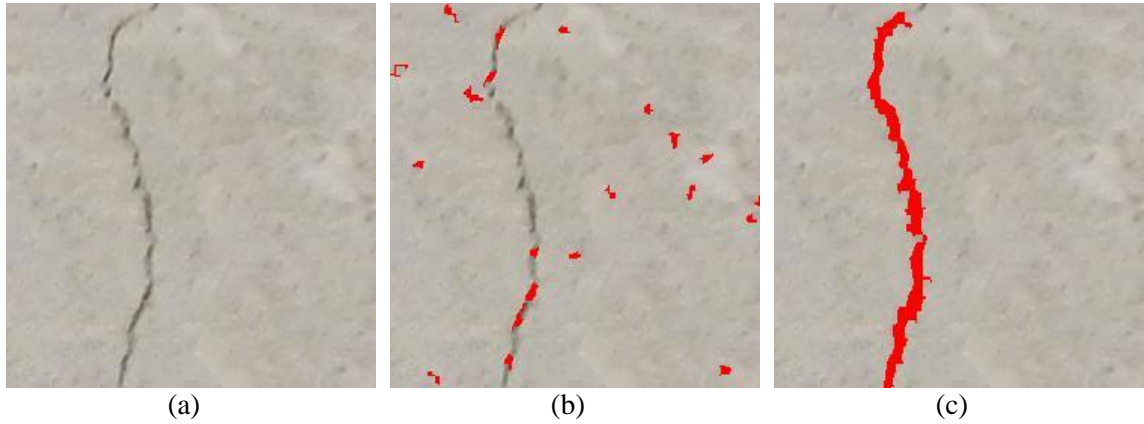
Fig. 6-2 The effect of edge enhancement on the final image of the edge detectors, Sobel, (a) original image, (b) final binary image superimposed on the original image (b) without the edge enhancement, (c) with the edge enhancement

The final binary image $\boldsymbol{B}$ is constructed by segmentation, which assigns a value of one to all pixels in which the intensity exceeds some threshold T and a value of zero to all

other pixels. In this study, a two level binarization is introduced: the first is based on a

pixel intensity threshold T_1 in the enhanced edge image and then based on an area

connectivity threshold T_2 on the binary image from the first level. The first threshold

operation filters the weak edges from the enhanced edge image (Eq. 6-11). By applying

T_1 the strong edges in the enhanced edge image (80% or stronger than the maximum

intensity, $0.8 \max(E_e)$) are preserved as cracks. At this point, the strong edges have been

identified in the first binary image; however, the surface roughness of the concrete can

cause residual noise.

$$T_1 = 0.8 \max(E_e) \qquad\qquad (6\text{-}11)$$

In order to gain more effective segmentations, the morphological operation

closing was carried out on the first level binary image. Closing consists of a dilation

followed by an erosion using an identical structuring element for both operations (see

Fig. 6). The purpose of the closing operation is to unify possibly the discrete parts of the

crack in the first binary image. Structuring elements define the spatial domain on the

binary image in which the morphological operation will be carried out. Circle-shaped

structuring elements with generic dimensions were used to perform the closing operation.

The radius of the structural element was defined as the minimum Euclidean distance

between the centroids of connected components in each binary image. The closing

operation on improved the results of each individual edge detector in terms of true

positives. Fig. 6-4 shows an example where not applying the closing operation cause the

LoG edge detector to miss the more than half the crack after applying the second

threshold operation.

The second binarization operation was designed to segment the cracks from the residual noises in the first binary image based on the area of the connected components in the first level binary image (Eq. 6-12). The connected area $A_c(x, y)$ is the number of contiguous pixels in a connected component, considering eight-neighbor connectivity. $\max(A_c)$ is the area of the largest connected component in the first level binary image. The idea for the area threshold is to control the noise in the final binary image as shown in Fig. 6-5 for the results of the Gaussian high pass filter.

$$T_2 = \max(A_c) \tag{6-12}$$

(a)   (b)   (c)
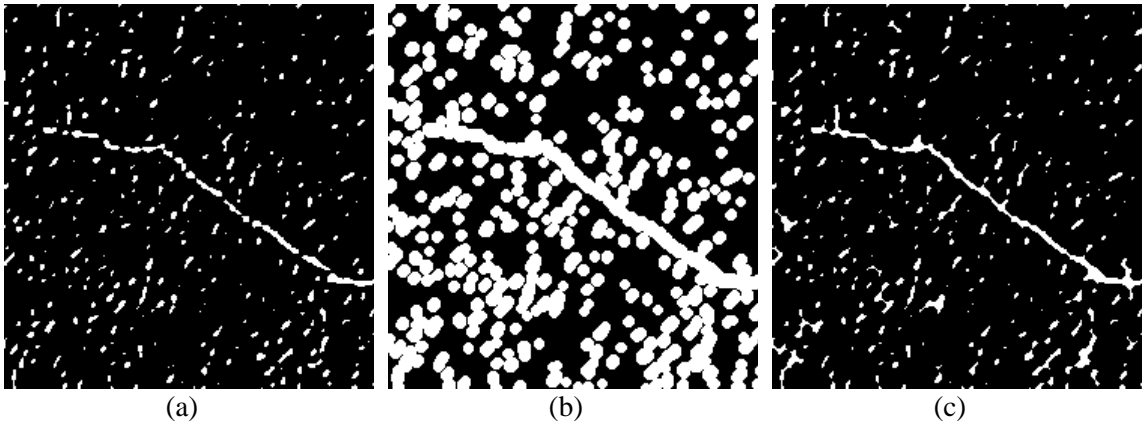
Fig. 6-3 Closing operation illustration (a) first level binary image, (b) dilation, and (c) erosion using a disk structuring element with diameter of 4 px. (LoG edge detector).
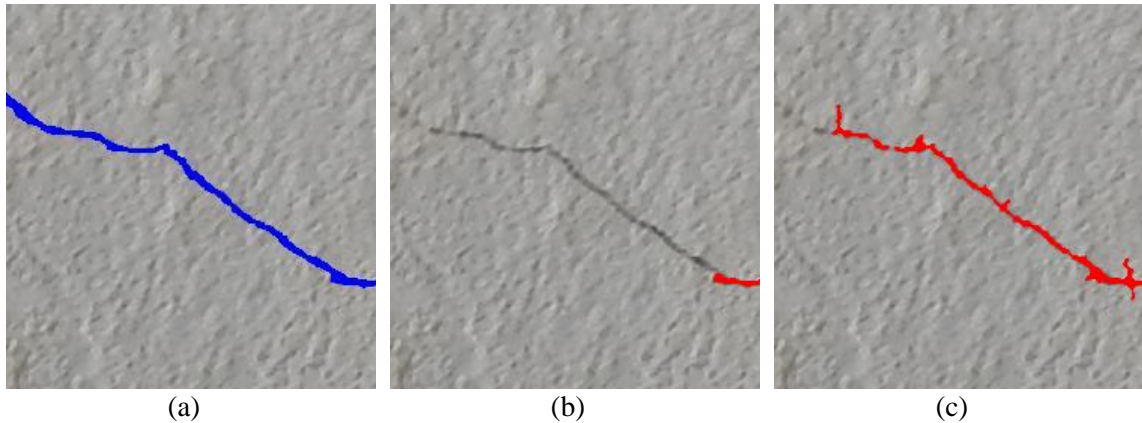
Fig. 6-4 Crack in the (a) ground truth, 1391 px, (b) without the closing operation 391 px correct detection (c) with closing operation 1215 px correct detection (LoG edge detector)
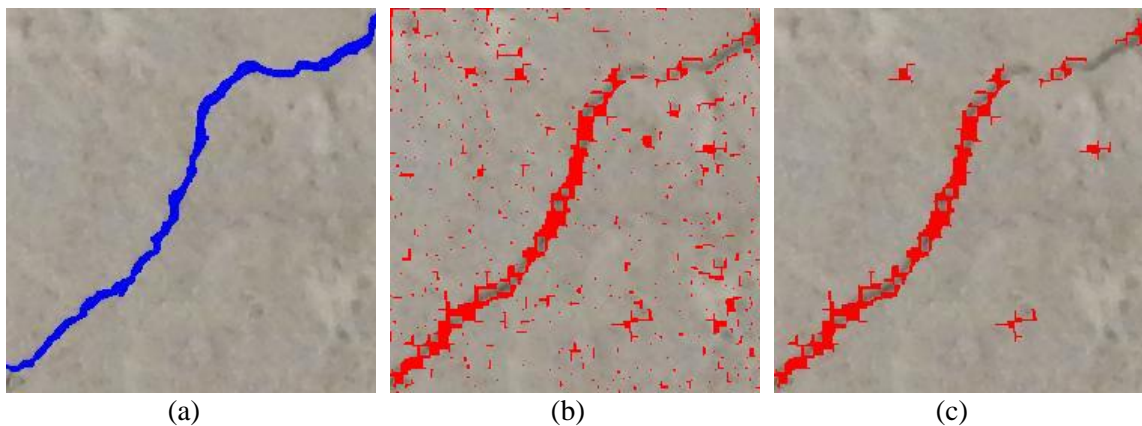
Fig. 6-5 Crack in the (a) ground truth, 2325 px, (b) without second level threshold operation 3672 pixels false detection (c) with second level threshold operation: 214 px false detection (Gaussian edge detector)

DCNN

Using direct image-processing techniques for concrete crack detection has several

drawbacks. First, the algorithms are tailored for certain images in the studied datasets

which affects their performance on new datasets. These algorithms may not be as accurate when tested on new datasets taken in more challenging situations such as low lighting condition, presence of shadows, low quality cameras, etc. Second, the image processing algorithms are often designed to aid the inspector in crack detection and still rely on human judgement for final results [29]. One solution is using machine learning algorithms to analyze the inspection images [46] [47]. Deep convolutional neural networks (DCNNs) are a type of feedforward artificial neural networks which have revolutionized autonomous image classification and object detection in the past 5 years [48]. A DCNN uses a set of annotated, e.g. labeled, images for training and calculates the learning parameters in the learning layers between the input and output layers thorough thousands to millions iterations.

A number of architectures have been employed to create neural networks providing excellent accuracy on open-source labeled datasets, such as ImageNet and MNIST, in the past 4 years [49] [50] [51]. Each architecture includes a number of main layers. The main layers are composed of sub-layers. The total number of layers defined in a software program, like MATLAB, to build an architecture is referred to as "Programmable Layers" in this study. Krizhevsky [49] proposed one of the first architectures of a DCNN, i.e. AlexNet. This architecture has 8 main layers (25 programmable layers) and was the winner of the image classification competition in 2012 (ImageNet [52]). Szegedy et al. proposed another architecture called GoogleNet with 22 main layers (144 programmable layers) and improved the accuracy by introducing inception module in the learning layers which won the 2014 competition [53]. Deep residual learning neural network, ResNet, was introduced in 2016 [54]. ResNet has 50

and 101 main layers (177 and 347 programmable layers) and was the winner of 2016 competition.

DCNNs have been used in vision-based structural health monitoring in recent years for crack detection [42], road pavement cracks [55, 56], corrosion detection [57, 58], multi-damage detection [41, 59] structural health monitoring [62]. Due to popularity of Unmanned Aerial Systems (UASs) for structural health monitoring and bridge inspection [63] applications of DCNNs in UAS-assisted inspections has begun to attract researchers for more robust non-contact damage detection [43, 64, 65].

In general, DCNN architecture includes an input layer, learning layers, and an output layer [66]. The input layer reads the image and transfers it to the learning layers. The learning layers perform convolution operations, applying filters to extract image features. The output layer classifies the image according to target categories using the features extracted in the learning layers. The neural network can be trained by assigning target categories to images in a training dataset and modifying filter values iteratively through back propagation until the desired accuracy is achieved.

DCNN can be used for crack detection in three ways: classification [42], localization [41], or segmentation. The goal of classification is to label each image as cracked or sound. The training and validation datasets comprise pre-classified cracked and sound images. The goal of localization is to determine bounding coordinates that identify the location of a crack within an image. As before, the training and validation datasets include both cracked and sound images, but the cracked images have bounding boxes drawn around the location of the crack. The goal of segmentation is to classify each pixel as cracked or sound, and the training and validation datasets comprise a very

large number of pre-classified pixels. The computational intensity of DCNN normally

necessitates subdivision of images to reduce computational requirements.

The AlexNet DCNN architecture, illustrated in Fig. 6-6 comprises five

convolution layers (C1—C5), three max pooling layers (MP1—MP3), seven nonlinearity

layers using the rectified linear unit (ReLU) function (ReLU1—ReLU7), two

normalization layers (Norm1—Norm2), three fully connected layers (FC1—FC3), two

dropout layers (DP1—DP2), one softmax layer (SM), and one classification layer (CL).

Each layer is applied to the image using the convolution operation (Eq. 6-1). Fig. 6-6

shows the architecture of the AlexNet along with its corresponding filter number and

size. The kernel values are determined iteratively through training, but the size, number,

and stride of the kernels are predetermined. The nonlinearity layers operate on the result

of each convolution layer through element-wise comparison. The ReLU function used for

nonlinearity is defined as the maximum value of zero and the input:

$$f(x) = \begin{cases} 0, & x < 0 \\ x, & x \geq 0 \end{cases} \qquad (6\text{-}13)$$

Following the non-linearity layer, a max pooling layer introduces a representative

for a set neighboring pixels by taking their maximum value. The max pooling layers are

essential to reduce the computational time and overfitting issues in the DCNN. After the

max pooling layer, one or several fully connected layers are used at the end of the

architecture. The fully connected layer is a traditional multi-layer perceptron followed by

a softmax layer to classify the image. The mission of the fully connected layers is to

connect the information from the past layers together in way that the softmax layer can

predict the results correctly during the training process. The optimum combination is

achieved from a process called backpropagation algorithm (partial derivatives of the

softmax layer output with respect to weights).
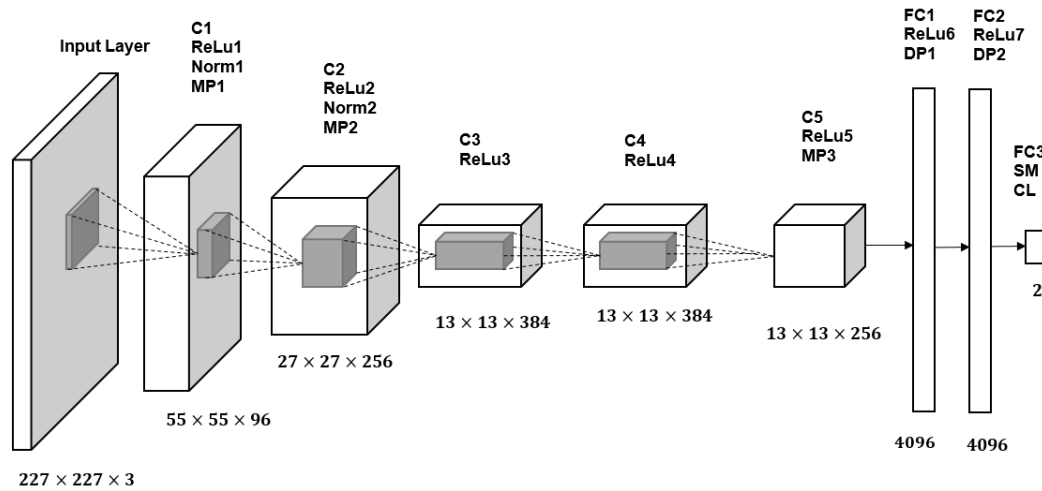
Fig 6-6 AlexNet DCNN architecture

The purpose of the softmax layer is to ensure the sum of probabilities for all

labels is equal to 1. In addition to these basic layers, a DCNN also includes

normalization, dropout, and classification layers. Normalization layer normalizes the

response around a local neighborhood to compensate with the possible unbounded

activations from the ReLu layer. The dropout layer is a probability-based threshold layer

that filters responses smaller than a threshold probability (50% is common). The

classification layer is similar to the fully connected layers. For detailed explanations of

function of each layer and their interaction, readers can refer to Reference [67]

Three modes are used for applying the network on the training dataset. The first

mode is to Fully Train (FT) the network from scratch (FT mode) on the training dataset.

In this mode all the weights are assigned with random numbers and the computed through

iterations based on the training dataset. Obtaining an annotated dataset for concrete

cracks as big as ImageNet is not currently feasible. Even if a large concrete crack dataset

was available, training process from scratch could take days to complete on hardware

with several graphic processor units (GPUs), and would therefore be prohibitively time

consuming. However, it is possible to apply a previously trained network (pre-trained

network) on a small dataset and obtain reasonable accuracy [68]. Pre-trained networks

can be applied on a new dataset in different ways [69]. These methods are usually

referred to as "domain adaptation" in the deep learning literature. One can use an already

trained DCNN on the ImageNet dataset as a classifier for new images. This type of

domain adaptation is referred to as Classifier (CL mode). In CL mode, only the last fully

connected layer needs to be altered to match the target labels in concrete dataset. The

network then uses the pre-trained weights and forms a classifier based on the training

dataset. Note that no actual training happens when CL mode is used. Another studied

domain adoption method is to partially retrain a pre-trained network and modify the

layers according to a new dataset. This approach is called fine-tuning or transfer learning

(TL mode). In the TL mode, the network has to be re-trained since both classifier and

weights have to be updated based on the new dataset. In the TL mode, the weights of the

lower-level layers (closer to the input image layer) are preserved. These weights are

computed from training on millions of images and consist of generic feature extractors

such as edge detectors. Therefore, the determined lower-level weights can be applied on

any dataset for feature extraction. On the other hand, the classifier layers (close to end of

network) are more sensitive to the training dataset and its labels. To adjust the network to

the new dataset, the weights in the high-level layers are updated through training on the new dataset.

Experimental Program

Computational Resources

All computations were performed on a desktop computer with 64-bit operating system, 32 GB memory, and 3.40 GHz processor running a GeForce GTX 750 Ti graphics processing unit (GPU). Image processing was performed in MATLAB.

Edge Detection Program

The testing dataset of 319 C and 3101 U sub-images was iteratively processed using each of the six edge detection schemes discussed in the edge detection section. Unlike the past studies [30, 26, 62], the metrics to evaluate the performance of each edge detector was defined very clearly on a pixel level. The final binary images were compared to the ground truth. True positive (TP) is when the edge detector identified a pixel on the crack pixels (Cp). False negative is when the edge detector did not identify a pixel on the crack pixels (Cp). True negative (TN) is when the edge detector did not identify a pixel on the sound pixels (Up), and false positive is when the edge detector identified a pixel on the sound pixels (Up). Note all comparisons were performed on the final binary images produced by each edge detector. Fig. 6-7 shows examples of how metrics are calculated: (a) the original image is segmented into 1,582 Cp pixels (highlighted) and 63,954 Up pixels, (b) the final binary image super imposed on the original image, Roberts edge detector, identified 2,276 Cp pixels (highlighted) and

63,260 Up pixels, (c) 1,367 pixels in the final binary image were TP, (d) 215 pixels in the final binary image were FN, (e) 63,046 pixels in the final binary image were TN, and (f) 909 pixels in the final binary image were FP. The metrics in the Fig. 6-7c through Fig. 6-7f are shown in white. Note that for U sub-images, TP and FN are meaningless and only TN and FP are recorded.

The team then rated each edge detection scheme in terms of true positive rate (TPR), true negative rate (TNR), accuracy (ACC), positive predictive value (PPV), negative predictive value (NPV), and F1 score, defined as follows

$$TPR = \left(\frac{TP}{TP+FN}\right) \tag{6-14}$$

$$TNR = \left(\frac{TN}{TN+FP}\right) \tag{6-15}$$

$$ACC = \left(\frac{TP+TN}{TP+FN+TN+FP}\right) \tag{6-16}$$

$$PPV = \left(\frac{TP}{TP+FP}\right) \tag{6-17}$$

$$NPV = \left(\frac{TN}{TN+FN}\right) \tag{6-18}$$

$$F1 = \left(\frac{2TP}{2TP+FN+FP}\right) \tag{6-19}$$

In addition, missed crack width (MCW), and computational time (T) are also compared between different edge detectors. MCW is defined as the coarsest crack that went undetected by a particular edge detection scheme, as determined by crack width measurement using a crack width microscope with 0.02 mm resolution. Computational time is defined as the average processing time for ten runs of a particular edge detection scheme, normalized by the number of images (180 sub-images).
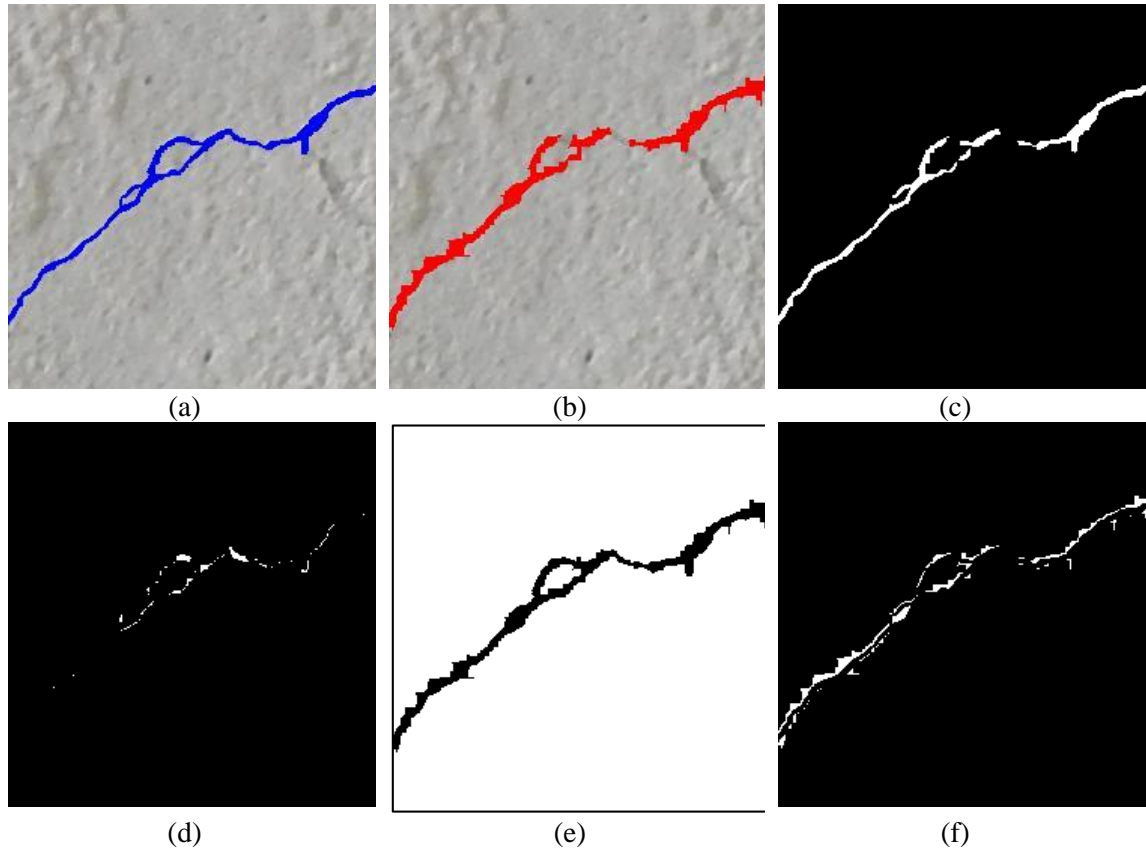
Fig. 6-7 Examples of metric, (a) ground truth, Cp=1,582 px, Up=63,954 px, (b) final binary image using Roberts edge detector, Cp=2276 px, Up=63,260 px (c) TP=1367 px, (d) FN=215 px, (e) TN=63,045 px, (f) FP=909 px (Robersts edge detector)

DCNN Program

Crack detection using DCNN was performed by classification of sub-images in the fully trained, transfer learning, and classifier modes. A total of 12,809 sub-images (1,129 labeled C and 11,680 labeled as U), were selected at random for inclusion in the training dataset, and 1,771 (125 labeled as C and 1,646 labeled as U) were selected for the validation dataset. The remaining 3,420 sub-images (319 labeled as C and 3101 labeled as U) made up the testing dataset.

Batch size number and validation criterion determine the number of iterations in training process. Larger batch sizes result in faster convergence, but batch size is limited by the available GPU memory. The selected batch size was 10. The training dataset has 12,809 sub-images. Number of iterations to cover all sub-images was simply calculated by dividing the total sub-images to the batch size, i.e. 1281 iterations. This number of iterations is known as an epoch. A maximum of 30 epochs were considered for back propagation on the network, meaning that the network performs as many $30 \times 1281 = 38,430$ iterations to finish the training. The network was set to stop iterating once the accuracy in the validation dataset stopped improving in three consecutive epochs. If the validation criterion is not met by the end of 30th epoch, more iterations cycles should be considered for the training.

The network in each mode is used to classify the sub-images in the testing dataset and the results are compared to the ground truth. TP is when the network correctly labeled a sub-image as C, and a FN when the network failed to do so. A TN is when the network correctly labeled a sound sub-image as U and a FN when the network labeled a sub-image as C in a sound sub-image. TPR, TNR, ACC, PPV, NPV, and F1 are calculated according to Eq. 6-14 through Eq. 6-19. T and MCW are evaluated in the same manner as the edge detector approach except that the training time is not considered when calculating the T for DCNN.

Results and Discussion

Edge Detection Results

A summary of results for the six edge detectors applied on the C class and U class

sub-images are shown in Table 6-3 and Table 6-4, respectively. The metrics for

comparison are shown Fig. 6-8a in terms of TPR, PPV, and in Fig. 6-8b in terms of TNR,

ACC, and NPV. The latter metrics were significantly affected by the data imbalance

between Cp and Up pixels. Nevertheless, the evaluated metrics in this chapter are on the

pixel-level which makes the comparison unique compared to previous crack detection

studies. LoG produced the highest TPR with 76% followed by Sobel and Prewitt with

76% and 69%. In the spatial domain, Robert edge detector produced lowest TPR, 53%,

which was still higher that the TPRs produced by frequency domain edge detector, where

Butterworth detected 41% and Gaussian detected only 31% of the crack pixels. LoG edge

detector also produced the highest PPV, 60%, followed by Sobel and Prewitt with 56%

and 54%. Gaussian high pass filter had only 18% PPV which was the lowest among the

studied methods. F1 scores ranged from 23% in sub-images segmented by Gaussian high

pass filter to 68% in sub-images segmented by LoG. Roberts and Gaussian high pass

filter produced the lowest TNR values, 96% and 97%, respectively and the lowest ACC,

both 95%. As for NPV, the lowest values were 95% and 96% when Gaussian and

Butterworth edge detectors were used, respectively. Again LoG was the most accurate,

98%, and produced the highest TNR=99% and NVP=99.5%. The difference in metrics in

Fig. 6-8b is only 2%-4% but note that these metrics are affected by the gigantic class

imbalance between Cp and Up pixels (only 2% of the pixels were Cp). To see this

difference better, percentage of reported FP pixels per sub-image, noise ratio (NR), for

each edge detector is shown in Fig. 6-8c. To calculate the noise ratio, first the average FN

for each method was calculated by dividing total number of FNs to the number of sub-

images in each class, 319 in C class, and 3101 in U class. The NR is then calculated as

the average FNs divided by total number of pixels in each sub-image, i.e. 256×256.
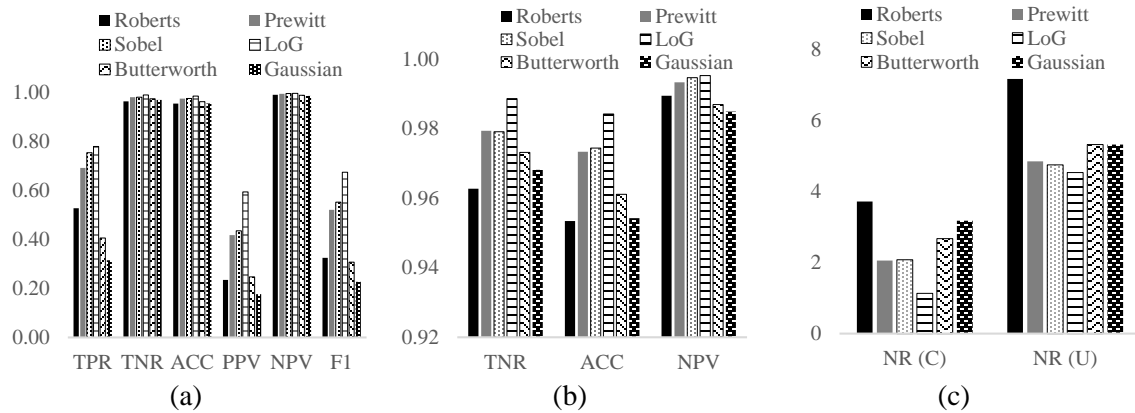
Fig. 6-8 Results of the studied edge detectors on the sub-images in the C class (a) TRP, PPV, and F1 (b) TNR, ACC, and NPV, (c) NR in C and U classes.

Table 6-3 Summary of edge detector performance on sub-images in the C class

Domain	Edge Detector	TPR	TNR	ACC	PPV	NPV	F1	MCW (mm)	T (s)
Spatial	Roberts	0.53	0.96	0.95	0.23	0.99	0.32	0.40	5.15
	Prewitt	0.69	0.98	0.97	0.42	0.99	0.52	0.20	4.13
	Sobel	0.76	0.98	0.97	0.44	0.99	0.56	0.20	4.64
	LoG	0.79	0.99	0.98	0.60	1.00	0.68	0.10	3.79
Frequency	Butterworth	0.41	0.97	0.96	0.25	0.99	0.31	0.20	5.76
	Gaussian	0.32	0.97	0.95	0.18	0.98	0.23	0.20	5.70

Table 6-4 Summary of edge detector performance on sub-images in the U class

Domain	Edge Detector	TNR	T (s)
Spatial	Roberts	0.93	5.46
	Prewitt	0.95	4.71
	Sobel	0.95	4.83
	LoG	0.95	4.05
Frequency	Butterworth	0.95	5.98
	Gaussian	0.93	5.86

As seen for sub-images in C class NR values, 2.4% on average, were almost half of the ones in the U class, 5.3% on average. This is due to the fact that the proposed methodology for crack detection is based on the assumption that there is a crack in the investigated image and it is the largest connected component in the first level binary image. Therefore, noise and irrelevant objects are preserved in the final binary image in U class as FN. In addition, the LoG edge detector produced the lowest NR values, 1.1% in the C class and 4.5% in the U class while Roberts and frequency domain detectors were the worst ones in both classes.

Factoring Roberts, overall the spatial domain edge detectors produced better binary images for crack detection compared to frequency domain ones. The same trend can be seen for values of T in Table 6-3 and Table 6-4 where the fastest method was LoG. Finally, LoG detected finer cracks than the rest of studied method with MCW of 0.1 mm. Fig. 6-9 shows an example of crack detection using different edge detectors along with the original image and ground truth. LoG edge detector performed better than all the other studied detectors in all considered metrics.

DCNN Results

Training and Validation

Fig. 6-10 shows the achieved accuracy of the DCNN under fully trained and transfer learning during training and validation. In fully trained mode, the validation criterion was met after 14 epochs (17934 iterations), which required 6,200 seconds processing time. The resulting validation accuracy was 97.50%. In transfer learning mode, the validation criteria were met after 7 epochs (8967 iterations), which required

4,100 seconds processing time. In classifier mode, the classifier was constructed in 299 seconds and achieved 98.1% accuracy on the validation dataset.

Testing

Table 6-5 summarizes the performance of DCNN crack detection in the testing dataset. In general, the DCNN crack detection algorithms performed exceedingly well compared to the traditional detectors. In fully trained mode, the algorithm scored 212 TPs out of 319 cracked sub-images and 3099 TNs out of 3,101 sound sub-images. In transfer learning mode, the algorithm scored more TPs but also scored more FPs. The network in the CL mode performance in terms of TP and TN were in the middle of the FT and TL modes (TP=267 and TF=52).
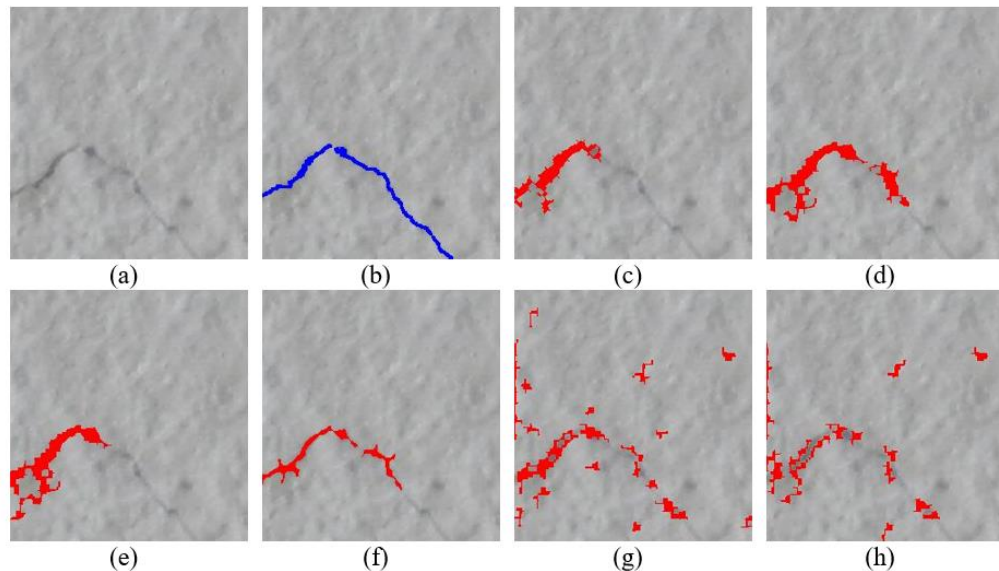
Fig. 6-9 An example of edge detector performance on a 0.02 mm crack (a) original image, (b) GT=1145 px, (c) Roberts, TPR=39% (d) Prewitt, TPR=60%, (e) Sobel, TPR=55%, (f) LoG, TPR=71%, (g) Butterworth, TPR=38%, (h) Gaussian, TPR=17%
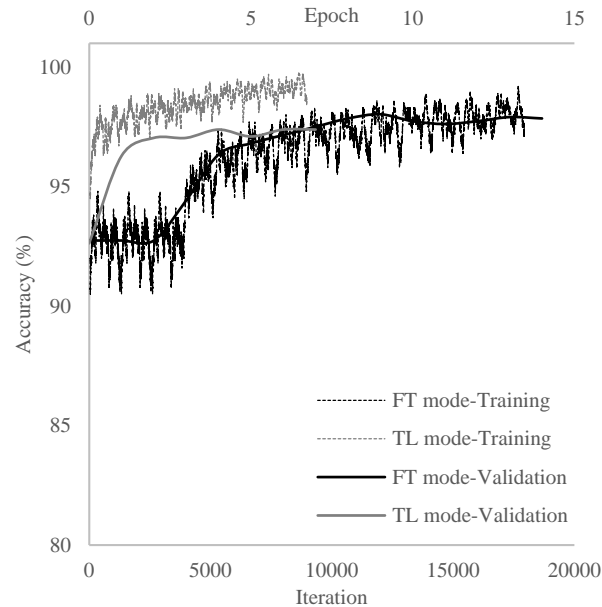
Fig. 6-10 DCNN accuracy during training and validation

In all three cases, the accuracy matched or exceeded 97%. However, the TL mode had NPV=99%, F1=89%, and ACC=98% which were the highest among the studied modes. The highest positive predictive value was in the FT mode (PPV=99%) while TL mode produced only PPV=92%. The CL mode produced the highest FPs which lead to the lowest NPV of 98% among the studied modes. The metrics are shown in Fig. 6-11. As seen the most tangible difference were observed in TPR, PPV, and F1 scores among different metrics since they are more affected by the TPs and C class had considerably less sub-images.
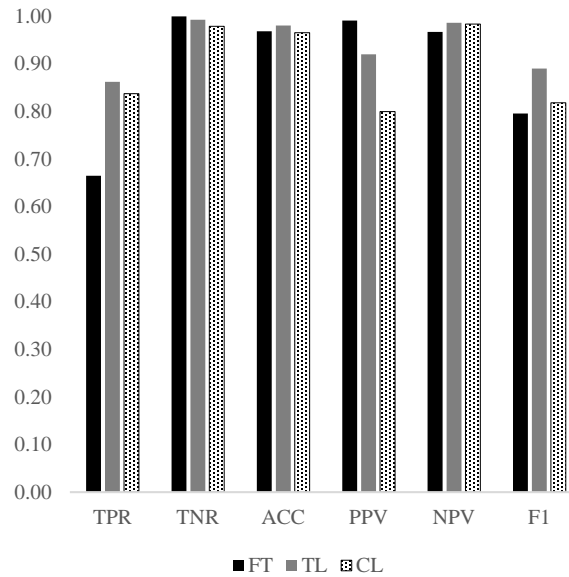
Fig. 6-11 Metrics for the DCNN in FT, TL, and CL modes

Table 6-5 Summary of DCNN results

Mode	TP	FN	TN	FP	TPR	TNR	ACC	PPV	NPV	F1	MCW (mm)	Time (s)
FT	212	107	3099	2	0.66	1.00	0.97	0.99	0.97	0.80	0.08	2.65
TL	275	44	3077	24	0.86	0.99	0.98	0.92	0.99	0.89	0.04	2.81
CL	267	52	3034	67	0.84	0.98	0.97	0.80	0.98	0.82	0.08	2.75

The MCW for fully trained and classifier modes was 0.08 mm. In transfer learning mode, the missed crack width was 0.04 mm. Fig. 6-12 shows fully trained, transfer learning, and classifier DCNN results for a sub-image containing a 0.08 mm crack. As shown in the figure, the 0.08 mm crack was detected only in transfer learning mode, and went undetected in fully trained and classifier modes. The computational time was similar for all three DCNN modes were comparable (2.65-2.81 seconds per 180 sub-images). However, the network in the FT mode required more time for training due to more performed iterations compared to the TL mode, which was expected. In the authors

experience, using an AlexNet-based network in TL mode can be up to 50% less time-consuming than the FT mode on concrete image dataset [37, 39]. On the other hand, the network on the CL mode has the advantage of not relying on the training and can be considered the fastest way of testing the network on new datasets. The absence of training in CL mode, however, adversely affected the TNR, ACC, and PPV of the network, which is also an expected outcome [37]. Transfer learning mode was the most accurate and detected the finest cracks, but also took the longest computational time.

| (a) | (b) | (c) |
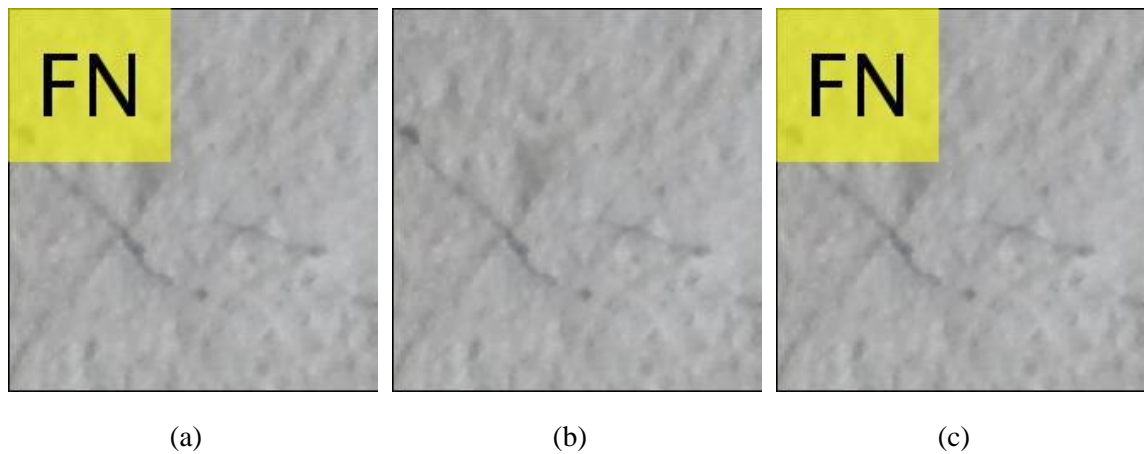
Fig. 6-12 DCNN results for a crack of width 0.08 mm: (a) FT mode, (b) TL mode, and (c) CL mode

Fig. 6-13a through c show representative results for DCNN in fully trained, transfer learning, and classifier modes, respectively. Since the objective is to find the cracks, sub-images in the U class are shaded and sub-images in the C class are shown clearly. Incorrectly labeled sub-images (FN and FP) are identified using a box indicating such.
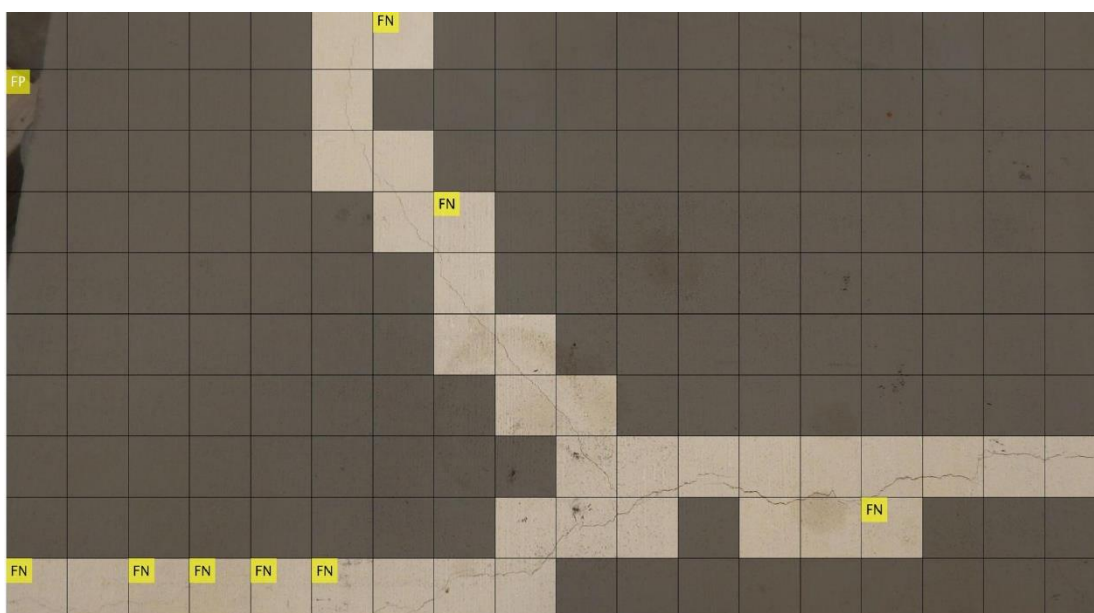
(a)
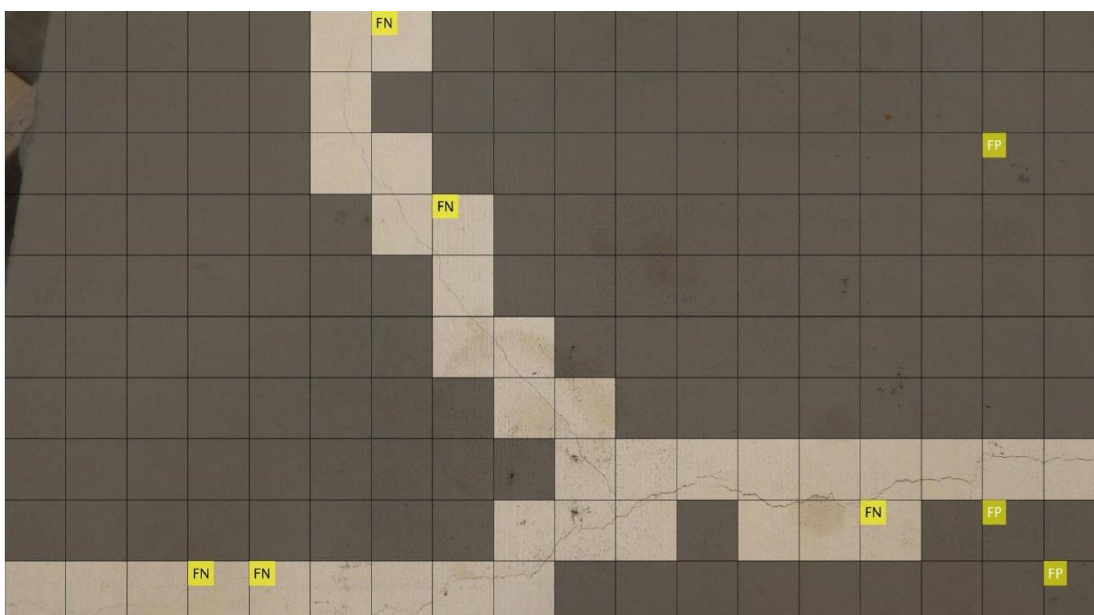
(b)
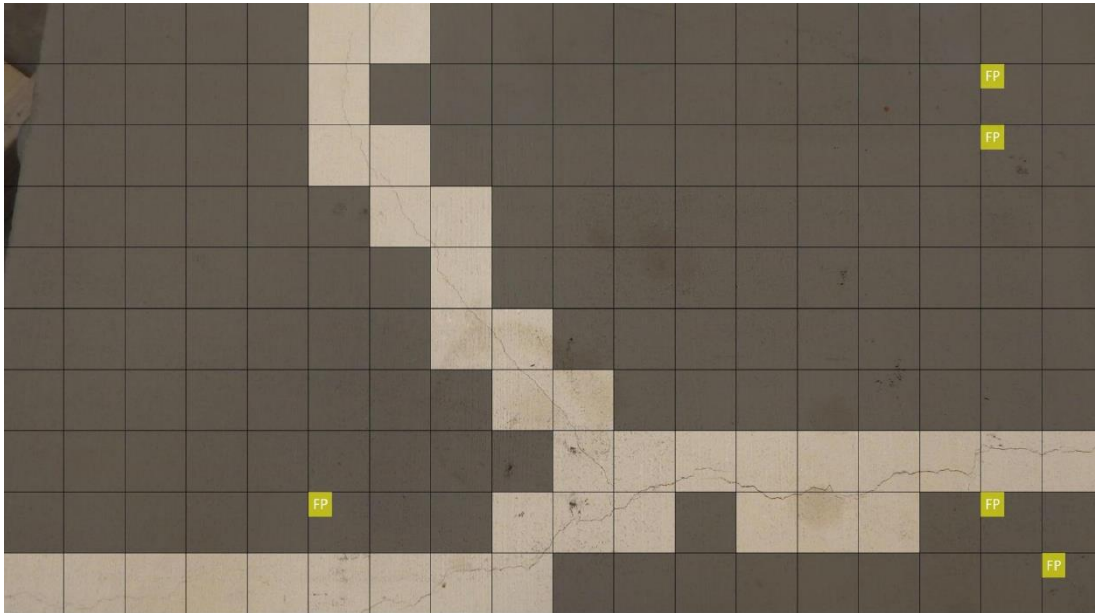
(c)

Fig. 6-13 Results of (a) fully trained DCNN crack detection, (b) transfer learning DCNN, and (c) classifier DCNN for crack detection on the original full scale images in the testing dataset

Comparison

As discussed before, the results presented in Table 6-3 and Table 6-4 for edge detectors and in Table 6-5 for DCNNs are not directly comparable because DCNN results consider sub-images while edge detection results were based on the pixels. However, comparison is possible since the same sub-images and metrics were used to evaluate both approaches. These results are given in Table 6-6.

All of the methods tested here performed better on sound sub-images than on cracked sub-images (i.e., TN > TF), and so the metric numbers skewed high. For example, only 32% of cracked pixels (Cp) were detected using the Gaussian edge detection scheme. Nevertheless, since more than 97% of sound pixels were correctly

detected, the reported accuracy was ACC=95% which is misleading because the PPV for

this edge detector was only 18%, which shows its inefficiency. Several noteworthy

results become apparent. First, while the previous section claimed that there was no clear

winner between DCNN in fully trained and transfer learning modes, the true positive rate

for transfer learning was 20% higher than for fully trained. At the same time, the true

negative rate for transfer learning was only one percent lower than for fully trained. This,

combined with smaller missed crack width and similar computation time requirements,

make transfer learning a clear winner among DCNN modes. F1 scores and PPV values

were significantly for DCNN in all modes were significantly greater than the edge

detector techniques.

Table 6-6 Comparison of DCNN and edge detection performance considering sub-images

Method		TPR	TNR	ACC	PPV	NPV	F1	MCW (mm)	Time (s)
DCNN	FT mode	0.66	1.00	0.97	0.99	0.97	0.80	0.08	2.65
	TL mode	0.86	0.99	0.98	0.92	0.99	0.89	0.04	2.81
	CL mode	0.84	0.98	0.97	0.80	0.98	0.82	0.08	2.75
Edge Detector	Roberts	0.53	0.96	0.95	0.23	0.99	0.32	0.40	5.30
	Prewitt	0.69	0.98	0.97	0.42	0.99	0.52	0.20	4.42
	Sobel	0.76	0.98	0.97	0.44	0.99	0.56	0.20	4.74
	LoG	0.79	0.99	0.98	0.60	1.00	0.68	0.10	3.92
	Gaussian	0.41	0.97	0.96	0.25	0.99	0.31	0.20	5.87
	Butterworth	0.32	0.97	0.95	0.18	0.98	0.23	0.20	5.78

This analysis also shows that DCNN methods performed better at image based concrete crack detection than any of the edge detection methods (expect for FT mode). The LoG edge detector exhibited the highest true positive rate of all six edge detectors, accurately identifying nearly 79% of cracked pixels. LoG also detected the finest cracks of any edge detector, with MCW of 0.1 mm. The TPR among DCNN methods was about 86% and 84% in TL and CL modes, respectively, which was a significant improvement over LoG. In addition, the TFR for the DCNN approach had superiority over the edge detectors due to the high NR ratios (refer to Fig. 6-8c). Furthermore, DCNN methods were able to detect finer cracks than edge detectors. In fully trained and classifier modes, the MCW was 0.08 mm, a marginal improvement over LoG. In transfer learning mode, the MCW was an impressive 0.04 mm.

Computational times also show the superiority of DCNN over edge detectors; computational time was almost 50% less for the DCNNs over edge detectors. However, crack detection using DCNN requires time for training (in FT and TL modes) and classifier construction (in CL mode), which are not taken into account when reporting the computational time. The assumption is that, in the future, pre-trained DCNN will be available for this purpose, so it is not necessarily appropriate to include training time in this comparison. In fact, DCNN can be trained using a very large dataset with images of varying quality (e.g., resolution, lighting condition, focus), making it more robust and applicable to most situations. Edge detectors are typically manually tuned to maximize performance for a particular dataset or subset, diminishing their robustness.

These results highlight the significant promise of DCNN methods for image based crack detection in concrete. The evidence presented here shows that edge detection

methods—which represent the current state of practice—perform reasonably well. DCNN methods provide autonomous crack detection and provide significant performance enhancements over edge detection schemes. The results presented here for DCNN are only a preliminary step in the development of DCNN methods for concrete crack detection. Future work will demonstrate the use of more advanced DCNN for the same problem in the hopes that more advanced networks will provide even better crack detection performance.

The reader should note that the results presented here are for high quality images taken in good lighting and free of vibration. The extension of these results to noncontact image-based inspection and damage detection will require application of the same methods to images with imperfections resulting from poor lighting, vibration, or other issues [43]. This work is ongoing, but the results presented here show promise for autonomous crack detection in concrete structures using noncontact image-based methods.

Despite being recently introduced to structural health monitoring and inspection, DCNNs have improved the vision-based structural defect detection. This study shows the superiority of an AlexNet DCNN over traditional edge detectors for concrete crack detection. The performance of the network can be further enhanced if more powerful architectures such as GoogleNet or RestNet are implemented for crack detection. Unlike edge detectors, the DLCCNs can be used for any types of defect in structures, if enough annotated images are available for training. Formation an annotated image dataset for structural defects, such as ImageNet, is vital for further applications of DCNNs in structural engineering. With this dataset available, new architectures can be developed to

focus on finding a handful of structural defects instead of 1000 different objects, which will reduce the computational time associated with training process. In addition, domain adaptation methods such as transfer learning, will be more effective if the network is previously trained on the structural defects dataset. Improving the performance of domain adaptation techniques makes real-time defect detection in robotic vision-based inspections feasible. In other words, a pre-trained DCNN on the structural defect dataset, can be directly used to accurately classify new images taken by an unmanned aerial system to different structural defects as the inspection is taking place.

Hybrid Crack Detector

Unless semantic networks are used for crack detection, edge detectors are still providing segmentation in the pixel level. This information puts the edge detector in favor of the DCNN for fine monitoring and measurements of cracks but creating the training dataset with classified pixels can be very time consuming and challenging. On the other hand, the sole use of edge detectors has the disadvantage of residual noise or non-crack objects misidentified as cracks. Even with the most effective edge detector, LoG, there was more than 4% of TN (combined of FNs of the images in both C class and U class) which is 9,457,066 sound pixels identified as cracks in the testing dataset. Fig. 6-14 shows examples of TN (highlighted in red) in the three C class sub-images after the final binary image from the LoG edge detector was super-imposed on the original images.

(a)   (b)   (c)
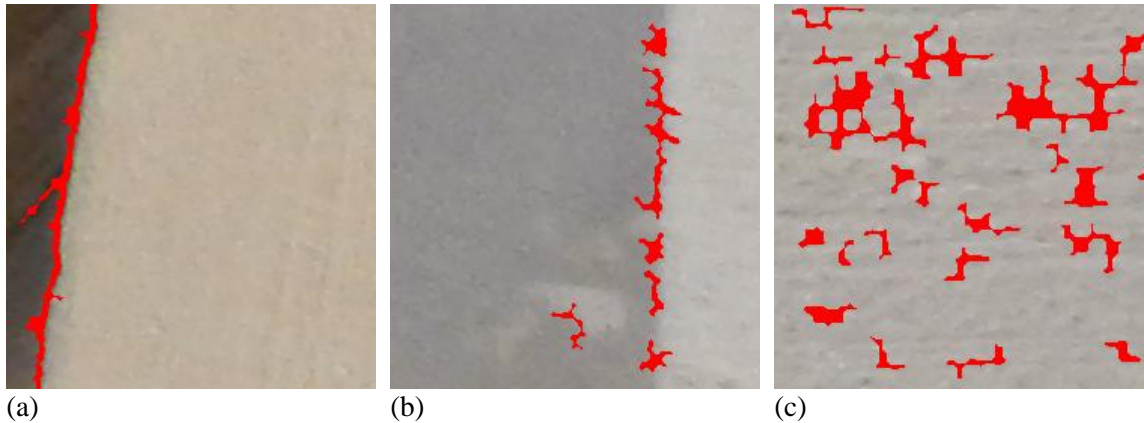
Fig. 6-14 Examples of FNs in the U class images (a) non-crack edge, (b) different surface finish, (c) noise due to the coarse concrete surface

Since the DCNN in FT mode provided such accurate classification for the U class sub-images, only two cases of FP, the network was first used to label all the sub-images in U and C classes. No edge detector was applied on the sub-images identified as U class by the network. The LoG edge detector was applied on the rest of the images in the testing dataset. Combining the two approaches, number of FNs were reduced to 70% of the ones reported only by the LoG edge detector. This leads to an average reduction of the NR values from 2.45% to 0.11%. This improvement can be seen in Fig. 6-15a for an image with crack, and Fig. 6-15b for an image without a crack.

Using this technique also improved the overall performance of the of the edge detectors. As mentioned before, the edge detectors performed better on the sub-images with cracks due the effect of second level threshold which was the reason to evaluate their performance on C class and U class sub-images separately in Table 6-3 and Table 6-4. However, PPV and F1 score metrics would be considerably lower if the both classes

were considered in calculating them. For the best edge detector, i.e. LoG, PPV=6% and F1=11% were achieved when both classes were used. However, using the hybrid technique resulted in the almost the same PPV and F1 score provided in Table 6-3 for the LoG since only C class images were analyzed (with exception of two sub-images in the U class).

(a)

(b)

(c)

(d)
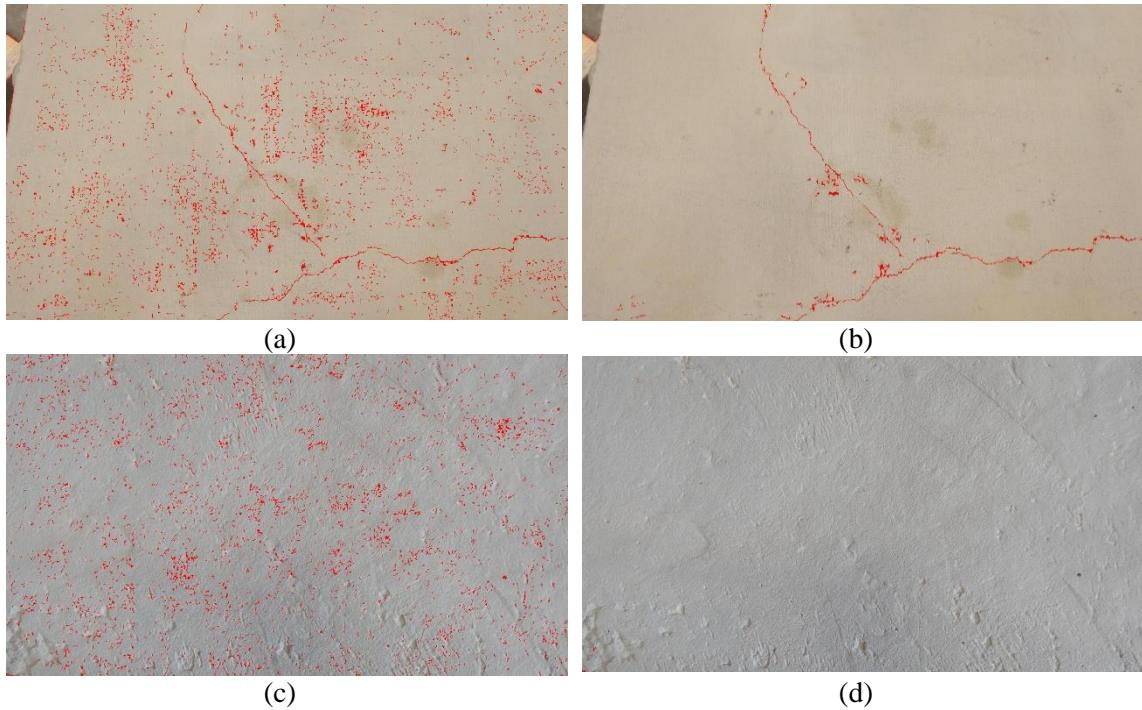
Fig. 6-15 Combination of DCNN and edge detectors (a) the superimposed image with crack using LoG on all sub-images, (b) the superimposed image with crack without using LoG on U class sub-images, (c) the superimposed image without crack using LoG on all sub-images, (d) the superimposed image without crack without using LoG on U class sub-images.

Conclusions

This chapter presents a comparison of edge detection and DCNN algorithms for image based concrete crack detection. The dataset consisted of 3420 sub-images of concrete cracks. Several common edge detection algorithms were employed in the spatial

(Roberts, Prewitt, Sobel, and LoG) and frequency (Butterworth and Gaussian) domains. AlexNet DCNN architecture was employed in its fully trained, classifier, and fine-tuned modes. Edge detection schemes performed reasonably well. The best method—LoG—accurately detected about 79% of cracked pixels and was useful in detecting cracks coarser than 0.1 mm. In comparison, the best DCNN method—the network in transfer learning mode—accurately detected 86% of cracked images and could detect cracks coarser than 0.04 mm. This represents a significant performance enhancement over edge detection schemes and shows promise for future applications of DCNN for image based crack detection in concrete. In addition, a methodology was proposed to reduce the FNs reports by 70% by applying the edge detectors only on sub-images not labeled as uncracked. In addition, a hybrid crack detector was introduced which combines the advantages of both approaches. In the hybrid detector, the sub-images were first labeled by the network in the fully trained mode. Since it produced the highest TNR, the edge detector is not applied on the sub-images labeled as U (uncracked) by the network. This technique reduced the noise ratio of the LoG edge detectors from 2.4% to 0.11% and has the similar effect on the other edge detectors as well.

This study shows the superiority of an AlexNet DCNN over traditional edge detectors for concrete crack detection. This superiority can be further improved when architectures such as GoogleNet or RestNet are implemented for crack detection. DLCCNs are able to classify multiple defects if enough annotated images are available for training. Formation an annotated image dataset for structural defects, such as ImageNet, is vital for further applications of DCNNs in structural engineering. With this dataset available, new architectures can be proposed to focus on finding structural defects

instead of random objects, which will reduce the computational time associated with training process. In addition, domain adaptation methods such as transfer learning, will be more effective if the network is previously trained on the structural defects dataset. Improving the performance of domain adaptation techniques makes real-time defect detection in robotic vision-based inspections feasible. In other words, a pre-trained DCNN on the structural defect dataset, can be directly used to accurately classify new images taken by an unmanned aerial system to different structural defects as the inspection is taking place.

References

[1]   Federal Highway Administration, "National Bridge Inventory," FHWA, McLean, VA, 2017.

[2]   Federal Highway Administration, "National Bridge Inspection Standards (FHWA–FAPG 23 CFR 650C)," FHWA, McLean, VA, 2017.

[3]   B. Chan, H. Guan, J. Jo and M. Blumenstein, "Tuwards UAV-based bridge inspection systems: A reivew and an application perspective," Structural Monitoring and Maintenance, vol. 2, no. 3, p. 283–300, 2015.

[4]   C. H. Yang, M. C. Wen, Y. C. Chen and S. C. Kang, "An optimized unmanned aeiral system for bridge inspection," in Proceedings of the Insternational Symposium on Automation and Robotics in Construction, Vilnius, Lithuania, 2015.

[5]   S. Dorafshan, M. Maguire, N. Hoffer and C. Coopmans, "Fatigue Crack Detection Using Unmanned Aerial Systems in Under-Bridge Inspection," Idaho Transportation Department, Boise, ID, 2017.

[6]   S. Dorafshan, M. Maguire, N. Hoffer and C. Coopmans, "Challenges in bridge inspection using small unmanned aerial systems: Results and lessons learned," in Proceedings of the 2017 International Conference on Unmanned Aircraft Systems, Miami, FL, 2017.

[7]   N. Gucunski, S. H. Kee, H. M. La, B. Basily and A. Maher, "Delamination and concrete quality assessment of concrete bridge decks using a fully autonomous RABIT platform," International Journal of Structural Monitoring and Maintenance, vol. 2, no. 1, p. 19–34, 2015.

[8]   R. S. Lim, H. M. Lag and W. Sheng, "A robotic crack inspectionand mapping system for bridge deck maintenance," ICCC Transactions on Automation Science and Engineering, vol. 11, no. 2, p. 367–378, 2014.

[9]   N. Gucunski, S. H. Kee, H. La, B. Basily, A. Maher and H. Bhasemi, "Implementation of a fully autonomous platform for assessment of concrete bridge decks RABIT," in Structures Congress 2015, Portland, OR, 2015.

[10]   S. Dorafshan and M. Maguire, "Bridge Inspection: Human Performance, Unmanned Aerial Vehicles and Automation," Journal of Civil Strucutral Health monitoring, pp. 1-34, 2018.

[11]   N. Metni and T. Hamel, "A UAV for bridge inspection: Visual servoing control law with orientation limits," Automation in Construction, vol. 17, no. 1, p. 3–10, 2007.

[12]   S. Dorafshan, M. Maguire and X. Qi, "Automatic Surface Crack Detection in Concrete Structures using OTSU Thresholding and Morphological Operations (UTC 01-2016)," Utah Transportation Center, Logan, UT, 2016.

[13]   S. German, I. Brilakis and R. DesRoches, "Rapid entropy-based detection and properties measurement of concrete spalling with machine vision for post-earthquake safety assessments," Advanced Engineering Informatics, vol. 26, no. 4, p. 846–858, 2012.

[14]   K. Vaghefi, T. T. M. Ahlborn, D. K. Harris and C. N. Brooks, "Combined imaging technologies for concrete bridge deck condition assessment," Journal of Performance of Constructed Facilities, vol. 29, no. 4, 2013.

[15]   H. Sohn, D. Dutta, J. Y. Yang, M. DeSimio, S. Olson and E. Swenson, "Automated detection of delamination and disbond from wavefield images obtained using a scanning laser vibrometer," Smart Materials and Structures, vol. 20, no. 4, 2011.

[16]   T. Omar and M. L. Nehdi, "Remote sensing of concrete bridge decks using unmanned aerial vehicle infrared thermography," Automation in Construction, vol. 83, p. 360–371, 2017.

[17]   A. Ellenberg, A. Kontsos, F. Moon and I. Bartoli, "Bridge related damage quantification using unmanned aerial vehicle imagery," Structural Control and Health Monitoring, vol. 23, no. 9, p. 1168–1179, 2016.

[18]   S. Dorafshan, R. Thomas and M. Maguire, "Fatigue Crack Detection Using Unmanned Aerial Systems in Fracture Critical," Journal of Bridge Engineering, 2018.

[19]   M. R. Jahanshahi and S. F. Masri, "Adaptive vision-based crack detection using 3D scene reconstruction for condition assessment of structures," Automation in Construction, vol. 22, pp. 567-576, 2012.

[20]   M. Hamrat, B. Boulekbache, M. Chemrouk and S. Amziane, "Flexural cracking behavior of normal strength, high strength and high strength fiber concrete

beams, using Digital Image Correlation technique," Construction and Building Materials, vol. 106, pp. 678-692, 2016.

[21]   A. Rimkus, A. Podviezko and V. Gribniak, "Processing digital images for crack localization in reinforced concrete members," Procedia Engineering, vol. 122, p. 239–243, 2015.

[22]   L. Li, Q. Wang, G. Zhang, L. Shi, J. Dong and P. Jia, "A method of detecting the cracks of concrete undergo high-temperature," Construction and Building Materials, vol. 162, pp. 345-358, 2018.

[23]   H. Kim, E. Ahn, S. Cho, M. Shin and S. H. Sim, "Comparative analysis of image binarization methods for crack identification in concrete structures," Cement and Concrete Research, vol. 99, p. 53–61, 2017.

[24]   T. Yamaguchi, S. Nakamuran, R. Saegusa and S. Hashimoto, "Image-based crack detection for real concrete surfaces," IEEJ Transactions on Electrical and Electronic Engineering, vol. 3, no. 1, p. 128–135, 2008.

[25]   M. R. Taha, A. Noureldin, J. L. Lucero and T. J. Baca, "Wavelet transform for structural health monitoring: a compendium of uses and features," Structural Health Monitoring, vol. 5, no. 3, pp. 267-295, 2006.

[26]   J. Kittler, R. Marik, M. Mirmehdi, M. Petrou and J. Song, "Detection of defects in colour texture surfaces," in IAPR Workshop on Machine Vision Applications, Kawasaki, 1994.

[27]   I. Abdel-Qader, P. Abudayyeh and M. E. Kelly, "Analysis of edge-detection techniques for crack identification in bridges," Journal of Computing in Civil Engineering, vol. 17, no. 4, p. 255–263, 2003.

[28]   I. Abdel-Qader, S. Pashaie-Rad, P. Abudayyeh and S. Yehia, "PCA-based algorithm for unsupervised bridge crack detection," Advances in Engineering Software, vol. 37, no. 12, p. 771–778, 2006.

[29]   J. K. Oh, G. Jang, S. Oh, J. H. Lee, B. J. Yi, Y. S. Moon, J. S. Lee and Y. Choi, "Bridge inspection robot system with machine vision," Automation in Construction, vol. 18, no. 7, p. 929–941, 2009.

[30]   H. Moon and J. Kim, "Intelligent crack detecting algorithm on the concrete crack image using neural network," in Proceedings of the 28th International Symposium on Automation and Robotics in Construction, Seoul, 2011.

[31]   H. Wang, Z. Chen and L. Sun, "Image preprocessing methods to identify micro-cracks of road pavement," Optics and Photonics Journal, vol. 3, no. 2, p. 99, 2013.

[32]   P. Zheng, "Crack Detection and Measurement Utilizing Image-Based Reconstruction," MS Thesis. Virginia Polytechnic Institute, Blacksburg, VA, 2014.

[33]   R. S. Lim, H. M. La and W. Sheng, "A robotic crack inspection and mapping system for bridge deck maintenance," IEEE Transactions on Automation Science and Engineering, vol. 11, no. 2, p. 367–378, 2014.

[34]   J. W. Kim, S. B. Kim, J. C. Park and J. W. Nam, "Development of crack detection system with unmanned aerial vehicles and digital image processing," in Advances in Structural Engineering and Mechanics (ASEM15), Incheon, 2015.

[35]   S. Sankararinivasan, E. Balasubramanian, K. Karthik, U. Chandrasekar and R. Gupta, "Health monitoring of civil structures with integrated UAV and image processing system," Procedia Computer Science, vol. 54, p. 508–515, 2015.

[36]   A. M. A. Talab, Z. Huang, F. Xi and L. HaiMing, "Detection crack in

image using Otsu method and multiple filtering in image processing techniques," Optik-International Journal for Light and Electron Optics, vol. 127, no. 3, p. 1030–1033, 2016.

[37]   S. Dorafshan, M. Maguire and M. Chang, "Comparing automated image-based crack detection techniques in spatial and frequency domains," in Proceedings of the 26th American Society of Nondestructive Testing Reseach Symposium, Jacksonville, FL, 2017.

[38]   S. Dorafshan and M. Maguire, "Autonomous detection of concrete cracks on bridge decks and fatigue cracks on steel members," in Digital Imaging 2017, Mashantucket, CT, 2017.

[39]   Y. Noh, D. Koo, Y. M. Kang, D. Park and D. Lee, "Automatic crack detection on concrete images using segmentation via fuzy C-means clustering," in Proceedings of the 2017 International Conference on Applied System Innovation, Sapporo, 2017.

[40]   G. K. Choudhary and S. Dey, "Crack detection in concrete surfaces using image processing, fuzzy logic, and neural networks," in In 2012 IEEE Fifth International Conference on Advanced Computational Intelligence (ICACI), , Nanjing, China, 2012.

[41]   Y. J. Cha, W. Choi, G. Suh, S. Mahmoudkhani and O. Büyüköztürk, "Autonomous Structural Visual Inspection Using Region-Based Deep Learning for Detecting Multiple Damage Types," Computer-Aided Civil and Infrastructure Engineering., 2017.

[42]   Y. J. Cha, W. Choi and O. Büyüköztürk, "Deep Learning-Based Crack Damage Detection Using Convolutional Neural Networks," Computer-Aided Civil and Infrastructure Engineering, vol. 32, no. 5, pp. 361-378, 2017.

[43]   S. Dorafshan, C. Coopmans, R. J. Thomas and M. Maguire, "Deep Learning Neural Networks for sUAS-Assisted Structural Inspections: Feasibility and Application," in ICUAS 2018, Dallas, TX, 2018.

[44]   A. Mohan and S. Poobal, "Crack detection using image processing: A critical review and analysis," Alexandria Engineering Journal, vol. In press., 2017.

[45]   M. Maguire, S. Dorafshan and R. Thomas, "SDNET2018: A concrete crack image dataset for machine learning applications," Utah State Universiy, Logan, 2018.

[46]   M. O'Byrne, F. Schoefs, B. Ghosh and V. Pakrashi, "Texture analysis based damage detection of ageing infrastructural elements," Computer-Aided Civil and Infrastructure Engineering, vol. 28, no. 3, pp. 162-177, 2013.

[47]   L. Wu, S. Mokhtari, A. Nazef, B. Nam and H. B. Yun, "Improvement of crack-detection accuracy using a novel crack defragmentation technique in image-based road assessment," Journal of Computing in Civil Engineering, vol. 30, no. 1, 2014.

[48]   J. Schmidhuber, "Deep learning in neural networks: An overview," Neural networks, vol. 61, pp. 85-117, 2015.

[49]   A. Krizhevsky, I. Sutskever and G. E. Hinton, "Imagenet classification with deep convolutional neural networks," Advances in neural information processing systems , pp. 1097-1105, 2012.

[50]   C. Szegedy, W. Liu, Y. Jia, P. Sermanet, S. Reed, D. Anguelov and A. ... & Rabinovich, "Going deeper with convolutions," CVPR, 2015.

[51]   K. He, X. Zhang, S. Ren and J. Sun, "Deep residual learning for image recognition," Proceedings of the IEEE conference on computer vision and pattern

recognition, 770-778.

[52] J. Deng, W. Dong, R. Socher, L. J. Li, K. Li and L. Fei-Fei, "Imagenet: A large-scale hierarchical image database," in IEEE Conference on Computer Vision and Pattern Recognition (CVPR), Miami, FL, 2009.

[53] K. He, X. Zhang, S. Ren and J. Sun, "Deep residual learning for image recognition," in IEEE conference on computer vision and pattern recognition, Seattle. WA, 2016.

[54] C. Szegedy, W. Liu, Y. Jia, P. Sermanet, S. Reed, D. Anguelov and A. ... Rabinovich, "Going deeper with convolutions," in CVPR, 2015.

[55] L. Zhang, F. Yang, Y. D. Zhang and Y. J. Zhu, "Road crack detection using deep convolutional neural network," in Image Processing (ICIP), 2016 IEEE International Conference on, 2016.

[56] A. Zhang, K. C. Wang, B. Li, E. Yang, X. Dai, Y. Peng, Y. Fei, Y. Liu, J. Q. Li and C. Chen, "Automated Pixel-Level Pavement Crack Detection on 3D Asphalt Surfaces Using a Deep-Learning Network," Computer-Aided Civil and Infrastructure Engineering, vol. 32, no. 10, pp. 805-819, 2017.

[57] F. C. Chen and M. R. Jahanshahi, "NB-CNN: Deep Learning-based Crack Detection Using Convolutional Neural Network and Naïve Bayes Data Fusion," IEEE Transactions on Industrial Electronics, 2017.

[58] D. J. Atha and M. R. Jahanshahi, " Evaluation of deep learning approaches based on convolutional neural networks for corrosion detection," Structural Health Monitoring, p. 1475921717737051, 2017.

[59] S. S. Kumar, D. M. Abraham, M. R. Jahanshahi, T. Iseley and J. Starr,

"Automated defect classification in sewer closed circuit television inspections using deep convolutional neural networks," Automation in Construction, vol. 91, pp. 273-283, 2018.

[60]   D. Feng and M. Q. Feng, "Identification of structural stiffness and excitation forces in time domain using noncontact vision-based displacement measurement," Journal of Sound and Vibration, vol. 406, pp. 15-28, 2017.

[61]   D. Feng and M. Q. Feng, "Computer vision for SHM of civil infrastructure: From dynamic response measurement to damage detection–A review," Engineering Structures, vol. 156, pp. 105-117, 2018.

[62]   Y. Bao, Z. Tang, H. Li and Y. Zhang, "Computer vision and deep learning–based data anomaly detection method for structural health monitoring," Structural Health Monitoring, p. 1475921718757405, 2018.

[63]   S. Dorafshan, R. Thomas, M. Maguire and C. Coopmans, "A Practitioner's Guide to Small Unmanned Aerial Systems for Bridge Inspection," in ICUAS18, Dallas, TX, 2018.

[64]   D. Kang and Y. J. Cha, "Autonomous UAVs for Structural Health Monitoring Using Deep Learning and an Ultrasonic Beacon System with Geo-Tagging," Computer-Aided Civil and Infrastructure Engineering, 2018.

[65]   D. Kang and Y. J. Cha, "Damage detection with an autonomous UAV using deep learning," in Sensors and Smart Structures Technologies for Civil, Mechanical, and Aerospace Systems 2018 (Vol. 10598, p. 1059804). International Society for Optics and Photonics, Denver, CO, 2018.

[66]   V. Dumoulin and F. Visin, "A guide to convolution arithmetic for deep learning," arXiv preprint arXiv:1603.07285..

[67]   Fei-Fei L., J. J and Y. S., Stanford University, 2017. [Online]. Available: http://cs231n.stanford.edu/. [Accessed 21 03 2018].

[68]   H. C. Shin, H. R. Roth, M. Gao, L. Lu, Z. Xu, I. Nogues and R. M. ... Summers, "Deep convolutional neural networks for computer-aided detection: CNN architectures, dataset characteristics and transfer learning," IEEE transactions on medical imaging, vol. 35, no. 5, pp. 1285-1298, 2016.

[69]   Z. Li and D. Hoiem, " Learning without forgetting," IEEE Transactions on Pattern Analysis and Machine Intelligence, 2017.

[70]   S. Dorafshan, R. Thomas and M. Maguire, "Image Processing Algorithms for Vision-based Crack Detection in Concrete Structures," Advanced Concrete Technology, 2018.

[71]   S. Dorafshan, C. Coopmans, R. Thomas and M. Maguire, "Deep Learning Neural Networks for sUAS-Assisted Structural Inspections: Feasibility and Application," in ICUAS2018, Dallas, 2018.

CHAPTER VII

DEEP LEARNING NEURAL NETWORKS FOR SUAS-ASSISTED STRUCTURAL

INSPECTIONS: FEASIBILITY AND APPLICATION

Abstract

This chapter investigates the feasibility of using a Deep Learning Convolutional Neural Network (DLCNN) in inspection of concrete decks and buildings using small Unmanned Aerial Systems (sUAS). The training dataset consists of images of lab-made bridge decks taken with a point-and-shoot high resolution camera. The network is trained on this dataset in two modes: fully trained (94.7% validation accuracy) and transfer learning (97.1% validation accuracy). The testing datasets consist of 1620 sub-images from bridge decks with the same cracks, 2340 sub-images from bridge decks with similar cracks, and 3600 sub-images from a building with different cracks, all taken by sUAS. The sUAS used in the first dataset has a low-resolution camera whereas the sUAS used in the second and third datasets has a camera comparable to the point-and-shoot camera. In this study it has been shown that it is feasible to apply DLCNNs in autonomous civil structural inspections with comparable results to human inspectors when using off-the-shelf sUAS and training datasets collected with point-and-shoot handheld cameras.

Introduction

Automation is changing all aspects of living in the 21st century. Civil and structural engineering is no exception to this change. The recent demand for nondestructive and non-contact methodologies [1, 2, 3] has provided a stage for small Unmanned Aerial Systems (sUAS) implementations in inspection [60], maintenance [5],

and monitoring of structures [6]. Federal law mandates a routine inspection every two years for bridges to ensure that the service requirements are met [7]. The recommended routine inspection is a physical inspection [8] which brings several limitations in practice such as traffic closure, safety risks to inspectors and public, and accessibility issues [65]. sUAS-assisted structural inspections can address some of these limitations by providing safer, repeatable, and cheaper inspections [66]. Despite facing certain challenges, using sUAS in structural inspections is a fast growing market. One crucial task in infrastructure inspection, maintenance, and monitoring is damage detection [11]. sUAS-assisted bridge inspections have been practiced by state Departments of Transportation (DOTs) in the United States: in Michigan, to detect cracks and delamination in concrete bridge decks [12]; in Minnesota for routine inspection [13, 14]; in Florida for crack detection [15]; and in Idaho for fatigue crack detection [60] in the past four years. Visual and thermal infrared cameras are the most common sensors on sUAS, thus, using image processing and machine learning techniques in inspection provides autonomous or semi-autonomous damage detection. Image processing techniques have been used to detect concrete cracks [72, 73, 74, 75], concrete spall [20, 21], concrete delamination [78], steel cracks [18, 23, 24] , and pavement cracks [25, 26, 27]. In addition, sUAS have been coupled with image processing and machine learning techniques for infrastructure inspection [6, 28] crack concrete detection [65, 85], post-disaster inspection [30], infrastructure 3-dimensional modeling [31, 32], displacement and structural stiffness measurements [33, 34],

Deep learning convolutional neural networks (DLCNNs) are a type of feedforward artificial neural networks which have revolutionized autonomous image classification and object detection in the past 5 years [35]. A DLCNN uses a set of

annotated, e.g. labeled, images for training and calculates the learning parameters in the

learning layers between the input and output layers thorough thousands to millions

iterations. Recent applications of DLCNNs for non-contact structural health monitoring

can be seen in [36, 37, 38]. Deep learning can be used for crack detection in three

different ways: classification [36], i.e. labeling an image as cracked or un-cracked,

localization [37], i.e. locate the region that the crack exists in an image using bounding

boxes, segmentation [39], i.e. segment the pixels of an image into cracked pixels and un-

cracks pixels. For classification task, the training dataset includes a set of labeled images

(i.e. "C" for cracked and "U" for un-cracked images). For localization task, the

coordinates of a bounding box(s) surrounding the crack(s) in each image must be

identified. For segmentation task, all pixels in each image in the training dataset have to

be labeled as either cracked or un-cracked. The general layout of a deep learning

architecture includes an input layer, learning layers, and a output layer [40]. The input

layer reads the image(s) and transfers it (thrm) to the learning layers. Deep learning

happens in the learning layers by applying filters to the input image through convolution

operations to extract image features. The output layer uses the features in the learning

layers to classify the image according to the target categories. Since the images are

already assigned to the target labels in training process, the network uses back

propagation to update and modify the filters to reach a desirable accuracy through

iteration.

The performance of a DLCNN depends on the number and arrangement of layers

(i.e., architecture) and the size and variety of training dataset. Krizhevsky [41] proposed

one of the first successful architectures of a DLCNN, i.e. AlexNet. This architecture has

25 layers and was the winner of the image classification competition in 2012 (ImageNet [42]). Szegedy et. el. proposed another architecture called GoogleNet with 144 layers including inception module in the layers which won the 2014 competition [43]. Deep residual learning neural network, ResNet, was introduced in 2016 [44]. ResNet had 177 to 347 layers and was the winner of 2015 competition.

Incorporating sUAS-assisted structural inspections with deep learning can be considered the state of the art of non-contact structural inspection, maintenance, and monitoring, which is investigated for the first time in this paper. This study investigates the feasibility of using a DLCNN trained on a set of high-quality point-and-shoot concrete images to label new images of concrete structures taken by sUAS. Since the presence of irrelevant objects or scenery in the inspection images compromises the efficiency of vision-based non-contact methods [45], the testing datasets in this study purposely have both. In addition, the quality of sUAS images depends on different parameters such as the specifications of the platform and the sensor (i.e., camera). Low quality, noisy, or blurry images mislead both inspector and conventional image processing-based crack detection methods. Even with the best available sUAS, there is a good chance that the sUAS images lack the desired quality due to uncontrollable environmental issues (e.g. wind speed or poor lighting conditions) [45]. Therefore, it is important to answer these questions: Are DLCCNs useful for sUAS-assisted structural inspections? If so, what are the requirements? The effects of using low-quality sensors on the performance of a DLCNN in structural health monitoring was proven to reduce the accuracy of the investigated network [46]; however, both noisy and sound data in this study were obtained through computer simulations.

Alex-Net Architecture

The AlexNet network consists of 5 convolution layers (C), 3 max pooling layers (MP), 7 non-linearity layers using ReLu function (ReLu), 2 normalization layers (Norm), 3 fully connected layers (FC), 2 dropout layers (DP), 1 softmax layer (SM), and 1 classification layer (CL). The layers are shown in Fig. 7-1 The convolution layers extract the features in each input image through convolution operation. The arrays in the kernels, i.e. weights, are obtained through several iterations in the training process; however, the size, number and stride of the kernels are usually assigned before the training. The non-linearity layer operates on the result of each convolution layer through an element wise comparison. One of the common non-linearity functions is Rectified Linear (ReLu) unit. The ReLu function is defined as the maximum value of 0 and the input. After the non-linearity layer, a max pooling layer is placed which introduces a representative for a set neighboring pixels by taking their maximum value. The max pooling layers are essential to reduce the computational time and overfitting issues in the DLCNNs. After the max pooling layer, one or several fully connected layers are used at the end of the architecture. The fully connected layer is a traditional multi-layer perceptron followed by a softmax layer to classify the image. The mission of the fully connected layers is to connect the information from the past layers together in way that the softmax layer can predict the results correctly during the training process. The optimum combination is achieved from a process called back propagation algorithm (partial derivatives of the softmax layer output with respect to weights). The purpose of the softmax layer is to ensure the sum of probabilities for all labels is equal to 1. In addition to these basic layers, a DLCNN also includes normalization, dropout, and classification layers. Normalization layer

normalizes the response around a local neighborhood to compensate with the possible

unbounded activations from the ReLu layer. The dropout layer is a probability-based

threshold layer that filters responses smaller than a threshold probability (50% is

common). The classification layer is similar to the fully connected layers.
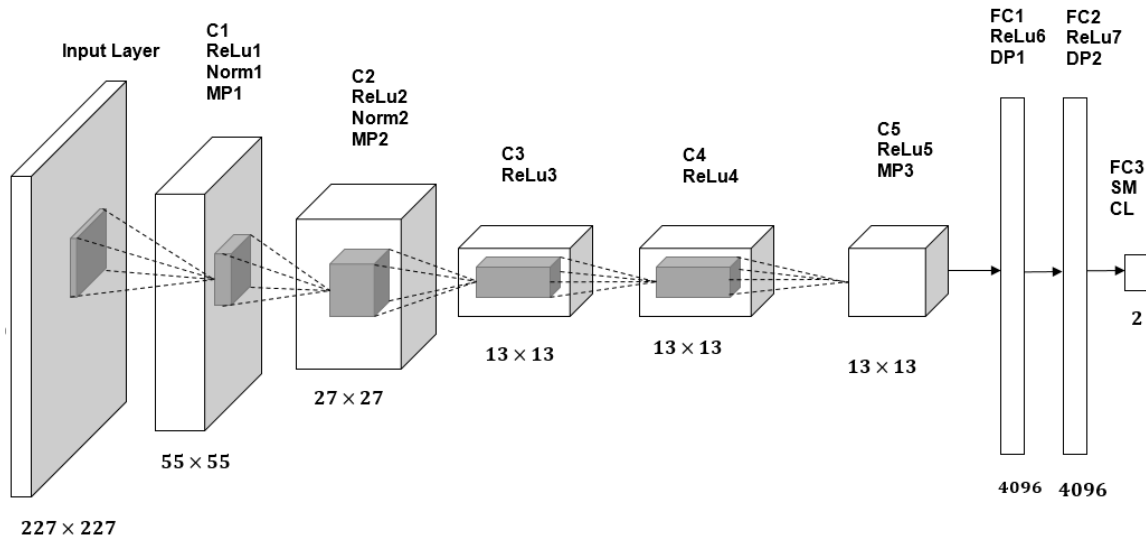
Fig. 7-1 The architecture of AlexNet adopted from [41]

Two modes are used for training in the AlexNet network on the concrete training

dataset. The first mode is to Fully Train (FT) the network from the scratch (FT mode) on

the training dataset. In this mode all the weights are assigned with random numbers and

the computed through iterations based on the training dataset. Obtaining an annotated

dataset for concrete cracks as big as ImageNet is not currently feasible. Even if a large

concrete crack dataset was available, training process from scratch could take up to a few

weeks to complete on hardware with several graphic processor units (GPUs), and would

therefore be prohibitively time consuming. However, it is possible to apply a previously

trained network (pre-trained network) on a small dataset and obtain reasonable accuracy

[47]. Pre-trained networks can be applied on a new dataset in different ways [48]. These methods are usually referred to as "domain adaptation" in the deep learning literature. One of these techniques is to partially retrain a pre-trained network and modify the layers according to a new dataset. This approach is called fine-tuning or transfer learning (TL mode). In this mode, a pre-trained network is used for classification task of the new images. However, the network has to be re-trained since both classifier and weights have to be updated based on the new dataset. In the TL approach, the weights of the lower-level layers (closer to the input image layer) are preserved. These weights are computed from training on millions of images and consist of generic feature extractors such as edge detectors. Therefore, the determined lower-level weights can be applied on any dataset for feature extraction. On the other hand, the classifier layers (close to end of network) are more sensitive to the training dataset and its labels. To adjust the network to the new dataset, the weights in the high-level layers are obtained through training on the new dataset.

Experimental Program

Inspected Structures

Cracks on four concrete bridge decks and one concrete building are inspected in this study. The bridge decks were previously made in the System, Material, and Structural Health (SMASH) lab building on Utah State University (USU) campus. The inspected building is the exterior walls of Russell/Wanlass Performance Hall building on USU campus.

Equipment

Two sUAS are used to produce the testing datasets: 3DR Iris and DJI Mavic, shown in Fig. 7-2. Table 7-1 shows the specifications of each sUAS. The 3DR Iris was used to inspect the bridge decks and the DJI Mavic was used to inspect both bridge decks and the building. A GoPro Hero4 camera was mounted on the 3DR Iris while the DJI Mavic had its own integrated camera. Also a Nikon COOLPIX L830 camera was used to capture the training dataset images. The specifications of these cameras are shown in Table 7-2. The graphic processor unit (GPU) device on the desktop used in this study was a GeForce GTX 750 Ti. All computations are carried out using single GPU mode in Matlab 2017b.

Datasets

The images in all datasets were divided into sub-images (227 pixels by 227 pixels) to comply with the AlexNet architecture. The training dataset includes 9011 sub-images, 1471 with C label and 7540 with U label, from two lab-made bridge decks using the Nikon camera with a clearance of roughly 0.5 m. The images in this chapter are a part of SDNET, a fully annotated image dataset dedicated to structural defects [49]. SDNET is free and publicly available for academic purposes. For the validation dataset, 10% of the images in the training dataset were used. Three sUAS testing datasets are gathered to evaluate the performance of the network.

Fig. 7-2 The sUAS used for inspection

Table 7-1 sUAS Specifications

UAS	3DR Iris	DJI Mavic
Cost (USD)	500	1,000
Weight (kg)	1.28	0.74
Type	Quadcopter	Quadcopter
Max Flight Time (m)	27	22
Payload (kg)	0.90	0.40
First Person View	Yes	Yes
Camera	GoPro	DJI Integrated

Table 7-2 Camera Specifications

Camera	Nikon	GoPro Hero4	DJI Camera
Resolution (MP)	16	12 MP	12
Image Dimensions	4068×3456	4000×3000	4000×3000
Sensor Type	CMOS	CMOS	CMOS
Lens Aperture	F3-5.9	F2.2	F2.8
Sensor Size (in)	1/2.3	1/2.3	1/2.3
ISO (max)	3200	1600	6400

The first testing dataset includes 1620 sub-images of one of the bridge decks

taken by the GoPro Camera mounted on the 3DR Iris. Images in this dataset are taken by

a lower quality camera during the 3DR Iris flight from same cracks in the training

dataset. The second testing dataset includes 2340 sub-images taken by the DJI Mavic of

the bridge decks. The effect of having undesirable surface conditions, i.e. moisture and

ice, in the testing dataset on the performance of the network is investigated by applying

the network on in this dataset. The third dataset includes 3600 sub-images taken by the

DJI Mavic of the USU Russell/Wanlass Performance Hall building. The cracks and

concrete textures in this dataset are different from training dataset. Fig. 7-3 shows

representative images of the training and testing datasets. The number of sub-images in

each dataset and their labels, C for cracked and U for un-cracked, are shown in Table 7-3.
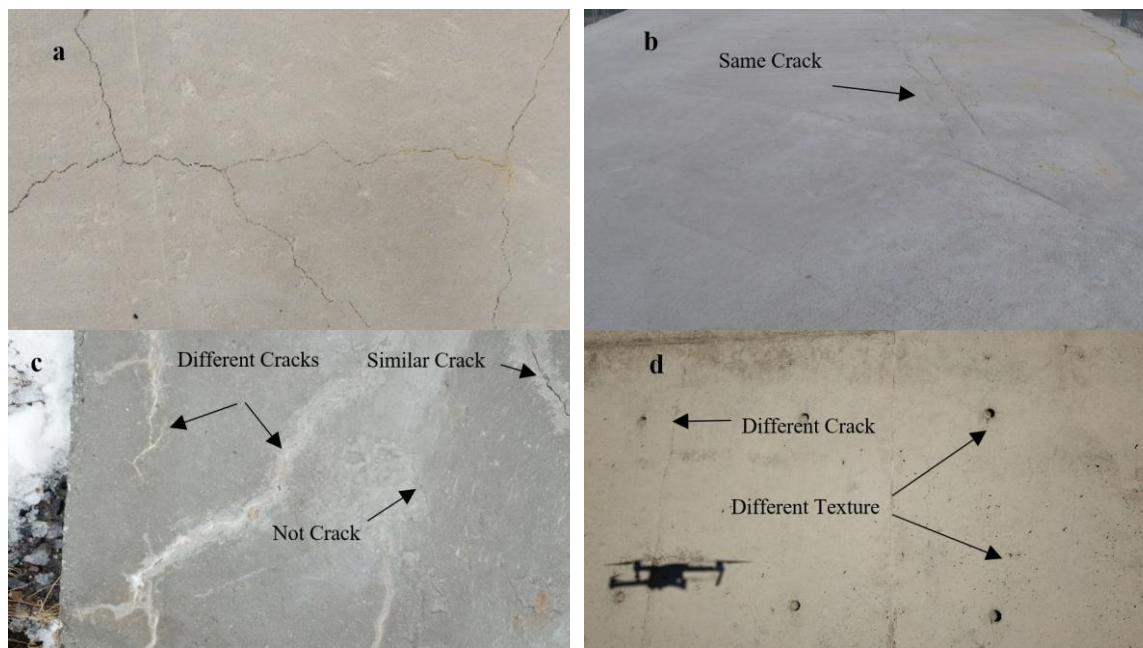

Fig. 7-3 Representative original images of (a) training dataset, (b) 1st testing dataset, (c)2nd testing dataset, (d) 3rd testing dataset

Table 7-3 The results of the first testing dataset prove the feasibility of using DLCNNs on sUAS images.

Dataset	C	U
Training	1324	6786
Validation	147	754
1st Testing	188	1432
2nd Testing	278	2062
3rd Testing	1719	1881

Results

Training

Two training procedures, FT and TL, are carried out to label the images in each testing dataset. In both modes, the training continued until the accuracy stopped improving in three consecutive epochs. Fig. 7-4 shows the accuracy and loss vs iteration for FT and TL modes. The training process in the TL mode has only a third iterations compared to the FT mode. The achieved validation accuracy is 94.7% for FT which is less than the validation accuracy in TL with 97.1%. This accuracy was calculated based on the total number of correct calls. The performance of the network in each mode is shown in Table 7-4. As seen, the FT mode performed better than the TL mode in terms of True Positives (TP), 91.2%. The total accuracy of TL mode was better than the FT mode due to higher True Negatives (TN). Having more sub-images labeled as U in the validation dataset, 754 sub-images, makes the accuracy more dependent on the TN than TP. The training process in the FT mode is 50% more time consuming than TL mode which is due to more performed iterations in the FT mode.
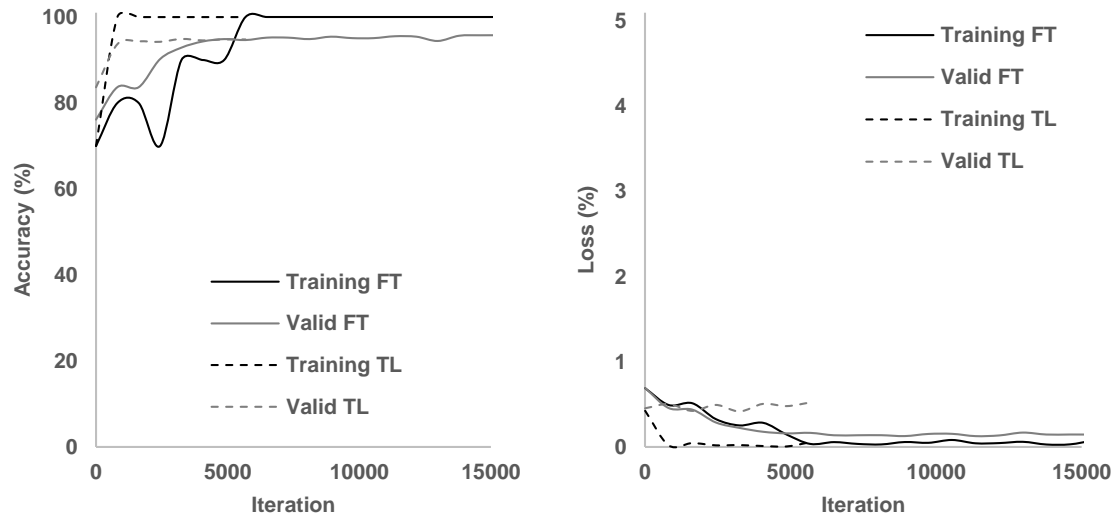
Fig. 7-4 The training process, (left) accuracy, (right) loss

Table 7-4 The Training Modes Results

Mode	Time (s)	TP (TPR)	TN (TNR)	Acc. (%)
FT	6210	134 (91.2%)	719 (95.3%)	94.7
TL	4123	131 (89.1%)	744 (98.6%)	97.1

Testing

Table 7-5 shows the results of applying the network in both modes on the testing

datasets. In the first testing dataset, the FT mode provides 6% more TPs than the TL

mode, which is consistent with validation results. The TNs reported by the FT mode is

80.2% which is almost 10% less than the TL mode. This puts the FT mode after TL mode

in terms of total accuracy in despite the FT mode superiority in TP reports. The TP, TN,

and total accuracy of both modes on the first dataset can be considered satisfactory when

compared to crack detection using conventional image processing techniques and human inspector [73].

Table 7-5 Testing Results

Dataset	Mode	TP	TN	Acc. (%)
1st Dataset	FT	153 (81.4%)	1149 (80.2%)	80.0
	TL	142 (75.5%)	1282 (89.5%)	87.9
2nd Dataset	FT	164 (59.0%)	1686 (81.8%)	79.0
	TL	128 (46.1%)	1959 (95.0%)	89.0
3rd Dataset	FT	864 (50.3%)	1240 (65.9%)	58.4
	TL	747 (43.5%)	1545 (82.1%)	63.7

In the second testing dataset, the FT mode provides 15% more TPs than the TL mode. The TNs reported by the FT mode is 81.8%, better than the first dataset, but is almost 7% less than the TL mode. This puts the FT mode after TL mode in both TN and total accuracy, despite the FT mode superiority in TP reports. The TN reports can be considered satisfactory, particularly in TL mode with 95.0%. However, the network fails to detect the cracks as good as the first dataset when they are not the similar to cracks in the training dataset. In addition, the presence of irrelevant objects, and the background scenery in the testing images challenged the network ability to detect the cracks correctly.

In the third testing dataset, the FT mode provides 7% more TPs than the TL mode. The TNs reported in the FT mode is only 65.9%, worst in all datasets and almost 16% less than the TL mode. The performance of FT mode is worse than TL mode in both TN and total accuracy, despite the FT mode superiority in TP reports. TN reports in the TL mode can be considered satisfactory with 82%. However, the network did not

perform well in crack detection for both modes or in TNs in the FT mode. The cracks in this dataset are new to the network in terms of size, shape, pattern, and concrete texture. This caused the network to perform rather poor and was unable to accurately identify cracks.

Discussion

The performance of the network in both modes declines when tested on challenging datasets as seen in Fig. 7-5. The images in the first dataset, of similar cracks, have lower quality since the GoPro camera is a less suitable camera for detailed photography than the Nikon, refer to Table 7-2 for camera specifications. These images also suffer from blurriness, which is due Iris vibrations during the deck inspections. The network detects more cracks in the FT mode than the TL mode in all testing datasets. In the FT mode, all weights are computed partially for detection of concrete cracks. Higher TP rates than the TL mode, can justify more training time associated with FT mode. Fig. 7-6 shows a sub-image in the first testing dataset which has been labeled correctly as C in FT mode; but, TL mode did not detect the crack on it. When network labeled the sub-image wrong, a shaded box is added on the right top corner of the label box for presentation purposes. The sub-images with shaded mark are associated with either false negative (FN) or false positive (FP). This trend can also be seen in the second training dataset with more tangible superiority of TP reports in the FT mode. Fig. 7-7 shows an example of the network better crack detection in the FT mode.
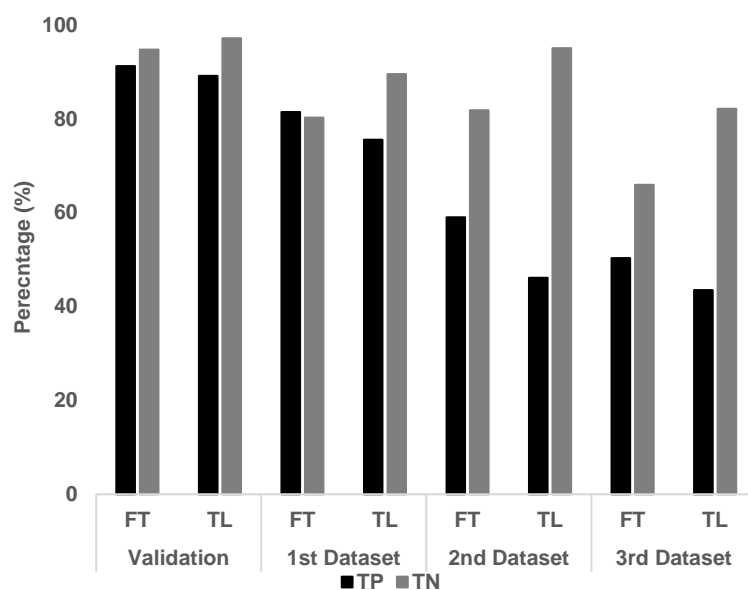
Fig. 7-5 The TP and TN rates for all datasets in both network modes

Fig. 7-6 Comparing TP reports in the 1st training dataset for, (a) FT mode correct label and (b) TL mode wrong label

(a)   (b)

**Fig. 7-7 Comparing TP reports in the 2nd training dataset for, (a) FT mode correct label
and (b) TL mode wrong label**

TP reports in the second dataset experienced a sudden drop which is mostly due to

presence of irrelevant objects on the decks in the testing dataset resembling the cracks

such as ice, snow, and grass chips. Fig. 7-8 shows an example of FP report due to

presence of an irrelevant object. The trend of higher TP reports in FT mode continues to

the third dataset too as seen Fig. 8-9; however, the TP rates dropped more drastically

compared to the second dataset. This is because the cracks on this dataset are on different

concrete textures, i.e. building walls, and have different patterns, and smaller sizes (Fig.

3d).

<div align="center">(a)   (b)</div>
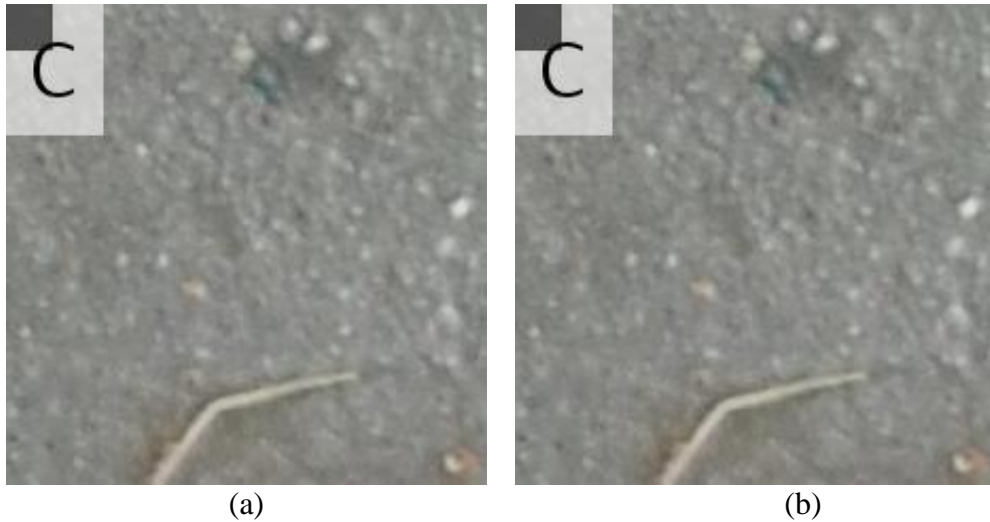
Fig. 7-8 False positives due to presence of irrelevant objects, (a) FT mode wrong label, (b) TL mode wrong label

The TN reports have a decreasing trend from the first to the third training dataset, from 82% to 66%, when the network is in the FT mode. Similar trend is observed in the TL mode but the range of TNs are greater, 95% in the first to 82% in the third dataset. Using the network in TL mode is more efficient when the images in the dataset have new features since the network has been trained on the ImageNet dataset with more than 1000 image categories. The network in TL mode produces higher TNs in both training and testing process. On the first dataset, the difference between TNs in FT and TL modes was almost 9%. The presence of irrelevant objects such as concrete edges or having a non-concrete background mostly make this difference (Fig. 7-10). This difference in the second dataset was almost 6% due to the presence of irrelevant objects as seen in Fig. 7-11. The TN reports in the TL mode is 16% higher in the third dataset. Presence of

irrelevant objects and different concrete texture are the reasons for this difference as seen

in Fig. 7-12.

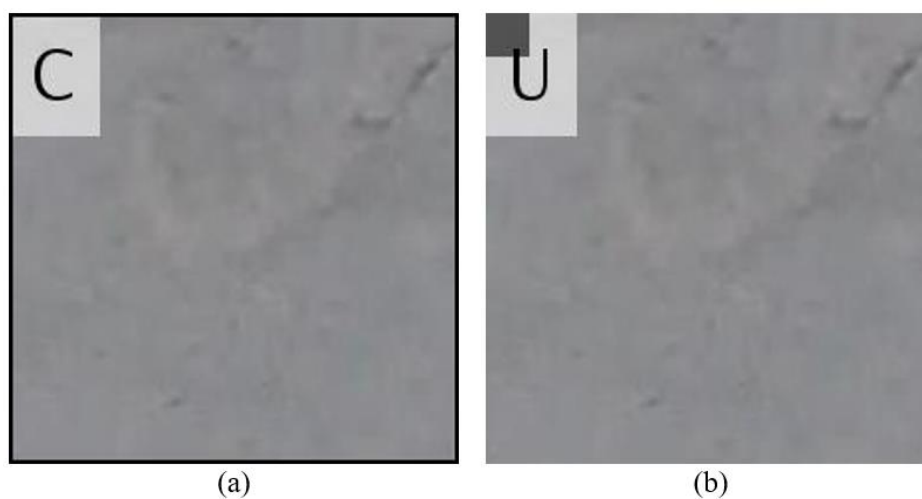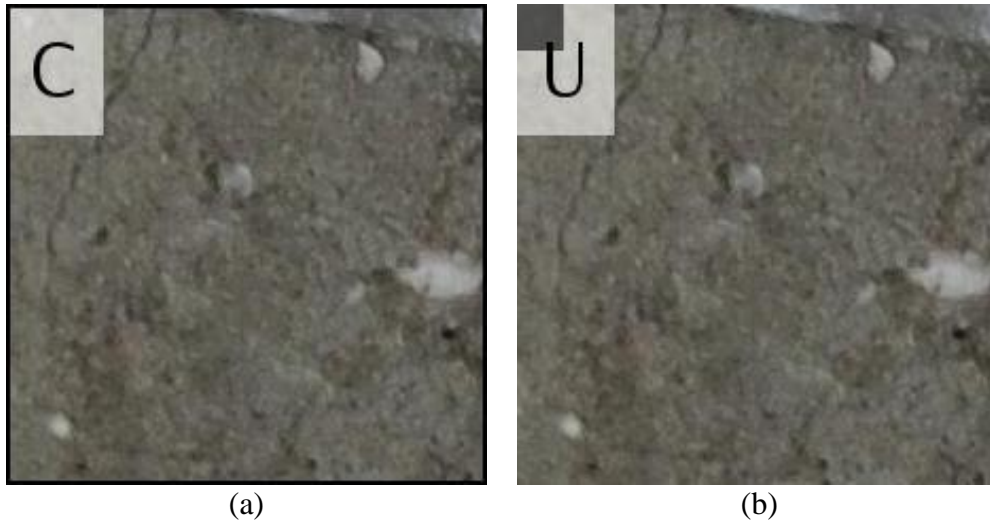(a)   (b)

Fig. 7-9 Comparing TP reports in the 3rd training dataset for, (a): FT mode correct label, (b): TL mode wrong label

(a)   (b)

Fig. 7-10 Comparing TN reports in the 1st training dataset for, (a) FT mode wrong label and (b) TL mode correct label
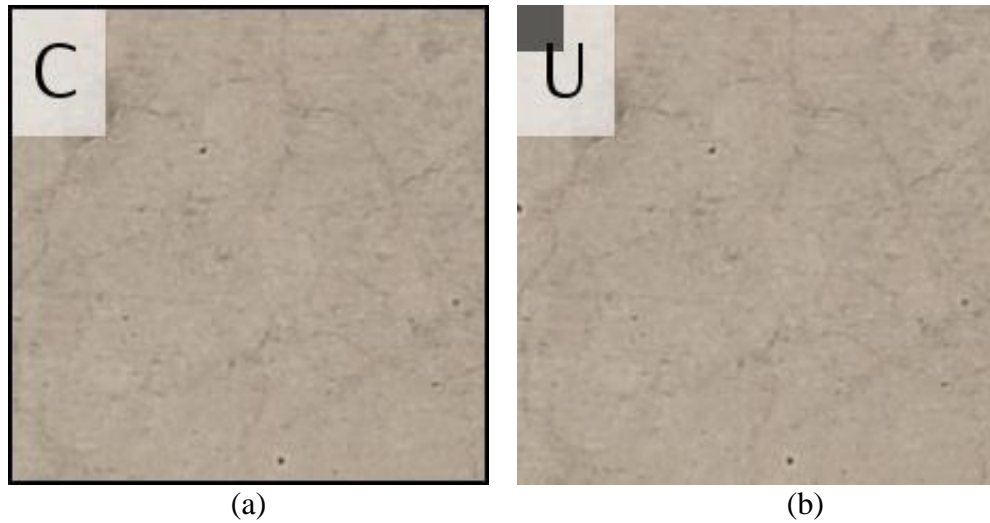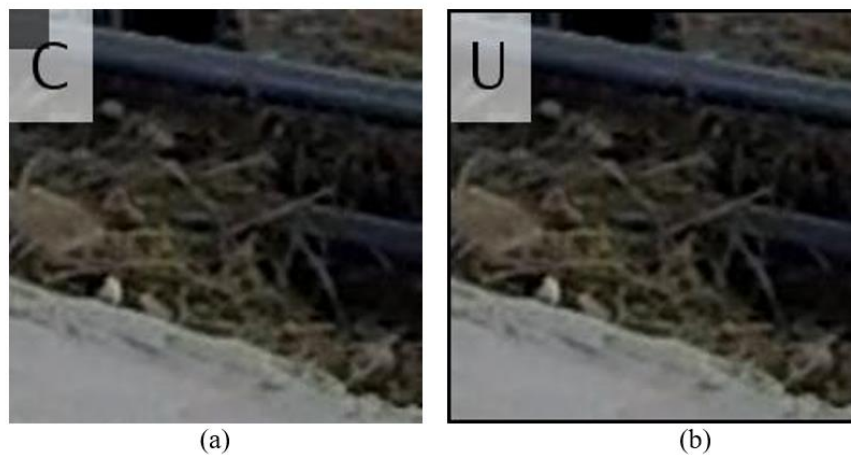
The challenges in the dataset images weaken the performance of the network,

such as lower quality camera, image blurriness, presence of irrelevant objects, different crack pattern and size, and different structure. Having similar cracks in both training and testing datasets, the lower quality camera did not affect the TP and TN results as the presence of the new features did due to background change, crack size, and crack pattern in the testing dataset. To improve the results, the training dataset should be more comprehensive and include the possible new features in the inspection images which are not necessarily associated to the concrete cracks. Using higher quality cameras on the sUAS helps the detection rate. The AlexNet architecture can be replaced with more advanced and accurate architectures such as ResNet, to improve the network performance however, multiple GPU devices might be required. In addition, gathering scientific images from cracks and other defects to generate a comprehensive dataset, such as ImageNet, will be extremely useful for sUAS-assisted inspections. Nevertheless, the results of this study proved the feasibility of using DLCNNs for sUAS-assisted structural inspections of infrastructure.

Conclusion and Future Work

The application of deep learning convolutional neural networks for sUAS-assisted inspection of concrete structures is investigated in this paper. A convolutional neural network using AlexNet architecture was fully trained on a set high-quality point-and-shoot images to achieve a desirable accuracy (FT mode). In addition to the FT mode, a pre-trained neural network with the same architecture, on the ImageNet, was re-trained on the training dataset using transfer learning for comparison purposes (TL mode).

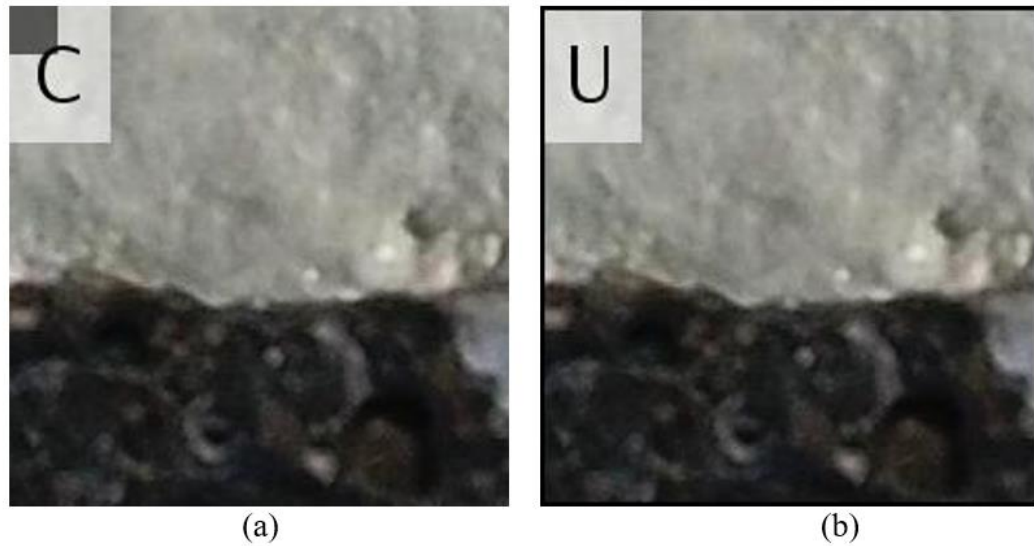**Fig. 7-11 Comparing TN reports in the 2nd training dataset for, (a) FT mode wrong label and (b) TL mode correct label**
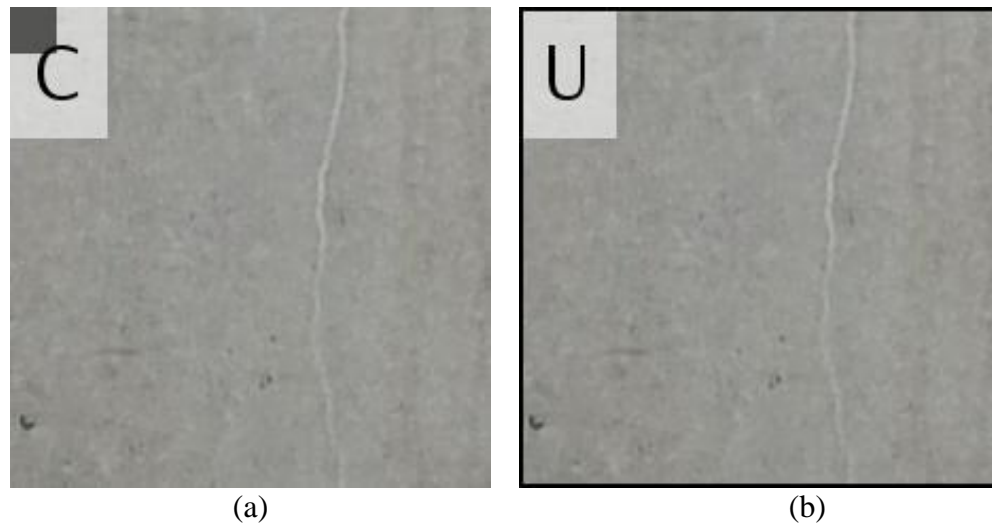

Fig. 7-12 Comparing TN reports in the 3rd training dataset for, (a) FT mode wrong label and (b) TL mode correct label

The training and validation process for FT mode was 50% more time-consuming; however, it provides better accuracy (about 3%) in validation process. The network in FT

mode on the other hand, performs better than the TL mode in crack detection (better true positive) in validation dataset. To investigate the challenges in sUAS-assisted structural inspections of infrastructure, three datasets are gathered and the network performance is evaluated in both modes. The image in the first dataset are from the same cracks but taken by a low resolution camera on a sUAS. The image in the second dataset are from the same structures, i.e. decks, but taken by a sUAS with comparable resolution to the point-and-shoot camera. The image in the third dataset are from a different structure, i.e. building, by a sUAS with comparable resolution. The results showed that the true positive (TP) reports were higher when the FT mode was used. However, using the network in TL mode improves the true negative (TN) reports over the FT mode. The accuracy of the network in both modes declined facing the new datasets from over 80% in the first dataset to 79% in the second dataset and to 58.4% in the third dataset in the fully trained mode. The accuracy in TL mode was 88% in the first dataset and decreased to 64% in the third dataset. The network in the FT mode detected more cracks in all datasets than the TL mode (between 6% to 15%); however, using transfer learning resulted the network achieved greater accuracies (7% to 15%). Both TP and TN reports decrease when the networks are tested on the testing datasets. The networks are shown to perform better in the first dataset showing it is important to have similar defects in the training and testing dataset. When the cracks are different but on similar structures, i.e. the second dataset, the accuracy dropped significantly and it got worse when the pattern, size, and the background of the cracks were changed in the third dataset. To improve the results, the training dataset should be more comprehensive to include the possible features in the inspection images. Using higher quality cameras on the sUAS helps the

detection rate. The AlexNet architecture can be replaced with different accurate architectures such as ResNet, to improve the network performance.

References

[1] S. Dorafshan, M. Maguire, N. Hoffer and C. Coopmans, "Unmanned Aerial Vehicle Augmented Bridge Inspection Feasibility Study," Center for Advanced Infrastructure and Technology, Piscataway. NJ, 2018.

[2] NIST, "Advnaced Sensing Technologies and Advanced Repair Materials for the Infrastructure: Water Systems, Dams, Levees, Bridges, Roads, and Highways," 2009. [Online]. Available: https://www.nist.gov/sites/default/files/documents/tip/prev_competitions/ci_wp_031909.pdf. [Accessed 2018].

[3] A. Zulifqar, M. Cabieses, A. Mikhail and N. Khan, "Design of a bridge inspection system (BIS) to reduce time and cost," George Mason University, Farifax, VA, 2014.

[4] S. Dorafshan, M. Maguire, N. Hoffer and C. Coopmans, "Fatigue Crack Detection Using Unmanned Aerial Systems in Under-Bridge Inspection," Idaho Department of Transportation, Boise, 2017.

[5] A. Khaloo, D. Lattanzi, K. Cunningham, R. Dell'Andrea and M. Riley, "Unmanned aerial vehicle inspection of the Placer River Trail Bridge through image-based 3D modelling," Structure and Infrastructure Engineering, vol. 14, no. 1, pp. 124-136, 2018.

[6] Y. Ham, K. K. Han, J. J. Lin and M. Golparvar-Fard, "Visual monitoring of

civil infrastructure systems via camera-equipped Unmanned Aerial Vehicles (UAVs): a review of related works," Visualization in Engineering, vol. 4, no. 1, p. 1, 2016.

[7] FHWA, 1994. [Online]. Available: https://www.fhwa.dot.gov/legsregs/directives/fapg/cfr0650c.htm. [Accessed 2018].

[8] G. Hearn, Bridge Inspection Practices, vol. 375, Transportation Research Board, 2007.

[9] S. Dorafshan, M. Maguire, N. V. Hoffer and C. Coopmans, "Challenges in bridge inspection using small unmanned aerial systems: Results and lessons learned.," in 2017 International Conference on Unmanned Aircraft Systems (ICUAS), 2017.

[10] S. Dorafshan and M. Maguire, "Bridge Inspection: Human Performance, Unmanned Aerial Vehicles and Automation," Journal of Civil Strucutral Health monitoring, In Press.

[11] J. Li, J. Deng and W. Xie, "Damage detection with streamlined structural health monitoring data," Sensors, vol. 15, no. 4, pp. 8832-8851, 2015.

[12] C. Brooks, R. J. Dobson, D. M. Banach, D. Dean, T. Oommen, R. E. Wolf, T. C. Havens, T. M. Ahlborn and B. Hart, "Evaluating the Use of Unmanned Aerial Vehicles for Transportation Purposes," Michigan Department of Transportation, Lansing, 2015.

[13] J. Zink and B. Lovelace, "Unmanned Aerial Vehicle Bridge Inspection Demonstration Project," Minnesota Department of Transportation, St. Paul, 2015.

[14] J. Wells and B. Lovelace, "Unmanned Aircraft System Bridge Inspection Demonstration Project. Project Phase II," Minnesota Department of Transportation, 2017.

[15] L. D. Otero, N. Gagliardo, D. Dalli, W.-H. Huang and P. Cosentino, "Proof

of Concept for Using Unmanned Aerial Vehicles for High Mast Pole and Bridge Inspections," Florida Department of Transportation, Tallahassee, 2015.

[16] S. Dorafshan, M. Maguire and X. Qi, "Automatic Surface Crack Detection in Concrete Structures Using OTSU Thresholding and Morphological Operations," Utah State University, Logan, Utah, USA, 2016.

[17] S. Dorafshan, M. Maguire and M. Chang, "Comparing Automated Image-based Crack Detection Techniques in the Spatial and Frequency Domains," in 26th ASNT Research Symposium, Jacksonville, FL, 2017.

[18] S. Dorafshan and M. Maguire, "Autonomous Detection of Concrete Cracks on Bridge Decks and Fatigue Cracks on Steel Members.," in Dgital Imaging 2017, Mashantucket, CT, 2017.

[19] T. Nishikawa, J. Yoshida, T. Sugiyama and Y. Fujino, "Concrete Crack Detection by Multiple Sequential Image Filtering," Computer-Aided Civil and Infrastructure Engineering, vol. 27, no. 1, pp. 29-47, 2012.

[20] S. German, I. Brilakis and R. DesRoches, "Rapid entropy-based detection and properties measurement of concrete spalling with machine vision for post-earthquake safety assessments," Advanced Engineering Informatics, vol. 26, no. 4, pp. 846-858, 2012.

[21] T. Dawood, Z. Zhu and T. Zayed, "Machine vision-based model for spalling detection and quantification in subway networks," Automation in Construction, vol. 81, pp. 149-160, 2017.

[22] H. Sohn, D. Dutta, J. Y. Yang, M. DeSimio, S. Olson and E. Swenson, "Automated detection of delamination and disbond from wavefield images obtained

using a scanning laser vibrometer," Smart Materials and Structures, vol. 20, no. 4, p. 045017, 2011.

[23] Y. Xu, S. Li, D. Zhang, Y. Jin, F. Zhang, N. Li and H. Li, "Identification framework for cracks on a steel structure surface by a restricted Boltzmann machines algorithm based on consumer-grade camera images.," Structural Control and Health Monitoring, vol. 25, no. 2, 2018.

[24] X. Kong and J. Li, "Vision-Based Fatigue Crack Detection of Steel Structures Using Video Feature Tracking.," Computer-Aided Civil and Infrastructure Engineering, 2018.

[25] E. Zalama, J. Gómez-García-Bermejo, R. Medina and J. Llamas, "Road crack detection using visual features extracted by Gabor filters," Computer-Aided Civil and Infrastructure Engineering, vol. 29, no. 5, pp. 342-358, 2014.

[26] E. Schnebele, B. F. Tanyu, G. Cervone and N. Waters, "Review of remote sensing methodologies for pavement management and assessment.," European Transport Research Review, vol. 7, no. 2, p. 7, 2015.

[27] H. Zakeri, F. M. Nejad and A. Fahimifar, "Image based techniques for crack detection, classification and quantification in asphalt pavement: a review," Archives of Computational Methods in Engineering, vol. 24, no. 4, pp. 935-977, 2017.

[28] X. Zhong, X. Peng, S. Yan, M. Shen and Y. Zhai, "Assessment of the feasibility of detecting concrete cracks in images acquired by unmanned aerial vehicles," Automation in Construction, vol. 89, pp. 49-57, 2018.

[29] M. H. Rafiei and H. Adeli, "A novel machine learning-based algorithm to detect damage in high-rise building structures.," The Structural Design of Tall and

Special Buildings, vol. 26, no. 18, 2017.

[30] C. A. F. Ezequiel, M. Cua, N. C. Libatique, G. L. Tangonan, R. Alampay, R. T. Labuguen and A. B. ... Loreto, "UAV aerial imaging applications for post-disaster assessment, environmental management and infrastructure development. In Unmanned Aircraft Systems," in 2014 International Conference on Unmanned Aircraft Systems (ICUAS), 2014.

[31] M. N. Gillins, D. T. Gillins and C. Parrish, "Cost-effective bridge safety inspections using unmanned aircraft systems (UAS)," in Geotechnical and Structural Engineering Congress, Phoenix. AZ, 2016.

[32] C. Eschmann and T. Wundsam, "Web-Based Georeferenced 3D Inspection and Monitoring of Bridges with Unmanned Aircraft Systems," Journal of Surveying Engineering, vol. 143, no. 3, p. 04017003, 2017.

[33] H. Yoon, J. Shin and B. F. Spencer, "Structural Displacement Measurement using an Unmanned Aerial System," Computer-Aided Civil and Infrastructure Engineering, vol. 33, no. 3, pp. 183-192, 2017.

[34] D. Feng and M. Q. Feng, "Identification of structural stiffness and excitation forces in time domain using noncontact vision-based displacement measurement," Journal of Sound and Vibration, vol. 406, pp. 15-28, 2017.

[35] J. Schmidhuber, "Deep learning in neural networks: An overview," Neural networks, vol. 61, pp. 85-117, 2015.

[36] Y. J. Cha, W. Choi and O. Büyüköztürk, "Deep Learning-Based Crack Damage Detection Using Convolutional Neural Networks," Computer-Aided Civil and Infrastructure Engineering, vol. 32, no. 5, pp. 361-378, 2017.

[37] Y. J. Cha, W. Choi, G. Suh, S. Mahmoudkhani and O. Büyüköztürk, "Autonomous Structural Visual Inspection Using Region-Based Deep Learning for Detecting Multiple Damage Types," Computer-Aided Civil and Infrastructure Engineering., 2017.

[38] F. C. Chen and M. R. Jahanshahi, "NB-CNN: Deep Learning-Based Crack Detection Using Convolutional Neural Network and Naïve Bayes Data Fusion," IEEE Transactions on Industrial Electronics, vol. 65, no. 5, pp. 4392-4400, 2018.

[39] A. Zhang, K. C. Wang, B. Li, E. Yang, X. Dai, Y. Peng and C. Chen, "Automated Pixel-Level Pavement Crack Detection on 3D Asphalt Surfaces Using a Deep-Learning Network," Computer-Aided Civil and Infrastructure Engineering, vol. 32, no. 10, pp. 805-819, 2017.

[40] V. Dumoulin and F. Visin, "A guide to convolution arithmetic for deep learning," arXiv preprint arXiv:1603.07285..

[41] A. Krizhevsky, I. Sutskever and G. E. Hinton, "Imagenet classification with deep convolutional neural networks," Advances in neural information processing systems , pp. 1097-1105, 2012.

[42] J. Deng, W. Dong, R. Socher, L. J. Li, K. Li and L. Fei-Fei, "Imagenet: A large-scale hierarchical image database," in IEEE Conference on Computer Vision and Pattern Recognition (CVPR), Miami, FL, 2009.

[43] K. He, X. Zhang, S. Ren and J. Sun, "Deep residual learning for image recognition," in IEEE conference on computer vision and pattern recognition, Seattle. WA, 2016.

[44] C. Szegedy, W. Liu, Y. Jia, P. Sermanet, S. Reed, D. Anguelov and A. ...

Rabinovich, "Going deeper with convolutions," in CVPR, 2015.

[45] S. Dorfshan, J. Thomas R. and M. Maguire, "Fatigue Crack Detection Using Unmanned Aerial Systems in Fracture Critical Inspection of Steel Bridges," Journal of bridge engineering, 2018.

[46] Y. Z. Lin, Z. H. Nie and H. W. Ma, "Structural Damage Detection with Automatic Feature-Extraction through Deep Learning," Computer-Aided Civil and Infrastructure Engineering, vol. 32, no. 12, pp. 1025-1046, 2017.

[47] H. C. Shin, H. R. Roth, M. Gao, L. Lu, Z. Xu, I. Nogues and R. M. ... Summers, "Deep convolutional neural networks for computer-aided detection: CNN architectures, dataset characteristics and transfer learning," IEEE transactions on medical imaging, vol. 35, no. 5, pp. 1285-1298, 2016.

[48] Z. Li and D. Hoiem, " Learning without forgetting," IEEE Transactions on Pattern Analysis and Machine Intelligence, 2017.

[49] S. Dorafshan, R. Thomas and M. Maguire, "SDNET: A fully-annotated image dataset for non-contact concrete crack detection," Data In Brief , In Press.

CHAPTER VIII

SDNET2018: AN ANNOTATED IMAGE DATASET FOR NON-CONTACT

CONCRETE CRACK DETECTION USING DEEP CONVOLUTIONAL NEURAL

NETWORKS

Abstract

SDNET2018 is an annotated image dataset for training, validation, and benchmarking of artificial intelligence based crack detection algorithms for concrete. SDNET2018 contains over 56,000 images of cracked and non-cracked concrete bridge decks, walls, and pavements. The dataset includes cracks as narrow as 0.06 mm and as wide as 25 mm. The dataset also includes images with a variety of obstructions, including shadows, surface roughness, scaling, edges, holes, and background debris. SDNET2018 will be useful for the continued development of concrete crack detection algorithms based on deep convolutional neural networks (DCNNs), which are a subject of continued research in the field of structural health monitoring. The authors present benchmark results for crack detection using SDNET2018 and a crack detection algorithm based on the AlexNet DCNN architecture. SDNET2018 is freely available at https://doi.org/10.15142/T3TD19.

Data Specifications

- Subject area: Structural health monitoring, deep learning, convolutional neural networks, artificial intelligence

- More specific subject area: Concrete crack detection, image classification

- Type of data: 2D-RGB image (.jpg)

- How data was acquired: Original images of cracked and non-cracked concrete bridge decks, walls, and pavements were captured using a 16 MP Nikon digital camera.

- Data format: Raw digital images (.jpg)

- Experimental features: 230 images of cracked and non-cracked concrete (54 bridge decks, 72 walls, 104 pavements) segmented into more than 56,000 sub-images (256 × 256 px)

- Crack widths from 0.06 to 25 mm

- Obstructions including shadows, surface debris, inclusions, scaling, etc…

- Data source location: Utah State University, Logan, Utah, USA

- Data accessibility: The dataset is freely accessible at [1] for any academic purposes

- Related research article: Parts of this dataset have been used in the following research items for image-based non-contact crack detection applications: [99] [100] [101] [102] [103] [72] [8]

Value of the Data

- SDNET2018 can be used for training, validation, and benchmarking of algorithms for autonomous crack detection in concrete;

- SDNET2018 has images of reinforced concrete decks (D) and walls (W), and unreinforced concrete pavements (P), which enables DCNNs training on it while also categorizing different types of concrete cracks;

- A DCNN trained on SDNET2018 can identify fine and wide cracks due to the size variety in it, widths from 0.06 mm to 25 mm;

- Images in SDNET2018 intentionally include irrelevant objects which may improve the accuracy of DCNNs trained on this dataset in real applications;

- SDNET2018 can be used to develop new DCNN architectures or modify the existing architectures, e.g. AlexNet or GoogleNet, in order to increase the efficiency of the network for concrete crack detection.

Data

The SDNET2018 image dataset contains more than 56,000 annotated images of cracked and non-cracked concrete, bridge decks, walls, and pavements. Its purpose is for training, validation, and benchmarking of autonomous crack detection algorithms based on image processing, deep convolutional neural networks (DCNN) [8], or other techniques. Such techniques are increasing in popularity in the structural health monitoring field. Continued advancement of crack detection algorithms requires an annotated diverse image dataset [9], which has not been available until now.

Images of bridge decks were taken at the Systems, Materials, and Structural Health (SMASH) Laboratory at Utah State University, where a number of full scale bridge deck sections were stored. Images of walls and pavements were taken on Utah State University campus. Table 8-1 lists the number of cracked, non-cracked, and total sub-images of each type included in SDNET2018. The sample images in Fig. 8-1 show the range of crack widths, surface conditions, and other environmental factors represented within SDNET2018. Images are 256×256-px RGB image files in .jpg

format. Each image is classified as cracked or non-cracked and stored in a corresponding

folder within the repository. Images are organized into three sub-directories: P for

pavements, W for walls, and D for bridge decks. Each subfolder is further organized into

sub-sub-directories with the prefix C for cracked and U for uncracked (e.g., :\D\CD for

images of bridge decks with cracks). With the exception of segmentation into sub-images

as discussed above, the images have not been modified from their original state.

Experimental Design, Materials, and Methods

SDNET2018 images were taken with a 16-MP Nikon camera at a working

distance of 500 mm without zoom. The sensitivity was 125 ISO and the image resolution

was 4068×3456 px. The surface illumination was between 1,500 and 3,000 lx. Each full

image was segmented into 256×256-px sub-images. Each image represents a physical

area of approximately 1000 mm $\times$ 850 mm and each sub-image represents a physical area

of approximately 60 mm $\times$60 mm.

Table 8-1 SDNET2018 image dataset description and statistics

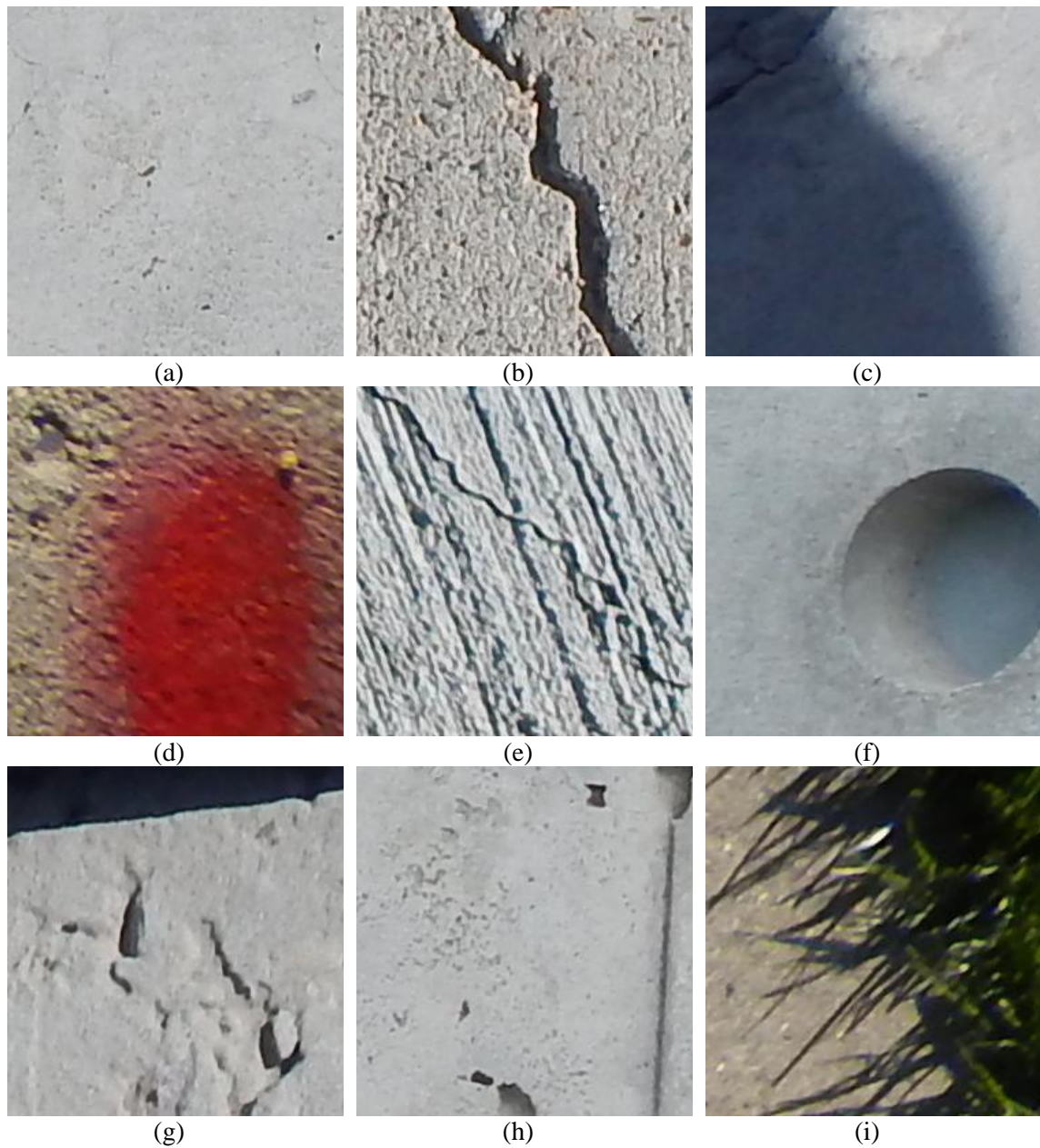| Image description		No. cracked	No. non-cracked	Total
Reinforced	Bridge deck	2025	11595	13620
	Wall	3851	14287	18138
Unreinforced	Pavement	2608	21726	24334
Total		8484	47608	56092

Fig. 8-1. SDNET2018 images include (a) fine cracks, (b) coarse cracks, (c) shadows, (d) stains, (e) rough surface finishes, (f) inclusions and voids, (g) edges, (h) joints and surface scaling, and (i) background obstructions

The authors analyzed the SDNET2018 dataset using the AlexNet DCNN

architecture in fully trained and transfer learning modes using the computational setup

and procedure described by Dorafshan et al. [8]. Benchmarking results, including the

sizes of the training and testing datasets, number of epochs required for training, and

accuracy of classification of the testing dataset, are presented in Table 8-2.

Table 8-2 Benchmark for SDNET2018 image classification using AlexNet

Image description	No. sub-images		DCNN mode	Training epochs	Accuracy (%)
	Training	*Testing*			
Bridge deck	12,259	1,361	FT	32	90.45
			TL	10	91.92
Wall	16,324	1,814	FT	30	87.54
			TL	9	89.31
Pavement	21,900	2,434	FT	30	94.86
			TL	10	95.52

References

[1]   Maguire M, Dorafshan S, Thomas RJ. SDNET2018: A concrete crack
image dataset for machine learning applications. Browse all Datasets. Paper 48.
https://digitalcommons.usu.edu/all_datasets/48. https://doi.org/10.15142/T3TD19.
[Accessed 18 05 2018].

[2]   Dorafshan S, Maguire M. Autonomous detection of concrete cracks on
bridge decks and fatigue cracks on steel members. in Digital Imaging 2017,
Mashantucket, CT, 2017.

[3]   Dorafshan S, Maguire M, Chang M. Comparing automated image-based
crack detection techniques in spatial and frequency domains. in Proceedings of the 26th
American Society of Nondestructive Testing Reseach Symposium, Jacksonville, FL,

2017.

[4]   Dorafshan S, Maguire M, Hoffer N, Coopmans C. Challenges in bridge inspection using small unmanned aerial systems: Results and lessons learned. in Proceedings of the 2017 International Conference on Unmanned Aircraft Systems, Miami, FL, 2017. DOI: 10.1109/ICUAS.2017.7991459

[5]   Dorafshan S, Maguire M. Bridge Inspection: Human Performance, Unmanned Aerial Vehicles and Automation. Journal of Civil Strucutral Health monitoring. 2018 8: 443–476. https://doi.org/10.1007/s13349-018-0285-4

[6]   Dorafshan S, Coopmans C, Thomas RJ, Maguire M. Deep Learning Neural Networks for sUAS-Assisted Structural Inpspections, Feasibility and Application. in ICUAS 2018, Dallas, TX, 2018.

[7]   Dorafshan S, Maguire M, Qi X. Automatic Surface Crack Detection in Concrete Structures Using OTSU Thresholding and Morphological Operations. Civil and Environmental Engineering Faculty Publications. Paper 1234. Utah State University. 2016.

[8]   Dorafshan S, Thomas RJ, Maguire M. Comparison of Deep Convolutional Neural Networks and Edge Detectors for Image-Based Crack Detection in Concrete. Construction and Building Materials, 2018 186:1031-1045.

[9]   Bashiri FS, LaRose E, Peissig P, Tafti AP. MCIndoor20000: a fully-labeled image dataset to advance indoor objects detection. Data In Brief. 2018 17:71-75.

CHAPTER IX

INFRARED IN-LINE WELD INSPECTION – FEASIBILITY STUDY

Abstract

The current practice of weld inspection is using ultrasonic waves (UT inspection) is associated with several limitations such as expensive inspector qualifications and storage times (for weld cool), no permanent record of inspection, and minimum base metal thickness. Using thermography can potentially improve weld inspection by addressing these issues. The feasibility of using infrared thermography (IRT) for in-line weld inspection is investigated in this report. Welded specimens include steel angles and plates with complete joint penetration welds. Defects in specimens were manufactured which included cracks, inclusions, lack of fusion, porosity, and overpass. After initial UT inspection, the regions with defects were identified. Using a heat gun, the condition of the in-line inspection is mimicked by increasing the temperature of the specimens to a certain point. A thermal camera is used to record the temperature decay of the specimens with time. An exponential fit function is fitted to each pixel of the recorded sequence through time. It is observed that the regions with possible defects (previously identified in UT inspection) lose the temperature faster; therefore, the area under the exponential fit function is smaller of defected regions compared to the sound regions. Eventually all specimens are cut at the locations with possible defects which showed reasonable agreement with the UT and IRT inspections.

Despite the success of the proposed IRT method in identifying defects, the high number of false positives reported limits using IRT for weld inspection. This can likely

be resolved with more investigation. The most likely solution to reduce the number of

false positives is using a thermal camera with high operating temperature, at least 10,000

°C, and higher sensitivity, 0.1°C. Nevertheless, using IRT in its infancy and likely a

viable technique and has vast potential to improve weld manufacturing and inspection.

Introduction

Verification of weld safety and workmanship is paramount to structural weld

inspection both during fabrication and in-service. Weld inspections are costly in terms of

time and money for both fabrication and in-service. There are many available non-

destructive evaluation (NDE) methods for weld inspection, but they are limited

depending on the situation. Ultrasonic (UT) technique has been widely used to detect

surface and sub-surface defects of welds. Despite the adequate accuracy, UT inspection

has certain drawbacks. UT uses a contact probe to transmit ultrasonic waves in a weld

specimen which makes in-line inspection challenging due to shop space and time

constraints. Depending on the type of welding and the base material, the temperature of

the weld ranges from 3,000 to 20,000° C. Because UT inspection is an inspection with

contact, the inspector needs to wait for the welds to cool down for up to 4 hours. This

adds time, and consequently cost, to the inspection process. The American Society of

Testing Materials (ASTM E494-15) limits the thickness of the specimen for UT

inspection to 5 mm (0.2 in.). This means UT inspection is not an option for steel joists

made of 3 mm (1/8 in.) angles, which are common. Using UT for weld inspection

requires a trained and experienced inspector to use the device and interpret the signal

attenuation. Additionally, UT provides no permanent record and the results can only be

interpreted in real time with no opportunity for review by others at a later date, making quality assurance and quality control difficult.

There are some challenges associated with infrared thermography (IRT) weld inspection. It can be difficult to provide the ideal situation for infrared thermography on a specimen since it requires a uniform energy deposit in a short period on a large surface. Also, irregular emissivity and thermal losses reduce the accuracy of the inspection considerably. These challenges have been identified on other civil structures inspected in the field but in a fabrication setting can be mitigated through changes to the weld inspection protocol, preparation, and post-processing. The purpose of this study is to investigate the potential and challenges of using IRT in weld inspection for sub-surface defect detection. IRT is a non-contact method and can be applied for in-line weld inspection using a high-temperature range thermal camera. Currently, high-temperature cameras that are commercially available measure up to 3,000°C. Therefore, using IRT has the potential to decrease the inspection time and cost. In addition, IRT can be applied to detect flaws in specimens with any thickness. Unlike UT inspection, the thermal sequences or images can be achieved and reviewed if necessary. Finally, using IRT equipped with a machine vision post-processing operation on the thermal sequences does not require training or knowledge.

There are very few studies under real world conditions where IRT techniques are used for construction weld inspection, but a common challenge is high number of false positives. Using IRT for weld defect detection has been investigated recently by Manuel and Washer (2017). Surface and subsurface defects, including lack of fusion, inclusion,

cracking and cutouts were attempted. The specimens were covered with high emissivity

black paint, which is not an efficient approach for in-line weld inspection, but to improve

the results of thermography. A pair of industrial heaters, a laboratory oven, propane

heaters, and a resistive heat element were used as excitation sources through 50 tests on

three specimens. A FLIR T620 camera was used to monitor the welds which is

considered a state-of-the-art thermal camera. Since the exact location of the defects was

known, the IRT inspection showed promising results; however, as seen in Fig. 9-1, there

are several sound locations on the specimens depicting similar behavior as defected

locations. Fig. 9-1b indicates considerable noise through the specimen and if the defect

locations were not known would be impossible to truly identify a defect and would result

in considerable false positive reports.

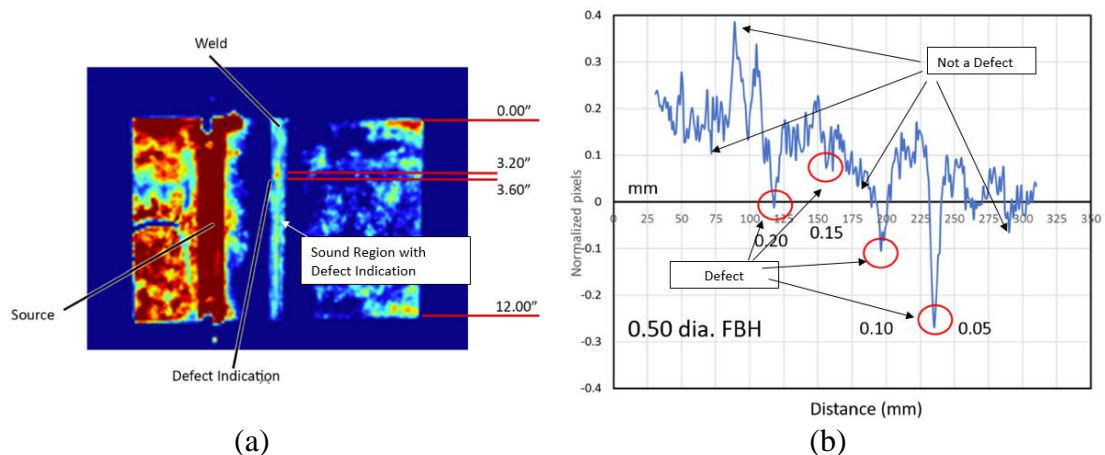(a)   (b)

Fig. 9-1 False positive in IRT weld inspections, images are from (Manuel and Washer 2017)

In order to investigate the possibility of using IRT for weld inspection for

Vulcraft, specimens with and without defects were manufactured and inspected using

IRT. This report summarizes the findings, conclusions, and recommendations of this study. Chapter 2 introduces the specimens and the process of defect manufacturing in this study. Chapter 3 explains the experiments performed on the specimens. Chapter 4 proposes the novel methodology to separate the defected regions from the sound regions. Chapter 5 presents the challenges and recommendations to improve the results of IRT weld inspection and chapter 6 presents the conclusions.

Specimens

Angles with two thicknesses, 3 mm (2/16 in.) and 8 mm (5/16 in.), were selected to manufacture the defects during welding. In addition, two 13 mm (8/16 in.) plates were also used to perform the multi-pass welds.

Defect Manufacturing

Initially, four common weld defects were proposed to be studied in this research. These defects were inclusion, porosity, cracking, and lack of fusion. To manufacture each defect, the following methods from past studies and experience were proposed:

Inclusion:

Method a: Drop a small piece of slag into the weld and weld over it;

Method b: Drill a small hole 1.5 mm (1/16 m) into the wall of the base metal;

Method c: Perform a multi-pass weld and drill a hole in first weld (Consonni et al, 2012).

Fig. 9-2 shows the process of inclusion manufacturing using method (a), i.e. putting slags in the welding bed. Fig. 9-3 shows the inclusion manufacturing using methods b and c.
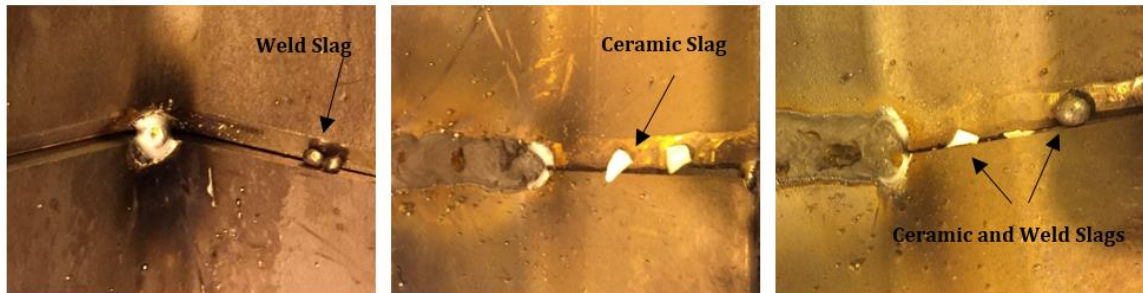
Fig. 9-2 Manufacturing inclusion in the welds using slag (method a)

Fig. 9-3 Manufacturing inclusion in the welds using drilling (method b and c)

Porosity:

Change amps/volts;

Introduce moisture to the welding bed (Kemppainen et al, 2003);

Introduce oil to the welding bed.

Method (a) created porosity on the back of the specimens while method (b) and (c) created both surface and sub-surface porosity. Fig. 9-4 shows how defected welds with porosity were manufactured.

Cracking:

Instead of a clean bevel, a small 6.35 mm (1/4 in). part of the angle square was left as is and welded around. As the weld cooled it created a very tight crack. Fig. 9-5 shows how the specimens were prepared before manufacturing the cracks in the welds.

Fig. 9-4 Manufacturing porosity in the welds by changing the voltage (method a), adding water (method b), and adding oil (method c)

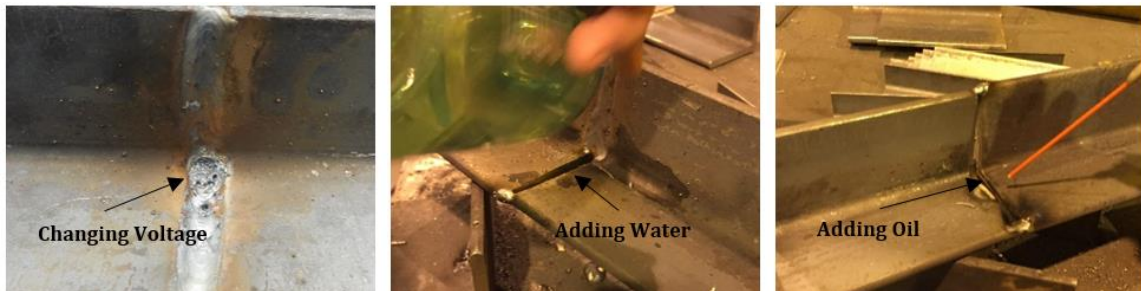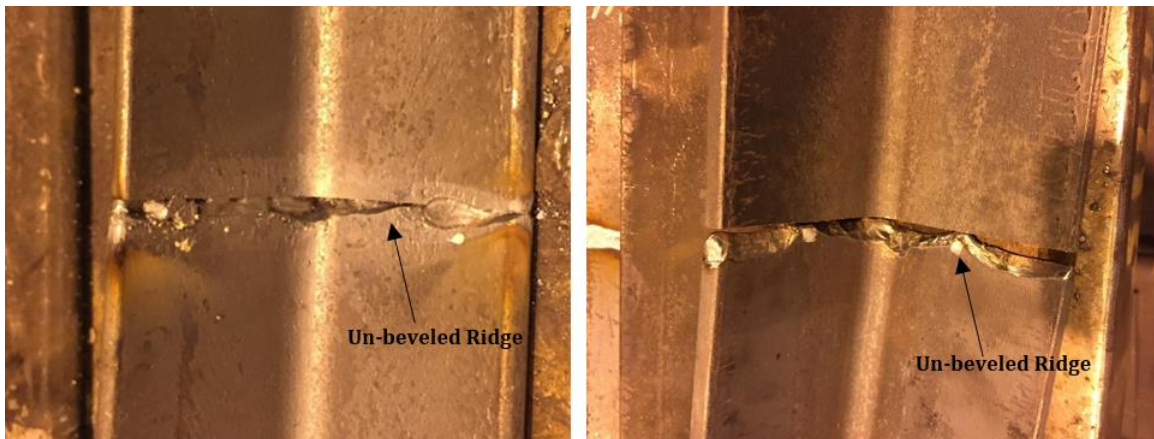**Fig. 9-5 Manufacturing cracks in the welds by leaving out a part of the bevels**

Lack of Fusion:

UT inspection, explained in the next section, showed that a couple of welds exhibited lack of fusion. These welds were made using a normal welding process and

were supposed to be sound. Since welds with lack of fusion were obtained, no additional process was used to create a lack of fusion defect in the specimens.

Experiments

UT Inspection

The total number of welded angles was 32, including 2 plates with thickness of 13 mm (8/16 in.), 14 angles with thickness of 8 mm (5/16 in.), and 8 angles with thickness of 3 mm (2/16 in.). A USN 58 L Ultrasound flaw detector was used to inspect the specimens. Fig. 9-6 shows the flaw detector and probe. The inspector swept the probe along the weld to locate defects. The regions with defects showed signal spikes in the monitor of the device. The results of the UT inspection are shown in Table 9-1. In this table, quantity represents the number of specimens, an angle leg or a plate surface, that was considered to have a certain defect after UT inspection. The specimens with 3 mm (2/16 in.) thickness were inspected, but the results are not valid due to the thickness limitation regulated by ASTM.

IRT Inspection

The aim of the IRT inspection was to investigate whether it is feasible to detect the same defects UT inspection identified previously. The thermal camera for this study was an FLIR SC640 thermal camera with an operating temperature range of -40 to 80°C. The camera also has a thermal sensitivity of 30 mK at 30°C, accuracy of $\pm$ 1°C, spectral range of 7.5-13 μm, resolution of 640 by 480 IR, and up to 30 Hz data acquisition frequency.
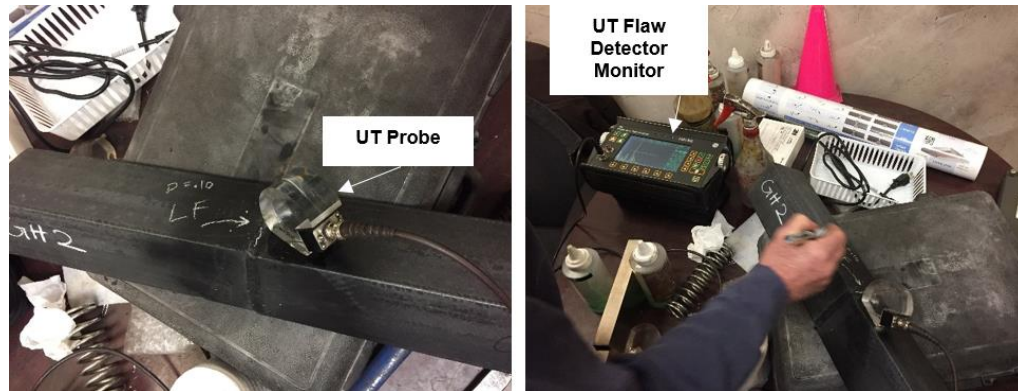
Fig. 9-6 USN 58 L Ultrasonic flaw detector

Table 9-1 Results of UT inspections

Specimen Thickness	Detected Defect	Quantity
13 mm (8/16 in.)	Inclusion	1
	Lock of Fusion	1
	Sum	*2*
8 mm (5/16 in.)	Sound	2
	Inclusion	1
	Porosity	11
	Cracking	2
	Lack of Fusion	10
	Over Pass	2
	Sum	*28*

In order to simulate in-line inspection, the specimens were heated up to a temperature in the range of the operating temperature of the camera using a Milwaukee Variable Temperature Heat Gun. The heat gun increased the temperature of the specimens, each leg of the angles at the time or the whole plate, through transmission mode. Fig. 9-7 shows the experiment set up. The heat gun, placed within 50 mm (2 in.) of the bottom of the specimens, increased the temperature of a Region of Interest (ROI) in

each specimen. For specimens with defects, the ROI covered the region with defects

determined by UT inspections. For sound welds, ROI was selected randomly on the weld.

The thermal camera was set on a tripod to monitor the surface emission of the weld.

When the maximum temperature reached almost 80°C, the heat gun was turned off and

the camera started recording thermal sequences with a 10 Hz frequency for 50 s. The

camera connected to a PC that provided a First Person View (FPV) of the specimens
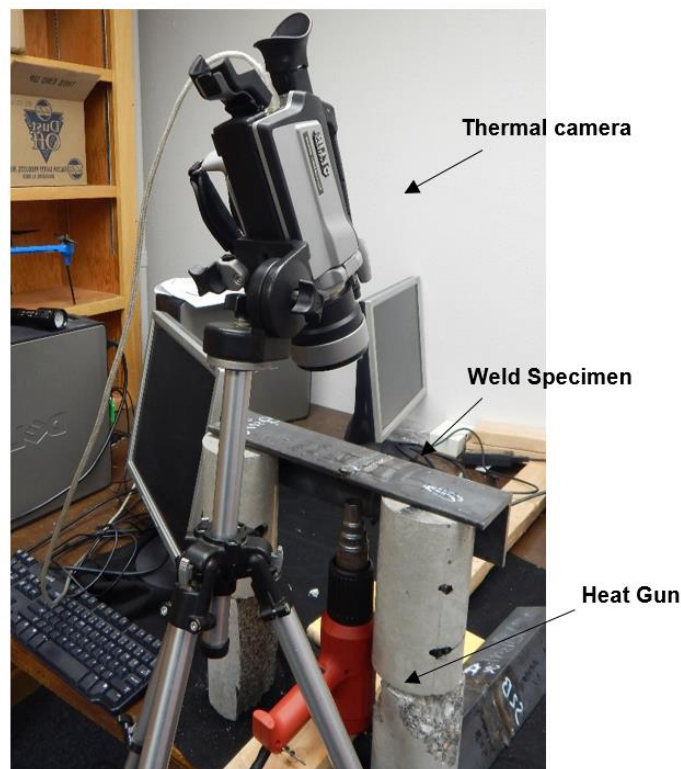
through Therma Vision Examine IR software.

Fig. 9-7 Weld inspection in a lab setting

Proposed Temperature Decay

Solving Newton's cooling law and specific heat formula, the temperature of any

given object changes in an exponential form as shown below:

$$T(t) = T_a + (T_0 - {}_a)e^{-kt} \qquad (9\text{-}1)$$

Where T is the temperature of a certain location at any time, T_a is the ambient

temperature, T_0 is the material temperature at the initial time, and k is a constant which

depends on the following: material heat transfer constant (α), area of the exposed surface

(A), mass of the material (m), and specific heat of the material (c).

$$k = \frac{-\alpha A}{mc} \qquad (9\text{-}2)$$

Presence of a defect disrupts the heat transfer by changing one or multiple

parameters in equation (9-2). Therefore, the ROIs with defects should theoretically have

different temperature functions than the sound ROIs.

The surface of the specimens in this study were not grinded or prepared, with the

exception of two specimens that were painted with black high emissivity paint. Each

sequence of thermal images shows the temperature of the specimen in different locations

as pixel intensities. By monitoring each pixel through time, one can fit an exponential

function and compare the sound and defected pixels to each other. However, fitting a

curve to each pixel in an image throughout the whole sequence can be time consuming

and computationally expensive. Therefore, sub-regions consisting of 10-30 pixels were

defined for each ROI in each specimen. The average temperature of each sub-region was

then calculated in each sequence and an exponential curve was fitted to the sub-region.

Results

Table 9-2 shows the specimens tag, ID, intended defect, identified defect using

UT, and observed defect after cutting through destructive testing (DT). The size of the

defects was measured using a HUMBOLDT HC-2950 microscope with 0.02 mm (0.0008 in.). The UT inspection results detected lack of fusion in 10 specimens despite the presence of other defects in them. UT inspection also did not result in conclusive defect identification for 3 mm (2/16 in.) specimens.

Table 9-2 The summary of specimens and their defects

Specimen Tag	Thickness (mm)	Intended Defect	Identified Defect (UT)	Observed Defect (DT)	Size (mm) L	W
IHc1	13	I	I	ND	-	-
IHc2	13	I	LoF	ND	-	-
S1A	8	ND	ND	ND	-	-
S1B	8	ND	ND	ND	-	-
CH1A	8	C	P	C	1.06	0.02
CH1B	8	C	P	C	1.68	0.42
				C	5.00	0.96
CH2A	8	C	C	C	1.20	0.04-0.20
				C	1.30	0.30
CH2B	8	C	C	I	2.46	1.22
GH2A	8	ND	LoF	ND	-	-
GH2B	8	ND	LoF	ND	-	-
IHa1A	8	I	LoF	I	2.94	0.68
IHa1B	8	I	LoF	I	0.92	0.56
IHa2A	8	I	LoF	C	5.00	0.08
IHa2B	8	I	LoF	I	0.20	0.20
IHa3A	8	I	P	C	1.82	0.12
IHa3B	8	I	OP	I	2.10	1.30
				I	3.06	0.26
IHa4A	8	I	I	ND	-	-
IHa4B	8	I	P	I	0.58	0.58
				C	1.00	0.22

NH1A	8	ND	LoF	I	0.30	0.30
				C	1.00	0.02
NH1B	8	ND	LoF	ND	-	-
NH2A	8	ND	LoF	ND	-	-
NH2B	8	ND	LoF	ND	-	-
PHa1A	8	P	P	P	1.02	1.02
				P	1.20	1.20
PHa1B	8	P	OP	I	0.50	0.50
PHa2A	8	P	P	I	2.18	0.54
				C	0.50	0.04
PHa2B	8	P	P	I	1.30	0.66
				I	1.36	0.72
PHb1	8	P	P	P	0.62	0.40
				I	1.00	0.24
PHb2	8	P	P	I	0.62	0.08
				I	1.10	0.22
PHc1	8	P	P	I	0.98	0.20
PHc2	8	P	P	ND	-	-
CL1	3	C	ND	I	0.18	0.12
GL1	3	ND	ND	ND	-	-
GL2	3	ND	ND	ND	-	-
GL3	3	ND	ND	ND	-	-
NL1	3	ND	ND	ND	-	-
NL2	3	ND	ND	ND	-	-
PLO	3	P	ND	ND	-	-
PLW	3	P	ND	ND	-	-

The proposed IRT technique was evaluated with respect to the UT results in the

following sections

UT Inspection

8 mm (5/16 in.) Specimens

Two specimens had sound welds according to the UT inspection. Fig. 9-8 shows

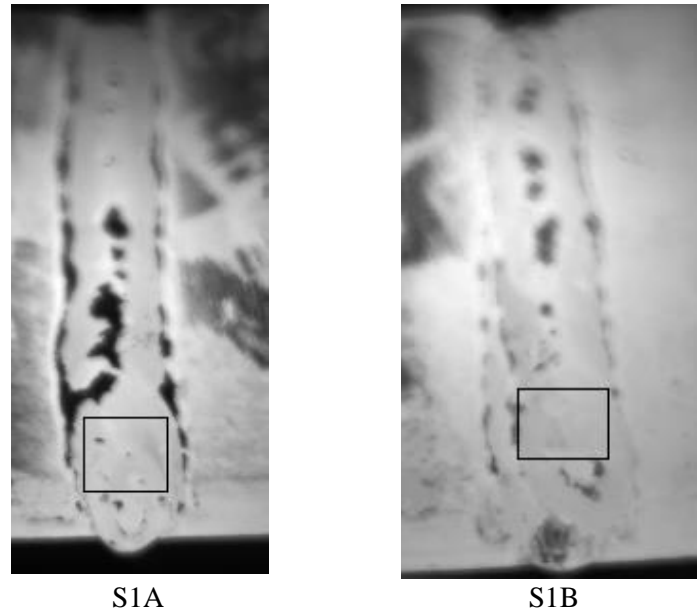the 8 mm (5/16 in.) sound specimens with the regions of interest.

S1A   S1B

Fig. 9-8 Eight mm (5/16 in.) sound specimens, S1A and S1B, with associated ROIs

The mean temperature in 5-pixel by 5-pixel sub-regions was calculated for each sequence. The general form of the fit function was as follows:

$$T(t) = ae^{-bt} \tag{9-3}$$

The mean of coefficients "a" and "b" for each specimen and the total number of sub-regions are shown in Table 9-3. The average of two ROIs is considered to be the fit function for the sound weld with thickness of 8 mm (5/16 in.). Fig. 9-9 shows the temperature decay graphs for sound welds, S1A and S1B, and for the average. The area under the temperature decay graph can be used as an indicator for heat loss (A_n).

The UT inspection detected defects in 8 mm (5/16 in.) specimens including 1 with inclusion, 11 with porosity, 10 with lack of fusion, 2 with sub-surface cracking, and 2 with over-pass (out of this study's scopes). The ceramic inclusion caused the weld to lose

temperature faster in specimen IHa4A than the sound weld, as seen in Fig. 9-10. A for

the ROI with inclusion was 3102, which was smaller than the sound specimen.

Table 9-3 Coefficients of the exponential fit functions for 8 mm (5/16 in.) sound welds

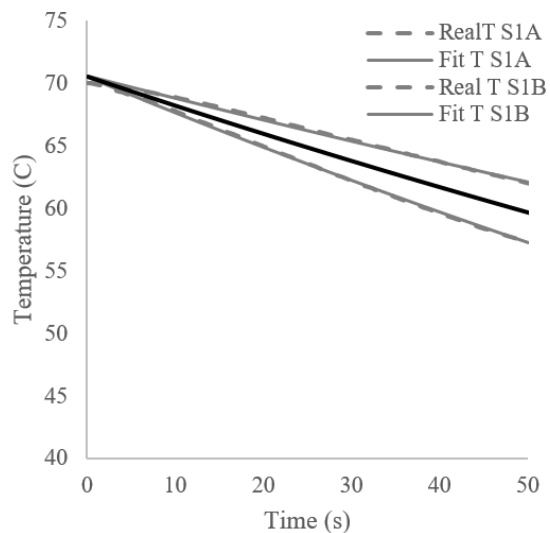| S1A				S1B				Average		
No of Sub-regions	A_n	a	b	No of sub-regions	Area	a	b	A_n	a	b
72	3176	70.53	0.00417	63	3307	69.53	0.00256	3242	70.03	0.003365

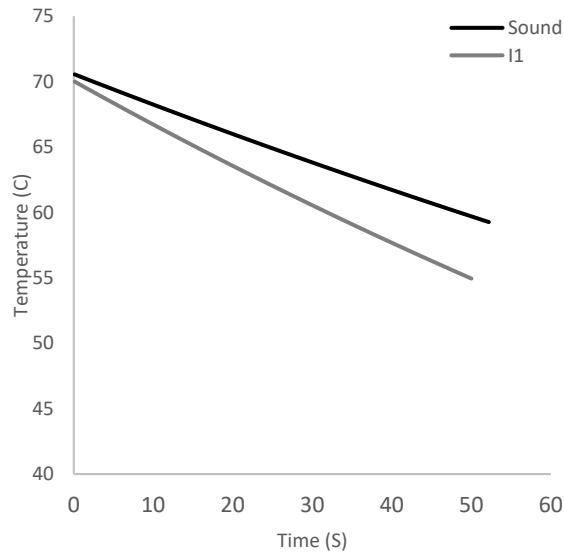**Fig. 9-9 The temperature decay for graph for sound welds**

Fig. 9-10 Temperature decay in sound weld and IHa4A with inclusion

A total of 11 specimens were diagnosed with porosity in the UT inspection. The porosity in three of them was caused by changing the voltage during welding. Fig. 9-11 shows the temperature decay graphs for welds with porosity manufactured by this method. As seen, the sound weld was more resistant to heat loss than the welds with porosity. The area A_n for P1, P2, and P3 (PHa1A, PHa2A, and PHa2B specimens) were 2982, 3046, and 3134, respectively, which were smaller than the sound area in all three cases.

The UT inspection showed signs of porosity in 2 specimens that were manufactured to have cracking. The temperature decay graphs for these specimens are shown in Fig. 9-12. The heat loss was faster in defected specimens than the sound weld. The values of A_n for P4 and P5 (CH1A and CH1B specimens) were 2732 and 2990, respectively.

The UT inspection showed signs of porosity in 2 specimens that were

manufactured to have inclusion. The temperature decay graphs for these specimens are shown in Fig. 9-13. The heat loss was faster in defected specimens than those with sound welds. The values of A_n for P6 and P7 (IHa3A and IHa4B specimens) were 3130 and 3085, respectively.

Introducing oil to the welding bed also caused porosity in two specimens. The temperature decay graphs for these specimens are shown in Fig. 9-15. The heat loss was faster in defected specimens than the sound weld specimens. The values of A_n for P10 and P11 (PHc1 and PHc2 specimens) were 3115 and 3080, respectively.

Introducing water to the welding bed caused porosity in two specimens. The temperature decay graphs for these specimens are shown in Fig. 9-14. The heat loss was faster in defected specimens than the sound weld specimens. The values of A_n for P8 and P9 (PHb1 and PHb2 specimens) were 3119 and 3114, respectively.

Using the proposed method to manufacture cracking, UT inspection verified regions with cracks in two specimens. The temperature decay graph for these specimens are shown in Fig. 9-16. The heat loss was faster in defected specimens than the sound weld. The values of A_n for C1 and C2 (CH2A and CH2B specimens) were 3101 and 3144, respectively.
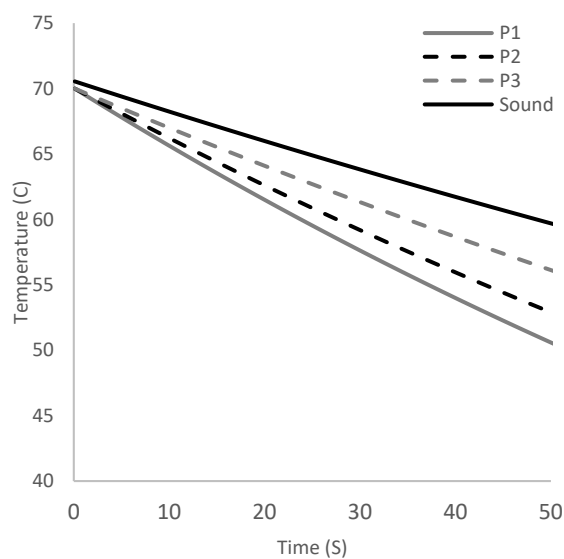
Fig. 9-11 Temperature decay of PHa1A, PHa2A, and PHa2B specimens with porosity (manufactured by changing voltage) and sound welds
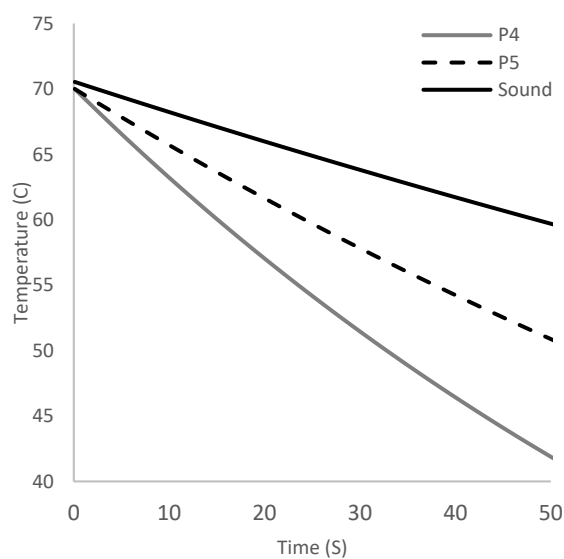
Fig. 9-12 Temperature decay of CH1A and CH1B specimens with porosity (manufactured for cracking) and sound welds
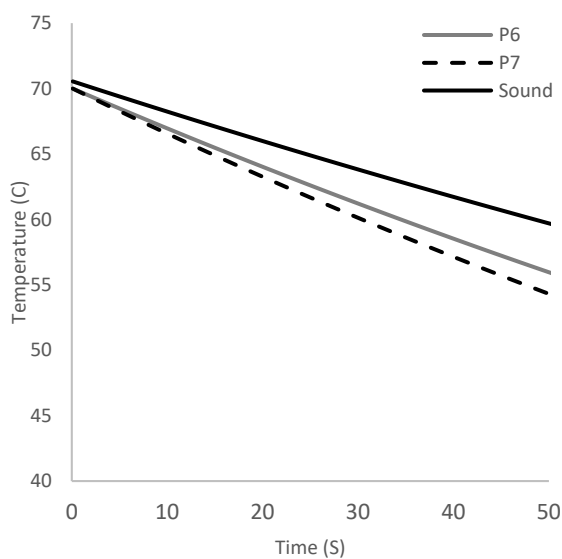
Fig. 9-13 Temperature decay of IHa3A and IHa4B specimens with porosity (manufactured for inclusion) and sound welds
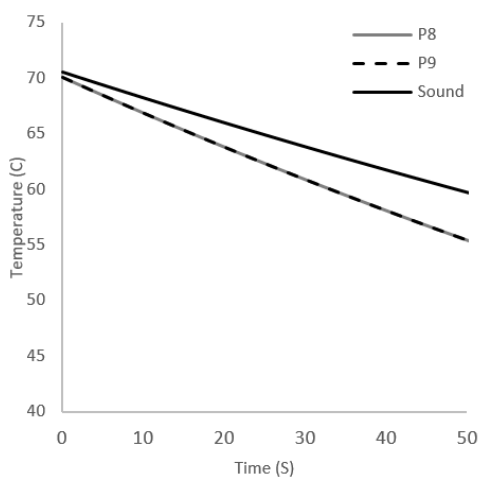
Fig. 9-14 Temperature decay of PHb1 and PHb2 specimens with porosity caused by water and sound welds
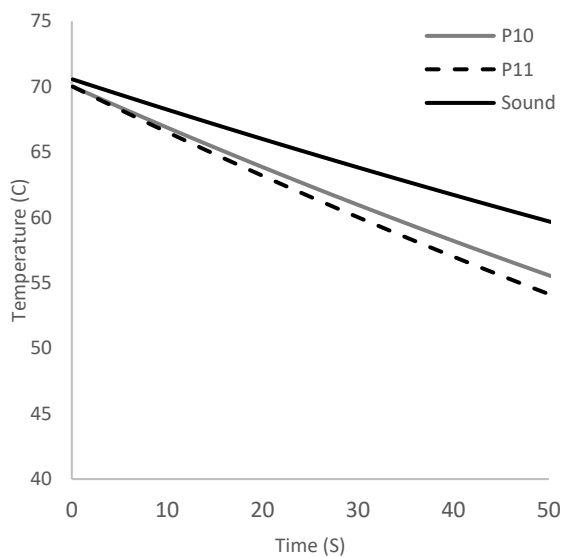
Fig. 9-15 Temperature decay of PHc1 and PHc2 specimens with porosity caused by oil and sound welds

Fig. 9-16 Temperature decay of CH2A and CH2B specimens with cracks and sound welds

A total number of 10 specimens were diagnosed with lack of fusion by the UT inspection . The lack of fusion in these specimens happened during the welding process and was not intentional. This defect was detected using UT inspection and prevented

identification of other defects, if existing, since the presence of lack of fusion disrupted the signal.

Two specimens with lack of fusion were originally built to be part of sound specimens. The welding bed was beveled and cleaned prior to welding of these specimens. The temperature decay graphs for these specimens are shown in Fig. 9-17. The heat loss was faster in defected specimens than the sound weld. The values of A_n for LoF1 and LoF2 (GH2A and GH2B specimens) were 2992 and 3037, respectively.
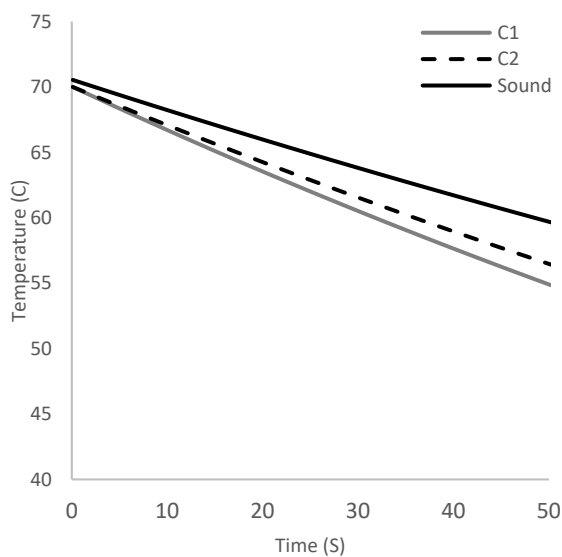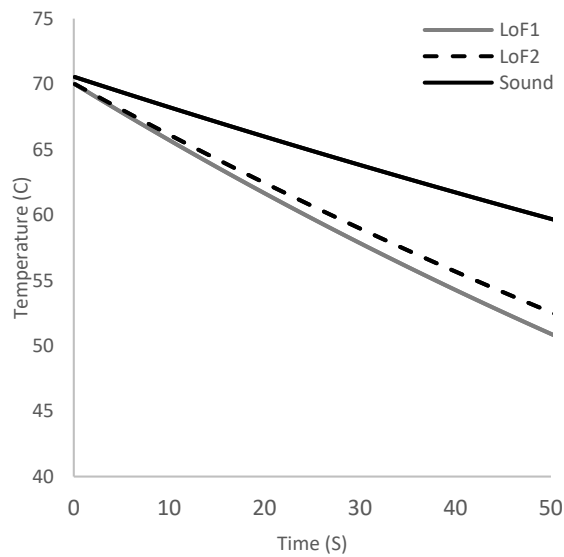

Fig. 9-17 Temperature decay of GH2A and GH2B specimens with lack of fusion in good welds and sound welds

Four specimens with lack of fusion were originally built to have inclusions. The temperature decay graphs for these specimens are shown in Fig. 9-18. The heat loss was faster in defected specimens than the sound weld. The values of A_n for LoF3, LoF4, LoF5, and LoF6 (IHa1A, IHa1B, IHa2A, and IHa2B specimens) were 3051, 2994, 2836,

and 2907, respectively.

Four specimens with lack of fusion were originally built to have no defects. Unlike specimens LoF1 and LoF2, the welding bed was not beveled prior to welding (normal welding process). The temperature decay graphs for these specimens are shown in Fig. 9-19. The heat loss was faster in defected specimens than the sound weld. The values of A_n for LoF7, LoF8, LoF9, and LoF10 (NH1A, NH1B, NH2A, and NH2B specimens) were 2947, 2917, 2892, and 2825, respectively.

In two specimens, UT inspection detected over-pass. Even though this defect was not in the scope of this study, these specimens were analyzed for comparison. The temperature decay graphs for these specimens are shown in Fig. 9-20. The heat loss was faster in defected specimens than the sound weld. The values of A_n for OP1 and OP2 (IHa3B and PHa1B specimens) were 3179 and 3077, respectively.

Table 9-4 shows the values A_n for all the specimens with 8 mm (5/16 in.) thickness.
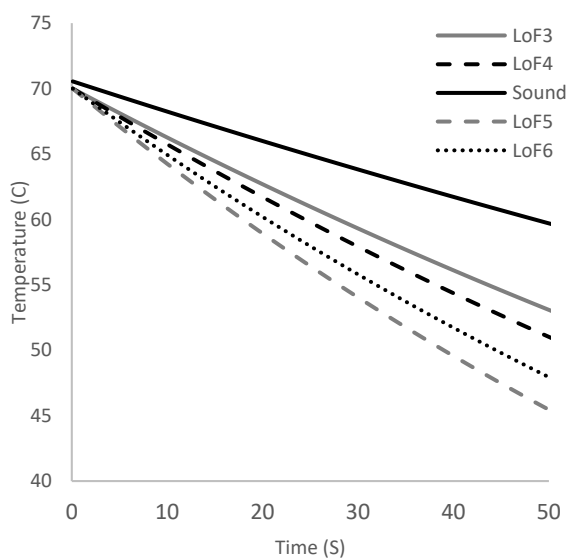
Fig. 9-18 Temperature decay of IHa1A, IHa1B, IHa2A, and IHa2B specimens with lack of fusion (intended to have inclusion) and sound welds
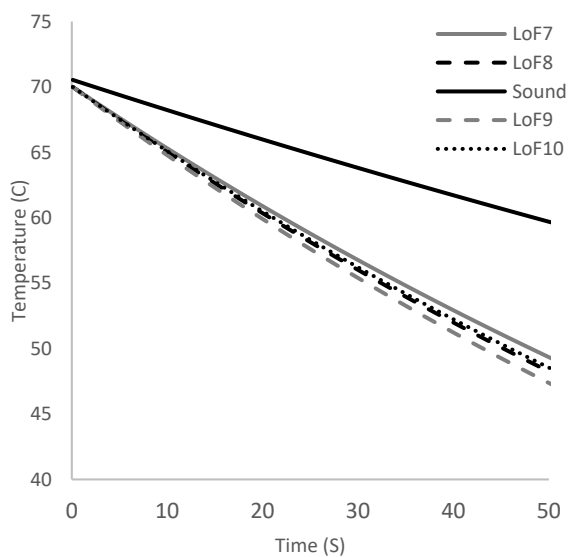
Fig. 9-19 Temperature decay of NH1A, NH1B, NH2A, and NH2B specimens with lack of fusion in normal welds and sound welds
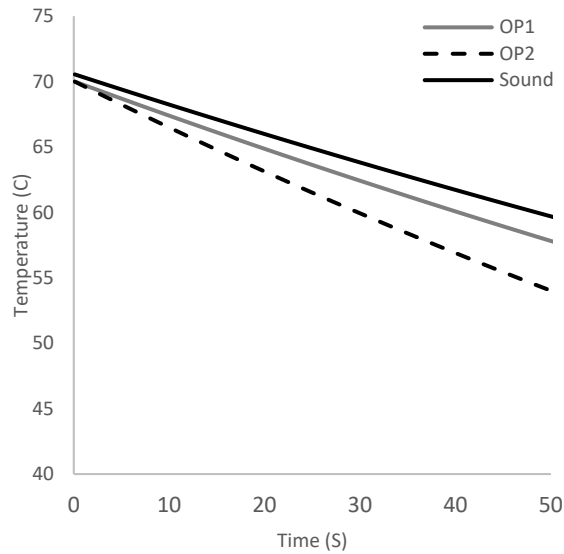
Fig. 9-20 Temperature decay of IHa3B and PHa1B specimens with lack of fusion and sound welds

13 mm (8/16 in.) Specimens

UT inspection showed both plates had defects in them: inclusions and lack of fusion. Therefore, no fit function associated with sound specimens can be calculated for 13 mm (8/16 in.) plates. In order to obtain the exponential fit function for sound regions, two ROIs were selected in the regions that passed the UT inspection as sound. Then each ROI was segmented to several sub-regions and the fit function for each sub-region was obtained. Table 9-5 shows mean of coefficients for the fit function and the A_n values over all sub-regions for the sound weld. UT inspection detected 3 inclusions in one of the specimens. The temperature decay graphs for ROIs with defects are shown in Fig. 9-21. The heat loss was faster in defected ROI than the sound weld. The values of A_n for I2, I3, and I4 (IHc1-1, IHc1-2, and IHc1-3 specimens) were 3046, 3244, and 3102, respectively.

Table 9-4 The values of A_n for 8 mm (5/16 in.) welds

Defect Type	Specimen Tag	Defect ID	A_n
Sound	S1	NA	3242
Inclusion	IHa4A	I1	3102
Porosity	PHa1A	P1	2982
	PHa2A	P2	3046
	PHa2B	P3	3134
	CH1A	P4	2732
	CH1B	P5	2990
	IHa4A	P6	3130
	IHa4B	P7	3085
	PHb1	P8	3115
	PHb2	P9	3114
	PHc1	P10	3119
	PHc2	P11	3080
Cracks	CH2A	C1	3101
	CH2B	C2	3144
Lack of Fusion	GH2A	LoF1	2992
	GH2B	LoF2	3037
	IHa1A	LoF3	3051
	IHa1B	LoF4	2994
	IHa2A	LoF5	2836
	IHa2B	LoF6	2907
	NH1A	LoF7	2947
	NH1B	LoF8	2917
	NH2A	LoF9	2892
	NH2B	LoF10	2825
Over-pass	IHa3B	OP1	3179
	PHa1B	OP2	3077

UT inspection detected lack of fusion in a part of the weld on the other plate. The temperature decay graph for the ROI with lack of fusion is shown in Fig. 9-22. The heat

loss was slightly faster in the defected specimen than the sound weld. The value of A_n for

LoF11 (IHc2 specimen) was 3341.

Table 9-6 shows the A_n values for all the specimens with thickness of 13 mm

(8/16 in.).

Table 9-5 Coefficients of the exponential fit functions for 13 mm (8/16 in.) sound welds

Specimen 1 (with inclusions)				Specimen 2 (with LoF)			
No of Sub-regions	A_n	a	b	No of Sub-regions	A_n	a	b
158	3354	70.01	0.00164	100	3353	70.02	0.00228
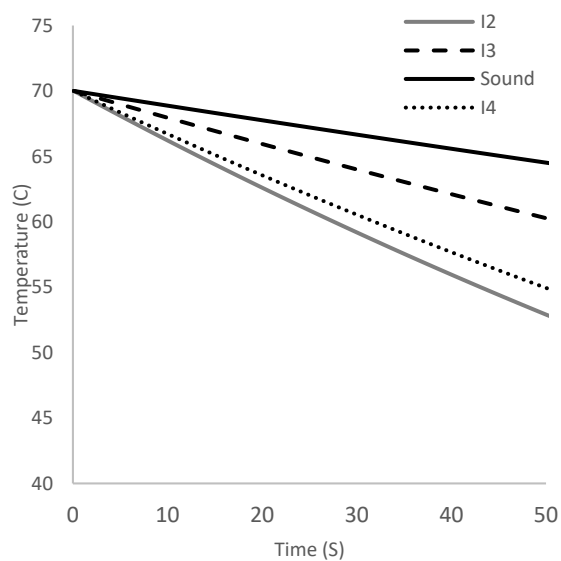
Fig. 9-21 Temperature decay of IHc1-1, IHc1-2, and IHc1-3 specimens with inclusions and sound weld
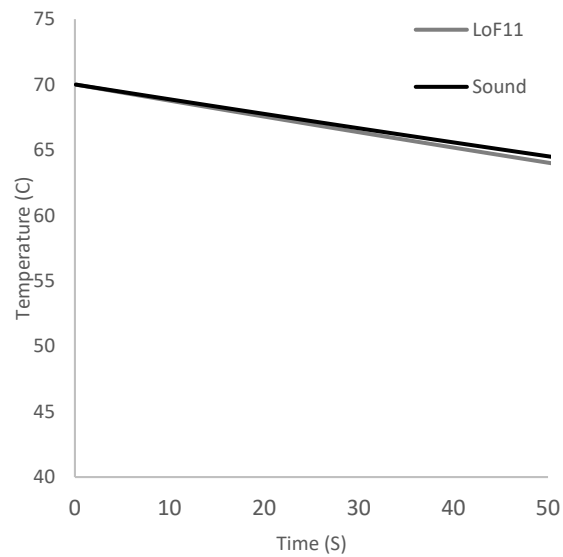
Fig. 9-22 Temperature decay of IHc2 specimen with lack of fusion and sound weld

Table 9-6 The values of An for 13 mm (8/16 in.) welds.

Defect Type	Specimen Tag	Defect ID	A_n
Sound	NA	NA	3354
Inclusion	IHc1-1	I2	3046
	IHc1-2	I3	3244
	IHc1-3	I4	3102
Lack of Fusion	IHc2	LoF11	3341

3 mm (2/16 in.) Specimens

The list of the 3 mm (2/16 in.) specimens with their intended defects are shown in

Table 9-7. Since the UT inspection results were not valid for these specimens, two of the

specimens, made using the normal process, were selected as sound specimens. The ROI

on each specimen, covering the whole area of the weld, was segmented into sub-regions.

The mean of coefficients "a" and "b" for all sub-regions and the total number of sub-

regions are shown in Table 9-8.

Table 9-7 IDs and possible defects in 3 mm (2/16 in.) specimens

Specimen ID	Specimen Tag	Possible Defect
L1	GL2	Sound
L2	GL3	Sound
L3	CL1	Cracking
L4	GL1	Porosity
L5	NL1	Lack of Fusion
L6	NL2	Inclusion
L7	PLW	Porosity
L8	PLO	Porosity

Table 9-8 Coefficients of the exponential fit function for 3 mm (2/16 in.) sound welds

L1				L2				Average		
No of Sub-regions	A_n	a	b	No of sub-regions	Area	a	b	A_n	a	b
2035	3060	69.29	0.0049	1292	3050	67.26	0.0038	3056	68.50	0.0045

$A_n = 3056$ was considered the area associated with the sound weld in 3 mm

(2/16 in.) specimens. The rest of the specimens were analyzed and the A_n value of each

sub-region was compared to 3056. If the area was less than 3056, the sub-region was

considered defected, since defected regions tend to lose heat faster than the sound ones.

Otherwise, the analyzed sub-region was sound.

For specimen L3, no defected regions were found in the ROI, the region inside of

the rectangle, as seen in Fig. 9-23. For specimen L4, no defected regions were found in

the ROI, the region inside of the rectangle, as seen in Fig 9-24. For specimen L5, six

regions were identified as defected in the ROI, the region inside of the rectangle, as seen

in Fig. 9-25. The defected regions were identified with solid rectangles on in the ROI.

The pattern of these solid rectangles indicates porosity. For specimen L6, no defected

regions were found in the ROI, the region inside of the rectangle, as seen in Fig. 9-26.

For specimen L7, six regions were identified as defected in the ROI, the region inside of the rectangle, as seen in Fig. 9-27. The defected regions were identified with solid rectangles in the ROI. The pattern of the detected defects indicates porosity on the rectangles on the right and lack of fusion on the rectangles on the left (edge of the weld).

For specimen L7, several regions were identified as defected in the ROI as seen in Fig. 9-28. The defected regions were identified with solid rectangles on the ROI. The pattern of the detected regions can be associated with porosity and/or lack of fusion.

Fig. 9-23 Specimen L3 and the ROI
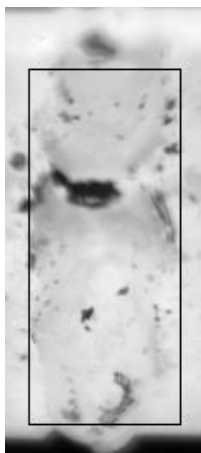
Fig. 9-24 Specimen L4 and the ROI
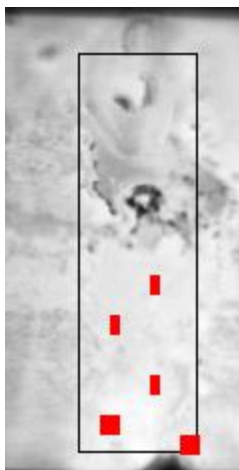
Fig. 9-25 Specimen L5 and the ROI, with the regions identified as defects in red
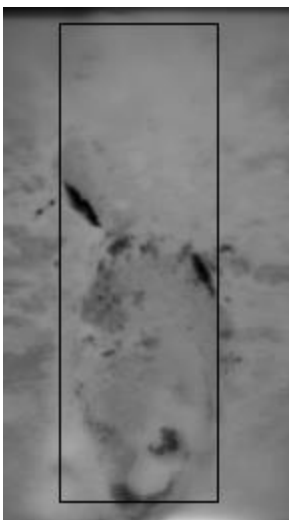
Fig. 9-26 Specimen L6 and the ROI
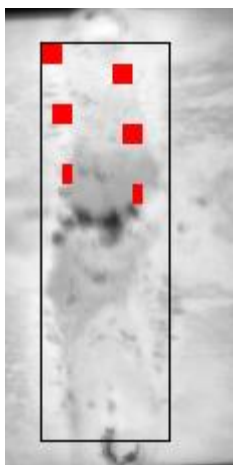
Fig. 9-27 Specimen L7 and the ROI, with the regions identified as defects in red
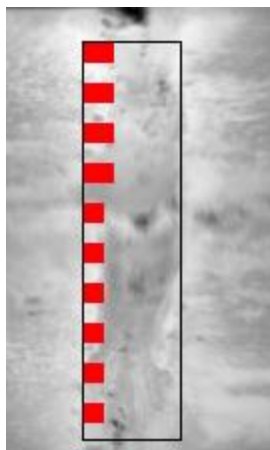
Fig. 9-28 Specimen L8 and the ROI, with the regions identified as defects in red

Destructive Testing of the Specimens

The destructive testing includes cutting the weld specimens longitudinally at susceptible locations. The susceptible locations are determined in the UT inspection. Fig. 9-29 shows a typical cut performed on specimens CH1A and CH1B. The observed defects and their size in all specimens are shown in Table 9-2. The cutting results for some specimens in this table indicated no defects (ND) despite being diagnosed with defects in UT and IRT inspections. Due to the small size of the defects, as seen in Table 9-2, the cut could have missed the defects. The other possible scenario is that UT and IRT inspection provided false positives in these specimens.
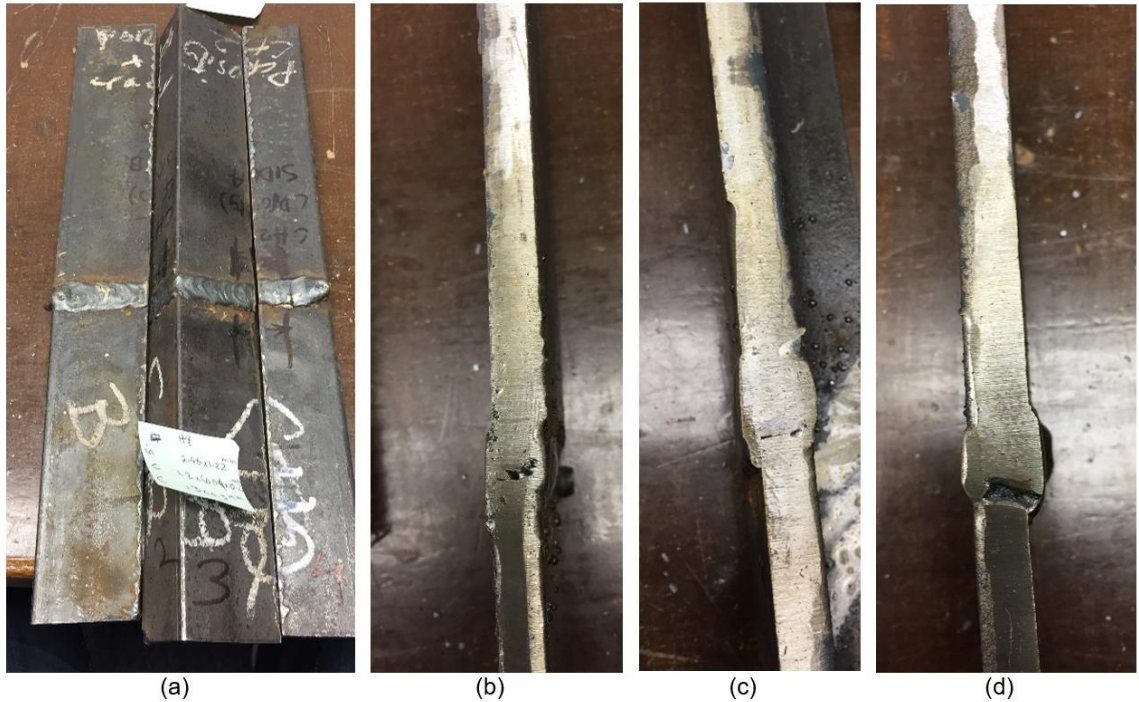
Fig. 9-29 Specimens CH1A and CH1B (a) cutting, (b) inclusion (c) crack, (d) inclusion

The sole use of the proposed IRT method for weld defect detection can identify the locations of defects, the regions with smallest values of A_n. Fig. 9-30 show the A_n values for the specimen IHc1 and the region on interest. Each column in the bar graph represents the average A_n for a sub-region (5 by 5 pixels) in the region of interest. The darker colors indicate lower A_n values which are associated with the defected regions. As seen, the middle of the weld had the least A_n values which is in agreement with 3 inclusions detected in the UT inspection, however, the DT results showed no signs of defects. Fig. 9-31 shows the A_n values and region of interest of the specimen IHc2 where the UT inspection identified lack of fusion. In the bar graph the lack of fusion can be seen on the edge of the weld with darker colors. Fig. 9-32 shows the A_n values for specimen PHa2b. The darker column in the bar graph were associated with defected

regions and also false positives, as indicated in the figure.
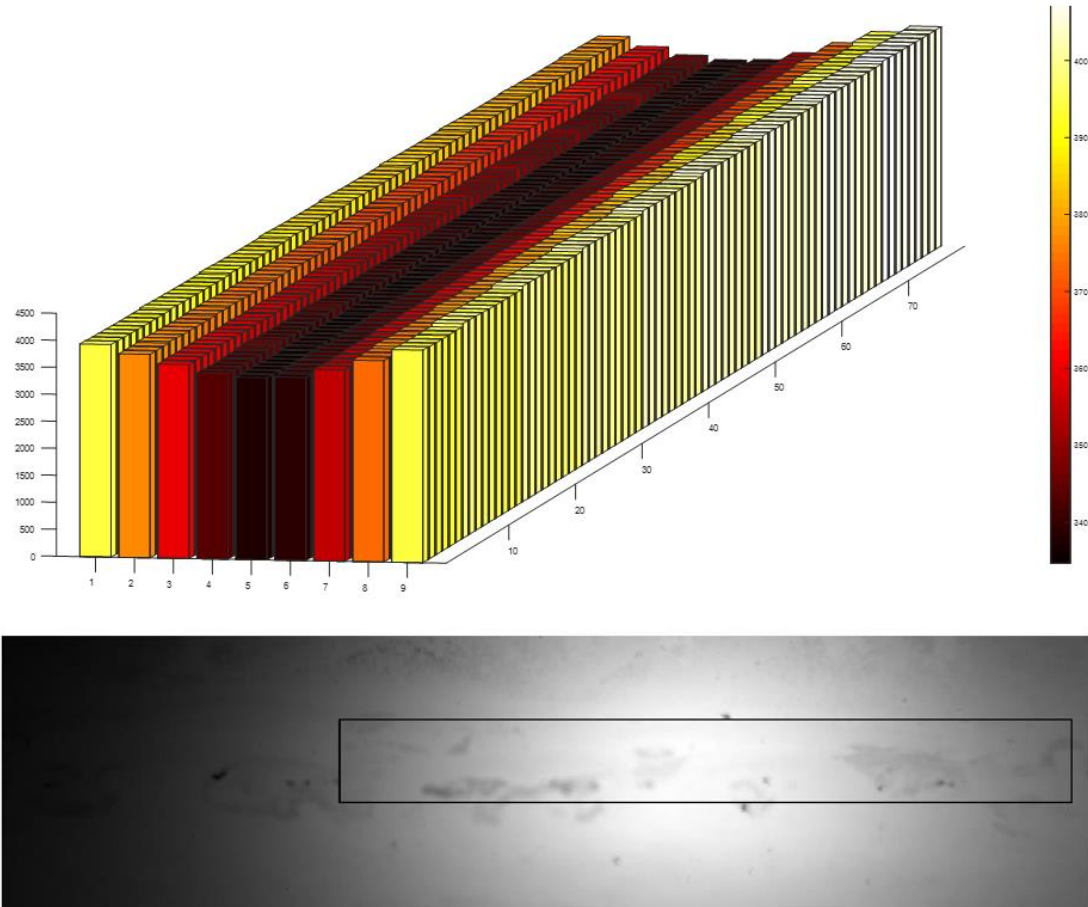
Fig. 9-30 The An values for specimen IHc1

Finding the defects using the proposed IRT method can be challenging or impossible due to false positives.

Challenges and Recommendations

The authors faced several challenges throughout this research. Using real-time IRT for weld inspection has not been done in the past studies.
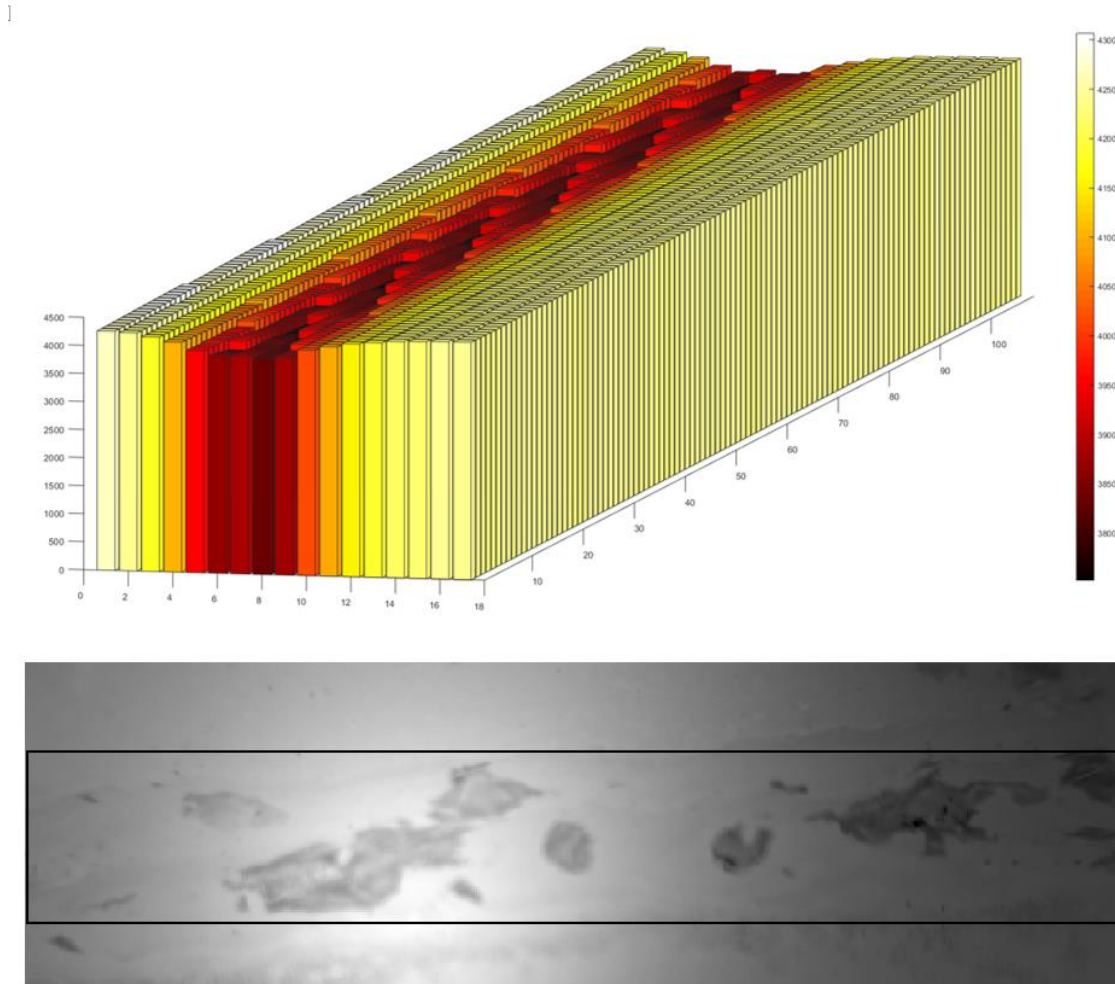
Fig. 9-31 The An values for specimen IHc2

Weld Surface

During the welding process, the specimens' surface manifested regions with irregularities such as difference in contrast or color and bumps, which affected the thermal images. These irregularities were not correlated with the presence of defects in the welds and can mislead the inspector viewing the captured thermal images. Fig. 9-33shows how the surface clutters can increase the false positive detections in a thermal image. Having these clutters changes the surface emissivity of the material and can cause

inaccuracy in the camera's readings. This issue is even more important when dealing with low-emissivity materials such as steel and welds.
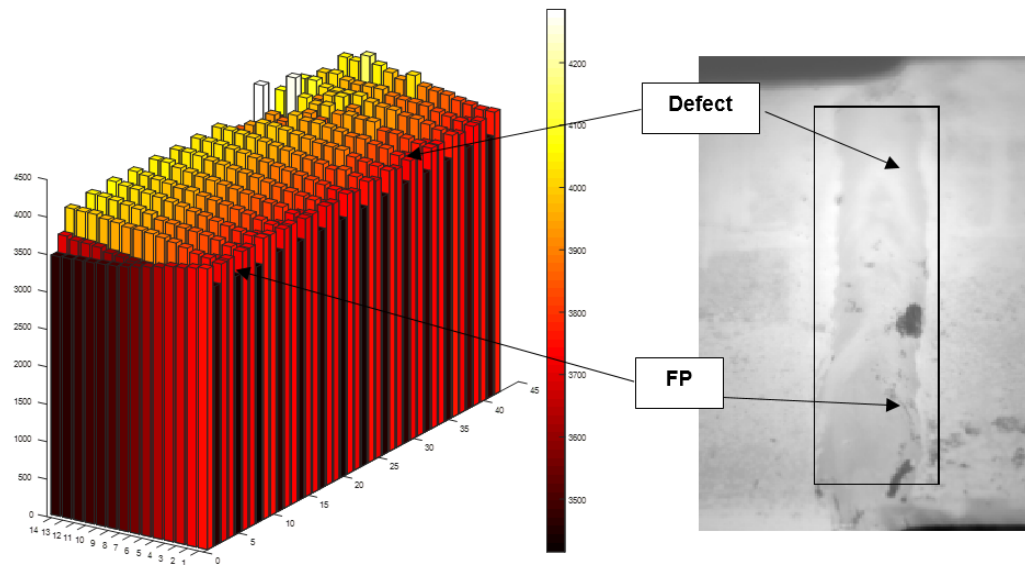
Fig. 9-32 The An values for specimen PHa2B

It is possible to grind the weld surface to get rid of the surface clutters and bombs but it would not be practical in a manufacturing process. Another option is covering the weld surface with high emissivity paint to provide a mono-contrast surface for thermography. All welds eventually get painted in the manufacturing process, but it is preferable to detect the defects before painting and right after they are built.
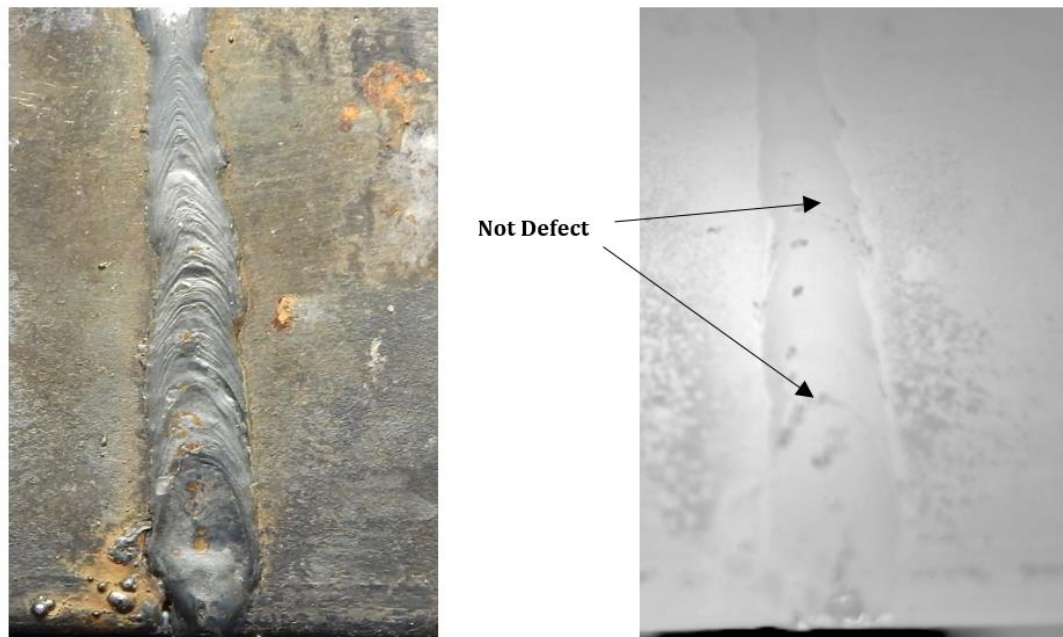
Fig. 9-33 Misleading surface clutters: left visual, right thermal

Camera

The specification of the infrared camera plays an important role in IRT weld inspection. The camera used for this study, FLIR SC 640, does not have comparable sensitivity and accuracy to the recent commercially available ones. In addition, this camera was not compatible with MATLAB and uses an old-fashioned chord for desktop connection, which is not well-suited to new desktops. However, the most important issue with the FLIR SC 640 was its low temperature range (-40 to 80°C) which does not allow real-time in-line weld inspection. FLIR SC 6100 measures up to 2,000°C and can record sequences up to 126 Hz. It is also possible to special-order cameras with even larger temperature ranges.

Uncontrolled and Uneven Heating

Excitation source is another factor affecting the success of IRT weld inspection.

In this study, a heat gun was used to simulate the temperature condition of a steel angle after welding in a lower scale. The heat gun provides a cheap, easy-to-use, and repeatable source for increasing the temperature of the welds; however, the transmitted energy from the heat gun is not homogenous. Some regions get hotter than the others. Using the fit function of the temperature decay instead of using actual temperatures diminished the effects of un-even heating to some extent, but it did not completely resolve it. The amount of energy created by the heat source could not be measured when the heat gun was used. Therefore, the heating is un-controlled. Common heat sources used in the literature for IRT defect detection are high power halogen and Ultraviolet (UV) lamps. Lumatic Superlite I07 UV lamp was used to detect weld cracks in a study and showed promising results (Broberg 2013).

Defect Manufacturing

Another challenge in this study was to manufacture realistic weld defects. Despite using standard methods to build defects, some defects were really hard to obtain. For instance, in 8 mm (5/16 in.) specimens, UT only detected inclusion in 1 out of 8 specimens. The methodology used to generate cracks was not conclusive to cracks even though UT inspection detected some anomalies in those specimens. Lack of fusion aside, porosity seemed to be the most convenient defect to manufacture by introducing water and oil to the welding bed; however, most of the obtained porosities were on the surface and visually detectable. Lack of fusion was manifested in welds when it was not supposed to; either they were built to have a different defect or no defects at all.

Welding Process

The process used to create the welds in this study was … which was highly uncontrolled due the extreme temperature and pressure imposed on the base metal. Some defects, such as inclusion, were almost impossible to create in this process, mainly because the slags were blown away from the welding bed. This welding process also resulted in more surface clutters than controlled welding. Tungsten inert gas (TIG) welding can be used to create the defects in a more controlled manner.

Conclusions

Verification of weld safety and workmanship is paramount to structural weld inspection both during fabrication and in-service. Weld inspections are costly in terms of time and money for both situations. Ultrasonic (UT) technique has been widely used to detect surface and sub-surface defects of welds. Because UT inspection is an inspection with contact, the inspector needs to wait for the welds to cool down for one to a six hours. This adds time, and consequently cost, to the inspection process. The purpose of this study is to investigate the potentials and challenges of using to IRT in weld inspection, particularly for sub-surface defect detection. IRT is a non-contact method and can be applied for in-line weld inspection using a high-temperature range thermal camera.

Four common weld defects were made to be studied in this research including inclusion, porosity, cracking, and lack of fusion. The total number of welded angles was 32, or 38 specimens, including 2 plates with thickness of 13 mm (8/16 in.), 14 angles with thickness of 8 mm (5/16 in.), and 8 angles with thickness of 3 mm (2/16 in.). UT inspection was used to detect defects in 13 mm (8/16 in.) and 8 mm (5/16 in.) specimens.

The specimens then were heated up using a heat gun in heat transmission mode. A thermal camera was set on a tripod and monitored the surface emission of the weld. When the maximum temperature in the ROI on the weld neared 70°C, the heat gun was turned off and the camera started recording thermal sequences with a 10 Hz frequency for 50 s. The recorded sequences were then analyzed to find the rate at which sub-regions in ROIs lost heat by fitting an exponential fit function and calculating the area under this function (A_n). The sound welds had larger values of A_n than the welds with defects. The results of the UT inspection and IRT inspection matched, proving the feasibility of using IRT for weld inspections. UT results for 3 mm (2/16 in.) specimens were not valid; therefore, the two specimens that were built as sound were analyzed to obtain A_n for sound welds. The sub-regions with areas less than sound weld A_n were identified as defected regions. Possible porosity and lack of fusion were detected by this method in 3 specimens, while no defects were detected in the other 3.

Challenges associated with using IRT for weld inspection were as follows:

- Surface clutters and bombs created during welding were not correlated with the presence of defects in the welds but they can be misleading in the captured thermal images. Having these clutters changes the surface emissivity of the material and can cause inaccuracy in the camera's readings, especially in low-emissivity materials.

- The camera used for this study, FLIR SC 640, only measures temperature in the range of -40 to 80°C, which is not suitable for in-line weld inspection. Because the camera is almost 10 years old it was not

compatible with current desktops and required a special chord for desktop connection.

- The transmitted energy from the heat gun used to increase the temperature of the specimens is not homogenous. Some regions got hotter than the others. Using the fit function of the temperature decay instead of using actual temperatures diminished the effects of un-even heating to some extent, but it did not completely resolve it.

- Despite using standard methods to build defects, some defects were hard to create, such as cracks and inclusions. The manufactured porosities were mostly on surface not sub-surface. Lack of fusion was manifested in welds when it was not supposed to; either they were built to have a different defect or no defects at all.

- Welding process which was used to create the welds was uncontrolled and made defect manufacturing very challenging, especially for inclusions. This welding process also resulted in more surface clutters than controlled welding.

- For further study and inspection, the following recommendations are proposed:

- Using high temperature range cameras coupled with a data acquisition system and software.

- Using controlled heat sources to excite the specimens, such as high power halogen or UV lamps.

- Modifying the welding process to a more controlled and less violent procedure such as TIG.

References

ASTM E494-15, Standard Practice for Measuring Ultrasonic Velocity in Materials, ASTM International, West Conshohocken, PA, 2015, www.astm.org

Broberg, P. (2013). Surface crack detection in welds using thermography. *NDT & E International*, *57*, 69-73. https://doi.org/10.1016/j.ndteint.2013.03.008

Consonni, M., Wee, C. F., & Schneider, C. (2012). Manufacturing of welded joints with realistic defects. *Insight-Non-Destructive Testing and Condition Monitoring*, *54*(2), 76-81. https://doi.org/10.1784/insi.2012.54.2.76

Kemppainen, M., Virkkunen, I., Pitkanen, J., Paussu, R., & Hanninen, H. (2003). Realistic Cracks for In-Service Inspection Qualification Mock-Ups. *Journal of Nondestructive Testing*, *8*(3), 1-8. http://lib.tkk.fi/Diss/2006/isbn9512282631/article2.pdf

Manuel, M., and G. Washer. 2017. *Use of Infrared Thermography for the Inspection of Welds in the Shop and Field.* Technical Report, Tallahassee: Florida Department of Transportation

Miller, John Lester. 1994. *Principles of infrared technology: a practical guide to the state of the art.* New York: Van Nostrand Reinhold.

Nelligan, Tom, and Dan Kass. n.d. "http://www.olympus-ims.com/." *http://www.olympus-ims.com.* Accessed 08 09, 2016. http://www.olympus-ims.com/en/ultrasonics/intro-to-pa/.

Wilkinson, Stuart, and Steven M. Duke. 2014. *Comparative Testing of*

Radiographic Testing, Ultrasonic Testing and Phased Array Advanced Ultrasonic Testing Non Destructive Testing Techniques in Accordance with the AWS D1.5 Bridge Welding Code. Technical Report, Tallahassee: The Florida Department of Transportation Research Center.

CHAPTER X

CONCLUSIONS

Summary

This dissertation investigates the applications of non-contact methods for structural assessments of infrastructure. The practice of remote structural health monitoring (SHM) has become very popular with states departments of transportations (DOTs). Remote SHM is supported by two foundations: using unmanned aerial systems (UASs) and applications of image processing and machine learning techniques. This study addressed both of these concepts. The first chapter introduces the research conducted in this dissertation. Chapters two through four of this dissertation are dedicated to the applications of UASs for bridge inspections. In the second chapter, an extensive review is performed in order to identify the potentials/challenges, current practice, and future needs of UAS bridge inspections. Chapter three investigates the minimum requirements for using UASs in inspection of bridges with fracture critical members (FCM). This chapter also includes two UAS-assisted FCM inspections as case studies. Chapter four determines the effects of having different inspections scenarios on the UAS-assisted FCM inspections and provides a comprehensive comparison to a set of hands-on inspection results. Chapter five through eight are dedicated to the applications of image processing and machine learning techniques in concrete crack detection. In chapter five, the performance of six image edge detectors is investigated to find surface cracks on concrete decks. Chapter six investigates using convolutional neural networks (CNNs) with deep learning algorithms for concrete crack detections autonomously. In addition,

the performance of the studied CNNs is compared to the performance of six edge

detectors and a hybrid edge detection methodology is presented. Chapter seven studies

the feasibility of using CNNs for UAS images for concrete crack detection with different

training datasets. Chapter eight presents an image dataset with more 56,000 labeled

images of structural defects (SDNET2018). Finally, in chapter nine, the feasibility of

using infrared thermography for in-line weld inspections is explored.

Conclusions of chapter two

This chapter has outlined the state-of-the-art for bridge inspections and UAS

technology with the aim of educating and informing academics and decision makers

about the current and future capabilities of UAS-assisted or automated bridge inspections.

The current state of practice for bridge inspections, especially in United States, is heavily

tied to visual inspections with minimal use of NDE. Bridge owners have demonstrated

reluctance to accept NDE methods unless they are absolutely required for bridge

evaluations. UAS-assisted bridge inspections have the potential to not only decrease

costs, but to also improve the adoption of NDE technologies, potentially increasing

inspection accuracy, however UAS inspections face major hurdles.

UASs have shown promising results in civilian applications as well as civil

engineering purposes, and many state DOTs have performed feasibility studies and found

significant limitations, but also successes. The most common UAS applications in DOTs

were traffic monitoring and surveillance, road condition assessment, and mapping;

however, significant effort has been put into bridge structure inspection with varying

degrees of success. The perception of UAS effectiveness for bridge inspection is tied to

several variables, including DOT expectations, pilot skill, weather condition, and off-the-shelf limitations. It was shown that, ideally, UASs can provide less expensive and less time-consuming inspections for under bridge regions without traffic closure, but not in all situations and there are obstacles to overcome. FAA regulations have recently relaxed, but impose significant limitations, including required line of sight and UAS certification. Using advanced NDE sensors or even visual images can become too burdensome to be effective for routine inspections. Current autopilot controls have become a severe limitation for under bridge inspections due to the loss of GPS signals, causing a UAS to rely on a vision positioning system or a suite of other sensors which are questionably useful in the severe under-bridge environment.

The literature identified two major potential functions for UAS based inspections: 3D model reconstruction and autonomous damage identification. Unfortunately, these functions face major implementation limitations in order to be functional for complex – or even routine – inspections. Programs capable of generating 3D reconstructed bridge models, from either SFM or MVS, using feature detectors and feature descriptors such as SIFT and SURF have been used for 3D model reconstructions of building, sites, and objects, but are very time consuming and require highly skilled technicians. These models have promising applications for UAS navigation but are unlikely to be accurate enough for bridge inspections without significant advancements. Autonomous defect detection methods are another promising advantage for UAS-assisted bridge inspections. Surface defect detection, for example, cracks, spalls, and surface degradation, have been successfully detected from visual images. Delaminated regions have been located and measured using thermal imagery on concrete bridge decks. A major hurdle to the

adoption of these methods for UAS bridge inspection is resistance from bridge owners that have historically not implemented NDE technologies.

Based on the synthesis of this state-of-the-art review of bridge inspection and UASs, the following conclusions can be made:

- The review of current bridge inspection practices makes it clear that there is a need for continuous improvement of bridge inspection procedures and cost reductions. Several NDE technologies were identified that can provide a better inspection but, based on DOT surveys, may not be worth the time, effort, post-processing, and cost associated with them. UAS sensors may also fall within this category. Improvements should take the form of reduced inspection time and increased inspector and public safety, as well as decreased inspection costs, all of which indicate the need for automated inspections. If automated inspection processes are going to replace standard practice, then they must be robust and require a similar amount time and effort to current bridge inspections techniques in order to gain widespread adoption.

- The recent advances of UASs and UAS have the potential to shift the bridge inspection paradigm by providing low cost options to gather previously difficult or expensive images.

- UASs have increased in popularity and functionality for many applications, but the challenging nature of bridge inspections has reduced their effectiveness in this area. UASs can also decrease the allocated time and

budget for large-scale bridge inspections by providing inspection data comparable to hands-on method.

- There have been mixed successes for UAS-assisted bridge inspections throughout the United States that have resulted in successful inspections of easily accessible locations where the UAS has access to GPS, the most reliable and effective tool for UAS autopilots (see Table 2-5).

- There is a major need for improvements in the areas of UAS controls, navigation, and image processing in order to maintain effectiveness.

- Weather currently plays too big of a role in UAS flight success, which is a very significant barrier for many state agencies with very tight inspection schedules. This can be mitigated with continued improvement of autopilot controls in GPS-denied environments. UAS controls need to improve such that a pilot can safely and effectively obtain stable images of every part of the bridge in any reasonable weather.

- For UAS inspections to become commonplace and cost-effective, automated inspection may need to become a reality, or at least, vast improvements will need to be made on autopilot controls. Based on the above syntheses, full automation during a bridge inspection is not possible given current technology and environmental challenges.

- Image processing techniques (3D mapping or damage detection) that can detect defects are a significant advantage of a UAS inspection, but without the possibility of a real-time inspection will not become a routine part of any

bridge inspection soon due to the level of detail required.

- Bridge owners must learn to accept and become comfortable with the non-contact NDE techniques unique to UAS inspections for the full potential of UAS bridge inspection to be realized. This places the burden on industry and researchers to develop accurate, generic algorithms for post-processing that can facilitate a real-time inspection or fit within existing local bridge inspection constraints.

- Current FAA restrictions are not too burdensome for an agency to perform some inspections, but provide significant challenges to be useful in all situations. Regulations will relax over time, as public perception, UAS reliability, and autonomous controls continue to improve.

Conclusions of chapter three

Previous literature demonstrates the application of UAS for initial inspection of bridges, visual and autonomous detection of delamination or cracking in concrete, and checking the surface condition of structures. This chapter investigated the application of UAS for detection of fatigue cracks in steel bridges during FCM inspections.

Laboratory investigations revealed the importance of camera quality and surface illumination on the maximum crack-to-camera (MCC) distance at which fatigue cracks can be detected. Observed MCC distances with stable cameras (fixed, not in flight) ranged from 0.3 m for the worst performing platform in dark lighting to 1.1 m for the best performing platform in bright light. Mock FCM inspections demonstrated the difficulties in detecting known cracks in GPS-denied or windy environments. Some platforms were

unstable in GPS-denied indoor environments and thus clear images were not obtainable.

The best performing platform has an achievable crack-to-platform (ACP) distance that

was far smaller than the previously determined MCC distance, meaning it was easily able

to obtain clear enough images for crack detection. This was true for both real-time

(inspection from FPV monitor during flight) and post-flight (inspection of recorded

images after flight) inspections. Note the results in this study do not cover all scenarios in

FCM bridge inspection and are valid for the described conditions of the mock inspection.

Nevertheless, the findings can serve as a guideline for bridge inspectors in order to

perform more successful UAS-assisted FCM inspections.

Two FCM inspections of structures with known fatigue cracks demonstrated the

ability of the UAS platform to identify fatigue cracks in the field. The first, at Fall River

Bridge in Ashton, ID, was inconclusive due to marker obscuring the potential fatigue

cracks. The inspector was able to rule out the presence of fatigue cracks in several

inspection locations. However, the inspector was unable to identify fatigue cracks in

locations that were known to contain them. This was mainly due to limited ACP

distances in gusting winds and obscuration of the cracks by markings from previous

inspections. The Falls River inspection also indicated that GPS denied navigation,

combined with the 10 m/s (22 mph) wind gusts made controlled flight near impossible.

Also, the stereo-vision positioning, which enables some control in when GPS-denied,

causes significant instability over water and FAA line of sight requirements eliminated

accessibility to nearly half of the structure due to sight conditions.

The second field inspection, at the S-BRITE Center training facility at Purdue

University, compared the performance of UAS inspections and human inspections. UAS

inspection was comparable to hands-on inspection in terms of the number of real cracks that were identified. However, UAS inspections took far longer and resulted in a much higher number of false positives. In general, the results of this laboratory and field study show that fatigue crack identification during FCM inspections is promising using UAS, however challenges exist and more research is needed prior to routine use of UAS for fatigue crack detection.

Moving from manned to unmanned inspections, particularly for bridges with Fracture Critical Members (FCM), requires using Unmanned Aerial Systems (UASs) with auxiliary positioning systems to compensate with the lack of GPS signals. The results of this study suggest that using UAS that rely heavily on GPS signals for navigation is very difficult and unlikely to produce fatigue crack detection. The stability of many systems in the GPS denied environment poses a risk to the UAS, pilot and mission. UAS pilots may not wish to risk their UAS in such situations until better autonomous position control is available. Among studied UASs, inspection using the DJI Mavic Pro was more successful than the others due to stereo-vision positioning system; however, this system causes instability when the UAS is over a current like a river (a common situation during FCM inspections). Future UASs for FCM bridge inspections are required to have small sizes, more reliable positioning systems in lieu of GPS signals, wind and turbulence resistivity, clearance measurement capability (laser range finder), 360-degree gimbal, onboard adjustable light source, and adjustable camera setting for exposure and optical zoom. As of now, a commercial UAS that meets these requirements does not exist. DJI Mavic family UASs satisfy some of the requirements making them a proper candidate for UAS-assisted FCM inspections. The results presented in this chapter

are based on limited number of inspections which definitely does not mimic all possible inspection scenarios. More UAS-assisted FCM inspections are required to draw a comprehensive conclusion on the performance of UASs in terms of accuracy, hits, and inspection time.

Conclusions of chapter four

Inspection of bridges with fracture critical members (FCM) is among the most challenging tasks for the bridge community to perform since these bridges are susceptible to fatigue cracks. The current practice for FCM inspection is hands-on inspection with application of some sort of non-destructive evaluation (NDE) method if necessary. Successful applications of Unmanned Aerial Systems (UASs) in state departments of transportation (DOTs) in the past make them an interesting option for FCM inspections; however, there are no studies investigating the factors for an effective UAS-assisted FCM inspection.

The research team conduct four UAS-assisted inspections on a probability of detection (POD) training structure at the Steel Bridge Research, Inspection, Training, and Engineering (S-BRITE) center at Purdue University to locate the fatigue crack(s). Each inspection included a different inspector, accompanied by a pilot flying a DJI Mavic UAS, inspecting different types of the specimens on the POD frame through a first person view (FPV) monitor. The video streamed to the FPC monitor was also recorded and stored for another phase of the study. The inspectors marked the location of cracks on a binder that was used to evaluate their performance. The metrics of this study were hit rate (HR), hit to call ratio (HCR), length of the largest crack missed (LCM), and

inspection time (T). The inspection videos of 54 specimens for each day of inspection were shared with 19 bridge inspectors to perform desk inspections by reviewing them and marking the cracks. The selected specimens included the three types of specimens on the POD frame: out of plane (OOP), welded cover plate (WCP), and riveted cover plate (RCP). Based on the results, the following remarks can be made:

- Wind speed had a noticeable effect on the metrics of both field and desk inspection. (results were better for the days with lower wind speeds)

- Inspectors performed considerably better on the OOP and RCP specimens than the WCP specimens due to the locations of WCP specimens and limited upward tilt-angle of the DJI Mavic.

- Lower workload experienced by the inspectors resulted in better inspection metrics.

- Inspectors employed by private agencies performed marginally better than the DOT inspectors.

- Using a media player with zoom and brightness adjustment improves the desk inspections.

- The hands-on inspections had better metrics than the UAS-assisted inspections for all specimens; however, the UAS-assisted inspections produced similar metrics, except for T, to the hands-on inspections for OOP and RCP specimens.

- The LCM was the only metric that was better in the desk inspections

- The desk inspections and the field inspections were 98% and 38% more

time-consuming than the hands-on inspections, respectively.

This study shows the potential of implementing UAS-assisted inspections for future FCM inspections. Considering none of the inspectors were trained or participated in UAS inspections before, the results are promising. The authors recommend the following for future work to improve the inspection results:

- Performing the inspections using a UAS with at least a 90-degree tilt-angle.

- Providing UAS-assisted training sessions for the inspectors before the inspection.

Preforming the desk inspections on similar monitors with equal or higher resolution than the videos.

Conclusions of chapter five

This study proposed a generic image-processing algorithm for detection of defects in concrete for the purpose of comparing different edge detection algorithms. The proposed algorithm involved edge detection, edge image enhancement, and segmentation. Edge detection was completed in the spatial domain using Roberts, Prewitt, Sobel, and LoG filters; and in the frequency domain using Butterworth and Gaussian filters. Fifty images of defected concrete and fifty of sound concrete were analyzed by the proposed algorithm in six iterations making use of the six aforementioned edge detection strategies). An inspector reviewed the resulting binary images from each iteration and identified cracks. The inspection results were compared to the ground truth, and the six edge detection methods were compared based on accuracy, precision, minimum

detectable crack width, and processing time per image. Edge detection in the spatial

domain using LoG filter yielded the highest accuracy (92%) and precision (88%), the

finest minimum detectable crack width, and the fastest processing time (1.18 s per

image). All but one of the remaining methods (edge detection in the spatial domain using

Roberts filter) yielded greater than 80% accuracy and were able to detect cracks as fine as

0.2 mm. While crack detection in the spatial domain using Roberts filter yielded the

lowest accuracy (77%), it also yielded the fewest false positives (10%) and its precision

(86%) was among the highest. In general, the processing time was longer for crack

detection in the frequency domain (1.8–1.9 s per image) than in the spatial domain (1.2–

1.7 s per image). Additionally, the second-level binary images (the final product of the

image processing algorithm) were much noisier in the frequency domain. According to

these results, crack detection in the spatial domain using LoG filter yields the best and

fastest results for detecting defects in concrete structures.

Conclusions of chapter six

This chapter presents a comparison of edge detection and DCNN algorithms for

image based concrete crack detection. The dataset consisted of 3420 sub-images of

concrete cracks. Several common edge detection algorithms were employed in the spatial

(Roberts, Prewitt, Sobel, and LoG) and frequency (Butterworth and Gaussian) domains.

AlexNet DCNN architecture was employed in its fully trained, classifier, and fine-tuned

modes. Edge detection schemes performed reasonably well. The best method—LoG—

accurately detected about 79% of cracked pixels and was useful in detecting cracks

coarser than 0.1 mm. In comparison, the best DCNN method—the network in transfer

learning mode—accurately detected 86% of cracked images and could detect cracks coarser than 0.04 mm. This represents a significant performance enhancement over edge detection schemes and shows promise for future applications of DCNN for image based crack detection in concrete. In addition, a methodology was proposed to reduce the FNs reports by 70% by applying the edge detectors only on sub-images not labeled as uncracked. In addition, a hybrid crack detector was introduced which combines the advantages of both approaches. In the hybrid detector, the sub-images were first labeled by the network in the fully trained mode. Since it produced the highest TNR, the edge detector is not applied on the sub-images labeled as U (uncracked) by the network. This technique reduced the noise ratio of the LoG edge detectors from 2.4% to 0.11% and has the similar effect on the other edge detectors as well.

This study shows the superiority of an AlexNet DCNN over traditional edge detectors for concrete crack detection. This superiority can be further improved when architectures such as GoogleNet or RestNet are implemented for crack detection. DLCCNs are able to classify multiple defects if enough annotated images are available for training. Formation an annotated image dataset for structural defects, such as ImageNet, is vital for further applications of DCNNs in structural engineering. With this dataset available, new architectures can be proposed to focus on finding structural defects instead of random objects, which will reduce the computational time associated with training process. In addition, domain adaptation methods such as transfer learning, will be more effective if the network is previously trained on the structural defects dataset. Improving the performance of domain adaptation techniques makes real-time defect detection in robotic vision-based inspections feasible. In other words, a pre-trained

DCNN on the structural defect dataset, can be directly used to accurately classify new images taken by an unmanned aerial system to different structural defects as the inspection is taking place.

Conclusions of chapter seven and eight

The application of deep learning convolutional neural networks for sUAS-assisted inspection of concrete structures is investigated in this paper. A convolutional neural network using AlexNet architecture was fully trained on a set high-quality point-and-shoot images to achieve a desirable accuracy (FT mode). In addition to the FT mode, a pre-trained neural network with the same architecture, on the ImageNet, was re-trained on the training dataset using transfer learning for comparison purposes (TL mode). The training and validation process for FT mode was 50% more time-consuming; however, it provides better accuracy (about 3%) in validation process. The network in FT mode on the other hand, performs better than the TL mode in crack detection (better true positive) in validation dataset. To investigate the challenges in sUAS-assisted structural inspections of infrastructure, three datasets are gathered and the network performance is evaluated in both modes. The image in the first dataset are from the same cracks but taken by a low resolution camera on a sUAS. The image in the second dataset are from the same structures, i.e. decks, but taken by a sUAS with comparable resolution to the point-and-shoot camera. The image in the third dataset are from a different structure, i.e. building, by a sUAS with comparable resolution. The results showed that the true positive (TP) reports were higher when the FT mode was used. However, using the network in TL mode improves the true negative (TN) reports over the FT mode. The

accuracy of the network in both modes declined facing the new datasets from over 80%
in the first dataset to 79% in the second dataset and to 58.4% in the third dataset in the
fully trained mode. The accuracy in TL mode was 88% in the first dataset and decreased
to 64% in the third dataset. The network in the FT mode detected more cracks in all
datasets than the TL mode (between 6% to 15%); however, using transfer learning
resulted the network achieved greater accuracies (7% to 15%). Both TP and TN reports
decrease when the networks are tested on the testing datasets. The networks are shown to
perform better in the first dataset showing it is important to have similar defects in the
training and testing dataset. When the cracks are different but on similar structures, i.e.
the second dataset, the accuracy dropped significantly and it got worse when the pattern,
size, and the background of the cracks were changed in the third dataset. To improve the
results, the training dataset should be more comprehensive to include the possible
features in the inspection images. Using higher quality cameras on the sUAS helps the
detection rate. The AlexNet architecture can be replaced with different accurate
architectures such as ResNet, to improve the network performance.

Conclusions of chapter nine

Verification of weld safety and workmanship is paramount to structural weld
inspection both during fabrication and in-service. Weld inspections are costly in terms of
time and money for both situations. Ultrasonic (UT) technique has been widely used to
detect surface and sub-surface defects of welds. Because UT inspection is an inspection
with contact, the inspector needs to wait for the welds to cool down for one to a six hours.
This adds time, and consequently cost, to the inspection process. The purpose of this

study is to investigate the potentials and challenges of using to IRT in weld inspection, particularly for sub-surface defect detection. IRT is a non-contact method and can be applied for in-line weld inspection using a high-temperature range thermal camera.

Four common weld defects were made to be studied in this research including inclusion, porosity, cracking, and lack of fusion. The total number of welded angles was 32, or 38 specimens, including 2 plates with thickness of 13 mm (8/16 in.), 14 angles with thickness of 8 mm (5/16 in.), and 8 angles with thickness of 3 mm (2/16 in.). UT inspection was used to detect defects in 13 mm (8/16 in.) and 8 mm (5/16 in.) specimens. The specimens then were heated up using a heat gun in heat transmission mode. A thermal camera was set on a tripod and monitored the surface emission of the weld. When the maximum temperature in the ROI on the weld neared 70°C, the heat gun was turned off and the camera started recording thermal sequences with a 10 Hz frequency for 50 s. The recorded sequences were then analyzed to find the rate at which sub-regions in ROIs lost heat by fitting an exponential fit function and calculating the area under this function (A_n). The sound welds had larger values of A_n than the welds with defects. The results of the UT inspection and IRT inspection matched, proving the feasibility of using IRT for weld inspections. UT results for 3 mm (2/16 in.) specimens were not valid; therefore, the two specimens that were built as sound were analyzed to obtain A_n for sound welds. The sub-regions with areas less than sound weld A_n were identified as defected regions. Possible porosity and lack of fusion were detected by this method in 3 specimens, while no defects were detected in the other 3.

Challenges associated with using IRT for weld inspection were as follows:

- Surface clutters and bombs created during welding were not correlated with the presence of defects in the welds but they can be misleading in the captured thermal images. Having these clutters changes the surface emissivity of the material and can cause inaccuracy in the camera's readings, especially in low-emissivity materials.

- The camera used for this study, FLIR SC 640, only measures temperature in the range of -40 to 80°C, which is not suitable for in-line weld inspection. Because the camera is almost 10 years old it was not compatible with current desktops and required a special chord for desktop connection.

- The transmitted energy from the heat gun used to increase the temperature of the specimens is not homogenous. Some regions got hotter than the others. Using the fit function of the temperature decay instead of using actual temperatures diminished the effects of un-even heating to some extent, but it did not completely resolve it.

- Despite using standard methods to build defects, some defects were hard to create, such as cracks and inclusions. The manufactured porosities were mostly on surface not sub-surface. Lack of fusion was manifested in welds when it was not supposed to; either they were built to have a different defect or no defects at all.

- Welding process which was used to create the welds was uncontrolled and made defect manufacturing very challenging, especially for inclusions.

This welding process also resulted in more surface clutters than controlled welding.

- For further study and inspection, the following recommendations are proposed:

- Using high temperature range cameras coupled with a data acquisition system and software.

- Using controlled heat sources to excite the specimens, such as high power halogen or UV lamps.

Modifying the welding process to a more controlled and less violent procedure such as TIG.

CHAPTER XI

CURRICULUM VITAE

Sattar Dorafshan

Ph.D.

Department of Civil and Environmental Engineering

Utah State University, Logan, UT-84321-4110

Cell phone: (435) 757-3740

E-mail: Sattar.dor@aggiemail.usu.edu

Education

Ph.D., Civil Engineering (Structural)	Aug
Utah State University, Logan, UT, USA.	2018
Dissertation: "Non-contact Evaluation Methods for Infrastructure Condition Assessment" Advisor: Dr. M. Maguire	
M.Sc., Civil Engineering (Structural)	May
Isfahan University of Technology, Esfahan, Isfahan, Iran.	2011
Thesis: "Green function calculation in irregular media using Condensed hyper-elements method (CHM)" Advisor: Dr. F. Behnamfar	
B.Sc., Civil Engineering	May
Tabriz University, Tabriz, Azarbayjan-Sharghi, Iran.	2008
Thesis: "Applications of shotcrete in tunnels", Advisor: Dr. M.H. Aminifar	

Research Interests

Structural health monitoring

Remotes sensing

Non-contact condition assessments

Data fusion

Earthquake engineering

Seismic rehabilitation and retrofit

Pre-stressed and reinforced concrete structures

Thermography

Deep learning Infrastructure inspections

Research Experience

Graduate Student/Research Assistant, Department of Civil and   2015-

Environmental Engineering, Utah State University   present

Studied applications of remote sensing for autonomous infrastructure   Logan, UT

condition assessment.

Developed novel image-based techniques for crack detection in concrete

structures.

Investigated deep learning neural networks for structural health

monitoring.

Explored and analyzed different thermography methods for weld

inspection.

Investigated friction values for slide-in bridge construction.

Developed deal impact factors for bridge moves in accelerated bridge

construction.

Identified common heat loss sources in sandwich wall panel systems.

Graduate Student/Research Assistant, Department of Civil and   2008-2011,

Environmental Engineering, Isfahan University of Technology   Isfahan, Iran

Developed a novel numerical method for analysis of soil-structure

interaction

Assessed the seismic performance of structures and equipment in

Isfahan power house and electrical post

Professional Practice

Professional Licensed Structural Engineer, Tehran Construction   2013-2015,

Engineering Organization   Tehran, Iran

Designed a 9-Story concrete building.

Designed the units for International Shahrood Resort Center.

Supervised the construction of a 9-story concrete building.

Supervised the construction of a 5-story concrete building.

Teaching Experiences

Co-instructor, Department of Civil and Environmental   2017-2018

Engineering, Utah State University   Logan, UT

Developed second-order analysis of the curriculum, grading,

preparing assignments, and grading.

"Advanced Steel Design", Spring 2017, Spring 2018

Co-instructor, Department of Civil and Environmental   2017-2018

Engineering, Utah State University   Logan, UT

Developed prestressed losses of the curriculum, preparing and

grading assignments.

"Precast/Prestressed Concrete", Fall 2017, Fall 2018

Instructor, Department of Civil and Environmental   2012

Engineering, Azad University.   Isfahan, Iran

Developed curriculum in all areas including instruction,

grading, preparing tests (quizzes, midterms, finals), holding

office hours, and assigning final grades.

"Strength of Materials Lab", Spring 2012

"Statics", Spring 2012

"Structural Analysis", Spring 2012

"Principal of Earthquake Engineering", Summer 2012

"Design of Steel Structures II", Summer 2012

Instructor, Department of Civil and Construction

Engineering, Payam-e-Noor University.

"Strength of Materials", Spring 2012

"Statics", Spring 2012

Instructor, Department of Civil and Construction

Engineering, Amoozesh Ali University.

"Strength of Materials", Spring 2012

"Precast and Prestressed Concrete", Spring 2012

"Concrete Building Regulations", Spring 2012

Instructor, Department of Civil Engineering, Allameh Naeeni   2011

University.   Naeen, Iran

"Design of Steel Structures I", Fall 2010

"Construction Materials", Fall 2010

"Computer Programming", Fall 2010

Professional Affiliations

Licensed structural engineer, Tehran Construction Engineering Organization (TCEO).

Prestressed/Precast Concrete Institute (PCI).

American Society for Non-destructive Testing (ASNT).

American Institute of Steel Construction (AISC).

American Society of Civil Engineers (ASCE).

American Wood Council (AWC).

Grants

Role	Year	Name	Funding Source	Amount ($)
Graduate Researcher	2015	Recommended Guidelines for Prefabricated Bridge Elements and Systems Tolerances and Dynamic Effects of Bridge Moves	National Cooperative Highway Research Program (NCHRP)	93,833
Graduate Researcher	2016	Unmanned Aerial System for Detecting Fatigue Cracks in Bridge Inspection	Idaho Transportation Department (ITD)	45,725
Graduate Researcher	2017	Database Logging and Decision Process for Steel Traffic Signal Replacement	Utah Department of Transportation (UDOT)	70,000
Graduate Researcher	2017	Infrared In-Line Weld Inspection-Feasibility Study	Nucor Building Systems	26,742

Publications and presentations

Journals:

Dorafshan, S., Thomas, R., Coopmans, C., Maguire, M., Practitioner's Guide to Small Unmanned Aerial Systems for Bridge Inspection, submitted to the Practice Periodical on Structural Design and Construction.

Dorafshan, S., Thomas, R., Maguire, M. SDNET2018: An annotated image dataset for non-contact concrete crack detection (Submitted to Elsevier Data in Brief)

Dorafshan, S., Johnson, K., Culmo, M., Maguire, M., Halling, M., Barr, P., Friction coefficients for slide-in bridge construction using PTFE and steel sliding bearings (Submitted to Journal of Bridge Engineering).

Dorafshan, S., Culmo, M., Maguire, M., Halling, M., Barr, P., Investigating the Dynamic Effects Caused by SPMT Bridge Moves, (Submitted to Journal of Bridge Engineering).

Dorafshan, S., Maguire, M., In-Line Weld Defect Detection in Steel Joists Using Thermography (Submitted to Infrastructures)

Dorafshan, S., Thomas, R., Maguire, M., Image Processing Algorithms for Vision-based Crack Detection in Concrete Structures (Submitted to Infrastructures)

Dorafshan, S., Thomas, R., Maguire, M., (2018). Comparison of Deep Convolutional Neural Networks and Edge Detectors for Image-Based Crack Detection in Concrete. Journal of Construction & Building Materials. 186. 1031-1045. https://doi.org/10.1016/j.conbuildmat.2018.08.011

Dorafshan, S., Maguire, M., Bridge Inspection: Human Performance, Unmanned Aerial Vehicles and Automation (2018). Journal of Civil Structural Health Monitoring.

8(3), 443-476. DOI: 10.1007/s13349-018-0285-4

Dorafshan, S., Thomas, R., Maguire, M., Fatigue Crack Detection Using Unmanned Aerial Systems in Fracture Critical Inspection of Steel Bridges (2018). Journal of Bridge Engineering. 23 (10) 04018078. DOI: 10.1061/(ASCE)BE.1943-5592.0001291

Behnamfar F., Dorafshan S., Taheri A., and Hashemi B.H., (2015) "A method for rapid estimation of dynamic coupling and spectral responses of connected adjacent structures", The Structural Design of Tall and Special Buildings, Published online in Wiley online library. DOI: 10.1002/tal.1247.

Dorafshan, S., Behnamfar, F., Khamesipour, A., & Motosaka, M. (2013). Condensed hyperelements method of non-vertical consistent boundaries for wave propagation analysis in irregular media. *Earthquake Engineering and Engineering Vibration*, *12*(4), 547-559.

Refereed Conferences:

Dorafshan, S., Coopmans, C., Thomas, R., Maguire, M. (2018). Deep Learning Neural Networks for sUAS-Assisted Structural Inspections: Feasibility and Application, ICUAS18. IEEE. Dallas Marriot City Center, Dallas.

Johnson, K., Halling, M., Dorafshan, S., Maguire, M., Barr., P., and Culmo, M., (2018) "Bearing friction values for slide-in bridge construction". 9th International Conference on Bridge Maintenance, Safety and Management, Melbourne.

Dorafshan, S., Maguire, M., Halling, M., and Barr, P., (2018) "Dynamic Effects Caused by SPMT Bridge Transport". 9th International Conference on Bridge Maintenance, Safety and Management, Melbourne.

Dorafshan, S., Maguire, M., Hoffer, N. V., & Coopmans, C. (2017, June). Challenges in bridge inspection using small unmanned aerial systems: Results and lessons learned. In *Unmanned Aircraft Systems (ICUAS), 2017 International Conference on* (pp. 1722-1730). IEEE. DOI: 10.1109/ICUAS.2017.7991459.

Al-Rubaye, S., Sorensen, T., Dorafshan, S., & Maguire, M. (2018). Matrix Model Accuracy of Partially Composite Concrete Sandwich Panels. PCI Convention, 2018. Precast/Prestressed Concrete Institute (PCI).

Sorensen, T., Dorafshan, S., & Maguire, M. (2017). Thermal Evaluation of Common Locations of Heat Loss in Sandwich Wall Panels. In Congress on Technical Advancement 2017 (pp. 173-184). https://doi.org/10.1061/9780784481011.017.

Non-Refereed Conferences:

Andalib, Z., Caputo, P., Dorafshan, S., Maguire, M., and Collins, W. (2018) "Investigation into the Behavior of an Open Web Steel Joist Bridge." Proceedings of *The International Bridge Conference, IBC 18-64*, National Harbor, MD, June 12.

Dorafshan, S., & Maguire, M. (2017, June). Autonomous Detection of Concrete Cracks on Bridge Decks and Fatigue Cracks on Steel Members. In *Digital Imaging 2017* (pp. 33-44), Foxwoods Resort and Casino in Mashantucket, CT. https://ndtlibrary.asnt.org/2017/AutonomousDetectionofConcreteCracksonBridgeDecksa ndFatigueCracksonSteelMembers.

Dorafshan S., Maguire, M., and Chang, M., (2017). Comparing Automated Image-Based Crack Detection Techniques in Spatial and Frequency Domains, 26th ASNT Research Symposium, Jacksonville, Florida.

Invited Conferences:

Dorafshan, S., Maguire, M., Detection of Delaminated Regions and Surface Cracks of a Concrete Bridge Deck Using Unmanned Aerial Systems, A Case Study. 9th International Conference on Structural Health Monitoring of Intelligent Infrastructure (SHMII-9). August 4-7 2019. St. Louis. Missouri.

Dorafshan, S., Campbell, L., Maguire, M., Connor, R., Post-Flight Inspection of Bridges with Fracture Critical Members using Unmanned Aerial Systems. 9th International Conference on Structural Health Monitoring of Intelligent Infrastructure (SHMII-9). August 4-7 2019. St. Louis. Missouri.

Dorafshan, S., Thomas, R., Maguire, M., Deep Learning Convolutional Neural Networks for Concrete Bridge Inspection, Maintenance, and Monitoring. ACI Concrete Convention Fall 2018. October 14-18, Rio All-Suites Hotel & Casino, Las Vegas, NV.

Dorafshan, S., Maguire, M., (May 2018), Investigating most common deep learning architectures for concrete crack detection. 2018 conference of Engineering Mechanics Institute (EMI 2018). Massachusetts Institute of Technology (MIT), Boston, MA.

Dorafshan, S., Coopmans, C., Maguire, M., (May 2018), Using deep learning neural network-based techniques for concrete crack detection from unmanned aerial system imagery. 2018 conference of Engineering Mechanics Institute (EMI 2018). Massachusetts Institute of Technology (MIT), Boston, MA.

Conference Presentation:

Bellon, W., Dorafshan, S., Maguire, M., Halling, M., and Barr, P. (2017). Standardizing Accelerated Bridge Construction, Poster Presentation, Utah Research on Capitol Hill. DOI 0.13140/RG.2.2.18933.17121.

Technical Reports:

Dorafshan, S., Maguire, M., (2018). "Infrared In-line Weld Inspection – Feasibility Study", Nucor Building Systems.

Johnson, K., Halling, M., Dorafshan, S., Maguire, M., Barr., P., and Culmo, M., (2018). "Dynamics and Friction of ABC Bridge Moves," CIAT-UTC-NC 13, Final Report.

Dorafshan, S., Maguire, M., Hoffer, V., Coopmans, C., Thomas, R., (2018)., "Investigating Unmanned Aerial Systems for Fatigue Crack Detection." CIAT-UTC-NC31, Final Report. Piscatway, NJ.

Dorafshan, S., Maguire, M., Hoffer, V., Coopmans, C., (2017). "Fatigue Crack Detection Using Unmanned Aerial Systems in Under-Bridge Inspection." Idaho Transportation Department, Final Report.

Dorafshan, S., Maguire, M., and Qi, Xi., (2016). Automatic Surface Crack Detection in Concrete Structures Using OTSU Thresholding and Morphological Operations, *Civil and Environmental Engineering Faculty Publications.* Paper 1234. https://digitalcommons.usu.edu/cee_facpub/1234

Dorafshan, S. and Salimi, M., (2010) "Qualitative and rapid seismic performance evaluation of electrical post of 400/62 k.v. Electrical post of Shahre-Kord buildings and equipment report", Esfahan regional electric company (Persian), Isfahan, Iran.

Dorafshan, S. and Salimi, M., (2009) "Qualitative and rapid seismic performance evaluation of Isfahan power plant buildings and equipment report," Esfahan regional electric company (Persian), Isfahan, Iran.

Honors and Awards

Winner of the Dissertation Fellowship Award, Office of Research and Graduate Studies, Utah State University, 2018.

Doctoral researcher of the year, Department of Civil and Environmental Engineering, Utah State University, 2016.

Winner of the ACI Intermountain scholarship award, Salt Lake City, 2015.

Graduate assistantship award, Department of CEE, Utah State University, 2015 to present.

Ranked 405 in national graduate entrance exam (Konkour-e-Arshad) among 20,000 participants, Iran, 2008.

Ranked 4,000 in national undergrad entrance exam (Konkour) among 300,000 participants, Iran, 2004.

Languages

Farsi: native

English: fluent